

**Deploying nanotechnology for oil and gas flow assurance: Understanding the transport and penetration of nano-particles in porous media**

**by**

**Boya Subhono**

**Submitted in accordance with the requirements for the degree of  
Doctor of Philosophy**

**The University of Leeds  
School of Mechanical Engineering**

**December 2014**

The candidate confirms that the work submitted is his own and that appropriate credit has been given where reference has been made to the work of others.

This copy has been supplied on the understanding that it is copyright material and that no quotation from the thesis may be published without proper acknowledgement.

The candidate confirms that the work submitted is his own, except where work that has formed part of jointly authored publications has been included. The contribution of the candidate and the other authors to this work has been explicitly indicated below. The candidate confirms that appropriate credit has been given within the thesis where reference has been made to the work of others.

The candidate undertook major tasks of the work presented in these published papers, such as undertaking experimental works, design, analysing and presenting the results. The co-authors reviewed and guided the candidate and provided valuable discussion.

This copy has been supplied on the understanding that it is copyright material and that no quotation from the thesis may be published without proper acknowledgement.

The right of Boya Subhono to be identified as Author of this work has been asserted by him in accordance with the Copyright, Designs and Patents Act 1988.

*Alhamdulillahirabbil Alamiin...*

*To my wife, Andira Aranandita, who has been patient, supportive, and shared many sacrifices for completing this thesis. To my mother and father, for their endless support. And to my first son, Abilashfachry Subhono for the short but meaningful togetherness*

*and also my first daughter*

*Sahsrakinaring Subhono*

*“One thousand of the holiest brightest light”*

## **ACKNOWLEDGEMENTS**

It is a great pleasure to thank everyone who helped and supported me throughout my PhD study to make this research successfully.

First, I owe the most sincere and earnest thanks to my main supervisor, Dr. Mark CT Wilson, for all of his supportive guidance, assistance, encouragement, and advice throughout the entire research. He has been my advisor, my tutor, and, in the same time, my best friend while pursuing the PhD degree in the University of Leeds.

Secondly, I owe my deepest gratitude to my second and third supervisor, Prof. Nikil Kapur and Prof. Anne Neville for their extraordinary constructive ideas, supports, and enlightening discussions, which guided me to spot the research point.

Thirdly, I am indebted to my Statoil colleagues Niall Fleming for sharing experiences, knowledge, and advice.

Fourthly, I would like to thank Flow Assurance and Scale Team (FAST) Joint Industry Project (JIP) consortium and the University of Leeds in the United Kingdom for their financial support throughout the study.

Finally, I would like to express appreciation and love to my father and mother in Indonesia for their infinite love and support. I would like to express my special thanks for my beloved wife, Andira Aranandita for encouragements and sharing good and hard times, my dear son, Abhilashfacy Subhono for the short but meaningful togetherness, and my beloved daughter that was born exactly in the same week with my final PhD viva, Sahsrakinaring Subhono.

## ABSTRACT

Scaling problem is one of the common engineering challenges in 'flow assurance' in the oil and gas industry. Since mechanical or chemical treatment frequently requires sacrifice in fluid production, it is often preferable to avoid this problem, for example by conducting a scale squeeze treatment. This treatment includes an injection of scale inhibitor to hinder scale formation in the rock. Its effectiveness corresponds to its attachment lifetime in the rock formation. This is where nanotechnology has an important role for its capability to enhance the attachment of the scale inhibitor on the rock surface. The question that arises is how and where the injected nanoparticles are distributed and attached on the walls of the rock pores. It is difficult and costly to perform evaluations in pores of a rock formation in an actual oil field. Therefore developing a computer simulation is necessary.

This research has successfully demonstrated a development of simulator to explore the science and engineering of nanoparticle transport in microchannels. The phenomenon in the system are explored using a combination of model experimental systems and novel Finite Element Analysis (FEA) computational simulations of fluid flow in microchannels of porous structures. The effect of the advection, diffusion, microchannel's surface roughness and curvature variety to the nanoparticle transport in the system are investigated. It is discovered that the adsorption is encouraged by diffusion when the advection is insignificant. When advection is significant, a plenty of injected nanoparticle is needed to achieve similar adsorption in a system with diffusion domination. Nanoparticles are transported less effectively in microchannel with high curvature configuration. The density of the adsorption distribution in this type of microchannel is less uniform than in microchannel with simpler curvature. Rough surface increases the adsorption, where the distribution of nanoparticles into dead-end region in the microchannel system is governed by diffusion. The modelling framework in this thesis is versatile to use for modelling any transport that is coupled with surface phenomenon in microchannel system by changing the utilised governing equations and assumptions.

---

## LIST OF CONTENTS

<b>Acknowledgements .....</b>	<b>iv</b>
<b>Abstract.....</b>	<b>v</b>
<b>List of Contents.....</b>	<b>vi</b>
<b>List of Figures .....</b>	<b>x</b>
<b>List of Tables.....</b>	<b>xxiii</b>
<b>Chapter 1 Introduction.....</b>	<b>1</b>
1.1 Background.....	1
1.2 Motivation .....	2
1.3 Aims and Objectives of the Research .....	3
1.3.1Aims of the Research .....	4
1.3.2Objectives of the Research .....	4
1.4 The Scope of this Research .....	5
1.5 Contributions of this research.....	5
1.6 Organization of the Thesis .....	6
<b>Chapter 2 Literature Review .....</b>	<b>8</b>
2.1 Introduction .....	8
2.2 Challenges in the oil industry .....	8
2.3 Overview of nanotechnology .....	13
2.4 The application of nanotechnology in the oil and gas industry ....	15
2.4.1Nano-coatings .....	15
2.4.2Nano-fluids .....	17
2.4.3Other nanotechnology innovations.....	19
2.5 Challenges of Nanotechnology Development and Application ....	20
2.6 Scale management.....	22
2.6.1Definition and the effect of scale .....	22
2.6.2Formation of scale .....	23
2.6.3Treatment of scale.....	24
2.7 Modelling transport and adsorption in rock formations .....	31
2.8 Summary .....	51
<b>Chapter 3 Methodology .....</b>	<b>53</b>
3.1 Introduction .....	53
3.2 Porous media .....	55

---

3.3	Key Assumptions and Governing Equations of the Model.....	60
3.3.1	Flow Conditions.....	60
3.3.2	Simulation domain.....	66
3.3.3	Representation of Nanoparticles.....	69
3.3.4	Boundary Conditions for Velocity.....	71
3.3.5	Boundary Conditions for Concentration.....	72
3.3.6	Adsorption and Desorption of Nanoparticles.....	72
3.3.7	Langmuir Adsorption Isotherm.....	76
3.3.8	Freundlich Adsorption Isotherm.....	77
3.4	Core flooding experiment for validation.....	79
3.5	Simulation Procedure.....	81
3.6	Computational Fluid Dynamic (CFD).....	82
3.7	Finite Element Analysis (FEA).....	84
3.8	Model Overview.....	85
3.9	Summary.....	87
<b>Chapter 4</b>	<b>Distribution of Nanoparticles in a Single Straight</b>	
	<b>Microchannel.....</b>	<b>88</b>
4.1	Introduction.....	88
4.2	Aims and Objectives.....	90
4.3	Simulation Setup.....	90
4.3.1	General Assumptions of the Simulation.....	90
4.3.2	Geometry Configuration.....	91
4.3.3	Governing Equation for the Simulation.....	92
4.3.4	Experiment Data and Result for Validation.....	92
4.4	Mesh sensitivity Study.....	96
4.5	Comparison with Experiments.....	97
4.5.1	Obtaining the Adsorption Parameters.....	99
4.5.1.1	2D Geometry - Langmuir Adsorption Isotherm.....	99
4.5.1.2	2D Geometry - Freundlich Adsorption Isotherm..	101
4.5.1.3	3D Axis-symmetric Geometry - Freundlich Adsorption Isotherm.....	107
4.6	The effect of velocity on the particle distribution in microchannel.....	109
4.6.1	Continuous nanoparticle injection.....	109
4.6.1.1	Continuous injection without diffusion.....	112
4.6.1.2	Continuous injection with diffusion.....	116

---

4.6.2	Discontinuous nanoparticle injection.....	120
4.6.2.1	Discontinuous injection without diffusion.....	122
4.6.2.2	Discontinuous injection with diffusion.....	124
4.7	Summary and Conclusion.....	129
<b>Chapter 5</b>	<b>Adsorption and Desorption in a Tortuous Microchannel.....</b>	<b>132</b>
5.1	Introduction.....	132
5.2	Aims and Objectives.....	134
5.3	Simulation Setup.....	134
5.4	Adsorption in Identical Length Tortuous Microchannel.....	136
5.4.1	Continuous Injection in Identical Length Tortuous Microchannels.....	137
5.4.2	Discontinuous Injection in Identical Length Tortuous Microchannel.....	141
5.4.3	The Relation between the Adsorption and the Tortuosity for Microchannel System with Similar Microchannel Length.....	147
5.4.4	Effect of tortuosity on the effluent and adsorbate concentration.....	149
5.5	Adsorption in Identical Inlet-Outlet Distance Tortuous Microchannel.....	152
5.5.1	Continuous Injection in Tortuous Microchannels with Identical Length in Identical Inlet-Outlet Distance.....	153
5.5.2	Discontinuous Injection in Tortuous Microchannels with Identical Length in Identical Inlet-Outlet Distance.....	158
5.5.3	The Relation between the Effluent Concentration and the Tortuosity for Microchannel System with Equal Inlet- Outlet Distance.....	162
5.6	Summary and Conclusion.....	165
<b>Chapter 6</b>	<b>Distribution of Nanoparticles in a Single Rough Surface Microchannel.....</b>	<b>169</b>
6.1	Introduction.....	169
6.2	Aims and Objectives.....	170
6.3	Simulation Setup.....	171
6.4	The Effect of the Wall Roughness to the Particle Transportation and Adsorption.....	173
6.4.1	Model Geometry Selection.....	174
6.4.2	Continuous Injection Flow.....	176
6.4.3	Discontinuous Injection Flow.....	180

---

6.4.4	Effect of Wall Roughness to the Change in the Concentration Distribution and Adsorption in a Microchannel for Continuous and Discontinuous Nanoparticle Injection.....	185
6.4.5	Adsorption on the Asperities of the Rough Microchannel Wall	188
6.4.6	Investigation of the Dead End Region in the Microchannel .....	189
6.5	Summary and Conclusion .....	195
<b>Chapter 7</b>	<b>Study of the Network Model.....</b>	<b>197</b>
7.1	Introduction .....	197
7.2	Aims and Objectives.....	198
7.3	Methodology .....	198
7.4	Microchannel segments with similar surface area .....	202
7.5	Microchannel segments with similar lattice dimension .....	210
7.6	Finding correlations for the concentration profiles and pressure difference for the microchannel segments .....	220
7.6.1	Concentration profile for single straight microchannel segment.....	223
7.6.2	Concentration profile for single bended microchannel segment.....	231
7.7	Network model.....	238
7.8	Summary and Conclusion .....	242
<b>Chapter 8</b>	<b>Summary and Conclusions .....</b>	<b>245</b>
8.1	Assessment and Research Objectives .....	245
8.2	Conclusions .....	248
8.3	Future Work.....	251
<b>References</b> .....		<b>253</b>
<b>APPENDIX A</b> .....		<b>267</b>
<b>APPENDIX B</b> .....		<b>269</b>
<b>APPENDIX C-1</b> .....		<b>277</b>
<b>APPENDIX C-2</b> .....		<b>285</b>

## LIST OF FIGURES

Figure 2.1: Top 10 risks in oil and gas industry (Reproduced from Oxford Analytica and Ernst & Young, 2008 [17]) .....	9
Figure 2.2: The historical and the forecast of the oil and gas production from the Norwegian Continental Shelf (NCS) in 2011 (Reproduced from NPD, 2011[13]).....	10
Figure 2.3: Recovery factor obtained according to the Enhanced Oil Recovery Method and Oil Viscosity (Reproduced from Total EP, 2008)[36].....	12
Figure 2.4: Nano particle in a beaker (left) and the image of a polysilicon observed under a TEM (right) (After Ju and Fan, 2009) [39] .....	13
Figure 2.5: Picture of a heavy scale deposition (After Statoil, 2007)[98] .....	22
Figure 2.6: Illustration of a general curve of inhibitor concentration vs. time for any scaly inhibitor (reproduced from Jasinski, 2004) [100].....	26
Figure 2.7: Inhibitor return curve showing the range of the Minimum Inhibitor Concentration, MIC. (reproduced from Jasinski, 2004) [100].....	27
Figure 2.8: Illustration of the basic element of Hydraulic Pore Network (Hypon) (reproduced from El Amin et.al, 2004 [136]) .....	31
Figure 2.9: Result of simulation for after 2 months of CO2 injection (reproduced from El Amin et.al, 2012 [136]) .....	32
Figure 2.10: Tested medium of the simulation. For the permeability, blue legend is 20 mD and red is 200mD, for nanoparticle concentration, blue legend is 0.005 and red is 0.08 (dimensionless) (reproduced from El Amin et.al, 2012 [137]) .....	33
Figure 2.11: (a) Porosity and (b) permeability distribution along the dimension distance at different injection PV (reproduced from Ju and Fan, 2009 [39]) .....	34
Figure 2.12: (a) Comparison between numerical results and experimental data, (b) Distribution of the component in the oil phase after 0.33 PV of CO2 injection (reproduced from Ju and co-workers, 2012 [138]) .....	35
Figure 2.13: (a) Cuboidal grid mode, (b) Hybrid grid mode (reproduced from Ju and co-workers, 2012 [138]).....	36

<b>Figure 2.14: Schematic illustration for (a) geometric model of porous media constructed from parallel capillaries and mixing chambers. (b) detail illustration of a single chamber with suspension mixing, (c) transversal flow cross section of the model of porous media (reproduced from Bedrikovetsky, 2012 [139]) .....</b>	<b>37</b>
<b>Figure 2.15: Fractional flow function for network model of the porous space derived from a bundle of parallel capillaries alternated by mixing chambers (reproduced from Bedrikovetsky, 2008 [139]) .....</b>	<b>38</b>
<b>Figure 2.16: Forces and force moment balance for the particle located on the internal cake surface. (reproduced from Bedrikovetsky, 2011 [140]) .....</b>	<b>39</b>
<b>Figure 2.17: Schematic illustration of the pore throat formed by three tangent grains and suspension flow through porous media represented by parallel capillary with mixing chambers (reproduced from You et.al [135]).....</b>	<b>40</b>
<b>Figure 2.18: Breakthrough curves of carbon nanoparticle in the presence of KCl salt (~pH 8.3) (reproduced from Yu et.al [141]) .....</b>	<b>41</b>
<b>Figure 2.19: Fluid-fluid distribution function <math>g_{ffr}</math> and fluid-matrix distribution function <math>g_{fmr}</math> from the MGOZ integral equation (solid line) and GCMC (dashed line) (reproduced from Vega et.al [143])......</b>	<b>43</b>
<b>Figure 2.20: (a) The Trajectories of magnetic nanoparticles in a channel at 1 kOe field and (b) Capture efficiency (<math>\eta</math>) of magnetic nanoparticles at different magnetic field 0-10 kOe. (reproduced from Sharma et. al [145]) .....</b>	<b>44</b>
<b>Figure 2.21: Binding of nanoparticle in a channel where red colour indicates the highest concentration and blue colours indicates lowest concentration (reproduced from Liu et al [146]) .....</b>	<b>45</b>
<b>Figure 2.22: Illustration of the basic element of Hydraulic Pore Network (Hypon) (reproduced from Acharya et.al, 2004 [147]) .....</b>	<b>46</b>
<b>Figure 2.23: Schematic illustration of the model where the light grey is subjected into diffusion effect (reproduced from Lionello et al [156]) .....</b>	<b>47</b>
<b>Figure 2.24: Schematic illustration of the model where the light grey is subjected into diffusion effect (reproduced from Lionello et al [156]) .....</b>	<b>48</b>
<b>Figure 3.1: Illustration of a Scale Inhibitor (SI) Injection, as the approach used in the research by the author in the University of Leeds. ....</b>	<b>54</b>

---

Figure 3.2: Packing of ideal uniform sphere grains (a) cubic, or wide pack and (b) rhombohedral, or close-packed. (After Graton and Fraser, 1935) [175].....	55
Figure 3.3: Schematic illustration of the experiment conducted by Henry Darcy of the water flow in sand. (After Hubbert, from Amyx, 1960) [176] .....	57
Figure 3.4: Theoretical figure of shear stress vs strain for different fluids characteristic (reproduced from Sleight, 2009) [186].....	64
Figure 3.5: The channel in the simulation is illustrated as one of the microchannels happens in the core.....	66
Figure 3.6: The 2D geometry microchannel configuration.....	67
Figure 3.7: The 3D axis symmetric geometry microchannel configuration.....	67
Figure 3.8: The illustration of the system for the simulation for the 3D axis-symmetric geometrical model.....	74
Figure 3.9: Illustration for the simulation procedure .....	81
Figure 3.10: Process of computational fluid dynamics .....	83
Figure 4.1: Geometry for the 2D model (units are $\mu\text{m}$ ) .....	91
Figure 4.2: Geometry for the 2D axis symmetric model (left) and the corresponding 3D appearance (right).....	92
Figure 4.3: Injection and the early post flush stage for the PPCA concentration (reproduced from Zhang et. al. [221]).....	93
Figure 4.4: PPCA concentration in the effluent vs the injected pore volume (reproduced from Zhang et. al. [221]) .....	94
Figure 4.5: Results for the mesh sensitivity study .....	96
Figure 4.6: The typical profile of the velocity magnitude at the inlet (left) and at the outlet (right).....	97
Figure 4.7: The typical profile of the pressure magnitude at the inlet (left) and at the outlet (right) .....	98
Figure 4.8: Flow rates at the post flush stage .....	98
Figure 4.9: PPCA Average Effluent Concentration for the Injection and Early Post flush Stage: Experiment and Simulation (Langmuir) .....	100
Figure 4.10: Post flush average effluent concentration vs pore volume (Langmuir Adsorption Isotherm) .....	101
Figure 4.11: Preliminary study for the kads sensitivity - Average Post Flush Effluent Concentration (Freundlich Adsorption Isotherm) .....	102
Figure 4.12: Preliminary study for the nads sensitivity - Average Post Flush Effluent Concentration (Freundlich Adsorption Isotherm) .....	103

Figure 4.13: Preliminary study for the <i>k<sub>des</sub></i> sensitivity (Freundlich Adsorption Isotherm) .....	104
Figure 4.14: Preliminary study for the <i>n<sub>des</sub></i> sensitivity (Freundlich Adsorption Isotherm) .....	104
Figure 4.15: The Comparison of the Post Flush Effluent concentration for the experiment (blue line) and the 2D geometry (green line) - Freundlich Adsorption Isotherm .....	106
Figure 4.16: Comparison of the Post Flush Effluent concentration from the experiment (blue), 2D geometry simulation (green) and 3D axis-symmetric simulation (red) - Freundlich Adsorption Isotherm .....	107
Figure 4.17: PPCA Effluent Concentration for the Injection and Early Post flush Stage: Experiment and Simulation (Freundlich) .....	108
Figure 4.18: Bulk and adsorbate concentration for 0, 0.2, 0.5, and 1 second from 10 seconds simulation time length for a continuous injection with diffusion in various times for injection velocity $v=2v_0$ and $v_0=8.08 \times 10^{-5}$ m/s (base case).....	110
Figure 4.19: Average effluent concentration for various inlet velocity in continuous flow without diffusion against the simulation time interval, $v_0=8.08 \times 10^{-5}$ m/s .....	112
Figure 4.20: Average effluent concentration for various inlet velocity in continuous flow without diffusion against the injected volume, $v_0=8.08 \times 10^{-5}$ m/s .....	113
Figure 4.21: Average adsorbate concentration for various inlet velocity in a continuous flow without diffusion against the simulation time interval, $v_0=8.08 \times 10^{-5}$ m/s .....	114
Figure 4.22: Average adsorbate concentration for various inlet velocity during an injection period in a continuous flow w/o diffusion against the injected volume, $v_0=8.08 \times 10^{-5}$ m/s .....	115
Figure 4.23: Cumulative adsorbate Mass for various inlet velocity during an injection period in a continuous flow w/o diffusion for 8 pore volume of injection, $v_0=8.08 \times 10^{-5}$ m/s .....	115
Figure 4.24: Average effluent concentration of various inlet velocities for continuous injection with diffusion in various pore volumes, $v_0=8.08 \times 10^{-5}$ m/s. Effluent concentration profiles for ( $c_A, v=0.1v_0$ ) and ( $c_A, v=0.5v_0$ ) are on top of each other .....	116
Figure 4.25: Equilibrium effluent concentration of various inlet velocities for continuous injection with diffusion in various pore volumes. Data points from left to right respectively are for injection velocity $v=0, 1v_0, v=0.5v_0, v=v_0, v=1.5 v_0$ , and $v=2v_0$ .....	117

Figure 4.26: Average adsorbate concentration of various inlet velocities for continuous injection with diffusion against the injection volume, $v_o=8.08 \times 10^{-5}$ m/s .....	118
Figure 4.27: Average adsorbate concentration of various inlet velocities for continuous injection with diffusion against the injection volume (extrapolation), $v_o=8.08 \times 10^{-5}$ m/s.....	118
Figure 4.28: Cumulative adsorbate mass of various inlet velocities for continuous injection with diffusion for 8 pore volume of injection, $v_o=8.08 \times 10^{-5}$ m/s.....	119
Figure 4.29: Bulk and adsorbate concentration for 0, 0.2, 0.5, and 1 seconds simulation time length for a discontinuous injection in various times for injection velocity $v=2v_o$ and $v_o=8.08 \times 10^{-5}$ m/s.....	121
Figure 4.30: Effluent concentration of various inlet velocities for discontinuous injection without diffusion in various time, $v_o=8.08 \times 10^{-5}$ m/s.....	122
Figure 4.31: Effluent concentration of various inlet velocities for discontinuous injection without diffusion against the injected volume, $v_o=8.08 \times 10^{-5}$ m/s .....	123
Figure 4.32: Adsorbate Concentration for various inlet velocities for discontinuous injection without diffusion against the injected time, $v_o=8.08 \times 10^{-5}$ m/s.....	123
Figure 4.33: Effluent concentration of various inlet velocities for discontinuous injection with diffusion against the simulation time, $v_o=8.08 \times 10^{-5}$ m/s .....	125
Figure 4.34: Effluent concentration of various inlet velocities for discontinuous injection with diffusion against the injected volume, $v_o=8.08 \times 10^{-5}$ m/s .....	126
Figure 4.35: Average adsorbate concentration of various inlet velocities for discontinuous injection in various time, $v_o=8.08 \times 10^{-5}$ m/s. Lines for $c_B, v=1,5v_o$ and $c_B, v=2v_o$ are on the top of each other.....	127
Figure 4.36: Maximum value of the average adsorbate concentration for various inlet velocities for discontinuous injection.....	127
Figure 4.37: Adsorbed concentration of various inlet velocities for discontinuous injection in various pore volume, $v_o=8.08 \times 10^{-5}$ m/s. Lines for $c_B, v=1,5v_o$ and $c_B, v=2v_o$ are on the top of each other.....	128
Figure 4.38: Cumulative adsorbed mass for various inlet velocities for discontinuous injection for 8 pore volume of injection, $v_o=8.08 \times 10^{-5}$ m/s.....	128
Figure 5.1: Determination of tortuosity through a porous material using the arc-chord ratio (after O'Connell et al., 2010)[237] .....	132

---

<b>Figure 5.2: Bulk concentration vs. pore volume at the 200-<math>\mu</math>m outlet boundaries for different tortuosity for continuous particles injection .....</b>	<b>138</b>
<b>Figure 5.3: Adsorbed concentration against the injection volume for continuous concentration injection – Freundlich adsorption isotherm. The inset is the profile of the adsorbate concentration at the corner of the concentration profile change. ....</b>	<b>139</b>
<b>Figure 5.4: The concentration propagation of 2 different channel configuration i.e. with tortuosity=1 (left) and tortuosity=1.4724 (right) at 0.8 seconds. Recalled, the tortuosity is measured for similar microchannel length of 200 <math>\mu</math>m.....</b>	<b>140</b>
<b>Figure 5.5: Effluent concentration vs. injection volume at the 200-<math>\mu</math>m outlet boundary for discontinuous injection for different tortuosity .....</b>	<b>143</b>
<b>Figure 5.6: Adsorbed concentration of the nanoparticles vs. injection volume at the 200 <math>\mu</math>m outlet boundary for discontinuous concentration injection .....</b>	<b>145</b>
<b>Figure 5.7 Velocity field magnitude and a typical streamlines at a corner in a microchannel bend. Taken one of the bends at microchannel C at simulation time 1.52 seconds. ....</b>	<b>147</b>
<b>Figure 5.8: The equilibrium adsorption and desorption concentration for similar length .....</b>	<b>148</b>
<b>Figure 5.9: Illustration for the geometries that have similar tortuosity but different configuration.....</b>	<b>149</b>
<b>Figure 5.10: The effluent concentration of different microchannel with similar tortuosity. ....</b>	<b>150</b>
<b>Figure 5.11: The concentration of the adsorbate for different microchannel with similar tortuosity.....</b>	<b>151</b>
<b>Figure 5.12: Effluent concentration at 200 <math>\mu</math>m channel length for continuous PPCA injection (ppm) .....</b>	<b>154</b>
<b>Figure 5.13: Effluent concentration at 200 <math>\mu</math>m channel length for continuous PPCA injection (ppm) .....</b>	<b>155</b>
<b>Figure 5.14: Effluent concentration at 200 <math>\mu</math>m channel length for continuous PPCA injection (ppm) .....</b>	<b>156</b>
<b>Figure 5.15: Average effluent concentration for discontinuous particles injection .....</b>	<b>159</b>
<b>Figure 5.16: Mass of the adsorbate for discontinuous particles injection .....</b>	<b>160</b>
<b>Figure 5.17: Concentration of the adsorbate for discontinuous particles injection .....</b>	<b>160</b>

<b>Figure 5.18: Adsorbate concentration for discontinuous particles injection for 3 difference velocities, i.e. <math>v_0</math>, <math>0.5x v_0</math>, and <math>2x v_0</math>, where <math>v_0=8.08x10^{-5}</math> m/s .....</b>	<b>163</b>
<b>Figure 5.19: Mass of the adsorbate for discontinuous particles injection for 3 difference velocities, i.e. <math>v_0</math>, <math>0.5x v_0</math>, and <math>2x v_0</math>, where <math>v_0=8.08x10^{-5}</math> m/s .....</b>	<b>164</b>
<b>Figure 6.1: (a) Grains of the clashash sample before injection that dominantly consist of quartz grains with open pore, (b) Post-test sample of the injection face of the core plug showing the occurrence of a very thin filter cake of particles but with large, open pores. (c) Post-test sample showing that the scattered kaolinite platelets on quartz grains are still held in place after successive treatments. (After Fleming et al[114]) .....</b>	<b>169</b>
<b>Figure 6.2 Illustration of the average surface roughness .....</b>	<b>172</b>
<b>Figure 6.3 Illustration of the microchannel geometry with the velocity fields. Taken from the microchannel in this study for <math>Ra = 1 \mu\text{m}</math> .....</b>	<b>173</b>
<b>Figure 6.4: Mass of the adsorbate for different time steps (in seconds) for continuous particles injection for (a) actual 3D microchannel geometry and (b) 3D symmetric axis geometry for <math>Ra = 0 \mu\text{m}</math> .....</b>	<b>175</b>
<b>Figure 6.5: Mass of the adsorbate for different simulation time (s) for discontinuous particles injection for (a) 3D microchannel geometry and (b) 3D axis symmetric geometry for <math>Ra = 1 \mu\text{m}</math> ....</b>	<b>175</b>
<b>Figure 6.6: Adsorbate mass for different time steps (0 - 10 seconds) for continuous particles injection for various average surface roughness (<math>Ra</math>).....</b>	<b>177</b>
<b>Figure 6.7: Adsorbate mass on the channel wall for continuous particles injection for against the injection volume for various average surface roughness (<math>Ra</math>).....</b>	<b>178</b>
<b>Figure 6.8: Effluent concentration at the outlet for continuous particles injection for different pore volume .....</b>	<b>179</b>
<b>Figure 6.9: Adsorbate mass for different simulation time (0-10 seconds) for discontinuous particles injection particles injection for various average surface roughness (<math>Ra</math>).....</b>	<b>181</b>
<b>Figure 6.10: Mass of the adsorbed particles on the channel wall for discontinuous injection as a function of injection volume for various average surface roughness (<math>Ra</math>) .....</b>	<b>183</b>
<b>Figure 6.11: Concentration of the adsorbed particles on the channel wall for discontinuous injection as a function of injection volume for various average surface roughness (<math>Ra</math>)...</b>	<b>183</b>
<b>Figure 6.12: Effluent concentration at the outlet for discontinuous particles injection as a function of injection volume for various average surface roughness (<math>Ra</math>).....</b>	<b>184</b>

Figure 6.13: Comparison for the deviation of the outlet effluent concentration ( $c_A$ , mol/m <sup>3</sup> ), adsorbate concentration ( $c_B$ , mol/m <sup>2</sup> ), adsorbate mol ( $n_B$ , mol) and adsorbate mass ( $m_B$ , mg) for different wall roughness – continuous injection.....	187
Figure 6.14: Comparison for the deviation of the outlet effluent concentration ( $c_A$ , mol/m <sup>3</sup> ), adsorbate concentration ( $c_B$ , mol/m <sup>2</sup> ), adsorbate mol ( $n_B$ , mol) and adsorbate mass ( $m_B$ , mg) for different wall roughness – discontinuous injection.....	187
Figure 6.15: The peak of the adsorbate mass distribution of the adsorbate for microchannel with $Ra= 1$ for 0.5 seconds simulation.....	188
Figure 6.16: Velocity magnitude, velocity field, streamlines in one of the cavity on the wall in this study. Red arrow is the direction of the flow .....	191
Figure 6.17: Flow schematic for open and cavity flow (Reproduced from Plentovich, 1993[264]).....	191
Figure 6.18: Velocity streamlines magnitude at a cavity on the wall (left) and the corresponding adsorbate mass (right) for microchannel with $Ra = 0 \mu m$ .....	192
Figure 6.19: Velocity streamlines magnitude at a cavity on the wall (left) and the corresponding adsorbate mass (right) for microchannel with $Ra = 0.25 \mu m$ .....	193
Figure 6.20: Velocity magnitude and stream lines at a cavity on the wall (left) and the corresponding adsorbate mass (right) for microchannel with $Ra = 0.5 \mu m$ .....	193
Figure 6.21: Velocity magnitude and stream lines at a cavity on the wall (left) and the corresponding adsorbate mass (right) for microchannel with $Ra = 0.75 \mu m$ .....	194
Figure 6.22: Velocity magnitude and stream lines at a cavity on the wall (left) and the corresponding adsorbate mass (right) for microchannel with $Ra = 1 \mu m$ .....	194
Figure 6.23: Adsorbate mass on the arc-length of the microchannel wall .....	195
Figure 7.1 Illustration of a pore channel network characterisation (Reproduced from Zhang et.al, 2011 [266]) .....	197
Figure 7.2: Channel geometry with similar adsorption surface area. Redlined arrow is indicates the inlet of the channel segment with 3x3 units lattice magnitude.....	199
Figure 7.3: Illustration of the lattice arrangement for the study with similar lattice magnitude dimension.....	200
Figure 7.4: Freundlich adsorption isotherm .....	202
Figure 7.5: Contours of velocity magnitude for the microchannel segment geometry with similar adsorption surface area .....	203

---

<b>Figure 7.6: Pressure profile for the microchannel segment geometry with similar adsorption surface area .....</b>	<b>204</b>
<b>Figure 7.7: The profile of (a) inlet-outlet pressure difference, (b) effluent concentration, (c) adsorbate concentration, and the (d) adsorbate mass for microchannel segment geometries with similar adsorption surface area.....</b>	<b>205</b>
<b>Figure 7.8: Inlet-Outlet Pressure Difference for different geometry with similar total adsorption surface area .....</b>	<b>207</b>
<b>Figure 7.9: Effluent concentration for different geometry with similar total adsorption surface area .....</b>	<b>208</b>
<b>Figure 7.10: Adsorbate concentration for different geometry with similar total adsorption surface area .....</b>	<b>209</b>
<b>Figure 7.11: Total adsorbate mass for different geometry with similar total adsorption surface area .....</b>	<b>209</b>
<b>Figure 7.12: The difference of the inlet and the outlet pressure for different channel segment geometries with similar channel lattice dimension .....</b>	<b>211</b>
<b>Figure 7.13: Pressure distribution for different channel segment geometries with similar channel lattice dimension .....</b>	<b>212</b>
<b>Figure 7.14: Velocity profile for different channel segment geometries with similar channel lattice dimension .....</b>	<b>213</b>
<b>Figure 7.15: Effluent concentration for different channel segment geometries with similar channel lattice dimension .....</b>	<b>214</b>
<b>Figure 7.16: Adsorbate mass for different channel segment geometries with similar channel lattice dimension .....</b>	<b>215</b>
<b>Figure 7.17: Adsorbate concentration for different channel segment geometries with similar channel lattice dimension .....</b>	<b>216</b>
<b>Figure 7.18: Inlet-Outlet pressure for different channel segment geometries under a constant inlet velocity for similar channel lattice dimension .....</b>	<b>218</b>
<b>Figure 7.19: Final effluent outlet concentration for different channel segment geometries for similar channel lattice dimension.....</b>	<b>219</b>
<b>Figure 7.20: Total adsorbate mass for different channel segment geometries with similar channel lattice dimension .....</b>	<b>219</b>
<b>Figure 7.21: Total adsorbate concentration for different channel segment geometries with similar channel lattice dimension .....</b>	<b>220</b>
<b>Figure 7.22: Effluent outlet concentration for different channel segment geometries with similar channel lattice. ....</b>	<b>221</b>
<b>Figure 7.23: Effluent outlet concentration for different channel segment geometries with similar channel lattice dimension .....</b>	<b>223</b>

---

Figure 7.24: The illustration for the flow direction for the straight microchannel segment (left) and velocity profile of the system after 10 seconds of the simulation time (right).....	224
Figure 7.25: The plot of the effluent concentration against the simulation time for different injection concentration (left) and injection velocity (right) for the straight microchannel.....	225
Figure 7.26: The plot of the effluent concentration against the inlet outlet pressure difference for various case of injection concentration .....	226
Figure 7.27: The mass of the adsorbate for different injection concentration (left) and velocity (right) for the straight microchannel segment. ....	227
Figure 7.28: The plot of the adsorbate mass against the inlet and outlet pressure difference for various case of injection concentration .....	228
Figure 7.29: The plot of the adsorbate concentration against the simulation time for the straight microchannel segment.....	229
Figure 7.30: The plot of the adsorbate concentration against the inlet outlet pressure difference for various case of injection concentration .....	230
Figure 7.31: Freundlich plot of the straight microchannel segment...	230
Figure 7.32: The illustration for the flow direction for the bended microchannel segment (left) and velocity distribution (right) of the system after 10 seconds of the simulation time .....	231
Figure 7.33: The illustration for the flow direction for the bended microchannel segment (left) and velocity profile of the system after 10 seconds of the simulation time (right).....	232
Figure 7.34: The plot of the effluent concentration against the inlet-outlet pressure difference for various case of injection concentration .....	233
Figure 7.35: Adsorbate mass against the injection volume for various injection concentration (left) and injection velocity (right) .....	234
Figure 7.36: Adsorbate mass against the inlet-outlet pressure difference for various injection concentrations.....	235
Figure 7.37: The plot of the adsorbate concentration against the inlet-outlet pressure difference for various case of injection concentration .....	236
Figure 7.38: The plot of the adsorbate concentration against the inlet-outlet pressure difference for various case of injection concentration .....	236
Figure 7.39: Freundlich plot of the bended microchannel segment ...	237

---

Figure 7.40: Network model from nodes and lines (a) to an established complex microchannel (b).....	238
Figure 7.41: Velocity and pressure profile distribution in the network applied in the simulation .....	239
Figure 7.42: Typical inlet-outlet difference profile of the microchannel network system.....	240
Figure 7.43: Typical inlet-outlet difference profile of the microchannel network system.....	241
Figure 7.44: Typical adsorbate mass and concentration profile of the microchannel network system .....	242
Figure B.0.1 : Post flush effluent concentration vs injection volume for different $k_{ids}$ between $1 \times 10^{-3}$ and $3.16 \times 10^{-7}$ for constant value of $k_{ids}$ $3.16 \times 10^4$ (Langmuir Adsorption Isotherm) .....	269
Figure B.0.2: Post flush effluent concentration vs injection volume for various $k_{ads}$ and $k_{des}$ (Langmuir Adsorption Isotherm).....	270
Figure B.0.3: Post flush effluent concentration vs injection volume for various $k_{ads}$ , $n_{ads}$ , $k_{des}$ , and $n_{des}$ . Preliminary study 1 (Freundlich Adsorption Isotherm) .....	270
Figure B.0.4: Post flush effluent concentration vs injection volume for various $k_{ads}$ and constant $n_{ads}$ , $k_{des}$ , and $n_{des}$ . Preliminary study 2 (Freundlich Adsorption Isotherm) .....	271
Figure B.0.5: Post flush effluent concentration vs injection volume for various $k_{ads}$ , $n_{ads}$ , $k_{des}$ , and $n_{des}$ . Preliminary study 3 (Freundlich Adsorption Isotherm) .....	271
Figure B.0.6: Post flush effluent concentration vs injection volume for various $k_{ads}$ , $n_{ads}$ , $k_{des}$ , and $n_{des}$ . Preliminary study 4 (Freundlich Adsorption Isotherm) .....	272
Figure B.0.7: Post flush effluent concentration vs injection volume for various $k_{ads}$ sensitivity (Freundlich Adsorption Isotherm).....	273
Figure B.0.8: Post flush effluent concentration vs injection volume for various $k_{ads}$ sensitivity (Freundlich Adsorption Isotherm) ....	273
Figure B.0.9: Post flush effluent concentration vs injection volume for various $k_{des}$ sensitivity (Freundlich Adsorption Isotherm) ....	274
Figure B.0.10: Post flush effluent concentration vs injection volume for various $n_{des}$ sensitivity (Freundlich Adsorption Isotherm) .....	274
Figure B.0.11: Post flush effluent concentration vs injection volume for various $n_{des}$ sensitivity (Freundlich Adsorption Isotherm) .....	275

---

Figure B.0.12: Post flush effluent concentration vs injection volume for various $n_{des}$ sensitivity (Freundlich Adsorption Isotherm) .....	275
Figure B.0.13: Post flush effluent concentration vs injection volume for various high $n_{des}$ sensitivity (Freundlich Adsorption Isotherm) .....	276
Figure B.0.14: Post flush effluent concentration vs injection volume for various high $n_{des}$ sensitivity (Freundlich Adsorption Isotherm) .....	276
Figure C-1.0.15 Concentration profile (left) and adsorbate concentration of the case of the continuous injection for time steps 0, 0.6, 1.4, and 2 seconds. ....	278
Figure C-1.0.16 Concentration profile (left) and adsorbate concentration of the case of the continuous injection for time steps 0, 0.6, 1.4, and 2 seconds .....	279
Figure C-1.0.17 Concentration profile (left) and adsorbate concentration of the case of the continuous injection for time steps 0, 0.6, 1.4, and 2 seconds .....	280
Figure C-1.0.18 Concentration profile (left) and adsorbate concentration of the case of the continuous injection for time steps 0, 0.6, 1.4, and 2 seconds .....	281
Figure C-1.0.19 Concentration profile (left) and adsorbate concentration of the case of the continuous injection for time steps 0, 0.6, 1.4, and 2 seconds .....	282
Figure C-1.0.20 Concentration profile (left) and adsorbate concentration of the case of the continuous injection for time steps 0, 0.6, 1.4, and 2 seconds .....	283
Figure C-1.0.21 Concentration profile (left) and adsorbate concentration of the case of the continuous injection for time steps 0, 0.6, 1.4, and 2 seconds .....	284
Figure C-2.0.22 Concentration profile (left) and adsorbate concentration of the case of the discontinuous injection for time steps 0, 0.3, 0.6, and 0.9 seconds .....	286
Figure C-2.0.23 Concentration profile (left) and adsorbate concentration of the case of the discontinuous injection for time steps 0, 0.3, 0.6, and 0.9 seconds .....	287
Figure C-2.0.24 Concentration profile (left) and adsorbate concentration of the case of the discontinuous injection for time steps 0, 0.3, 0.6, and 0.9 seconds .....	288
Figure C-2.0.25 Concentration profile (left) and adsorbate concentration of the case of the discontinuous injection for time steps 0, 0.3, 0.6, and 0.9 seconds .....	289

---

<b>Figure C-2.0.26</b>	<b>Concentration profile (left) and adsorbate concentration of the case of the discontinuous injection for time steps 0, 0.3, 0.6, and 0.9 seconds .....</b>	<b>290</b>
<b>Figure C-2.0.27</b>	<b>Concentration profile (left) and adsorbate concentration of the case of the discontinuous injection for time steps 0, 0.3, 0.6, and 0.9 seconds .....</b>	<b>291</b>

---

## LIST OF TABLES

<b>Table 2.1: Types of mineral scales in oilfields (after Jasinski, 2004) [100] .....</b>	<b>24</b>
<b>Table 3.1: Legend for the Darcy's law, in field units .....</b>	<b>59</b>
<b>Table 3.2: The difference between laminar and turbulent flow [186] ....</b>	<b>65</b>
<b>Table 4.1: Data for calculating diffusivity coefficient .....</b>	<b>95</b>
<b>Table 4.2: Freundlich Adsorption Isotherm Investigation (2D geometry) .....</b>	<b>105</b>
<b>Table 4.3: The parameters used for the Freundlich equation for the 2D and 3D axis-symmetric geometry .....</b>	<b>130</b>
<b>Table 5.1 : Simulation setup for the study of the effect of tortuosity to the particle distribution in microchannel .....</b>	<b>135</b>
<b>Table 5.2 : Flow sequence of the concentration flow and the corresponding adsorbate concentration profile for geometry E for a discontinuous injection. Units for the x-axis is in <math>\mu\text{m}</math> .....</b>	<b>142</b>
<b>Table 5.3 : Distribution profile of the injected nanoparticle and the corresponding adsorbate concentration on the wall for geometry A, B, and D for continuous injection. The unit in x-axis is in <math>\mu\text{m}</math>. .....</b>	<b>157</b>
<b>Table 5.4 : Distribution profile of the injected nanoparticle and the corresponding adsorbate concentration on the wall for geometry A, B, and D for discontinuous injection. The unit in x-axis is in <math>\mu\text{m}</math>. .....</b>	<b>161</b>
<b>Table 6.1: The geometry of the simulation setup .....</b>	<b>171</b>
<b>Table 6.2: Comparison for the deviation of the outlet effluent concentration (<math>c_A</math>, <math>\text{mol}/\text{m}^3</math>), concentration of the adsorbate (<math>c_B</math>, <math>\text{mol}/\text{m}^2</math>), mol of the adsorbate (<math>n_B</math>, mol) and the mass of the adsorbate (<math>m_B</math>, mg) for different wall roughness. ....</b>	<b>186</b>
<b>Table 7.1: The magnitude of (a) inlet-outlet pressure difference, (b) average effluent concentration, (c) average adsorbate concentration, and the (d) average adsorbate mass for the microchannel segment geometry with similar adsorption surface area.....</b>	<b>206</b>
<b>Table 7.2: Summary for the similar lattice dimension .....</b>	<b>217</b>
<b>Table 7.3: Sensitivity study configuration to find correlation for the concentration and pressure difference for the microchannel segments .....</b>	<b>222</b>

# Chapter 1

## Introduction

### 1.1 Background

Flow assurance, or the “Guarantee of Flow” in petroleum industry is defined as the satisfaction of demand for transporting hydrocarbon from reservoirs to the processing plants and point of sale [1, 2]. Flow assurance is an important key concern in the oil and gas industry because lacking of it results inefficiency in production, even leads to zero hydrocarbon production. It possesses a number of engineering challenges and difficulties, such as erosion, corrosion, and the accumulation of mineral scale and other foulants. Moreover, flow assurance is a very crucial task in deep-water oil and gas production due to the involvement of relatively high contrast of pressure and temperature between the reservoir and the ambient condition above the seabed. The involvement of these parameters along the flowline can lead to deposition that commonly jeopardise the flow assurance [3]. Injection of salt water to the reservoir is also a common way to maintain the reservoir pressure. However, salt water can be incompatible with the formation fluid and as a result can inflict a serious scaling problem [4, 5]. The cost and risk in curing the scaling problem is often high and sacrifices fluid production.

To have the “Guarantee of Flow”, it is often preferable to prevent problem to occur, e.g. scaling formation, instead to cure the problem because curing the problem is more costly and risky than the prevention. Scaling prevention is commonly conducted by reducing the utilisation of incompatible injection water and introducing scale inhibitor to the flow line and the reservoir formation. Introducing a scale inhibitor is the most common one and is known as the ‘scale squeeze treatment’. The effectiveness of a scale inhibitor relates closely to its attachment lifetime in the rock formation since the idea is to inject scale inhibitor into the formation to let it adsorbed onto internal rock surface and slowly desorb to maintain a supply of inhibitor. Utilisation of nanotechnology has a promising implementation to enhance the attachment of the scale inhibitor on the rock surface [6, 7]. However, nanotechnology is not yet a well-established approach; but in fact, it is still new and speculative. Proven effectivity and efficiency, as well as health,

---

safety, and environment issues are to be resolved for implementation of nanoparticles in the oil and gas industry.

It is important to understand the distribution and attachment of the injected nanoparticles in the porous system in the reservoir due to reasons explain previously. This thesis establishes novel method and computational fluid dynamics simulator that models transportation of injected diluted nanoparticles in microchannel system with different injection properties and geometrical variances. In the simulator, flow and penetration of nanoparticles in microchannel are observed by investigating the effluent concentration, the adsorption and desorption process are perceived by examining the profile of adsorbate mass and concentration. Dispersion and spatial distribution of the injected nanoparticle are also discussed by investigating the movement profile of the concentration in the microchannel domains. The effect of injection velocity, injection concentration, microchannel geometry that includes longitudinal and surface variance is also discussed. Hence the key aspects to be understood include the flow and penetration of nanoparticles into fluid saturated rock microchannels, adsorption and desorption rates, dispersion behaviour, and spatial distributions are visited.

## **1.2 Motivation**

Maintaining an elective supply of energy has been a large issue for decades due to the world demands for a vast supply of oil and gas from the industry. This is a challenging condition because of the limitations in finding new discoveries, and maximizing the production from the current reservoirs.

Nanotechnology has a promising utilisation as an enabler to exploit more fossil-based fuels. Nanoparticles has particular properties such as high propensity for adsorption and good candidate for injection into the near wellbore region because of their small sizes [8]. On the other hand, nanoparticles also have to present a reasonably mobility, because the use will not be feasible if they do not transport into the area of interest [9]. Nanotechnology in oil industry is still an emerging approach that requires study and investigation to gain understanding the benefit to the industry and the risk to the health, safety, and environment. It is not always practical to establish a field and laboratory model for investigation, therefore establishing a representative and observable computational model is important.

---

### 1.3 Aims and Objectives of the Research

There is a rapid growth of interest in nanotechnology in the oil and gas industry. The example of the applications include the utilisation of nanoparticles as agents for modifying surface wettability, mobilization agents for recovery of residual oil, enhancing mineral scale management systems, enhanced drilling fluids, water shut-off, etc.

In reservoir scale management system, nanoparticles are injected into the reservoir to increase the adsorption area of the rock surface and enhance the attachment of the scale inhibitor on the surface of the rock pores. There are many uncertainties in the downhole pore configuration; on the other hand, the nanoparticles need to be delivered to the required location. It is crucial for a health, safety, and environment (HSE) approval to gain knowledge about the penetration, distribution, and the placement of the injected nanoparticles in the reservoir.

This study is conducted to establish an understanding of the transportation, penetration and the adsorption/desorption of injected nanoparticles in porous media. By this understanding, it will be easier to control or modify the distribution path of the injection that is in accordance with the operation and the HSE approval. Having the knowledge of the injected nanoparticles deliverance might assist in predicting the effect of the injection to the rock formation and environment.

The preceding investigations about nanoparticle distribution in rock porous media were mostly conducted for porous media domain where the flow is affected by permeability, i.e. where Darcy's Law is valid to use. The effect of microchannel geometry variation and advection-diffusion mechanism to the distribution and adsorption-desorption process has not been much covered. Therefore, more investigation to the process at micro-pore-channel is required to enhance the understanding of the nanoparticle distribution and adsorption in the porous media. The approach used in the study in this thesis accommodates the method use in studying nanomedicine delivery in human body where microchannel is used as the domain.

The approach used adopts a pore-scale Computational Fluid Dynamics (CFD) to explore and understand the effects of flow and the microchannel configuration on nanoparticle transport and adsorption and desorption. Finite Element Analysis (FEA) is used in the simulation by

considering the concentration flow in idealized pore-scale geometries and infers the behaviour observed in much larger pore networks.

This thesis is dedicated to establish a numerical model to simulate the nanoparticle transport, distribution and adsorption/desorption process in micro-pore channel. In brief, the aims and objectives of the research are expressed in following sub-chapters.

### **1.3.1 Aims of the Research**

This thesis takes role as one of the starting points of investigation of nanotechnology implementation in the oil and gas industry. The aims of this research are to establish methodology and understanding of nanoparticle penetration into rock pores. The model developed considers the nanoparticles flow in the microchannel and the adsorption/desorption process on the microchannel walls. It considers the mechanism of the nanoparticle concentration transport, adsorption/desorption process, dispersion behaviour and spatial distributions in microchannels. Since the framework relates the transport mechanism in microchannel bulk and the corresponding surface wall, the methodology is applicable for future investigation that includes concentration flow and surface transport mechanism in flow assurance in the oil and gas industry, e.g. scale inhibitor attachment and corrosion.

### **1.3.2 Objectives of the Research**

The aim is achieved by developing a simulator that can model the flow, distribution, and adsorption/desorption of diluted nanoparticles inside a simple microchannel. The simulator is validated using results from a published laboratory experiment.

Then, some sensitivity studies are conducted which include the investigation of the distribution of nanoparticles in a single straight and tortuous microchannel. The investigation of channels with different geometrical roughness is also conducted. Finally, the study is wrapped up by investigating the distribution of nanoparticles in a complex microchannel network.

## **1.4 The Scope of this Research**

This research presents a guideline and methodology to understand better how the transport and penetration of nano-particles in porous media by investigating the phenomenon in the microchannel. In the study, the nanoparticles are treated as diluted species that the transport and distribution are dominated by advection, and diffusion process due to nanoparticle concentration gradient rather than mass. The main scope points to be discussed are:

1. To present a guideline to develop a simulation of particle flow in a microchannel from a point of view of scale squeeze treatment.
2. To validate the simulator with results from a scale squeeze experimental core flood.
3. To investigate and characterize transport and penetration of nanoparticles in microchannel domain with various geometry configuration.

## **1.5 Contributions of this research**

Nanotechnology is still quite new with not yet many applications in the oil and gas industry. Furthermore, there are Health, Safety, and Environment (HSE) concern that need to be considered for implementing this technology. It is important to understand the distribution and placement of the injected nanoparticles in porous media. Many studies have been conducted to investigate the behaviour of nanoparticles in porous media; however, the studies were mostly conducted for porous media in a macroscopic-scale system. Study for the behaviour of injection of nanoparticles in the microchannel-scale need to be conducted more for investigation. Furthermore, it appears that there is none yet established a simulation that focus specifically on the adsorption and desorption mechanism inside the microchannel of the porous media itself.

This thesis contributes in nanotechnology research field by developing a versatile simulator that is based on Finite Element Analysis method to help investigating the penetration, distribution and the adsorption-desorption of injected concentration of nanoparticles in a microchannel as an analogue of injection steps in a scale squeeze process. In the study, the investigation is more thorough than the previous studies where mostly the porous media is treated as bulk domain where the flow phenomenon is closely related with

the porosity and permeability of the domain. In this thesis, the porous media is approached by microchannel domain and the simulation framework is developed by simple physics logic that is easy to process and investigate. The surface phenomenon on the microchannel wall is the process of adsorption and desorption whose mechanisms are separately distinguished by equations that concerns the effect of the geometry of the pore channel of the pore network in the core. The simulator is also adaptable to any microchannel geometry characterisation to modelling particles distribution in simple pore channel geometry to in a more complex pore-channel network. The flow distribution and adsorption/desorption of the particles in the microchannel are observable and easy to understand hence it can be used to investigate the mechanism in the pore channel and in the porous media in general.

## 1.6 Organization of the Thesis

The thesis is organized and divided into eight chapters, and the outline of each chapter is summarised as follows:

**Chapter 1** introduces the motivation, aims and objectives for the development of the simulator to study the penetration of injected concentration in microchannel with various geometries. It also presents the scope and the contributions of this research.

**Chapter 2** presents a brief literature overview of the background information and recent discoveries that are relevant to the study. The chapter includes the potential application of nanoparticles in the oil and gas industry, the scale management and the relation with nanotechnology, the modelling of transport in rock formation, and the core flooding for validation of the study.

**Chapter 3** introduces methodology that is utilised in the study to understand the distribution and adsorption/desorption process of the injected concentration in the microchannel. A brief discussion about porous media, porosity and permeability is included as two of main parameters that widely used in the industry. Key assumptions and the related governing equation for various aspects considered in the study are discussed, which includes the flow condition, representation of the nanoparticles as concentration, boundary condition for the velocity and concentration, adsorption isotherm-mechanism approach and the simulation procedure. Finally, a brief review of the Finite Element Analysis (FEA) used in the model is also discussed.

**Chapter 4** presents the validation of the model to a set of laboratory results, including model simplification for obtaining the suitable equations and parameters. The obtained equations and parameters then are used to study the effect of velocity on the particle distribution in the microchannel.

**Chapter 5** presents the discussion of the behaviour of the particle distribution and adsorption/desorption in the microchannel with different tortuosity. The simulation was carried out for continuous and discontinuous concentration injection for tortuous microchannel with various length and inlet-outlet distance.

**Chapter 6** presents the discussion of the distribution of the injected concentration to microchannel with various wall roughnesses. The investigation for the concentration and adsorption desorption distribution at the dead end region of the microchannel is also discussed.

**Chapter 7** assesses the application of the model in establishing a flexible simulation tool to create a complex microchannel network-model that established from arranging a set of basic microchannel segment that transport and distribution of injected nanoparticles within can be investigated. A few configurations of microchannel segment geometry are introduced as the basis for developing a more complex microchannel-network model. The concentration distribution for similar total adsorption area and similar network dimension are discussed.

**Chapter 8** revisits the objectives of the study, and summarises the thesis contributions, and discusses recommendations for future work.

## **Chapter 2**

### **Literature Review**

#### **2.1 Introduction**

This chapter reviews background information and recent research findings that are relevant to the study. Section 2.2 exposes challenges in the oil industry nowadays as a preface for the utilisation of nanotechnology, that later is discussed in section 2.3 and 2.4. The fundamental idea for the nanotechnology application is to enhance the scale management. The brief review of scale management and nanotechnology is discussed in section 2.5. Some substantial literature on modelling the squeeze treatment is also reviewed. The focus of the PhD is discussed in section 2.6, which is about the modelling of nanoparticle transport in rock formation. In this section, the discussion starts with a brief review about the previous work and inventions that are relevant to the study, including the transport modelling and adsorption/desorption simulation. The review includes the techniques used, the assumptions, and limitations of the models. This chapter is wrapped up with a summary in section 2.7.

#### **2.2 Challenges in the oil industry**

Energy demand is a worldwide issue nowadays because of the fast growth of human population the world. One of the most versatile energy sources is the petroleum industry. Petroleum, which includes oil and gas, is easy to transport and convert to fulfil the need of energy. In addition, derivative products, especially from oil, also have a significant role in many industries in the world, e.g. industry to manufacture clothing, households, etc.

Although oil and gas industry is versatile, they also are characterized as *'a high cost due to high risk'* industry, because it is dangerous to the environmental if it is not handled carefully and the resource is discovered in challenging environment for most of the time. High standard of capital and technology implementation is required. This requirement starts from the early phase of exploration, to drilling, production, and utilisation.

A study that was conducted by Oxford Analytica and Ernst & Young [10] examined the strategic risks for the oil and gas industry. This study is

based on a structured consultation with industry leaders and subject matter professionals from around the world. The risks in oil and gas industry are divided into three parts: macro threats, sector threats, and operational threats as seen on **Figure 2.1** below [10, 11]. The risks explained considers many constraints, e.g. the constraint of human and natural resources, nature and environment, politics, economy, management, and also technical constraint. Furthermore, these constraints are all linked with each other resulting in a high level of complexity.



**Figure 2.1:** Top 10 risks in oil and gas industry (Reproduced from Oxford Analytica and Ernst & Young, 2008 [17])

To balance the high risk, optimum oil and gas recovery is extremely important. On the other hand, the production of oil and gas from the current discovered reservoirs declines as the depletion of the reservoir pressure and the average recoverable reserve. As an illustration, **Figure 2.2** shows the historical and the forecast of the oil and gas production from the Norwegian Continental Shelf (NCS) in 2011. The production of oil and gas from the NCS started on 15 June 1971 and data are from one of the largest oil field in the world, Ekofisk [12]. Total production in the NCS increased until around 2005, and then it went down until 2010. The significant production increase at the beginning of the period happens due to many new discoveries. The attempt of exploring new discovery for oil and gas reserve has been continuing in NCS continually.

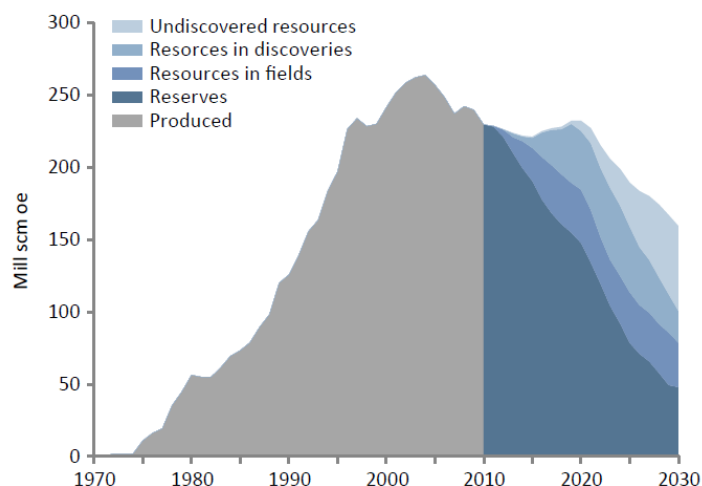


**Figure 2.2:** The historical and the forecast of the oil and gas production from the Norwegian Continental Shelf (NCS) in 2011 (Reproduced from NPD, 2011[13])

There are two main methods to increase and maintain the oil and gas recovery. The first method is to discover and produce the oil and gas from a new reservoir. Finding a new discovery consists of a long journey of many processes, i.e. research, survey, exploration and drilling. Drilling a well is one of the most expensive and risky activities in the exploration phase. It needs to have good planning, establish drilling rigs and support facilities provide the drilling assembly, drill pipes, chemicals, infrastructures and safety support. The uncertainty is also considerably high because there is always a large chance to find a dry well (zero oil). The risk and cost per day of this activity may become exponentially high for an unproven area i.e. wildcat well drilling [14, 15]. In order to reach the difficult and deep petroleum reservoir, ultra-deep and extra-long drilling is developed. The risk is significantly high in this type of drilling operation [16] which require high-end technology and tool quality to face the drilling challenges. A successful drilling should be harmless to the surrounding environment. It also has to be conducted as quickly as possible and as safely as possible, reaching the oil and gas target reservoir.

The second method is to optimise the production from the existing wells and reservoir. This also is challenging because the disruption of flow can happen anywhere, i.e. in the flowlines, in the well, or even within the reservoir itself. Fluid that transports from the reservoir often bring incompatible substances that might deposit in the flow line and reduces the

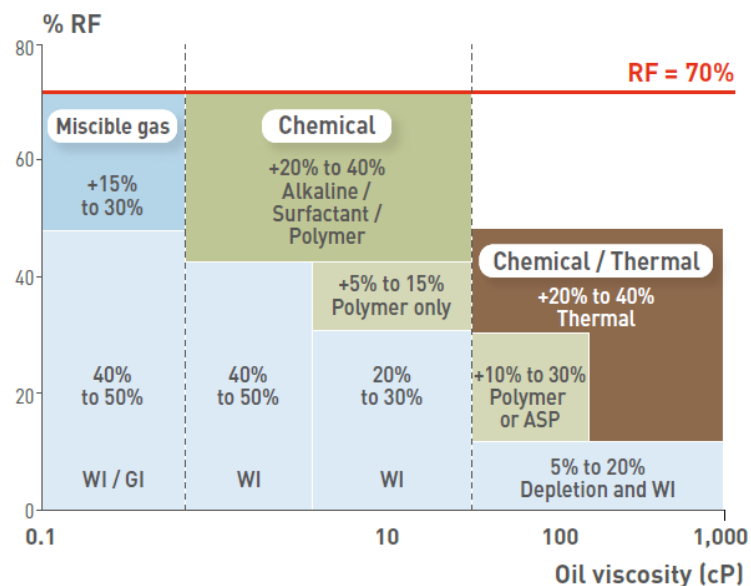
production. This deposit is known as scaling which can happen due to the change of pressure, temperature, pH or the mixing of incompatible substances [17]. In a severe case, scaling can even totally block the flowline. It would be relatively easy to treat if the scaling happened in a surface flowline, but it would be far more difficult if it happened inside a well or in the flow line on a deep-sea bed. Furthermore, scaling also might occur in the reservoir that makes the effort for remedy becomes much more challenging because the mechanism of mechanical remedial must be drop and leaving chemical remedial treatment for solution that include more certainty since it is being injected to the porous media in the rock formation. Scales deposit inside the pores, change the rock permeability, and decrease the production. Apart from scaling, corrosion is also a problem that often appears in the flowline. Acidic substance along with the flow in such high pressure and temperature might cause the corrosion in the flowline.

The consequence of scaling and corrosion are high cost and technically challenging. For severe problem, replacing the production line sometimes is unavoidable in order to remedy flowline disruption. The time for replacement often leads to a significant production loss. It is always better to avoid these problems than conducting remedial treatment. Some of the methods that is used to decrease or to avoid these problems are mechanical removal, coating application, and the use of the resistant alloy [18, 19]. The other way to prevent scaling problem is to introduce chemical inhibitors to the surface of the rock formation surrounding the well by injection through the production lines [20, 21]. This treatment is known as scale inhibitor treatment, which is a common method for prevent scaling problem in the oil and gas industry. After the inhibitor is injected through the production lines to the rock formation, the well undergoes a shut in period for a certain time until being reopened for production. The injected inhibitor is attached in the rock formation and reducing the scaling deposition process.

The utilisation of inhibitor sometimes is challenging according to the case on place. It is common for scale inhibitor to be combined with other substances for a gaining specific purpose, e.g. enhancing inhibitor placement. The combined inhibitor might induce formation of protective layer on the surface of the flow line that alters the flow line's properties [22, 23]. The protective layer formed might be harmful for the pipe or the surrounding area if ingredient include hazardous materials, e.g. phosphorous substance or heavy metals [24]. Therefore, the selection of chemical used is important

to optimise the utilisation and minimise the risk follows. The utilisation of inhibitor that is environmentally friendly is strongly required [25-27]. This type of inhibitor is known as the green inhibitor. The utilisation has four objectives, i.e. to eliminate the environmentally discharge, minimise potential compatibility problems, reduce cost, and green for the environment [28]. Many studies and discoveries are being conducted for both in these areas [29-35].

It is also important to maintain the reservoir pressure for production optimisation. Reservoir pressure depletes after the oil and gas in the reservoir is produced for a certain time. This depletion results in a decrease of the fluid production. In order to have the reservoir pressure maintained, it is often necessary to inject certain fluids to the reservoir in methods that are known as the Enhanced Oil Recovery (EOR). However, current applied EOR technology has only been able to recover at maximum 70% of oil and gas from the reservoir [36]. The comparison of the recovery factor (RF) for different EOR methodology is shown on **Figure 2.3**.



Legends: RF= Recovery Factor, WI = Water Injection, GI = Gas Injection,  
ASP = Alkaline/Surfactant/Polymer

**Figure 2.3:** Recovery factor obtained according to the Enhanced Oil Recovery Method and Oil Viscosity (Reproduced from Total EP, 2008)[36]

In order to achieve the production gain with maximum efficiency, the industry should be adaptive to explore and utilise the available information, innovation and technology. The adaptation also has to be parallel with maintaining a high standard level of health, safety and environment. One of the solutions that are in accordance with both of these objectives is the implementation of nanotechnology.

### 2.3 Overview of nanotechnology

Nanotechnology itself is defined as a study, development, manipulation and the application of technology for particles with critical diameter of 1-100 nm that have unique properties due to their small sizes. Nanotechnology is an interdisciplinary technology that combines the chemistry, physics, biomedical, mathematics and engineering [37, 38].

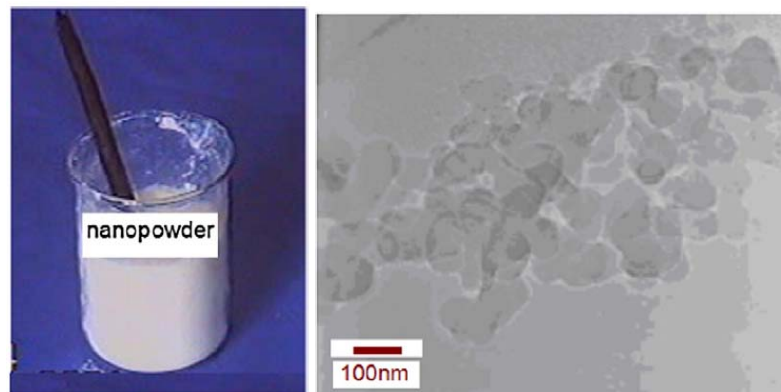


**Figure 2.4:** Nano particle in a beaker (left) and the image of a polysilicon observed under a TEM (right) (After Ju and Fan, 2009) [39]

Nano is derived from a Greek word "nanos" which meaning is dwarf. In science, nano is a prefix to express a magnitude of one billionth of a unit. For example in lengthwise, nanometer means one billionth of metre or 10 Angstrom ( $\text{\AA}$ ). As an analogy, if the approximate dimension of one hydrogen atom is 1  $\text{\AA}$ , therefore 1 nanometer (nm) is about 10 hydrogen atoms [37, 38]. Nanoparticles normally appear as powders. Figures of nanoparticles in a beaker and under a TEM (Transmission Electron Microscope) are displayed on **Figure 2.4** [39].

There are two methods to manufacture nanoparticles. The first one is the top-down method, which is to mechanically mill a large scale of material continuously until the required size of nanoparticles is obtained. This method results in a broad distribution of size (10-1000 nm), varied particles, geometry and some impurities. The other method is the bottom-up method, where each particle is manufactured one at a time. This approach includes pyrolysis, inert gas condensation, *solvothermal* reaction, sol-gel fabrication, and the structured media. This approach results in more uniform nanoparticles [37, 40]. Nanoparticles formulation is also important to avoid the manufactured nanoparticles forming agglomerate that increase the overall size of the particles.

Nanoparticles can be synthesised from any material, e.g. carbon, gold, aluminium, etc. The properties of nanoparticles link those belong to both of their macro and atomic/molecular structures. The properties of both macro and atomic structures of a material are normally different. This difference presents because the quantum effect appears more in the material's atomic structure than when it materials as macro structures [37]. These differences occur for both physical and chemical properties that originated in such complexity from the material's atomic and molecular foundation. The properties of macro-structures are relatively constant regardless of the size. The amount of the atoms on its surface is insignificant against the number of atoms in its bulk. However, this is not the same when the material stands in its molecular size, e.g. nanoparticle. In this state, every single nanoparticle significantly affects each other that determine the physical and the chemical properties of the overall structure. Nanoparticles also have other unique characteristics that the specific functional surface area (i.e. surface area per unit volume) is remarkable wide [41, 42] that allows interaction among the nanoparticles themselves. This vast functional surface area, in such ways, dominates the contribution for the overall material's properties that induces different properties than its macrostructure characteristics. Nanoparticles also are small enough to be able to confine their electron to expose quantum properties that affect the appearance, electrical, temperature and magnetic properties [43, 44]. As an example, in contrast with a solid-solid composite, thermal conductivity of particles in fluid is increased when the particles' size is reduced [45]. Therefore, the thermal conductivity of nano-structured material is significantly higher than its macro-structured state. Nanoparticles structure is also more adept to dilute in

suspensions than the macrostructure. This important physical property allows a strong particle-solvent interaction that overwhelms the density contrast. Nanoparticles are also proficiently able to diffuse in solvent due to a temperature difference. On the other hand, macro-structured material only has two interactions with the liquid, i.e. sinking or floating.

Nanoparticles can also be manufactured together with other substance to increase the strength and durability of a product. For instance the incorporation of the clay nanoparticle with polymer matrices to make a stronger plastic [46]. Nanoparticles also can be manufactured to establish a certain structural geometry. A particular example for this is the carbon nanotubes (CNTs) [47-50]. CNT is a special structured material because it has particular form and properties that other materials do not have. CNTs can transport electron 10 times faster and 100 times more current capacity than the conventional silicon material. CNTs also can disperse the heat better [51]. There are plenty possibilities for innovation and development for the implementation of nanotechnology. In the industrial sector, this includes communication and information, medical, space, structures, clothing and also oil and gas [39, 52].

## **2.4 The application of nanotechnology in the oil and gas industry**

There is a huge potential for nanoparticle technology application in the oil and gas industry because nanoparticles can be manufactured abundantly as required as it was discussed previously in Section 2.2. The size of an individual nanoparticle (1-100 nm [37, 38]) is generally much smaller than the average size of a rock pore [53]. The consequence of this size, nanoparticles can be injected to the rock pores where the vast total surface area can be exploited to enhance the property of the rock as required [54]. In this section, the discussion of the application of nanotechnology in the oil and gas industry is divided into (1) nano-coating, (2) nano-fluids, and (3) other innovations.

### **2.4.1 Nano-coatings**

Nanoparticles have unique properties to enhance the strength and durability of other material. Not only for the polymer (plastic) [46], this property has been utilised by US Navy to strengthen shipboard and submarines by spraying nanostructured alumina–titanium coatings on their

exterior parts [55]. In oil and gas industry, this coating can be used to increase the quality and strength of the drilling assembly without altering its dimension significantly. This coating also can be customized to increase its sturdiness to withstand the condition of high pressure and temperature in the borehole. Drilling assembly that has a higher durability for toughness will have longer lifespan, less maintenance, lower equipment cost overtime, and furthermore, longer drilling path and allow for extreme trajectory. This will be significantly beneficial for deep sea and ultra-deep sea drilling activities.

Nano-coatings also have potency for the control of the aquatic fouling that happens in marine environment. This anti fouling technology prevents attachment of any organism on to the surface. Nano-coating is a non-toxic protection method and environmentally friendly since there is no involvement of any biocide compounds [56]. Materials that have been strengthened by incorporation these nanoparticles also can be used for the infrastructure at the harsh environments (e.g. desert, deep sea, jungles, etc.) where maintenance is difficult to do [57, 58].

Nano-coatings can also be used to cover the surface of the production line. Customized nanoparticle can be used as an insulator on the outside of the production line. An example of a suitable nanoparticle for insulation is the metallic Carbon Nano Tubes (CNTs). Carbon Nanotubes (CNTs) are allegedly the strongest material known today in term of the tensile strength and elastic modulus [59, 60]. The tensile strength of a multi-walled carbon nanotube reaches 63 GPa. This means that the CNTs can withstand tension of a weight equivalent to 6422 kg (14,158 lbs) on a cable with cross-section of 1 mm<sup>2</sup>. The metallic nanotubes display very high conductivities because the electrons inside the CNT only transport along the tube and do not scatter, which is known as a ballistic transport [61]. In the inside, the configured nanoparticles can be functioning as an anti-scaling layer. In the same time, it will reduce the corrosion possibility due to the increase the material resistance [62]. It is also harder than diamond [63], therefore CNTs can be, even more, manufactured to replace a diamond bit that is currently use in drilling hard rock formation in the oil and gas industry.

Gas hydrate is a structure that is highly unwanted in the flow path of oil and gas in the petroleum industry. It is originated from crystalline structures which are constructed from a trapped gas molecule inside of a hydrogen-bonded cage of water molecules [64] that has the tendency to agglomerate and block the flow path [65-67]. In severe case, hydrate also

can damage the valves, production instrumentations, and facilities. Nanotechnology also can be utilised as an anti-agglomeration agent for hydrate formation. One of the examples is to use Ni-Fe nanoparticles as an agent dissolve hydrate formation [68]. The size of the Ni-Fe particles is small enough (50 nm) to penetrate the cavity of the hydrate (86-95 nm). The temperature of the Ni-Fe particles increase by themselves up above 40°C and magnetized due to hysteresis and relaxation process [69, 70]. This occurrence disturbs the thermodynamic equilibrium of the hydrate and dissolves the hydrate establishment.

Deposition of wax and paraffin is also a challenging problem for the flow assurance in the oil production flowline. Wax and paraffin, that are originally soluted in the produced oil, precipitate due to the reduction of temperature, pressure and the amount of dissolve gas in the flow line. The severity of the precipitation depends on the amount of the paraffin originally in the fluid. However precipitation is the worst in location with low geothermal gradient and temperature [71]. An example of nanoparticle that can be used to combat wax and paraffin precipitation is Co-Ni nanoparticles [72]. To fight the wax and paraffin precipitation in the flowline, the Co-Ni nanoparticles are introduced with an exclusive polymer into the annulus of the production well throughout the lifetime of the well. Magnetic fields in the casing force the Co-Ni nanoparticles to vibrate and heat up. This temperature increase will melt the precipitated wax and paraffin in the flowline.

Scaling also can happen in the reservoir, blocking the rock pores and significantly reducing the total flow. Central tendency of the pore-throat size for a conventional reservoir rocks is 2 mm in diameter, 0.03 mm to 2 mm in tight-gas sandstone, and 0.005 mm to 0.1 mm in shales [53]. On the other hand, the size of a nanoparticle is much less than this magnitude i.e. 1-100 nm [37, 38] , allowing the nanoparticles to penetrate deeper to the reservoir. Adding nanoparticle to the scaling inhibitor (SI) increases the attachment of the SI onto the formation rock and enhances its lifetime regardless the temperature effect in the reservoir [35].

#### **2.4.2 Nano-fluids**

Synthetic nanoparticles also can be manufactured as an ingredient of the drilling mud to enhance the mechanical, thermal, electrical and magnetic

properties. Mud suspension is utilised in order to maintain the pressure balance between the formation and the wellbore while well drilling is conducted. In addition, the mud suspension also has a necessity to decrease the temperature of the bottom hole assembly and to bring rock, debris and monitoring signals to the surface. Customizable nanoparticles can be added to improve the property of muds towards these functions [38]. The nanoparticles also can be added to completion fluid to enhance its property as needed.

The tendency of nanoparticle to be agglomerated and adsorbed on the rock surface can be problematic if the nanoparticles are intended to inject far into the rock pores. To reduce this tendency, the nanoparticles can be coated by special substances that reduce the particles attachment on the rock hence it can be transported inside the pore system for a long distance. One example of the coating type that is suitable for this purpose is by introducing a super-paramagnetic property to the nanoparticles. The super-paramagnetic property induces an oscillating magnetic field that creates an interface motion between the disperse nanoparticles and the carrier fluids at the pore scale with the effect of a magnetic force is in place [73, 74]. The dispersion of the nanoparticle in the carrier fluids due to the super-paramagnetic property is quite stable even for a high salinity system. This occurrence is caused by the presence of electrostatic repulsions between the nanoparticles and the negatively-charge sandstone and carbonate lithology [75, 76]. The coated nanoparticles can be utilised as a tracer to monitor immiscible fluid distribution in the subsurface in order to bring up the detail image of the subsurface [77, 78]. This tracer can be used to gain more advance subsurface mapping in order to increase the certainty of finding the oil and gas in the rock formation.

The petroleum industry also has started to review the possibility of implementing the nanotechnology as a pivoting role to enhance the oil recovery [33, 79-82]. One important aspect in enhancing the oil recovery is to change the natural wettability of rock from oil wet to water wet [83]. Oil wet property is an affinity of rock to adsorb oil than other fluid, and water wet property is an affinity of rock to adsorb water than other fluid. Oil extraction from rock formation with water-wet property is conducted easier than from rock formation with oil-wet property. Nanotechnology has a good prospect to alter the rock wettability from oil wet to water wet. Certain nanoparticles in solution creates an extra osmotic pressure that drives and induces the oil

delamination from the rock surface [84, 85]. One of the possible applications is introducing magnesium and sulphate ions to alter wettability of an oil-wet calcite surface into a water-wet surface [86, 87].

In oil and gas industry, water production should be minimized because its mobility is higher than the produced oil. Water production as well brings unwanted problems to the flow assurance, e.g. corrosion and scaling problem [88]. Nanotechnology also can be utilised for shutting of water zone in the well effectively. Adding bentonite type of nanoparticles into a hydrogel gives a positive result of establishing nano-hydro-gel to plug fracture area that produces water from the formation [89].

Fine particles migration in the rock formation can introduce many problems, for example reduce of rock permeability, adding skin to the surrounding formation of a production well, even to induce severe sand problems to the production system. It is discovered that fines migration can be reduced by introducing MgO, SiO<sub>2</sub>, and Al<sub>2</sub>O<sub>3</sub> nanoparticles into the reservoir [8]. Soaking the porous material with these nanoparticles increases the ability for the fine grains sticking on the rock grains and hindering the migration. In detail, adding 0.1 wt.% of MgO and SiO<sub>2</sub> nanoparticles reduces the fine migration by 15% compare to the reference case without nanoparticle utilisation. The utilisation of the MgO is more effective even for a high flow rate when it is used at higher concentration.

Although there are many possibility of nanoparticle utilisation in the reservoir, the real challenge is the manufacture and the transport of the nanoparticles in to reach the designated location in the reservoir [90]. Therefore, it is essential to study the transport behaviour of the injected manufactured nanoparticles in porous media.

### **2.4.3 Other nanotechnology innovations**

Nanotechnology allows further discovery and innovation for material that has improved properties. The use of nanotechnology in electronics and communications gives better quality and performance. One of the recent innovations is the nanosponge. Nanosponge is a reusable highly hydrophobic but petrophilic substance which can be used to remove the oil spill from water [91]. The oil that is absorbed in the nanosponge can be extracted or burned, with the nanosponge remain intact.

Nanosolar is also an option for energy source. The surface area to volume of a nanoparticle is large due to its small size. This allows the solar energy to be transferred efficiently. In addition, nanoparticles can be manufactured as demand that in agreement with the standard of health, safety and environment [92, 93]. There also is a possibility to develop nanobots, which are programmable tiny robots that can be used to reach difficult areas in the industry (e.g. flow lines, reservoir, etc.) to perform surveillance or maintenance [94].

## **2.5 Challenges of Nanotechnology Development and Application**

Nanotechnology has a bright future recalling the usage to overcome current challenges in the oil and gas industry. Furthermore, it offers promising advances in many other sectors, such as material technology, energy, electronics, medical technology, biotechnology, and many other applications. There are also many available rooms for possibilities for its innovation and application. This helps to discover higher quality materials with longer lifespan, less maintenance, environmentally customised, thus resulting a more efficient industry.

Nanotechnology is the results of a complex interdisciplinary interaction, thus a wide range of research and study is compulsory. Let alone the research and the study, this new technology also needs manufacture system and real-on-field application. Successful and unsuccessful result should be experienced in the process.

Currently, it is conceivable that this technology demands high focus and capital. Furthermore, any commercial success for this technology is also still arguable at least for the short future [38]. However, it is certain that the contribution of the nanotechnology in the future will become more vital since it can be applied in almost any aspect for a higher life standard.

There are some practical challenge for the development and improvement of the nanotechnology, which are related to the employment sectors, education level, regulation and investment.

**Employment sectors:** A new technology that offers more application that is efficient might bring disadvantages. For example, nanotechnology can be

applied to manufacture a lighter and stronger material. It is understandable that less maintenance is required for this material. It is also easier to be transported from one location to another. This by chance can result in the rising of unemployment in certain sectors. However, other sectors shall revitalise, for instance the raw material suppliers, accesses to the nanotechnology research facilities and factories. For large scale of research, facilities and factories require more supports such as housing for the employees, security, caterers, advertisement, etc. These will balance, even adding the sector for employment.

**Education level:** Experts in nanotechnology are needed to guarantee the sustainable and continuous development of the nanotechnology. Let alone the experienced experts, it is also important the level up education of the people of the nation. High educated people will easily adapt with new technologies, even to provide feedback for improvements. This will have a mutual benefit where supply and demand from the producer and consumer will balance and supporting each other [95].

**Regulation and investment:** Nanoparticles can be synthesized from any material, yet a comprehensive study for the benefit and the impact for humans and the environment are necessary. Validation methods are required to measure the toxic level of the synthesized nano-material, including the model for prediction. In addition, it is a challenge to develop an assessment tool and reverse system if the nanoparticles are harmful to human and environment [96]. Moreover, it should be beneficial if the nanoparticles can be synthesized from recycled waste. Therefore, the role of the government becomes important where there should be a proper and clear regulation system to control and monitor the syntheses and utilization of the nanotechnology. The supportive regulations also are required to invite the domestic and international investors for providing the capital support. The stakeholders of the oil and gas industry also welcome to contribute to the emerging of the nanotechnology, especially since the applications directly intersect with the necessities in the industry.

## 2.6 Scale management

### 2.6.1 Definition and the effect of scale

Scaling is a common problem happens in the oil industry. Scale is a crystalline deposition that is brought by produced water from the reservoir. It occurs in the flow path of the hydrocarbon that may hinder the production significantly. A picture of a heavy scale deposition in a section of production pipeline is displayed in **Figure 2.5**. Typically the oilfield scales consist of one or more types of inorganic material. Some other debris might be as well included, such as sand, corrosion product, organic precipitates, etc. [97].



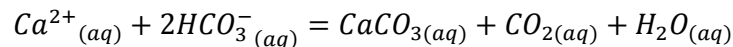
**Figure 2.5:** Picture of a heavy scale deposition (After Statoil, 2007)[98]

Scale deposition can cover the surface of almost any material, such as rock or metal. Scale problem can be happening along the production facilities, pipeline, valves, downhole equipment, perforation, and the rock formation itself. Many further problems happen due to scaling deposition. Deposition that happens near the wellbore area, perforation or the gravel pack introduces formation damage (skin) to the production system. Scale that is deposited in the flow line reduces the flow assurance in the production system. In severe condition, scaling problem can even block the flow line completely. Scaling deposit also can reduce the lifetime of the production facilities, e.g. induces failure to the safety valve and chokes, wears the pump, and induces corrosion along the production system. Some scales even contain some radioactive materials such as the uranium, radon, and radium. This radioactive scale ingredients, which is also known as NORM (Naturally Occurring Radioactive Material), are hazardous in the term

of Health and Safety Environment [99]. Therefore it is urgent to cope with scaling problem, as well to prevent its formation.

### 2.6.2 Formation of scale

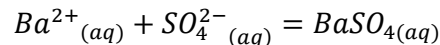
Scaling happens due to its nature to deposit by itself (self-scaling) or due to chemical reactions [100]. “Self scaling” means that the scale deposition occurs due to the alteration of pressure and temperature. When the fluid is produced from the reservoir rock formation to surface, pressure and temperature change causing salt precipitation from the brine water. This salt will attach itself on the surface of rock and other materials as scale. The example of this type of scale is calcite deposition, where CO<sub>2</sub> in the water is released as the pressure decreases. The release of CO<sub>2</sub> removes the carbonic acid that bind the dissolved calcite in the water. Temperature decrease might also decrease the solubility of calcite in the water. Carbonate precipitation occurs due to alteration of pressure and/or temperature on site which chemically reacts as follows.



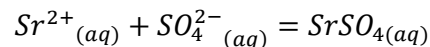
The second cause of scale construction is the chemical reaction of the incompatible water composition. The example for this occurrence is the development of the barite scale, which is caused by the mixing of the high sulfate in the sea water and barium in the formation water.

Some of common mechanisms of the scaling formation due to chemical reaction of the incompatible brines are shown below:

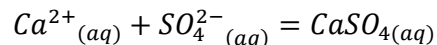
- Deposition of barium sulphate



- Deposition of strontium sulphate



- Deposition of calcium sulphate



Type of scales that typically happens in the oilfield is shown by **Table 2.1**:

Formula	Scaling Mineral
BaSO <sub>4</sub>	Barite
CaCO <sub>3</sub>	Aragonite, Anhydrite, Calcite, Gypsum and Vaterite
CaF <sub>2</sub>	Fluorite
FeS	Mackinawite
FeS <sub>2</sub>	Pyrite
NaCl	Halite
PbS	Galena
SrSO <sub>4</sub>	Celestite
ZnS	Sphaerelite

**Table 2.1:** Types of mineral scales in oilfields (after Jasinski, 2004) [100]

### 2.6.3 Treatment of scale

It is risky and sometimes very expensive to remove scale, even though wide selections of chemical and mechanical remedial methods are available. For the case with a severe scaling problem, changing the flow facilities or instrument sometimes is unavoidable. It is believed that “scale prevention is better than curing”.

Scientists and experts have conducted years of thorough study to understand the rock formation and ways to overcome the scaling problem [5, 101-104]. Many treatments have been developed to handle scaling problem and the most common treatment is the scale squeeze treatment.

A frequent way to precede this attempt is to introduce scale inhibitor to the system. The purpose of inducing the scaling inhibitor is to cover the active scaling crystal that form the scale, and hinder those crystals to join together, building up further scale. Inhibitors are manufactured with phosphorous containing chemical compound are commonly used for this attempt [105]. A common method use to deliver the inhibitor is the one known as “scale inhibitor squeeze”.

In the treatment, a solution that contains scale inhibitor is injected into the formation. Then some of the inhibitor will stay on the rock surface, and the rest will slowly detached itself back into the produced water phase.

---

There are 2 types of inhibitor squeeze treatments according to the attachment mechanism to the rock surface [100]:

1. Adsorption squeeze, where inhibitor is to be adsorbed onto the rock surface by a physio-chemical process. The mechanism happens due to the electrostatic and isothermic van der Waals interaction between the inhibitor and the formation minerals. This mechanism is a function of the temperature, pH, mineral substrate and cations (e.g.  $\text{Ca}^{2+}$ ). The retaining time is the most effective in sandstone environment, which is about 3 to 6 months.
2. Precipitation squeeze, where inhibitor is to be phase-separated onto the rock surface by adjusting the pH, and temperature, and the ion concentration of the inhibitor. The purpose is to place more than one type of inhibitor per scale squeeze. The life time of this treatment could exceed the adsorption squeeze.

As a scale inhibitor, it is common to use phosphonate based chemical to prevent scale nucleation and formation [106]. In the scale squeeze treatment, the scaling inhibitor is induced in to the production system according to a certain procedure, which commonly includes injection of preflush, pill, overflush, and well shut in period [107]. The details of the procedure are found in APPENDIX A.

The success of the scaling inhibitor injection is observed by investigating the return profile of the return 'waste' concentration of the inhibitor. Successful scale squeeze is when the return inhibitor concentration is at or above the critical concentration needed to prevent scaling. This critical concentration is known as MIC (Minimum Inhibitor Concentration). Good inhibitor should be able to have good interaction attaching itself with the rock matrix for quite long period. It also should be stable in the formation environment and the brine system, without significantly reduce the permeability of the formation itself. Then, the inhibitor concentration that comes from the return waste is plotted against the time. The example of the plot is displayed in **Figure 2.6**. At the beginning, a large amount of the inhibitor will return to the surface, which is shown by rapid decrease of inhibitor concentration curve shown in the figure. After some time, the inhibitor concentration the curve is slowly declining until it reaches a defined level of Minimum Inhibitor Concentration (MIC). A successful scale squeeze treatment is when this curve does not fall below the designed MIC, which means scale deposition is not happening in the system. When the line drops

below MIC level, inhibitor is required to be injected again in the system. The level of MIC is obtained from the core flooding experiment in laboratory. An example for the curve with the MIC is shown by the **Figure 2.7**. In the figure, the MIC level is displayed as the minimum inhibitor range.

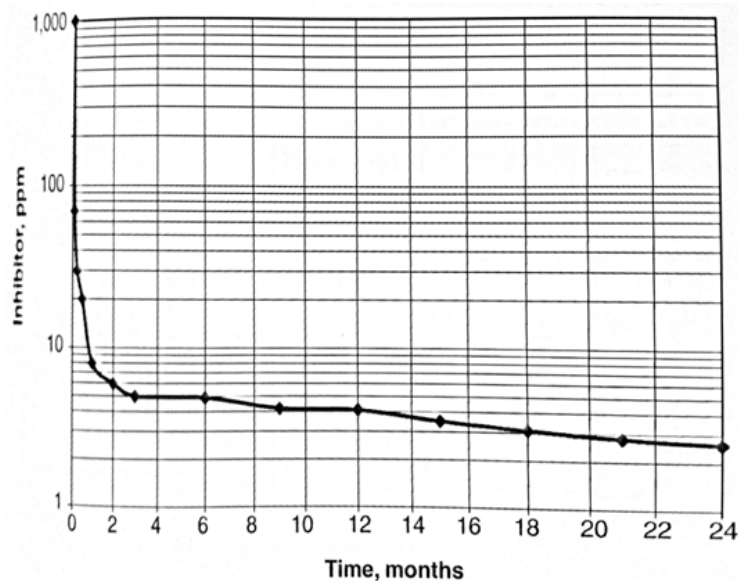


**Figure 2.6:** Illustration of a general curve of inhibitor concentration vs. time for any scaly inhibitor (reproduced from Jasinski, 2004) [100]

The lifetime of the scale squeeze treatment depends on the concentration of the inhibitor injected during the treatment, the characteristic of the inhibitor and the inhibitory performance [108]. The selection of inhibitor and injected fluid should be conducted according to the type of the formation. In the operation, sometimes inhibitors are mixed with other chemical substance. A wrong selection might bring harmful outcome. When the mixed inhibitor is injected through the flow line, it might form a thin layer on the surface of the flow line and alters its original properties [22, 23]. Altering the surface properties of the flow line might lead to a contra-productive result to the flow assurance. Some inhibitor chemical also might include hazardous material as its ingredients, e.g. phosphorous substance or heavy metals, that are harmful to the environment [24]. Therefore it is wise to have this scale squeeze treatment well-planned. The utilisation of inhibitor that is 'green' to the environment is also necessary [25-27]. The utilisation of the green inhibitor has four objectives, i.e. to eliminate the

environmentally discharge, minimise potential compatibility problems, reduce cost, and green for the environment [28].

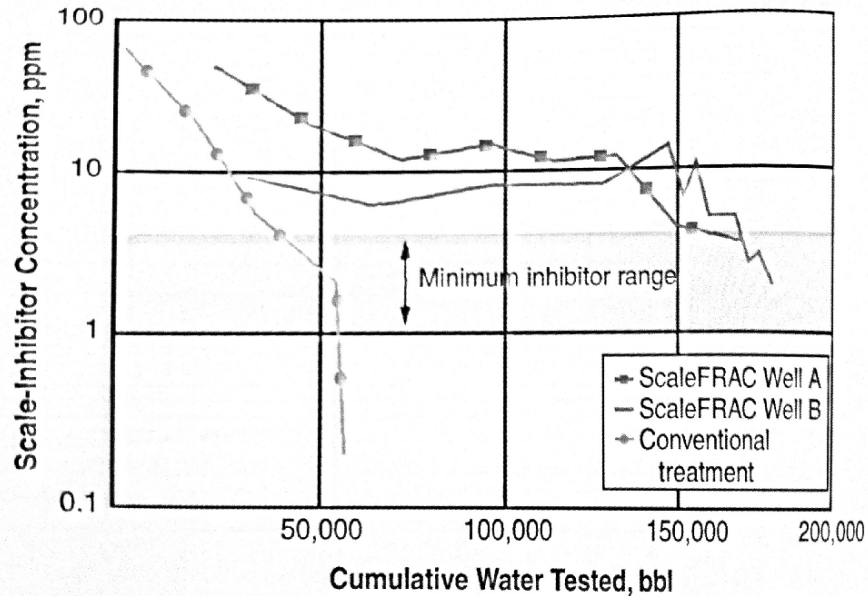


**Figure 2.7:** Inhibitor return curve showing the range of the Minimum Inhibitor Concentration, MIC. (reproduced from Jasinski, 2004) [100]

Enhancing the lifetime of scale inhibitor attachment has attracted much research attention, e.g. by inducing an improved precipitation and adsorption additive for the scale inhibitor [109, 110], utilisation of cross-linking inhibitors [108] and altering pH solution, calcium for the adsorption of the squeeze treatments [109-111] and applying kaolinite to modify the properties of near wellbore surface [112-114].

Considerable amount of studies has been conducted to understand the adsorption of the scale inhibitor in the formation. Baraka-Lokmane and Sorbie [115] investigated the adsorption of scale inhibitor in the carbonate core for various concentration and pH values. They discovered that the effluent pH of the injected brine with pH 4 and 6 was stabilised at level 7 where the level of calcium and magnesium remained constant on these pH levels. Calcium dissolution was observed for injection of brine with pH 2 where pH of the system was increased above 8. It was also discovered that more calcium dissolution observed in the environment with high concentration of Scale Inhibitor (SI) and low pH. Their experiment also shows that the SI bonds quite strongly with both calcium and magnesium in

---

this condition. The effect of Ca dissolution dominates the retention of Ca-SI. Therefore, the calcium always shows an increase on the effluent injection. The Mg effluent, however, shows a clear dip on the placement and peak in the postflush. The model developed that follows Freundlich adsorption isotherm mechanism satisfied a simple adsorption model, however it did not represent all that was happening in the floods. Gdanski [116] discussed how formation mineralogy can improve successful design of scale squeeze treatments. He stated that the main stage of squeeze treatment should consist of no more than 5% inhibitor product at pH neutral. If swell-able clays are present in oil-bearing layers of the producing well, the base fluid should consist of 1 Molar brine. Typical overflush volume is ranged between 2 to 8 of the volume of the inhibitor main stage, depending on formation porosity, total mineral content, and compositional distribution of non-quartz mineralogy. He also proposed that the compatibility of the main stages with formation fluid should be achieved with preflush, and not by lowering the pH of the main stage since the dissolution of the  $\text{CaCO}_3$  and percolating of aluminium from clay.

Many also have been trying to develop models and simulators to model the adsorption process of scale inhibitor. Hong and Schuler [117] developed a mathematical model to describe the process of scale inhibitor adsorption based on derived algebraic equations. The results from the simulation were validated with field and laboratory data. It was found that the model provided the most conservative prediction of the squeeze lifetime since it still requires incorporation of the kinetics effect when the resident time is short compared with the time require to reach equilibrium. Zhang and Sorbie [118] developed a two-phase multi-component near well bore numerical modelling to simulate scale inhibitor squeeze treatment for horizontal wells as it requires modification compare with the treatment in the vertical wells. They claimed that the simulator could be used for preliminary assessment and design of the treatment in the horizontal well. The result of the simulation was comparable to result from ECLIPSE, which is commercial transient reservoir simulation software in the oil and gas industry. However, the calculation only use one set of squeeze operational data, i.e. preflush, injection, and overflush parameter, therefore general conclusion cannot be made from the limited simulation. Sorbie et.al. [119-121] investigated and modelled the coupling of adsorption and precipitation of the Scale Inhibitors (SI) in porous media. The study was conducted by laboratory experiment

---

where the system exhibited either adsorption only or the coupling of adsorption and precipitation. The modelling for the adsorption follows the Freundlich adsorption isotherm mechanism and the precipitation follows the formation of the calcium salt on the SI that include the equilibrium solubility product,  $K_{sp}$ . Coupling of the two mechanism results in an equation to solve that can predict the apparent adsorption of the SI where both of the adsorption and precipitation mechanisms occurred. The results agreed qualitatively with the experiment conducted.

In the oil and gas industry, nanoparticles can be injected into the reservoir to cover the surface of the rock and alter the property of the reservoir rock's surface area [6, 7]. This alteration of the rock property has potential for implementation to enhance the attachment lifetime of the scale inhibitor. Shen et.al. [122] investigates the control placement of scale inhibitor in the formation with stable Ca-DTPMP (Diethylene-triamine-pentatakis) nanoparticle suspension in porous media. DTPMP is commonly used in the oil industry as a scale inhibitor. Incorporating the DTPMP with calcium might enhance the adsorption of the scaling inhibitor [109-111]. In the study, the Ca-DTPMP is coated with Poly-Phosphino Carboxylic Acid (PPCA). In the study, PPCA acts as a dispersant to stabilise inhibitor nanoparticles in the aqueous solution. PPCA increases the Ca-DTMP negative surface charge, reduces the particle deposition, and increases the particle movement in porous media. In their study, they also included KCl concentration in the system. They found that the increase of the KCl concentration increase the adsorption of the PPCA-coated Ca-DTPMP. PPCA is common to be used in the oil industry to treat the produced water because of its nature to have a strong inhibition capability [123]. Ghorbani et.al. [35] conducted a laboratory experiment to investigate the adsorption of PPCA as a common scale inhibitor onto a C-based nanoparticle (CBN). The experiment is validated by comparing the result with the attachment of PPCA on North Sea sands, silica powder, and porous silica particles. Since the adsorption is highly proportional with the surface area, it is presumed that the surface area of all samples is similar. They discovered that there is no PPCA adsorption on the silica sands. This happens because the presence of calcium ion is needed for the PPCA adsorption [124]. However, it is discovered that the attachment of the PPCA on the Carbon Nano-tube (CNT) is significantly higher than on various types of sands, even without the presence of any calcium ion. The adsorption time of the PPCA on the CBN

---

was only 30 minutes, compared to hours for typical squeeze treatment. Therefore, CBN has a potential as a mediator for adsorption. They suggested that the mass of the adsorbent was the key factor in the adsorption of the PPCA on the CBN as it related directly to the active site of the nanoparticles [35].

Zhang et.al. [90] developed a synthesis route for constructing nanometer-size metal-phosphonate particle to use for scale inhibitor. The size of the synthesised particle is about 50-200 nm and can withstand 70°C in 2% KCl for more than one week. Zhang and co-workers [125] continued the study by incorporating zinc to the DTPMP based on the previous discovery that adding the first transitional element cation (e.g. zinc) in the phosphonate inhibitor solution could enhance the inhibition efficiency and the squeeze lifetime of some scale inhibitors [126]. They utilised zinc chloride to the surface of 22-nm silica particle, then followed by a gradual induction of DTPMP to form a nanometer-sized particles in the presence of sodium dodecylbenzene sulphonate (SDBS). Then the nanoparticles are transported in to crushed packed columns of calcite and sandstone. Investigating the normalised return volume profile, they stated that the inhibitor long-term return flow and the squeeze lifetime have improved by a factor of 60 without significantly affecting the cost.

For a high temperature environment, polymeric scale inhibitors have a better performance to avoid scaling problem than phosphonate due to its nature of the thermal stability [127-130]. Yan et.al. [131-133] developed polymeric scale inhibitor nanoparticles that is synthesised from Boehmite ( $\gamma$ -AlO(OH)) nanoparticles with size from 3-10 nm. The Boehmite nanoparticles are used to cross-linked sulphonated polycarboxylic acid (SPCA) to increase their adsorption in the formation by converting free water-soluble scale inhibitor into a viscous gel.

Sorbie et.al. [134] studied the effect of including mutual solvent (MS) on a scale squeeze treatment for single and multilayer near well system design model, for high and low water cut. Including the MS in the preflush increases the scale squeeze treatment clean up time without altering the oil production. However, the pressure drop for production is lower and beneficial for the fluid mobility from the reservoir.

## 2.7 Modelling transport and adsorption in rock formations

Nanotechnology is a new technology and there are yet many literatures that discuss modelling of transport and distribution of nanoparticles in porous media that is related to the oil and gas industry. It is also challenging to model the transport and distribution of nanoparticles in porous media. Since a nanoparticle has a large surface area per unit volume, nanoparticles tends to agglomerate and difficult to remove from stationary porous media.

In the modelling of nanoparticle transport, usually the nanoparticles are simplified as a volumetric concentration of diluted species due to the nature of the nanoparticle size [39, 135]. This treatment is valid because in the injection, nanoparticles are diluted in solution that is known as nano-fluid. The contrast in magnitude between a nanoparticle and the pore channel is also significant. However, it is important to also assume that the diameter of the nanoparticle is constant, which means no agglomeration [136]. If agglomeration is considered, the process catalyses further agglomeration mechanism until the nanoparticles can no longer treated as concentrations.

There are many ways of modelling porous media in rock formation. Porous media is modelled as a network of pore throats that is present in a core sample. In this pore system, the flow can be approached with Darcy's law where the pore configuration is represented by permeability.

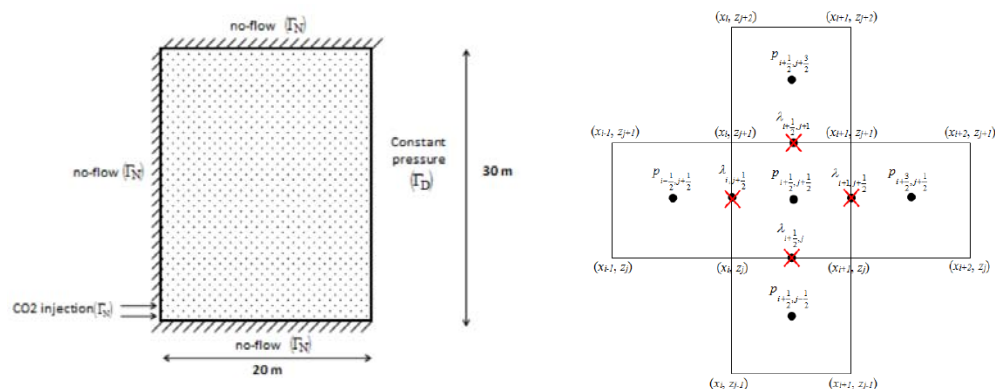


**Figure 2.8:** Illustration of the basic element of Hydraulic Pore Network (Hypon) (reproduced from El Amin et.al, 2004 [136])

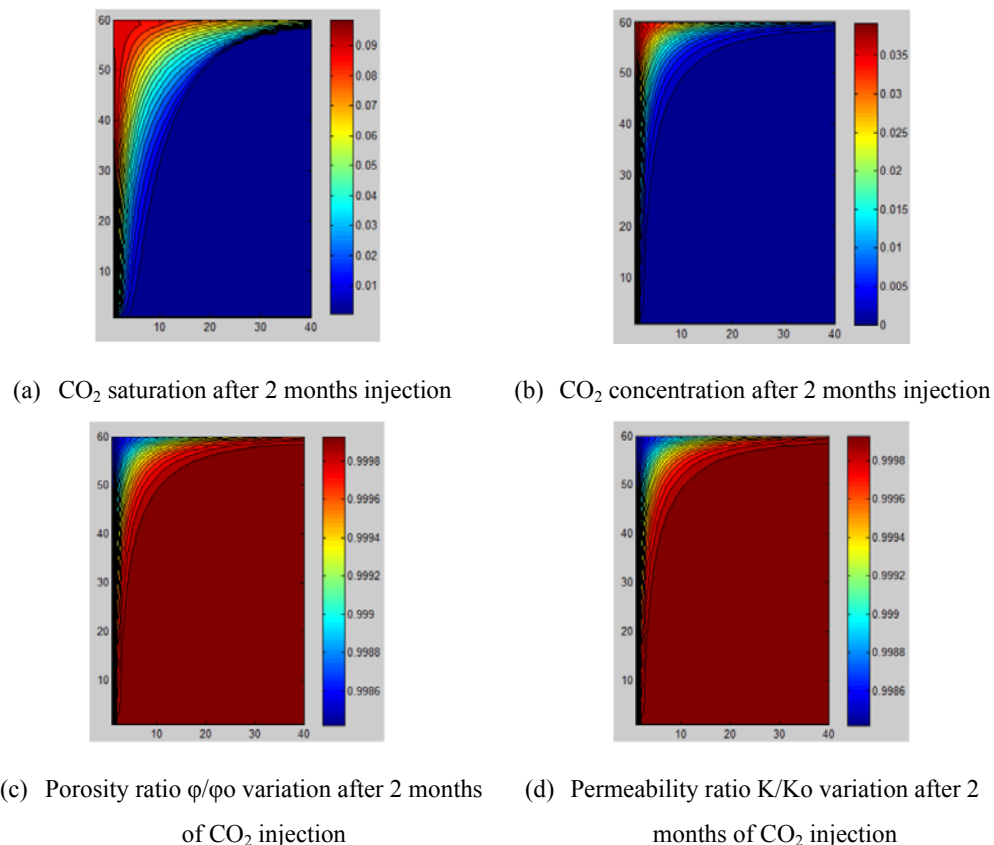


**Figure 2.9:** Result of simulation for after 2 months of CO<sub>2</sub> injection (reproduced from El Amin et.al, 2012 [136])

One example of study of nanoparticle transport in porous media is the one conducted by El-Amin, Sun, and Salama [136] who developed a mathematical and numerical model for simulating diluted nanoparticles transport in an injected CO<sub>2</sub> in two-phase immiscible compressible flow in heterogeneous porous media. The domain of the model is 2D rectangle with certain boundary condition as it is shown in **Figure 2.8 (left)**. Darcy's law and equation of mass conservation are implemented in the study where the solution is obtained based on the Cell-Centered Finite Difference (CCFD) and the Implicit Pressure Explicit Saturation-Concentration (IMPESC) scheme with consideration of buoyancy effect, capillary force, and Brownian diffusion. The CCFD utilised is illustrated in **Figure 2.8 (right)**. In the modelling, the transported species was treated as a moving diluted species in a two-dimensional porous media. The simulator can predict the distribution of nanoparticles and the ratio of the porosity and the permeability in a planar domain for different time steps, where examples of the results

are shown **Figure 2.9**. Based on the simulation, they found that nanoparticles in CO<sub>2</sub> reduce the saturation of the non-wetting phase in the porous media significantly. It also found that the nanoparticle reduces porosity and permeability. Using similar numerical approach, El-Amin and other co-workers [137] expanded the study in establishing numerical modelling of nanoparticle transport with two-phase flow in porous media. Two dimensional porous with regular heterogeneous and random permeability cases were used as the domain of the study, which is illustrated in **Figure 2.10** (a) and (c) respectively. Nanoparticle concentration is injected to the domain from the left boundary and the propagation is observed. The results for each permeability case are shown in **Figure 2.10** (b) and (d) for the regular heterogeneous permeability and random permeability case respectively. The model developed can predict the distribution of injected nanoparticles in permeable porous media. It also can predict the reduction of porosity due to the precipitation of the nanoparticles in the domain.

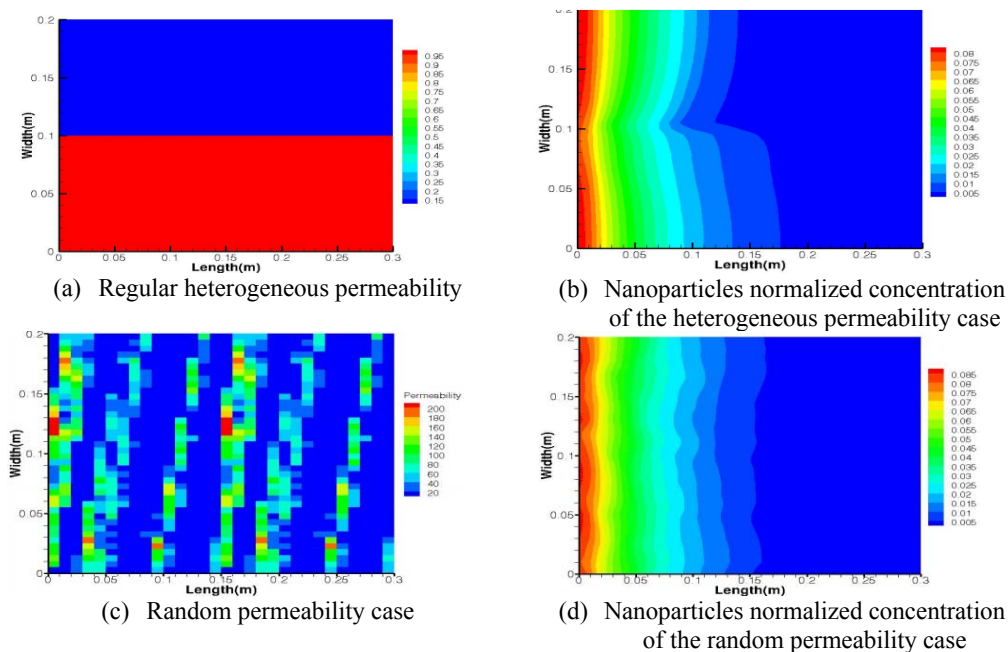


**Figure 2.10:** Tested medium of the simulation. For the permeability, blue legend is 20 mD and red is 200mD, for nanoparticle concentration, blue legend is 0.005 and red is 0.08 (dimensionless) (reproduced from El Amin et.al, 2012 [137])

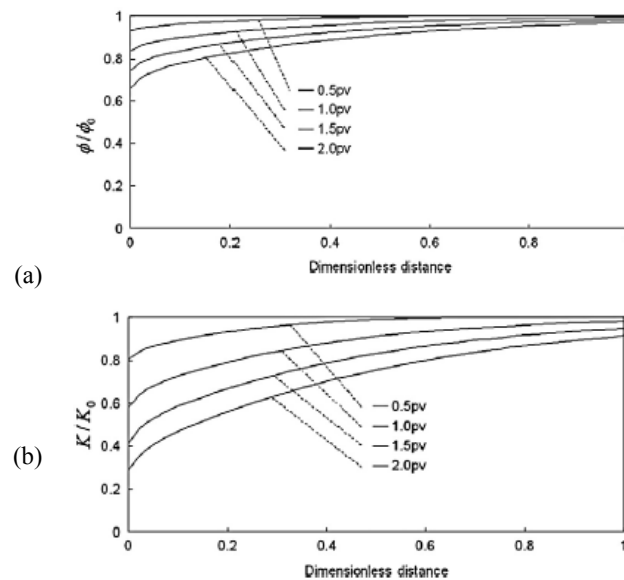


**Figure 2.11:** (a) Porosity and (b) permeability distribution along the dimension distance at different injection PV (reproduced from Ju and Fan, 2009 [39])

Another example for the mathematical model for nanoparticle transport in porous media is the one developed by Ju and Fan [39]. In order to investigate the physical properties of the injected Polysilicon Nanoparticle (PN), they utilised Darcy's law with combination with Brownian diffusion in a sandstone porous media. In the study, the PN was treated as a volumetric concentration that was transport in the pores. The properties of the sandstone were previously investigated using a mercury injection experiment. The attachment of the PN inside the porous media was investigated by Transmission Electron Microscope (TEM). The alteration of wettability from oil wetting to water wetting of the sandstone surface due to the attachment of the PN was also discussed. They discovered that although the PN injection decreased the absolute permeability of the porous sample, it increased the water injectivity 1.6 to 2.1 times of the original value. This happened because the adsorption of the PN on the pore surface and the PN plugging at the pore throat. Then, Ju and Fan established a one-dimensional numerical simulator for PN transport in porous media to simulate application examples based on the data. In their simulator, the flow is assumed to be one dimensional, isothermal condition, incompressible system,

heterogeneous porous media, gravity force is neglected, discretisation of nanoparticle into  $n$  size interval, and Newtonian fluid with constant viscosity and density. The distribution of porosities and permeabilities, the alteration of water injectivity and oil recovery was modelled in the simulator, which examples of the results are found in **Figure 2.11**. They found that the PN was effective to improve water injectivity and improve the oil recovery.

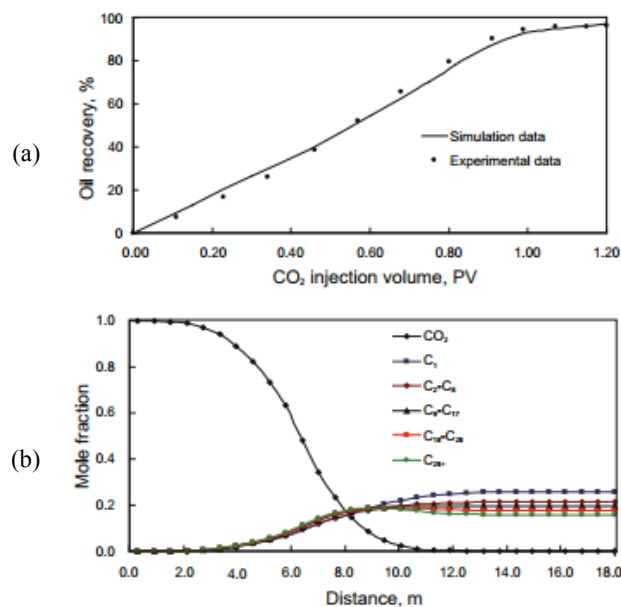


**Figure 2.12:** (a) Comparison between numerical results and experimental data, (b) Distribution of the component in the oil phase after 0.33 PV of CO<sub>2</sub> injection (reproduced from Ju and co-workers, 2012 [138])

Ju and co-workers [138] continued investigating CO<sub>2</sub> miscible-flooding for enhance oil recovery. It was not an investigation for nanoparticle transport in porous media, however the modelling of the flow mechanism of the CO<sub>2</sub> in the porous media is valuable to mentioned. The simulation was conducted for one-dimensional miscible flooding model, where the results were compared with slim tube experimental data. The mathematical governing equations utilised were multiphase Darcy's law and multi component diffusion with adsorption and precipitation considered. The mathematical governing equations for the model were discretized in space using an integral finite difference method. The oil formation was assumed heterogeneous and compressible with heat transfer considered. These

assumptions are taken to resemble actual reservoir condition. The physical properties of the fluid were treated as mass components that include oil with some pseudo-oil components,  $H_2O$  and  $CO_2$ . The mass components were also allowed to be adsorbed on the rock surface. It was also assumed that the flooding process was miscible and the formation damage was caused by asphaltene deposition on the pore wall. Iteratively the nonlinear equation system for mass and energy conservation was solved using the Newton-Raphson method. Using the simulation, they can predict the oil recovery increases approximately linearly with the continuous injection of  $CO_2$  until 0.90 pore volume of injected  $CO_2$  as it is shown in **Figure 2.12** (a). In addition, the mol fraction of the injected  $CO_2$  and the displaced hydrocarbon at along the model during the  $CO_2$  injection as it is shown in **Figure 2.12** (b). The simulation shows that the  $CO_2$  displaces the in-place hydrocarbon with piston-like mechanism, which is shown by the flat displacement front at the **Figure 2.12** (b). Hence, they applied the methodology for a three-dimensional porous geometry. The porous geometry is discretized into two grid selections, i.e. cubical grid mode and hybrid grid mode, which is shown in **Figure 2.13** below. They found that the distribution of the  $CO_2$  in the oil phase is affected by the grid direction, hence proposing that the simulation results using hybrid grid mode are more accurate than the one using the cuboidal grid mode.

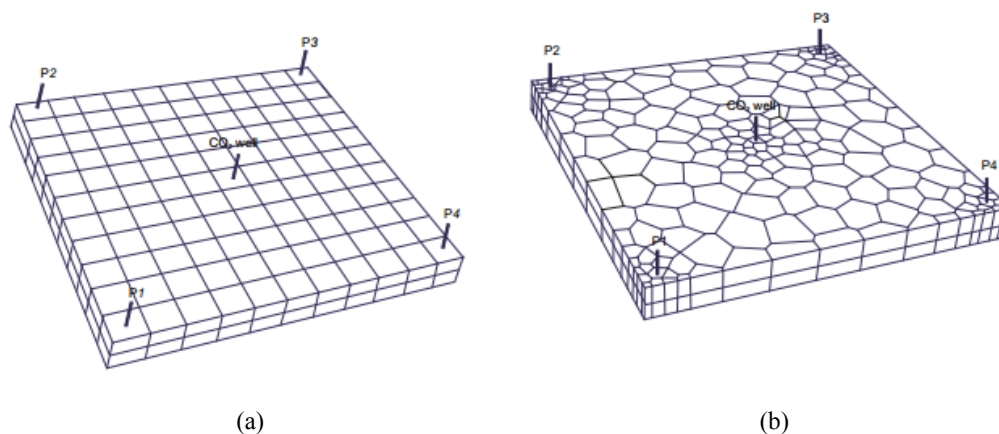


**Figure 2.13:** (a) Cuboidal grid mode, (b) Hybrid grid mode (reproduced from Ju and co-workers, 2012 [138])

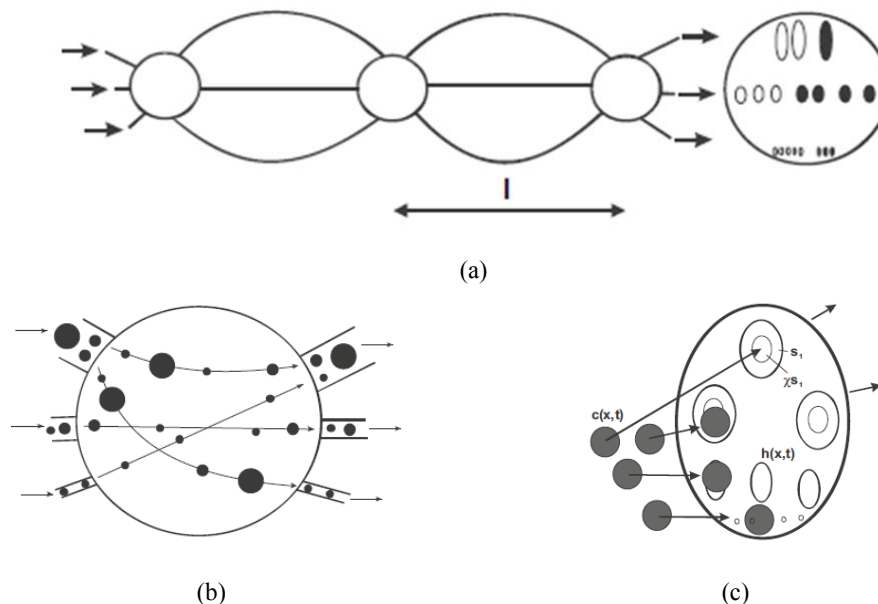


**Figure 2.14:** Schematic illustration for (a) geometric model of porous media constructed from parallel capillaries and mixing chambers. (b) detail illustration of a single chamber with suspension mixing, (c) transversal flow cross section of the model of porous media (reproduced from Bedrikovetsky, 2012 [139])

The geometry of the porous media can be approached by modelling the domain as a set of parallel capillaries. As an example, Bedrikovetsky [139] used this approach by illustrating the porous media as a parallel set of capillaries that was alternated by mixing chambers. The illustration is shown in **Figure 2.14**. Parameter  $l$  in the figure is the distance between the chamber volume and it was assumed that the chamber volume is small compared to the capillary volume. Although the capillary pipes were used to approach the porous media, the capillary pipes themselves are not considered as the domain. Instead, this geometry assumption was used as a starting point to establish the domain of porous media by defining the porosity of the domain as the ratio of the surface of the total pore cross section with the total rock cross section. The porous space geometry was defined via number of pores with size variation that cross the unitary cross section. The total pore concentration was obtained from the integral of the pore concentration distribution. Particles in various sizes were transported inside the capillaries to the chamber. Large particles do not enter thin pores and then are captured at the outlets of the chamber. Additionally, the volume

of the chamber was neglected compare to the pore volume. Then, he conducted a simulation of the concentration transport using a self-proposed microscale population balance equations derived for suspension transport in porous media with several particle capture mechanism, e.g. particle captured due to plugging. Poiseuille-type flow in cylindrical pore coupled with Darcy flow is utilised. The simulator was able to predict fractional flow function of the porous space where the example of the result is shown in **Figure 2.15**. The simulation results then were validated with a laboratory test of mono-sized particle flow. There were deviations between the simulation and the laboratory test; however, the modified model did not explain the reason behind the discovered deviations.

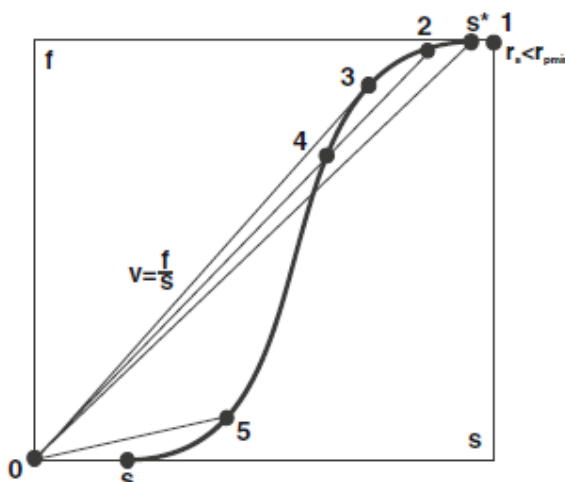


**Figure 2.15:** Fractional flow function for network model of the porous space derived from a bundle of parallel capillaries alternated by mixing chambers (reproduced from Bedrikovetsky, 2008 [139])

Bedrikovetsky [140] continued the work with some co-workers deriving mathematical model for particle detachment based on mechanical equilibrium of a particle positioned on the internal cake matrix surface in the pore space. Instead of only considering the diffusion effect and concentration differences, the model developed considered the torque balance of the drag, electrostatic, lifting and gravity forces on the particles from the matrix and moving fluids. The illustration of the forces for the particles is shown in **Figure 2.16** below, that includes  $F_l$  (lifting force),  $F_d$  (drag force),  $F_e$  (electrostatic force),  $F_g$  (gravity force),  $l_n$  (the length corresponds for the normal force) and  $l_d$  (the length for the drag force). The balance of the force is shown by Equation 2.1.

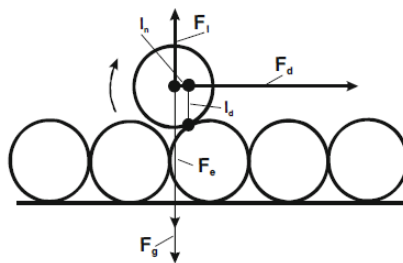


**Figure 2.16:** Forces and force moment balance for the particle located on the internal cake surface. (reproduced from Bedrikovetsky, 2011 [140])

$$F_d l_d + F_l l_n = (F_e + F_g) l_n \quad (2.1)$$

The torque balance has the significant role to determine the maximum retention during the particle capture. The equilibrium of the particle torque was determined by a dimensionless ratio between the drag and normal forces acting on the particles. Particle capture in the domain is governed if the total torques for electrostatic and gravity forces prevails over that for drag and lifting forces, so the resulting torque presses the particle towards the matrix or the internal cake. An exact solution for the one-dimensional core flooding model for porous media that utilising Darcy flow was established for limited particle retention in a constant filtration of a one-dimensional core flood simulation. This model could predict the maximum retention concentration and the breakthrough of injected concentration that are then validated qualitatively using two core flood tests.

You et.al. [135] that presented an analytical mathematical model for nanoparticle concentration transport and retention in oil rock grain under net repulsion condition between the particles and the rock matrix. The simulation conducted follows an analytical method whose governing equations utilised the method proposed Bedrikovetsky [139] that was discussed previously in this section. The derivation is based on assumption that the porous media is represented by parallel capillary with mixing chambers. The pore throat is assumed to be built from the tangent of three 2D circular geometries that represents rock grains whose pore throat shape was triangular. The maximum pore throat radius that approximately resembles the curvilinear pore throat. The illustration for the geometry is shown in **Figure 2.17**. When the nanoparticles are injected, some of them will be suspended, or

completely mixed inside the domain and distributed. The model developed then was validated with a laboratory test. They stated that using net repulsion provides a more efficient way to model a retention mechanism of nanoparticles on the rock pores since this method avoids the expensive and difficult characterisation of the solid surface interaction. However, they utilised many simplifications in their simulation, i.e. incompressible rocks and particles, one particle for each one pore plugging, the concentration of the captured particles was negligible to the vacant pore concentration, and net repulsion considered between the particles and rock matrix.

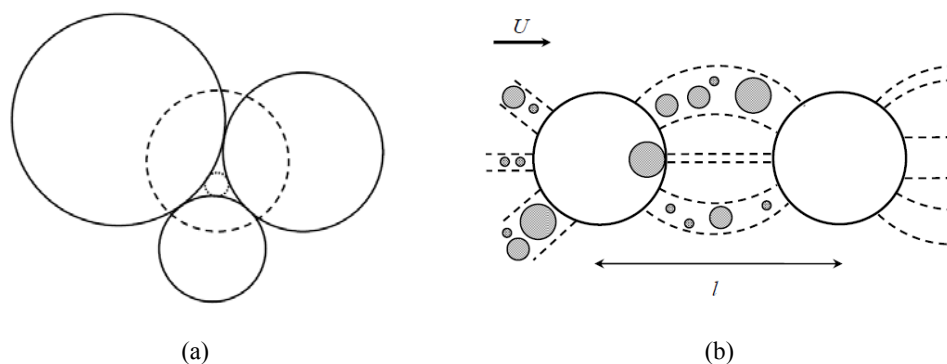


**Figure 2.17:** Schematic illustration of the pore throat formed by three tangent grains and suspension flow through porous media represented by parallel capillary with mixing chambers (reproduced from You et.al [135])

Yu et.al [141] developed a 1-D advective and dispersion model that include removal term to obtain transport parameters for injected nanoparticles without agglomeration. The model was established based on an experiment that previously conducted to investigate the transport and retention properties of carbon nanoparticles in a clean dolomite core material where the carbon nanoparticles were injected into the core along with synthetic seawater at room temperature. The governing equation for the nanoparticle transport [142] they used follow as below

$$R \frac{\partial c}{\partial t} = D \frac{\partial^2 c}{\partial x^2} - v \frac{\partial c}{\partial x} - \gamma c \quad (2.2)$$

Where  $R$  is retardation factor,  $D$  is the dispersion coefficient ( $\text{cm}^2/\text{min}$ ), and  $\gamma$  ( $\text{min}^{-1}$ ) is the first-order removal rate constant. The first-order removal rate

constant is considered in the model if agglomeration is included in the modelling.  $R$  is written as

$$R = 1 + \frac{\rho_b k_d}{\theta} \quad (2.3)$$

Where  $\rho_b$  is the rock bulk density,  $k_d$  is the partition coefficient, and  $\theta$  is the porosity of the system. They found that the presence of salt ion (in their case is KCl) significantly delays nanoparticle breakthrough time and increases the retainment. This result is shown by **Figure 2.18** where higher amount of KCl reduces the magnitude of the nanoparticle concentration ratio at the outlet. They stated that the transport, retardation and the retention of injected nanoparticles depends on the degree of interaction between the particles, salt ion in solution, and the surface of the porous medium.

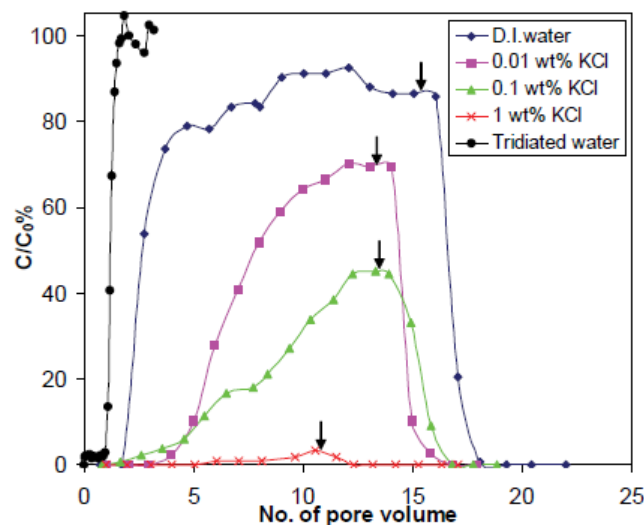


**Figure 2.18:** Breakthrough curves of carbon nanoparticle in the presence of KCl salt ( $\sim$ pH 8.3) (reproduced from Yu et.al [141])

Vega et al [143] investigated the adsorption of methane in a disordered silica xerogel porous media using integral equation theory that was developed by Madden and Glandt [144]. The equation is named MGOZ (Madden-Glandt-Ornstein-Zernike) equations, because the relations derived accommodate solutions from Ornstein-Zernike distribution function. It is shown as equations 2.4-2.8, where  $h_{ij}(r) = g_{ij}(r) - 1$  relates the fluid-fluid,

fluid-matrix, and matrix-matrix total correlation functions, and  $c_{ij}(r)$  is the direct correlation function.

$$h_{mm}(r_{12}) = c_{mm}(r_{12}) + \rho_m \int c_{mm}(r_{13})h_{mm}(r_{32})dr_3 \quad (2.4)$$

$$h_{mf}(r_{12}) = c_{mf}(r_{12}) + \rho_m \int c_{mm}(r_{13})h_{mf}(r_{32})dr_3 + \rho_m \int c_{mf}(r_{13})C_{ff}(r_{32})dr_3 \quad (2.5)$$

$$h_{fm}(r_{12}) = c_{fm}(r_{12}) + \rho_m \int c_{fm}(r_{13})h_{mm}(r_{32})dr_3 + \rho_f \int c_{ff}(r_{13})h_{fm}(r_{32})dr_3 \quad (2.6)$$

$$h_{ff}(r_{12}) = c_{ff}(r_{12}) + \rho_m \int c_{fm}(r_{13})h_{mf}(r_{32})dr_3 + \rho_f \int c_{ff}(r_{13})h_{ff}(r_{32})dr_3 \quad (2.7)$$

where  $C_{ff}(r_{32})$  is given by

$$C_{ff}(r_{12}) = c_{ff}(r_{12}) + \rho_f \int c_{ff}(r_{13})C_{ff}(r_{32})dr_3 \quad (2.8)$$

In the equations above, subscripts  $m$  and  $f$  refer to the matrix and fluid respectively, and  $\rho_m$  and  $\rho_m$  are the number densities of matrix and fluid particles respectively. Introducing thermodynamics from integral equation theory to the equation derived, numerical method was established to model methane adsorption process in a microporous silica gel. From the simulation, fluid-fluid distribution function  $g_{ff}(r)$  and fluid-matrix distribution function  $g_{fm}(r)$  were obtained. Typical result for the simulation for MGOZ equation is shown in **Figure 2.19** (solid line), where the profile is compared with results from Grand Canonical Monte Carlo (GCMC) method (dashed line). The grain of the porous media is assumed spheres where  $r$  ( $nm$ ) is the radius of the sphere and  $\sigma$  ( $nm$ ) is the sphere's diameter. They stated that the theory give a decent prediction for adsorbate-matrix and adsorbate-adsorbate distribution function at temperature that higher than the bulk critical temperature. The agreement for the low density is remarkably good; however, the simulation does not consider the attractive intermolecular force in the system where the effect is dominant in the system with lower temperature.

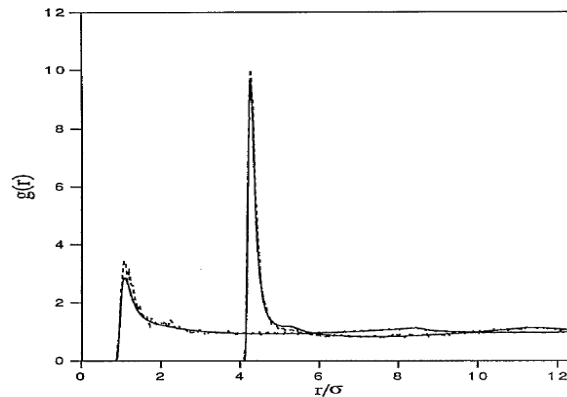


**Figure 2.19:** Fluid-fluid distribution function  $g_{ff}(r)$  and fluid-matrix distribution function  $g_{fm}(r)$  from the MGOZ integral equation (solid line) and GCMC (dashed line) (reproduced from Vega et.al [143]).

The geometry of these previous studies considers the porous media as a bulk of porous network of a rock samples. In order to gain access to understand the migration of nanoparticles in porous media, it is important to investigate particles distribution process and mechanism in the pore channel. Hence, instead of investigating a bulk system of porous media (e.g. core sample), the pore throat and channel of the porous media are examined.

Sharma et. al [145] developed a mathematical model to simulate the effect of magnetic field of injected nanoparticle in a blood vessel. In the simulation, the blood vessel was assumed a cylindrical channel with 6 mm diameter. Initially, the magnetic nanoparticles are assumed to be uniformly distributed in the domain. Stoke's flow is then introduced in the system and a magnetic field is subjected from the external of the channel domain. The flow behaviour of the magnetic particles in the fluid is investigated, where only magnetic and fluidic forces are considered in the modelling. The applied external magnetic field is written as

$$m \frac{d^2 r}{dt^2} = F_m + F_f \quad (2.9)$$

Where  $m$  is the mass of the nanoparticles,  $F_m$  is the magnetic force that is governed by

$$F_m = \mu_o V_p (M \cdot \nabla) H \quad (2.10)$$

Where  $M$  is the magnetisation,  $\mu_o$  is the magnetic permeability of vacuum,  $V_p$  is the volume of the particles, and  $H$  is the applied magnetic field. The last term  $F_f$  is the fluidic drag force, which is governed by

$$F_f = 6\pi\mu r_p(u_f - u_p) \quad (2.11)$$

Where  $u_f$  and  $u_p$  are the velocity of the fluid and particle respectively. The capture efficiency ( $\eta$ ) of the magnetic nanoparticle is investigated, which is defined as the ratio between the total number of particles ( $n$ ) deposited along the microchannel walls and the total number of release particles. It is mathematically written as follows

$$\eta = \frac{n_{in} - n_{out}}{n_{in}} \quad (2.12)$$

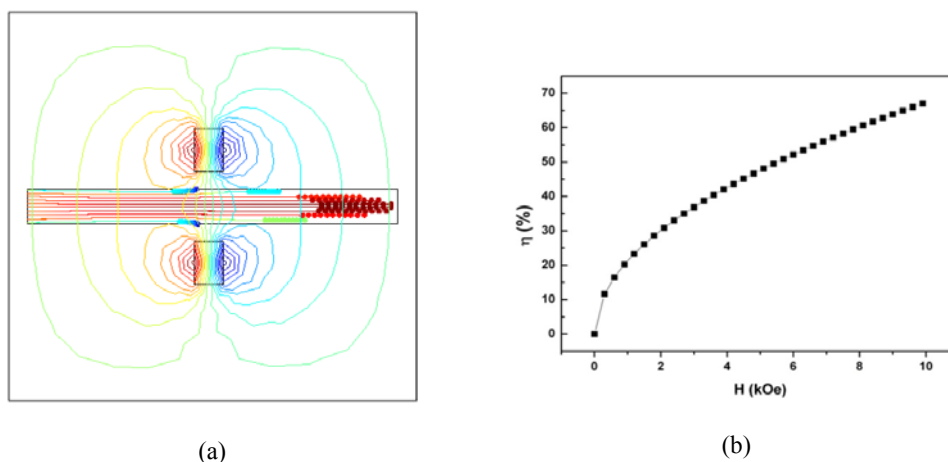


**Figure 2.20:** (a) The Trajectories of magnetic nanoparticles in a channel at 1 kOe field and (b) Capture efficiency ( $\eta$ ) of magnetic nanoparticles at different magnetic field 0-10 kOe. (reproduced from Sharma et. al [145])

Illustration of the typical system and the trajectory of the magnetic nanoparticle are shown in **Figure 2.20** (a). From the simulation, it is found that the capture efficiency increases from 22 to 67 % as the magnetic field is increased from 1 to 10 kOe, which is shown in **Figure 2.20** (b).

Liu et al [146] proposed characterisation of the delivery of nano-sized medicine in vascular environments. They demonstrated that the dissolution of the drug particles in the vascular system follows the first order of kinetics, which is governed by concentration difference in the system, where nanoparticle is modelled as dilute concentration. The effect of convection and diffusion and the reaction model should be considered in the modelling. The vessel is modelled as 10- $\mu\text{m}$  microchannel where initially 1000 mol/m<sup>3</sup> nanoparticle concentration presents in the domain. A receptor coated reaction surface is prepared on one of the boundary of the microchannel where the adsorption happens. Then, 0.1 mm/s constant flow rate introduces from the inlet and the profile of the nanoparticle concentration in the system is shown. The nanoparticle binding on the microchannel wall happens on a designated adhesive location, which is shown in **Figure 2.21**. The effect of the nanoparticle shape to adsorption is also investigated, where non-spherical shape nanoparticle has higher probability to be adsorbed then the spherical nanoparticle. The increase in shear rates happens in the system decreases binding probability of nanoparticles, but the degree of reduction of binding probability varies with different shape aspect ratio of nanoparticles.

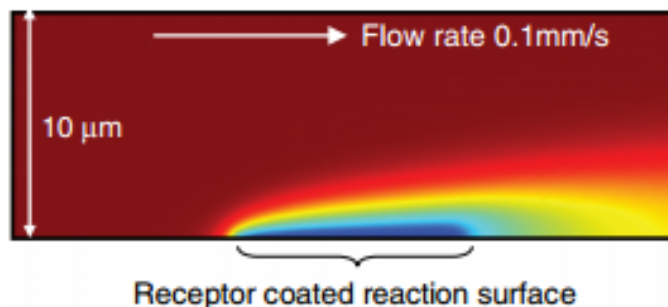


**Figure 2.21:** Binding of nanoparticle in a channel where red colour indicates the highest concentration and blue colours indicates lowest concentration (reproduced from Liu et al [146])

For modelling the porous media, another approach is to use an advanced 3D geometry configuration. One example is the study conducted by Acharya and Van der Zee [147, 148]. They conducted a study to model the transport of nonlinearly adsorbing soluble solutes in physically macroscopic heterogeneous and isotropic pore networks, as it has spatially

variable pore size. The pore network was in 3-dimensional geometry that was established from basic element of hydraulic pore network (Hypon) i.e. biconical abscissa-asymmetric concentric (Bacon) bond which are shown in **Figure 2.22**. Each elementary pore unit was perfectly mixed and the molar diffusion was ignored where advection dominates the transport. The adsorption occurs was assumed homogeneous, which was constant in any location. Traveling wave (TW) behaviour was investigated to study the movement of the soluble solutes in the network. Advection dispersion equation and Freundlich adsorption equation are used in their simulation, however the effect of the diffusion and desorption is neglected. They stated the pore network should include more than a million pore units to assess a developed travelling wave behaviour, which size varies with degree of heterogeneity. The minimum network size obtained depends on pore body variability, hydraulic and chemical parameter. On the other hand, they found that the transport did not show the traveling wave behaviour for a heterogeneous pore system. However, the validation of this case was not yet conducted. They also stated it was quite demanding to assess all these dependencies numerically using the approach they used. It is important to investigate the flow and adsorption behaviour in the channel itself to understand and support conclusion for the system of porous media.

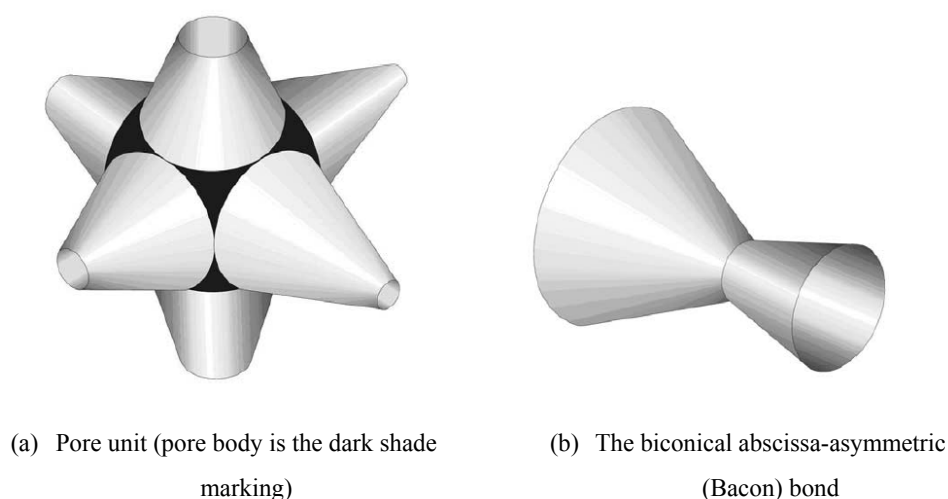


**Figure 2.22:** Illustration of the basic element of Hydraulic Pore Network (Hypon) (reproduced from Acharya et.al, 2004 [147])

Many other geometry configuration is also been utilised to study the flow in microchannel with different geometry configurations, e.g. trapezoidal shape [149-152], rectangular microchannel [153], triangular microchannel [154], and also three-dimensional serpentine microchannels with designed roughness [155]. They mainly studied the flow properties i.e. the friction factor and the Reynolds number.

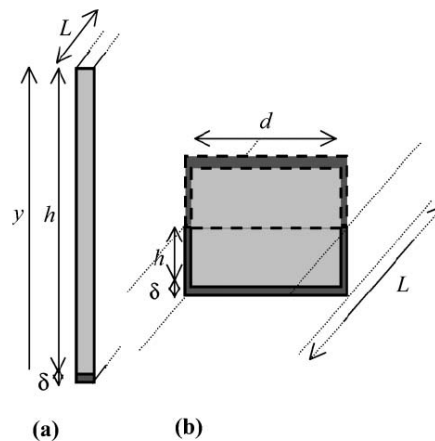


**Figure 2.23:** Schematic illustration of the model where the light grey is subjected into diffusion effect (reproduced from Lionello et al [156])

Lionello et al [156] developed a numerical model for the adsorption kinetics of proteins on the walls of a microchannel using the finite element method (FEM) to address the coupling with diffusion phenomena in restricted microchannel volume under a static condition. The model developed can be used to observe adsorption limitation due to the bulk solution reduction. The model is formulated in a 2-D Cartesian geometry and calculations are performed in 1-D and 2-D geometries as shown in **Figure 2.23** (a) and (b) respectively. For the 1-D geometry,  $h$  is  $200\ \mu\text{m}$  and  $\delta$  is  $0.1\ \mu\text{m}$ . For the 2-D geometry,  $h$  is  $50\ \mu\text{m}$ ,  $\delta$  is  $5\ \mu\text{m}$ , and  $d = 200\ \mu\text{m}$ ). Bulk solution presents in the domain and adsorption kinetic mechanism happens that follows Langmuir condition. The simulation is conducted and the coverage of nanoparticles on the microchannel wall is investigated. The typical solution is shown in **Figure 2.24** below. From the study, it is discovered that the adsorption can be limited by the depletion of the bulk solution, due to the micro-dimensions of the system.

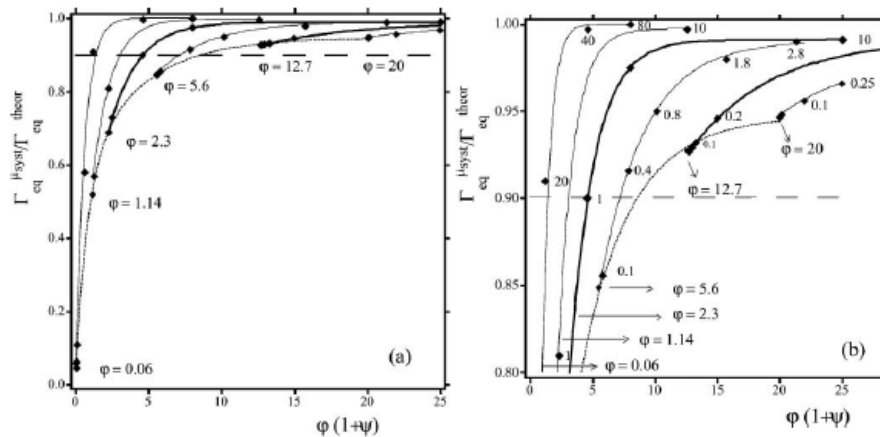


**Figure 2.24:** Schematic illustration of the model where the light grey is subjected into diffusion effect (reproduced from Lionello et al [156])

In order to model distribution, adsorption and desorption process of injected substance, combination of the adsorption isotherm equations and advective-dispersive equations are needed. The selection of adsorption and desorption reaction gives significant effect to the shape and spatial distribution of injected substance over time. The shape of the concentration distribution also can be used for investigation, for example the occurrence of scale deposition is indicated by retarded and non-symmetric concentration profile with a presence of back tails and sharp front ends [157].

Langmuir and Freundlich adsorption isotherm are common methods to use in modelling the adsorption and desorption mechanism. Langmuir approaches the adsorption and desorption mechanism linearly. Freundlich mechanism approaches the adsorption and desorption more non-linearly than the former by introducing exponents in the equation. There are many assumption that usually utilised in the modelling, thus adopting a nonlinear model of contaminant migration is better than utilising a linear model to give a more realistic representation of concentration propagation [157]. Therefore, Freundlich isotherm adsorption mechanism is able to reproduce results from adsorption and desorption laboratory experiment [158].

Sorbie and Gdanski [159] enlisted sets of proposed equation to model the transport and adsorption of scale inhibitor in porous media, i.e. core sample. They analysed various approaches concerning the mathematical structure of various transport equations. They also analysed the equations based on the surface chemistry assumption and models to describe the

attachment in the rock mainly by adsorption process. They particularly compared the retention equation that they developed (HW) using a numerical integration and the one proposed by Gdanski and Funkhouser (G-F) [160], i.e.:

$$\frac{d\Gamma(t)}{dt} = -k_{des}[\Gamma(t) - \Gamma_{eq}]^2 \cdot \Gamma(t) \quad (2.13)$$

where  $\Gamma(t)$  is the current adsorption isotherm at time  $t$ ,  $\Gamma_{eq}$  is the underlying equilibrium adsorption isotherm, and  $k_{des}$  is the desorption rate constant. The mathematical structure of both HW and G-F approaches are similar. The form difference of both equations presented due to the difference in units given. The retention part was somehow different. HW model uses the first order of the rate law, and on the other hand, the G-F model uses the second order of the rate law, which considers more to the effect of the rate to the retention. The G-F approach assumes the rock as a collection of mineral, thus only considers Langmuir form for solving the equilibrium isotherm adsorption, i.e.:

$$\Gamma(c) = \frac{\alpha \cdot c}{(1 + \alpha \cdot c)} \Gamma_{max} \quad (2.14)$$

where  $c$  is the concentration for the inhibitor and  $\alpha$  is the ratio between the adsorption and desorption constant. This was supported by the mineral separation from their experiment result. Since HW method utilises a numerical approach, it is more versatile to accommodate Langmuir, Freundlich, or table of number for modelling the adsorption than the G-F approach.

Another basic equation for concentration distribution in water flooding was proposed by Zeinjahromi et.al. [161]. Water salinity variation with migration, retainment, and detachment of fine particles are considered in the derivation. In the modelling, the concentration of the diluted small particles that dispersed in the pores was the function of water salinity and saturation. It was assumed that the transported fines were water-wet particles and inert and the effect of clay swelling was neglected. The volumetric concentration

of the particles was also neglected compare to the porous space. There was no dissipation effect of diffusion and capillary pressure was neglected. It was also assumed that the alteration of the water salinity affects the attachment of the concentration more strongly than the advection, thus the latter was neglected. The system was simulated under a constant temperature, incompressible fluids and constant fluid viscosity. The initial salt concentration in the system was the critical salt concentration for the reservoir fines. This meant that at the beginning of the simulation, the attached particles start to leave the rock surface along with the decrease of the concentration on the surface. In the modelling, polymer injection black-oil model in [162] ECLIPSE Reservoir Engineering Software was used to simulate the displacement of the oil by water in five-spot patten of a homogenous one-layer reservoir. The model could show permeability decline during a water injection due to the alteration of the injected fluid composition that induced fine migration. The permeability reduction improved the water-flood sweep efficiency by delaying water breakthrough and reducing the watercut.

Efforts of modelling the adsorption on the wall structures has been conducted for decades. However it is still difficult to model adsorption mechanism on a rough surface due to the limited geometry configuration to model the heterogeneity and the uniqueness of the adsorbing surface [163, 164]. Sonwane[165] proposed construction of the heterogenous adsorption surface using cylindrical MCM-41-like silica. An unstructured surface is achieved, however the exact structural and energetic site distribution function is undefined; therefore a smooth smooth cylinder was actually used in the modelling. Newer model of the MCM-41 pores become more realistic by considering the distribution of the adsorption sites [166]. Simulation results of using this model has high accuracy to model the real heterogenous pore wall structure, however not very efficient to reproduce due to the computer power and resource it needs. Computer simulations using the Grand Canonical Monte Carlo (GCMC) or the Density Functional Theory (DFT) are also used for simulation of the adsorption on to heterogenous site surface [166, 167].

Sbai and Azaroual [168, 169] developed a computational numerical simulation to predict micro and nano-particle transportation and capture in porous media system at the aquifers and reservoir scale. Utilising the IMPES (Implicit Pressure Explicit Saturation) and IMPSAT (Implicit Pressure

and Saturation) schemes, the mathematical model was based on a combination between incompressible two-phase flow equation for reservoir simulation and movement of each fluid phase and interphase particulate mass species transfer. To model the spatial distribution of salinity, the insitu colloidal fines migration in the aqueous phase was modelled by an optional advection-dispersion solute transport equation. The model was validated to simulate CO<sub>2</sub> injection in heterogeneous subsurface porous media. It was stated the developed simulator can predict the change of permeability and recovered volume due to surface wettability alteration.

The previous investigations for modelling of nanoparticle in rock porous media, especially which relates with the oil industry, were mostly conducted for porous media domain where the flow is affected by permeability, i.e. where Darcy's Law is valid to use. More investigation at the micro pore channel is required to enhance the understanding of the nanoparticle distribution and adsorption in the porous media. The approach used in the study in this thesis accommodate the method use in studying nanomedicine and drug delivery in human body [145, 146] where microchannel is used as the domain. In addition, it seems that there is none yet established a study or simulation that focus especially on the adsorption and desorption mechanisms of injected nanoparticle to microchannel with different geometry, which specifically considers the effect of flow and diffusion. Hence, these aspects are investigated and discussed in this thesis. In order to obtain a broader understanding for the adsorption and desorption process, modified Freundlich adsorption isotherm mechanism that is derived by Skopp[170] is utilised. The unique feature for this approach is to consider the term of adsorption and desorption separately. This allows investigation for each term more thorough and accessible. This approach is discussed in Section 3.5.

## **2.8 Summary**

Nanotechnology has an essential role that is potentially beneficial to be applied in the petroleum industry [38]. In the oil and gas industry, nanoparticles can be injected and introduced into the reservoir to envelop the surface of the rock and alter its property [6, 7] to enhance the processes concerning the adsorption in the rock pores. One example of the application is for enhancing the attachment of the Scaling Inhibitor (SI) onto the rock in the scale squeeze treatments.

Scale squeeze treatment is initially established by injecting a fluid containing a concentration of a Scale Inhibitor into the reservoir through a well. The well then is shut from production, allowing the reservoir soaked by the SI. The treatment is ended by opening the well and letting the fluid in the reservoir flow up to the surface. The adsorbed SI will be desorbed along with produced fluid until its amount on the rock surface cannot hinder scaling deposition any longer. By introducing nanoparticles on the surface area of the rock, the surface area of the rock increases and this enhances the attachment and the lifespan of the scale inhibitor.

Focusing on nanoparticles, in addition to getting them to where they are needed, an important question is where do they go? This is crucial for designing the treatment operation as well to deal with issues that relate with health, safety and environment approval. Therefore, it is required to understand the behaviour of the injected nanoparticles in the pore channel, i.e. the transportation, distribution, adsorption, and desorption. The behaviour of nanoparticles in porous media has been conducted for more than a decade [54, 171]. However, the studies are mainly conducted in porous media or reservoir model [104, 117-119, 121]. As far as the author is aware, there is none yet established a study or simulation that focus especially on the adsorption and desorption mechanisms for different domain geometry for injected nanoparticles inside the pore-channel itself that specifically consider the effect of flow and diffusion. Understanding the behaviour and distribution of the injected nanoparticle in the microchannel is providing constructive advantage to deduce and predict behaviour, distribution and the placement of the nanoparticles transport in much larger pore networks.

## **Chapter 3**

### **Methodology**

#### **3.1 Introduction**

This chapter introduces the methodology for studying the transportation of nanoparticles in porous media. The approach of the study is to understand the transport phenomena in micro-sized channels that include the occurrence of adsorption/desorption, diffusion and dispersion behaviour, spatial distributions and residence times.

A particle is identified as a nanoparticle when its diameter is between 1 and 100 nm [37, 38]. The size of the pore throat in the study is selected based on the central tendency of the sandstone pore throat magnitude i.e. 2-0.33 mm in diameter [53]. Due to the size difference between the nanoparticles and the channels and following the previous studies [39, 135], it is decided that the transported nanoparticles are treated as a concentration field. Intermolecular interaction of the nanoparticle in the concentration species is represented by the diffusion that is considered in the system [172]. In the study, the nanoparticles are injected either continuously or discontinuously into the system. The study will provide directions to understand particle penetration, coverage, and attachment to the pore wall.

Refer to Chapter 2, in the oil and gas industry, nanoparticles can be injected into the reservoir to cover the surface of the rock and alter the property of the reservoir rock's surface area [6, 7]. This property alteration might be utilised to enhance the adsorption processes on to the formation, for instance the attachment of the Scaling Inhibitor (SI) onto the rock in the scale squeeze treatments. Scale squeeze is conducted initially by injecting fluid containing a concentration of a scale inhibitor into the reservoir. The target zone is allowed to be soaked by the fluid for a period to maximise the adsorption of the scale inhibitor onto the formation surfaces and then ends by the return flow from the reservoir to the surface. Increasing the internal surface area of the rock formation by introducing nanoparticles enhances the amount of the scale inhibitor and its lifespan.

It is important to study how the nanoparticles are placed inside the pore channels. However, the pores in the rock are arbitrary and often are

very complex and heterogeneous. There is also a possibility for agglomeration of nanoparticles that join together and block the pores. There is an immense importance to understand how the particles transport and be distributed through the pores in the reservoir.

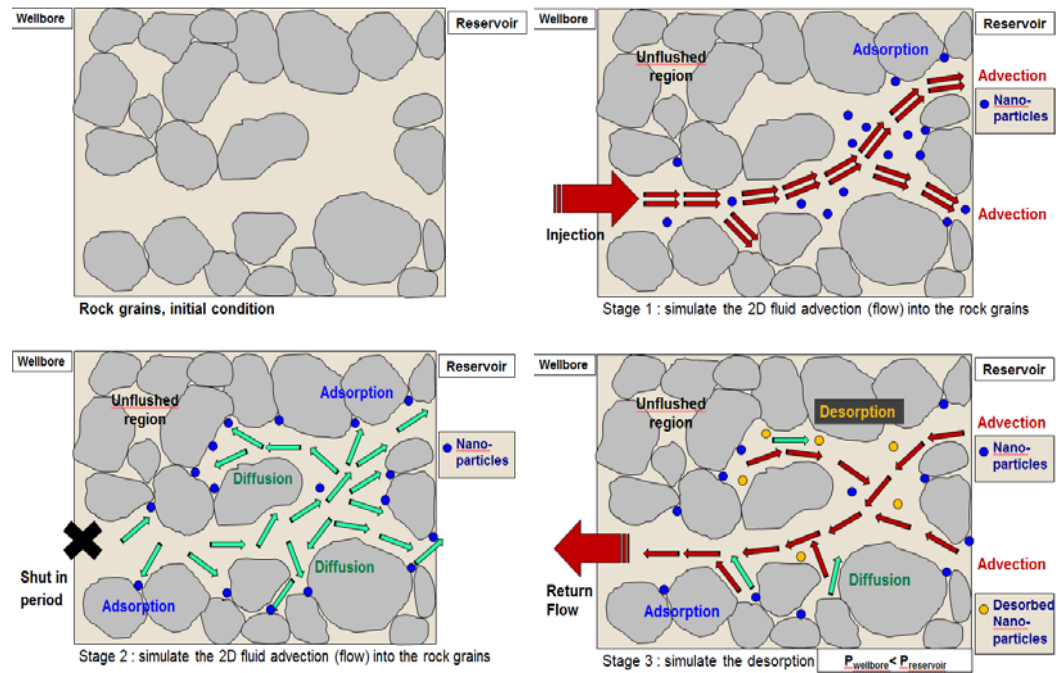


**Figure 3.1:** Illustration of a Scale Inhibitor (SI) Injection, as the approach used in the research by the author in the University of Leeds.

A simulator is developed in this thesis to model the flow of the nanoparticle concentration within the pore itself, considering the advection, diffusion, adsorption, and desorption under the different micro-channel geometry. This investigation is focused on the penetration and the flow of the injected nanoparticle concentration in the channel, adsorption/desorption rates, diffusion and dispersion behaviour, spatial distribution and the residence time. The simulator is also fundamentally able to use as a close approach to simulate the injection of the Scale Inhibitor into the reservoir [98], which include the phase of injection (advection dominated), shut in period (diffusion) and the backflow (adsorption and desorption). This mechanism is illustrated in **Figure 3.1**, beginning from empty system, injection, shut in period, and the return flow. This expectedly will bring one-

step further to understand the phenomena of nanoparticle migration and distribution in the rock.

### 3.2 Porous media

Porous medium is defined as regularly distributed void-space between the size of cavities and molecular interstices in a medium. There are two types of pores, which are un-connected pores and interconnected pores. Interconnected pores are the important ones since within this type of pores the fluid is able to flow from one location to the other location. In the oil industry this is also known as the effective pores. According to the size, the pore space can be divided into three classifications, which are void, capillary and force space [173]. Pores are characterized as void when the walls do not have any significant effect on the hydrodynamics inside the pore. If the effect is significant, the pore is characterized as capillary. Force space is where the molecular structure of the fluid is taken into consideration [174].

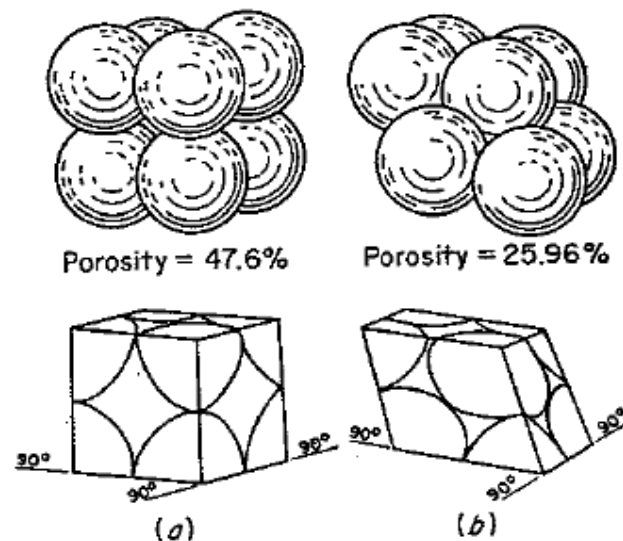


**Figure 3.2:** Packing of ideal uniform sphere grains (a) cubic, or wide pack and (b) rhombohedral, or close-packed. (After Gratton and Fraser, 1935) [175]

Porosity of the porous media is one of the most important properties of porous media. It is defined as the ratio between the void spaces of a porous media to its bulk volume. Based on its origin, porosity is classified into original porosity and induced porosity [176]. Original porosity is the

porosity that is developed in the material geological deposition. It is characterized by the intergranular, intercrystalline and oolitic porosity that usually has uniform properties. Induced porosity is characterized by the development of fracture and caves in the rock. This type usually has non-uniform properties. Porosity is dependent of the grain packing arrangement and the grain size. Referred from the work conducted by Graton and Fraser [175] who computed the porosity of various packing arrangements of uniform spheres, it is discovered that the porosity of the least compact arrangement (cubical packing) is 47.6%, and for the most compact arrangement (rhombohedral) is 25.96%. The illustration is shown in **Figure 3.2**. Correlation of pore diameter ( $\delta$ ) and porosity ( $\Phi$ ) is introduced by Krumbein and Pettijohn [177] that is shown on equation 3.1 which is valid for a 2D porous geometry.

$$\delta(mm) = (0.5)^\Phi \quad (3.1)$$

Grain size distribution and grain angularity are also important. In general, larger grain size distribution and smaller angularity are likely to decrease the porosity while a decrease in range of particle size tends to increase the porosity.

In the industry, there are two types of porosity, which are total porosity and effective porosity. Total porosity is the ratio between total void space and total bulk volume of the porous medium. Effective porosity is the ratio of the interconnected void space to the total bulk volume of the porous medium. This type of porosity is the one that is more relevant in relation with the oil recovery, since only fluid that is contain in the effective porosity can be transported [178]. The specific internal surface area of the pore is also important, which is the ratio between the internal area of pores and its total bulk volume [174]. The internal area of the pore is the main focus for investigating the adsorption and desorption in the porous media.

There is also a term that expresses the kinematic ratio between the total length of one pore and its distance, called tortuosity (T). Tortuosity also can be defined as an average elongation of fluid paths or as a impedance factor that measures the resistance of a porous medium to the flow. In other words, tortuosity represents the degree of complexity of the channel configuration. There is also a correlation between the tortuosity and the

effective porosity of the media, which shown by Equation 3.2 that is valid for 2D channel geometry.

$$T = T_{hydraulic} = \frac{\Phi \cdot A_{effective}}{8k\pi} \quad (3.2)$$

where  $A_{effective}$  the effective area of the pore,  $\Phi$  is the porosity and  $k$  is permeability. The last parameter will be discussed in the next section. A discussion for simulation that relates the distribution of nanoparticle concentration in microchannel is discussed in Chapter 5.

The ability for a fluid to transport in porous media is known as permeability. It expresses the level of easiness of fluid being transported in a tortuous porous media. Permeability also is known as the coefficient of proportionality, which is the scalar value of specific discharge per unit hydraulic gradient [176]. The higher permeability, the easier the flow conducted. However, permeability can be as well treated as an anisotropic property of the rock, since it is as well depends on the matrix properties (e.g. grain/pore size distribution, shape of grains/pores, tortuosity, specific surface, and porosity) and the fluid properties (e.g. density and viscosity).

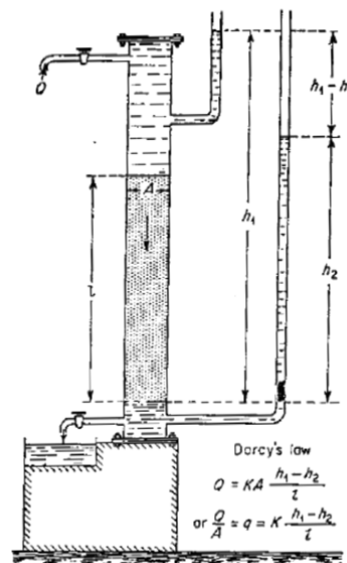


**Figure 3.3:** Schematic illustration of the experiment conducted by Henry Darcy of the water flow in sand. (After Hubbert, from Amyx, 1960) [176]

Permeability is introduced based on an experiment conducted by Henry Darcy in 1856 [179-183]. He established a vertical experiment apparatus that is illustrated in **Figure 3.3**. He used 0.35 m diameter steel pipe with the height of 3.5 m. At the outlet at the bottom, a reservoir was prepared by supporting a set of screen from its base. A level of sand was prepared inside the steel pipe and water was poured from the inlet at the top to the outlet at the bottom. The volume of the water at the outlet was measured and compared with the pressure difference measured by the mercury U-tube manometer at the apparatus.

Darcy came with a conclusion that the flow rate of fluid in porous media is proportional with the cross sectional area, differential in water level elevation of the inflow and outflow, and inversely proportional with the length of the pore. Darcy's conclusion can be written mathematically as Equation 3.4 where  $k$  is the coefficient of proportionality, and later known as permeability.

$$Q = kA \frac{(h_1 - h_2)}{L} \quad (3.3)$$

Introducing the term of hydrostatic pressure and viscosity, Craft and Hawkins[178] derived the equation above to be the Equation 3.4 below:

$$Q = \frac{kA (\Delta P)}{\mu L} \quad (3.4)$$

With slight modification, Darcy's law states that the velocity of a homogenous fluid in a porous medium is inversely proportional to the fluid viscosity and proportional to the driving force of the system. Mathematically, it is written as:

$$v = -0.0001127 \frac{k}{\mu} \left[ \frac{dp}{dt} - 0.433 \gamma' \cos \alpha \right] \quad (3.5)$$

where the variables are defined in **Table 3.1**.

The legends are in the **Table 3.1** below (in field units):

Parameter	Unit	Note
$v$	bbls/day-ft <sup>2</sup>	the noticeable velocity
$k$	milidarcies (md)	permeability
$\mu$	cp	fluid viscosity
$p$	psia	pressure
$s$	feet	distance along flow path
$\gamma'$		fluid specific gravity comparatively to water
$\alpha$	Deg	the angle measured counter clockwise from the downward vertical to the positive s direction

**Table 3.1:** Legend for the Darcy's law, in field units

$\left[ \frac{dp}{ds} - 0.433\gamma' \cos \alpha \right]$  corresponds to the driving force, which consists of pressure gradients along the flow and the hydraulic gravitational gradients of  $0.433\gamma' \cos \alpha$ . Practically, the hydraulic gravitational gradients are small compare to the fluid pressure gradients. Therefore, this parameter often is neglected. The minus sign before 0.001127 in Equation 3.5 specifies that pressure decrease from the beginning until the end point of the flow; hence, the flow is taken positively in the positive direction. [178]

Permeability is a tensor that is measured in basic units of Darcy (d). 1 Darcy permeability is a measure for a fluid of 1 cp viscosity that move at velocity of 1 cm/sec under a pressure gradient of 1 atm/cm. In the industry, permeability usually is split into horizontal permeability and vertical permeability. Horizontal permeability is the permeability that is parallel to the bedding plane of the stratified rocks. The magnitude of the horizontal and vertical permeability depends on the depth and the sedimentation process of the rock formation where the measurement is taken.

Darcy's law is only valid for laminar flow. Much higher velocity occurs under a turbulent flow; hence, pressure gradient increases quite significantly. Darcy's law is not valid for flow with individual pore channels, but statistically is reasonable to be used to solve flow in portion of rock where the dimension is relatively large comparing to the size of pore

---

channel. The value used in Darcy's Law is the average of those inside the pores. Since actual velocity of each point is not measurable, apparent velocities is used in order to keep porosity and permeability separated.

In order to gain a broader understanding about the flow in porous media, it is important to study the flow in the channels of the pore. Although the term porosity and permeability is very important for discussing the porous media, these parameters will be set aside for a while in the study, however, without neglecting their importance. The method considers simulation of a one-way coupling of a single-phase continuous flow in 2D dimensional geometry. This method is then validated and the details are included in Chapter 4. The equations obtained are then used to investigate the concentration transport in a single straight microchannel (Chapter 4), single tortuous microchannel (Chapter 5), single rough-surface microchannel (Chapter 6) and a network model based on the results from single channels (Chapter 7).

### **3.3 Key Assumptions and Governing Equations of the Model**

#### **3.3.1 Flow Conditions**

It is important to understand the theory behind the flow. There are two aspects of the fluid flow mechanics. The first one is the microscopic flow and the second one is the macroscopic flow. In the microscopic flow, the molecular structure of the fluid is put into consideration, where it adds some minor correction effects to the equation of the continuous matter theory in the calculation. The second one is the macroscopic flow. In this mechanism, the fluid is treated as a continuous substance whose movement is measured at every material point and expressed in mathematical equation. This correlates with the continuous matter theory [174].

There are three physical conditions that govern the macroscopic flow includes continuous matter theory [176]:

a) Continuity equation

There are three continuity equations that usually used to calculate and model the flow:

1. The law of conservation of mass

The material balance equation is expressed as below:

$$\frac{\partial \rho}{\partial t} + u \cdot \nabla \rho + \rho \nabla \cdot u = 0 \quad (3.6)$$

where  $\rho$  is the fluid density (kg/m<sup>3</sup>),  $t$  is time (s), and  $u$  is the velocity (m/s).

## 2. The law of conservation of momentum

The material balance equation is expressed as below, where  $u$  is the velocity at x-direction,  $v$  is the velocity at y-direction and  $w$  is the velocity at z-direction:

(i) For the x-direction

$$\begin{aligned} \frac{\partial}{\partial t} \rho u = & - \left( \frac{\partial}{\partial x} \rho u u + \frac{\partial}{\partial z} \rho w u + \frac{\partial}{\partial y} \rho v u \right) \\ & - \left( \frac{\partial}{\partial x} \tau_{xx} + \frac{\partial}{\partial z} \tau_{xy} + \frac{\partial}{\partial y} \tau_{yx} \right) - \frac{\partial P}{\partial x} + \rho g_x \end{aligned} \quad (3.7)$$

(ii) For the y-direction

$$\begin{aligned} \frac{\partial}{\partial t} \rho v = & - \left( \frac{\partial}{\partial x} \rho u v + \frac{\partial}{\partial y} \rho v v + \frac{\partial}{\partial z} \rho w v \right) \\ & - \left( \frac{\partial}{\partial x} \tau_{xy} + \frac{\partial}{\partial y} \tau_{yy} + \frac{\partial}{\partial z} \tau_{zy} \right) - \frac{\partial P}{\partial y} + \rho g_y \end{aligned} \quad (3.8)$$

(iii) For the z-direction

$$\begin{aligned} \frac{\partial}{\partial t} \rho w = & - \left( \frac{\partial}{\partial x} \rho u w + \frac{\partial}{\partial y} \rho v w + \frac{\partial}{\partial z} \rho w w \right) \\ & - \left( \frac{\partial}{\partial x} \tau_{xz} + \frac{\partial}{\partial y} \tau_{yz} + \frac{\partial}{\partial z} \tau_{zz} \right) - \frac{\partial P}{\partial z} + \rho g_z \end{aligned} \quad (3.9)$$

For incompressible flow, equations above are known as the Navier Stokes equations.

### 3. The law of conservation of energy

Types of energy are being transferred when a fluid flows. Those types of energy normally are kinetic, potential, internal, and mechanical energies. The sum of energies leaving the system should be the same as the sum of energy that entering the system [184]. The equation follows:

$$\begin{aligned}
 & \frac{\partial}{\partial t} \left[ \rho \left( e + \frac{u^2}{2} \right) \right] + \nabla \cdot \left[ \rho \left( e + \frac{u^2}{2} u \right) \right] \\
 & = \rho \dot{q} dx dy dz + \frac{\partial}{\partial x} \left( k \frac{\partial T}{\partial x} \right) + \frac{\partial}{\partial y} \left( k \frac{\partial T}{\partial y} \right) \\
 & + \frac{\partial}{\partial z} \left( k \frac{\partial T}{\partial z} \right) - \frac{\partial (up)}{\partial x} - \frac{\partial (vp)}{\partial y} - \frac{\partial (wp)}{\partial z} \\
 & + \frac{\partial (u\tau_{xx})}{\partial x} + \frac{\partial (u\tau_{yx})}{\partial y} + \frac{\partial (u\tau_{zx})}{\partial z} + \frac{\partial (v\tau_{xy})}{\partial x} \\
 & + \frac{\partial (v\tau_{yy})}{\partial y} + \frac{\partial (v\tau_{zy})}{\partial z} + \frac{\partial (w\tau_{xz})}{\partial x} + \frac{\partial (w\tau_{yz})}{\partial y} \\
 & + \frac{\partial (w\tau_{zz})}{\partial z} + \rho g u
 \end{aligned} \tag{3.10}$$

where  $\dot{q}$  is the rate of volumetric heat addition per unit mass.

#### b) Newton's law of motion

Newton's law of motion is the basic knowledge needed to understand the physics behind a moving object, which consists of three:

- (i) Newton's first law of motion, which describes that an object will continue to be on its current condition (static or move) as it has before until an unbalanced force acts upon it.
- (ii) Newton's second law of motion, which states that the change of such object's position and velocity is a function of its acceleration. This law is expressed by the rate of change of momentum equals the force applied.
- (iii) Newton's third law of motion that states about the origin of forces which states that there is always an equal reaction to every action that is applied upon two bodies that directed to contrary parts. This law is also known as the law of "action and reaction".

#### c) Rheological condition, which is the connection between the stress and strains in the fluid.

Rheology can be defined as a study of fluid's response towards an infliction of stress and strain. Rheology has a short correlation with the viscosity and type of the fluid, whether the fluid is Newtonian or non-Newtonian fluid. In this thesis, the study is conducted for non-Newtonian fluid.

There are two components of stress exist in fluid motion. The first component is the normal stress, which is a stress orthogonal/perpendicular with the fluid flow. This stress is governed by the gravity. The component stress is known as the shear stress ( $\tau$ ), which is the stress in the same direction with the movement of the fluid.

For the x-direction, shear stress is expressed by:

$$\tau = \mu \frac{du}{dy} \quad (3.11)$$

The equation above is also known as the Newton's Law of Viscosity.

Viscosity ( $\mu$ ) is the inherent property of fluid that tries to restrain the relative movement of the adjacent fluid layer. In Newtonian fluid viscosity is constant regardless the condition of the flow. The examples of Newtonian fluid are water and air. In Non-Newtonian fluid, its viscosity might change due to the change of flow condition, for example the change of velocity or the change of applied force. [184]

In non-Newtonian fluid, which is the type of fluid used in this thesis, viscosity is a function of shear rate, but not a function of time of the application of shear. The behaviour has a constitutive relation between the shear stress ( $\tau$ ) and the shear rate ( $\dot{\gamma}$ ) [185].

$$\tau = f(\dot{\gamma}) \quad (3.12)$$

Some model has been widely used to describe the rheological behaviour as a function of viscosity, which is illustrated in **Figure 3.4**.

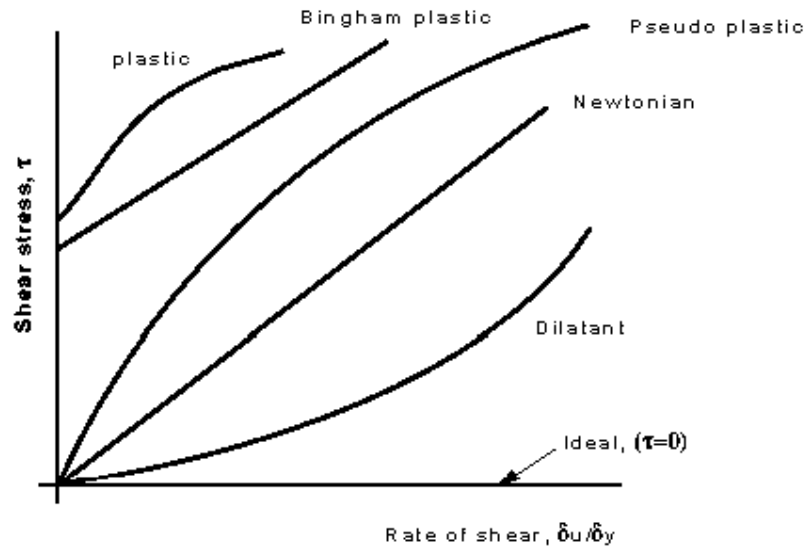


**Figure 3.4:** Theoretical figure of shear stress vs strain for different fluids characteristic (reproduced from Sleight, 2009) [186]

Depart from the theory of viscosity, there is a term that is known as Reynolds Number. This term was introduced initially by Osborn Reynolds in 1883 that since then has been widely used in many aspects of fluid mechanic. [187]

Reynolds number is mathematically expressed by following equation:

$$Re = \frac{\rho U D}{\mu} \quad (3.13)$$

where Re is the Reynolds number, U is the mean velocity of the flowing object (m/s), D is the hydraulic diameter of the flow container (m),  $\nu$  is kinematic viscosity ( $m^2/s$ ),  $\mu$  = dynamic viscosity of the fluid (Pa.s), and  $\rho$  = the density of the fluid ( $kg/m^3$ ).

Since

$$\nu = \frac{\mu}{\rho} \quad (3.14)$$

Then equation (25) can be also expressed as:

$$Re = \frac{UD}{\nu} \quad (3.15)$$

Reynolds number can be used to distinguish the fluid's flow regime, which is laminar, transitional, or turbulent flow. According to McGraw-Hill Science & Technology Encyclopaedia, laminar flow defined as a layered, smooth and structured type of viscous fluid motion at low-to-moderate deformation rates. Turbulent flow has a characteristic of having irregular and oscillating velocity, pressure, particle movement, and other flow quantities in time and space. [188]. Transitional flow takes place between those two flow regimes. Sleigh and Noakes stated that physical meaning of Reynolds number is the ratio between inertial forces and viscous forces exist in the flow system.

$$Re = \frac{\text{inertial forces}}{\text{viscous forces}} \quad (3.16)$$

At low Re and slower fluid flow, viscous force is dominant where the fluid flows in layers, and then laminar flow happens. At the inverse condition, when Re is larger and the fluid flow faster, inertial forces takes over the viscous forces, and the flows becomes transient [186], although the boundary condition remains steady. This condition creates Eddy current which carry on into the fluid at intervals which cause the turbulence [174]. The comparison of laminar flow and turbulent flow is shown in **Table 3.2**.

Laminar Flow	Turbulent Flow
Re < 2000	Re > 4000
'low' velocity	'high' velocity
Regular particles path in straight lines	Irregular particle paths with the average motion is in the direction of the flow
Possible to be analyzed by simple mathematic	Cannot be seen by the naked eye and fluctuations are very difficult to detect.
Rare in practical daily life	Mathematical analysis very difficult - so experimental measures are used
	Most common type of flow

**Table 3.2:** The difference between laminar and turbulent flow [186]

In modelling the flow through a microchannel representing a pore throat within a rock sample, it is important to establish the relevant magnitude of the fluid velocity. This is done here by relating the velocity to

the flow rate through a core sample as it would be used in a typical core-flood test.

### 3.3.2 Simulation domain

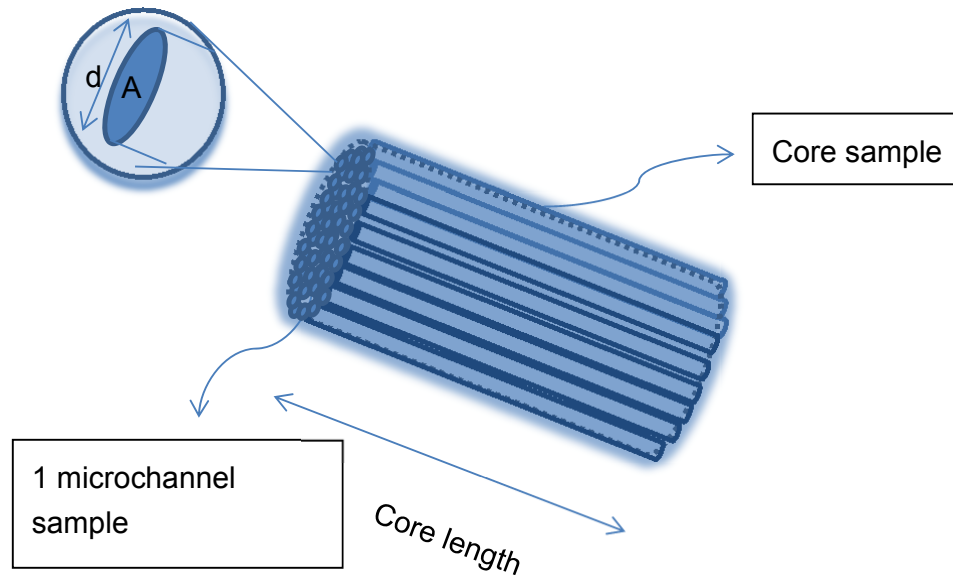


**Figure 3.5:** The channel in the simulation is illustrated as one of the microchannels happens in the core

A simple approach is to represent the core as a bundle of homogenous parallel tubes as it is shown in **Figure 3.5** where microchannel is used as the simulation domain [145, 146]. Referring to Chapter 4 where the methodology is validated, a Clashach-type sandstone is used in the study as the sample of the porous media. It is assumed that the diameter of one tube is  $20\ \mu\text{m}$  which is as a typical pore-throat size of medium grain-sized sandstone [53]. The validated equation is obtained by this assumption where 13 cm length as the dimension of the core used in the actual laboratory experiment. However, the tube with a length of interest of 10 times of its diameter is used in this thesis for the study. This value is taken to satisfy the computer resource and power availability to run the simulation and conduct sensitivity study efficiently. The length and diameter ratio is considered adequate to simulate the microchannel system with geometrical variance.

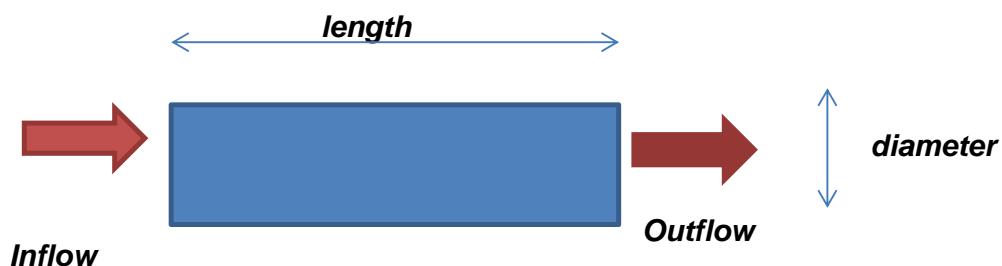


**Figure 3.6:** The 2D geometry microchannel configuration

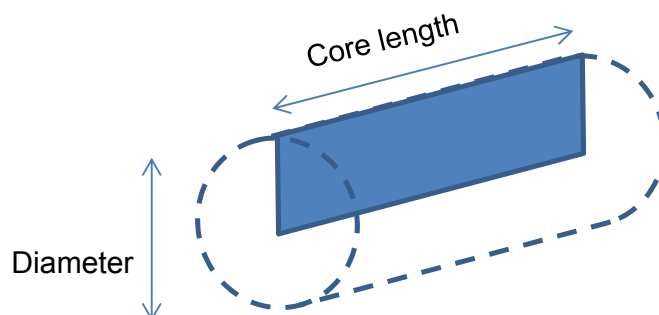


**Figure 3.7:** The 3D axis symmetric geometry microchannel configuration

The pore channel is simplified into two-geometry configurations i.e. 2D geometry and the 3D axis-symmetric geometry. A real 3D geometry is also used since it models cylindrical microchannel assumed in the study, however only at the preliminary level to validate simulation results from 2D and 3D axis-symmetric geometry. The 2D geometry is assumed a micro-sized channel between two 1 metre depth parallel flat planes as shown in **Figure 3.6**. The 2D geometry is used to model the microchannel with the interest of the longitudinal geometry variation, e.g. microchannels with tortuosity variation. The 3D axis symmetrical geometry is used for investigating the behaviour in microchannel with radial geometry variation, e.g. microchannel with different surface roughness and micro with dead-end region. Simulation domain with 3D axis symmetrical geometry is illustrated in **Figure 3.7**. The simulation using these two geometry approach can be scaled up accordingly to establish a more complex pore-network model to simulate the behaviour in a core. The detail of the scaling up is discussed in Chapter 7.

If PV is the pore volume of the core and  $L_{core}$  is the length of the core, then the total cross sectional area of the pores ( $A_p$ ) can be calculated as follow

$$A_p = \frac{PV}{L_{core}} \quad (3.17)$$

Corresponding average velocity for the parallel pores is below:

$$u = \frac{Q_{core}}{A_p} \quad (3.18)$$

Substituting 3.17 to 3.16 results in

$$u = Q_{core} \cdot \frac{L_{core}}{PV} \quad (3.19)$$

where  $u$  (m/s) is the average fluid velocity in the microchannel,  $Q_{core}$  ( $m^3/s$ ) is the flow rate introduced to the core,  $L_{core}$  (m) is the length of the core length, and PV (dimensionless) is the pore volume of the core.

Using the core data from the model validation in Chapter 4, the typical velocity of the fluid in the system is in the order of  $10^{-4}$  m/s and the corresponding Reynolds number is in the magnitude of  $10^{-4}$ . For such low value Reynolds number (i.e.  $Re \ll 1$ ), the inertial effect is neglected in comparison with the viscosity, hence the Stoke's flow equation is suitable to use in the study [189]. For simplification, the fluid is assumed incompressible which flows in a steady state condition.

There are two stresses in pores, which are neutral stress and effective stress. Neutral stress is the stress in the fluid inside the pore and effective stress is the difference between total stress prevailing in the fluid filled pore and the neutral stress. It is believed that the effective stress governs the deformation in porous media [174]. Since it is assumed that there is no rock compaction, the effective stressed are neglected, resulting in constant microchannel dimension along the simulation time.

The Navier-Stokes Equation that describes the flow can be simplified by neglecting the inertia terms to represent a creeping flow, since when the viscosity is large; the viscous forces dominates the flow, therefore

$$\rho \frac{Du}{Dt} = \rho \left( \frac{\partial u}{\partial t} + u \cdot \nabla u \right) = -\nabla p + \mu \nabla^2 u + \rho g \quad (3.20)$$

and

$$\rho \left| \frac{Du}{Dt} \right| \ll \mu |\nabla^2 u| \quad (3.21)$$

Thus, the Navier Stokes momentum equation is reduced to the Stokes Equation

$$0 = -\nabla p + \mu \nabla^2 u + \rho g \quad (3.22)$$

In the simulation, Equation 3.21 is expressed as a balance of forces in the flow due to the difference in pressure ( $p$ ), identity matrix ( $I$ ), viscosity ( $\mu$ ), velocity ( $u$ ), and the gravity force ( $F$ ) as expressed below:

$$0 = \nabla \cdot [-pI + \mu(\nabla u + (\nabla u)^T)] + F \quad (3.23)$$

The measured velocity profile in the microchannel is consistent with solution from Stokes equation where the no-slip boundary condition is accommodated [190], where the viscous forces dominates and the velocity happens in layers where the highest velocity is in the middle of the microchannel and the lowest at the wall boundary.

### 3.3.3 Representation of Nanoparticles

The nanoparticles are treated as a continuous concentration field that flows inside the channel. This assumption is valid since the size of the nanoparticle is small, i.e. 1-100 nm [37, 38]. The size of the channel selected is 20  $\mu\text{m}$  in diameter [53] which is based on the central tendency of

the conventional rocks pore throat diameter magnitude. The inertia of the particles is neglected, no effect from gravity, and there is no interaction between particles which hinders the process of agglomeration and repulsion of each other. It is also assumed that there is no slip velocity between the fluid and the particles allowing particles to freely transport by advection. Since the nanoparticles are treated as free particles, this movement is only governed by the physical properties, i.e. velocity, pressure, time, injection pore volume, etc.

The change of the nanoparticle concentration in time is governed by diffusion and advection. The diffusion follows an expression which is known as Fick's First Law equation as follows [191, 192]:

$$J = -D_{AB}^o \frac{\partial c}{\partial x} \quad (3.24)$$

where  $J$  (mol/ (m<sup>2</sup>.s)) is the diffusive transport,  $D_{AB}^o$  (m<sup>2</sup>/s) is the mutual diffusion coefficient of solute A in solvent B, and the  $c$  (mol/m<sup>3</sup>) is the concentration of the diluted species. Equation 3.24 valid only for one-dimensional geometry, i.e. x-direction. Therefore, this expression is converted into the three-dimensional space that follows the domain in the study. The three-dimensional equation then is included into the advection equation for the nanoparticle concentration, which is written as follows:

$$\frac{\partial c_A}{\partial t} + \nabla \cdot (-D_{AB}^o \nabla c_A) + u \cdot \nabla c_A = 0 \quad (3.25)$$

where  $c_A$  (mol/m<sup>3</sup>) is the concentration of the nanoparticles in the fluid bulk and  $u$  (m/s) is the fluid velocity.

The diffusion coefficient is calculated using the Wilke-Chang [193-195] which its permits easy calculation that holds good for and correlates most of the experimental values within an average deviation of  $\pm 13\%$ . The technique follows:

$$D_{AB}^o = 7.4 \times 10^8 \frac{(\phi M_B)^{1/2} T}{\eta_B V_A^{0.6}} \quad (3.26)$$

where

$D_{AB}^o$	=	mutual diffusion coefficient of solute A in solvent B, $cm^2/s$ . Later on in the study, $D_{AB}^o$ is written as $D_p$ .
$M_B$	=	molecular weight of solvent B, $g/mol$
$T$	=	absolute temperature, $K$
$\eta_B$	=	viscosity of solvent, $cP$
$V_A$	=	molar volume of solvent A at its boiling temperature, $cm^3/mol$
$\phi$	=	Association factor of solvent B, <i>dimensionless</i> . For water the value is 2.6.

Agglomeration is very importance to consider its tendency to happen for nanoparticles in microchannel due to the degree of interaction between the particles, salt ion in solution, and the surface of the porous medium. However, agglomeration of the nanoparticles is neglected to simplify the simulation. In reality, agglomeration of nanoparticle can be avoided by coating the nanoparticles with other substance that introduce a super-paramagnetic property to the nanoparticles [73, 74]. If agglomeration is considered, a term of first-order removal term ( $\gamma, \text{min}^{-1}$ ) [142] should be included in the Equation 3.25, hence it becomes.

$$\frac{\partial c_A}{\partial t} + \nabla \cdot (-D_{AB}^o \nabla c_A) + u \cdot \nabla c_A + \gamma c_A = 0 \quad (3.27)$$

### 3.3.4 Boundary Conditions for Velocity

Initially there is no flow in the domain. The fluid velocity  $u$  at the inlet boundary is specified by Equation 3.18. The velocity profile, however, is defined by introducing an entrance length ( $L_{entr}$ ) of the inlet channel outside the model domain. This length should be large enough thus the flow can develop a fully parabolic profile. Experiments show that for steady laminar flow and Stokes flow through a well-rounded inlet into long straight pipe, the entrance length  $L_{entr}$  follows  $0.06\text{Re}D$  [196, 197] where the  $\text{Re}$  is the Reynolds number and  $D$  is the diameter of the geometry, in this case, is the diameter of the cylindrical pipe approximated by the microchannel geometry [198-200]. This equation is valid for  $\text{Re} \leq 2000$ . The expression is shown by Equation 3.28 where, in our case, the  $L_{entr}$  equals 1 m.

$$\begin{aligned} L_{entr} \nabla \cdot [-pI + \mu(\nabla u + (\nabla u)^T)] &= -pn, \\ \nabla \cdot u &= 0 \end{aligned} \quad (3.28)$$

No slip is introduced in between the fluid and the microchannel wall thus the velocity at the wall equals zero. Certain velocity is introduced at the inlet boundary that causes a constant pressure difference between the inlet and outlet boundary of the microchannel domain. Nevertheless, constant pressure difference does not mean that the pressure gradient is zero. Introducing inlet velocity or pressure difference between inlet and outlet boundary is interchangeable in the study.

### 3.3.5 Boundary Conditions for Concentration

Initially there is no concentration of nanoparticles in the domain. At the inlet, concentration of all species  $c = c_{in}$  is specified. The boundary condition of the material balance for the surface species follows

At the outlet, the concentration of the nanoparticles is transported out of the model domain by a fluid flow. It is assumed that advection is the dominating transport mechanism across the outflow boundary, and therefore that diffusive transport can be ignored, that is:

$$n \cdot (-D_p \nabla c_A) = 0 \quad (3.29)$$

Thus, the boundary condition at the outlet is as follow:

$$n \cdot (-D_p \nabla c_A + c_A \cdot u) = n \cdot c_A \cdot u \quad (3.30)$$

### 3.3.6 Adsorption and Desorption of Nanoparticles

Adsorption is a process that takes place when a fluid accumulates and forms a molecular film (adsorbate) on the surface of another material (adsorbent). Rouquerol and Sing [201] defined adsorption as the accumulation in the density of fluid or material in the surrounding area of an interface.

---

Generally, adsorption processes are classified into two different processes, which are physical adsorption and chemical adsorption [202]. In physical adsorption, the process occurs without any reaction among the adsorbate molecules with the adsorbent. These molecules are weakly bounded due to Van der Waals forces. This type of adsorption is relatively fast and reversible, because it happens under the critical temperature adsorbate that is relatively low, leading to a low heat. Since the bound is weak, the adsorbate molecules are able to move easily from one location to another. This process also happens without any activation energy and this causes the adsorbate molecules attach in many layers on the adsorbent [203]. Chemical adsorption happens due to the existence of chemical reaction between the adsorbate and the adsorbent. This type of adsorption commonly happens above the critical temperature of the adsorbate, irreversible reaction, creating monolayer film, and the heat emanation is relatively high [203].

Adsorption is affected by adsorbate pressure, adsorbate absolute temperature, and the potential interaction between the adsorbate and the adsorbent. High adsorbate pressure can increase the adsorbed molecules on the adsorbent. However, during the process of adsorption, energy is liberated at the walls of the container as an exothermic process [174]. Therefore, the temperature increase of the adsorbate decrease the adsorption [204].

There is an existence of special affinity among the adsorbents and the adsorbates that can be divided into two types:

1. Polar adsorbent (hydrophilic). This type of affinity includes silica gel, zeolite, and active alumina with water as the adsorbate.
  2. Non-polar adsorbent (hydrophobic). This type of affinity includes active carbon and polymer adsorbent with oil acts as the adsorbate.
- [202]

There are numbers of adsorption mechanism models that has been developed by the scientists [205, 206]. In this thesis, only Langmuir and the Freundlich adsorption isotherm are discussed, following the analytic expressions for the spreading pressure and concentration. These two empirical approaches are well established to represent adsorption from the experimental data and result without indicating any essential validation of any particular model. These two approaches satisfy the assumption of the

single component adsorption parameter that is assumed in the study. The detail and the governing equations are conversed shortly after in Section 3.3.6 and 3.3.7.

In the study, the adsorption and the desorption occur on the wall along the microchannel. The adsorption and desorption of the nanoparticles on the surface of the microchannel are governed by the concentration difference between the fluid bulk and the microchannel wall. The illustration of the microchannel system is displayed in

**Figure 3.8** where  $u$  is the inlet creeping velocity,  $c$  is the concentration of the nanoparticles,  $D_p$  is the diffusivity coefficient in the fluid bulk,  $D_s$  is the surface diffusivity,  $k^f$  is the forward adsorption coefficient,  $k^r$  is the reverse reaction coefficient (i.e. corresponding to desorption). The figure shows the model geometry with symmetry axis where surface adsorption happens along the wall of the microchannel.

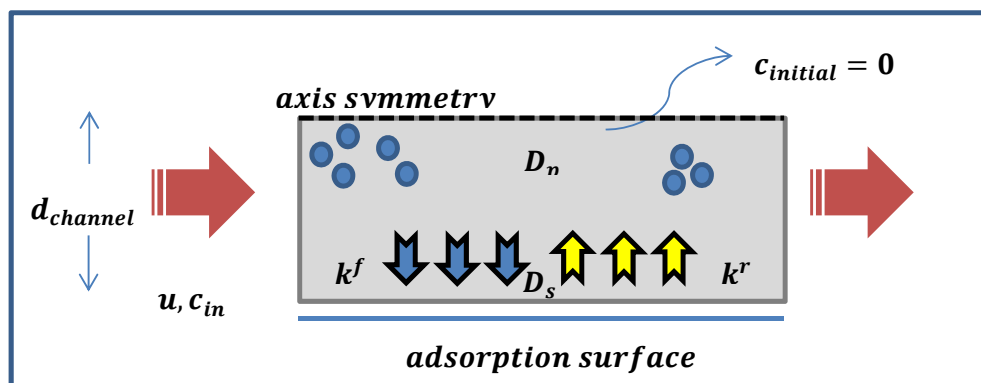


**Figure 3.8:** The illustration of the system for the simulation for the 3D axis-symmetric geometrical model.

The governing equation for the surface concentration on the wall follows similar approach as Equation 3.26 where the concentration transport is governed by concentration difference and diffusion, however without advection included. The equation is written as follows

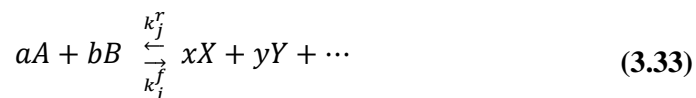
$$\frac{\partial}{\partial t} c_{s,i} + \nabla_t \cdot (-D_{s,i} \nabla_t c_{s,i}) = R_{s,i} \quad (3.31)$$

where  $c_{s,i}$  (mol/m<sup>2</sup>) is the surface concentration,  $D_{s,i}$  (m<sup>2</sup>/s) is the surface diffusion coefficient, and  $R_{s,i}$  (mol/ (m<sup>2</sup>.s)) is the sum of all sources due to surface reaction and adsorption/desorption phenomena.

The second term of the left hand side of Equation 3.31 is the mass movement between locations on the surface of the microchannel wall. The movement is governed by the concentration difference and the surface diffusion coefficient ( $D_s, m^2/s$ ). Surface diffusion is a process that consists of the motion of the molecules and the atomic clusters at solid material surfaces [207]. In this case, the surface diffusion can be neglected because the size of the channel is not comparable with the range of the nano-sized particle interaction with the channel wall [208]. This simplifies the adsorption process on the channel wall which then it is only governed by the concentration difference between the wall and the fluid. Therefore, Equation 3.31 becomes as follows

$$\frac{\partial}{\partial t} c_{s,i} = R_{s,i} \quad (3.32)$$

The adsorption mechanism used here is based on the mass action law shown below:



where  $A$  and  $B$  are the reactants,  $X$  and  $Y$  are the products, and  $a$ ,  $b$ ,  $x$ , and  $y$  are the appropriate integers that satisfy the balance of the reaction.  $k_j^r$  is the reverse reaction constant and  $k_j^f$  is the forward reaction constant.

Thus the adsorption and desorption reaction  $R_{s,i}$  (mol/m<sup>2</sup>.s) from Equation 3.31 can be written as below

$$R_{s,i} = k_{s,i}^f \cdot \prod k c_i^{-v_{ij}} - k_{s,i}^r \cdot \prod k c_i^{v_{ij}} \quad (3.34)$$

where  $k_{s,i}^f$  is the forward reaction constant,  $k_{s,i}^r$  is the reverse reaction constant,  $c_i$  is the species concentration in mol/m<sup>3</sup>,  $v_{ij}$  is the stoichiometric coefficient where the sign (-) for reactant and (+) for product.

In this study, the adsorption process is simplified as a physical adsorption without considering precipitation or crystallisation processes. It is also assumed that the effect of pH is neglected and system works under a constant temperature. There are two approaches selected as candidates for the solution of the  $R_{s,i}$ . The first approach is to use the Langmuir adsorption isotherm equation and the second one is to use the Freundlich adsorption isotherm equation.

### 3.3.7 Langmuir Adsorption Isotherm

The first approach, the Langmuir adsorption isotherm, is selected considering that the investigation of the effect of the adsorption and desorption is easy to conduct [209]. Some assumptions are needed for the validity of the Langmuir adsorption isotherm such as the surface containing the adsorbed is homogeneously flat without any corrugation, the adsorbates are adsorbed into an immobile state, all adsorption sites are equivalent, there is only one molecule adsorption layer (mono-layer adsorption), and there are no interactions between adsorbate molecules on the adjacent sites [209].

In this case, it is assumed that there is only one substance of nanoparticles in the fluid bulk (represented by  $A$ ) that can be reversibly converted into the adsorbed nanoparticles (represented by  $B$ ) on the channel wall. This can simply be written as follows:



where  $A$  represents the concentration of the nanoparticles in the bulk and  $B$  represents the adsorbed nanoparticles on the microchannel wall.  $k_f$  is the forward reaction (adsorption) constant and  $k_r$  the reverse reaction (desorption) constant. Since monolayer adsorption is one of the requirements of the Langmuir adsorption isotherm, the available adsorption site ( $\theta$ ) should be considered. The adsorption stops when the available adsorption site ( $\theta$ ) saturated with the adsorbate. Thus, the reaction rate is written below:

$$\frac{dc}{dt} = k_{ads} \cdot c_A (1 - \theta) - k_{des} \cdot c_B \quad (3.36)$$

where  $k_{ads} = k_f$ ,  $k_{des} = k_r$ ,  $c_A$  is the concentration in the fluid next to the channel wall and  $c_B$  is the concentration on the surface of the channel wall.

In detail, for the rate of adsorption is

$$\left(\frac{dc}{dt}\right)_{ads} = k_{ads} \cdot c_A (1 - \theta) \quad (3.37)$$

and for the rate of desorption is

$$\left(\frac{dc}{dt}\right)_{des} = k_{des} \cdot c_B \quad (3.38)$$

where  $c$  is the corresponding concentration of the nanoparticles.

### 3.3.8 Freundlich Adsorption Isotherm

The second approach to be investigated is the Freundlich adsorption isotherm mechanism. The Freundlich adsorption is an empirical correlation with limited coefficient interpretation [210-212] that is widely used to match adsorption isotherm from the experiment [158]. It is widely used in cases where the actual identity of the solute is not known. The Freundlich adsorption isotherm assumed that the adsorption rate is a function of the pressure. The adsorption occurs until the saturation pressure of the system achieved. Thus, Freundlich adsorption isotherm works well for the heterogeneous adsorbent surface with different adsorption sites. However, this assumption makes the Freundlich adsorption isotherm fails in a condition with high pressure. Since the pressure is proportional to the concentration, thus the adsorption rate of the Freundlich adsorption isotherm is the function of the concentration. Hence, the equilibrium pressure of adsorbate in the adsorption measurement for the liquid phase is approached by use of the equilibrium concentration of the adsorbate in solution. In general, the Freundlich equation given by:

$$\frac{dc}{dt} = k_f \cdot c^n \quad (3.39)$$

where  $c$  is the concentration of the substance as a function of time is,  $k_f$  is the fractal coefficient, and  $n$  is the fractal dimension [170, 213]. Efforts of deriving the Freundlich equation based on the thermodynamics have been conducted [214-216], however the derivations are mostly difficult to apply and interpret [170]. The other approach for deriving the Freundlich equation using the statistical mechanical approach are also conducted [217, 218].

However, the original Freundlich adsorption isotherm equation cannot clearly show the term of adsorption and desorption. Therefore, modified Freundlich equation conducted by Skopp [170] is used for the study. Skopp derived Freundlich adsorption isotherm equation by introducing term of adsorption and desorption separately, allowing to study adsorption and desorption process more easily. Again, in this study, there is only one substance of nanoparticles in bulk (A) that can be reversibly converted into adsorbed nanoparticles (B) on the channel wall. The mechanism follows the one in Langmuir approach that is discussed in Section 3.3.7, that is again written as Equation 3.34. The reaction rate for modified Freundlich adsorption isotherm approach derived by Skopp [170] is displayed in Equation 3.40 where the concentration of the nanoparticles in the bulk (A) and on the rock surface (B) are considered.

$$r = k_{ads} \cdot c_A^{n_{ads}} - k_{des} \cdot c_B^{n_{des}} \quad (3.40)$$

where  $k_{ads} = k_f$  and  $k_{des} = k_r$ . Parameters of  $n$  is the order of the reaction where the subscript *ads* and *des* are for adsorption and desorption respectively [119, 170].

In this study, it is assumed that the adsorption and desorption are important and should be addressed separately. The process is again represented by the Equation 3.38. However, the reaction rate is derived [170] by separating the adsorption and desorption rate following Equation 3.41, hence:

$$\frac{dc}{dt} = k_{ads} \cdot c_A^{n_{ads}} - k_{des} \cdot c_B^{n_{des}} \quad (3.41)$$

where  $k_{ads} = k_f$ ,  $k_{des} = k_r$ ,  $n_{ads}$  is the Freundlich adsorption exponent constant, and  $n_{des}$  is the Freundlich desorption constant. Equation 3.41 is different from the Langmuir adsorption isotherm in Equation 3.36 because

---

the former does not relate to the available adsorption-site surface area on the microchannel wall ( $\theta$ ). In other words, Equation 3.41 allows multilayer adsorption where the adsorption mechanism presents as long the bulk concentration is larger than the concentration on the wall.

In the original Freundlich equation, parameter  $n$  is proposed to be between 0 and 1 [148]. On the other hand, others found that the value of  $n$  can be larger than 1 [170, 219]. However, there is no specific requirement for the Equation 3.41. Therefore, the parameters selected for the simulation that result are those in the closest fit with the data obtained from the laboratory experiment.

It is experimentally determined that the degree of adsorption differs proportionally with pressure until saturation pressure is reached. Applying higher pressure than the saturation point surfeits the adsorption rate, thus the Freundlich adsorption isotherm fails at higher pressure [205, 220]. The utilisation of the Freundlich adsorption isotherm method in the study is still valid because the pressure difference between the adsorption surface and its surrounding is small.

### **3.4 Core flooding experiment for validation**

The model development is begun from the application of nanoparticles for the scale inhibitor squeeze. Therefore, a suitable laboratory experiment required for validation. A core-flood experiment result conducted by Zhang and co-workers [221] to investigate a non-equilibrium adsorption and precipitation of scale inhibitor is selected.

In the experiment, Zhang et.al utilised a 13cm length Clashach sandstone core that is completely coated with epoxy resin that was placed inside an anti-leakage core holder. Two types of fluid were used in the experiment i.e. penta-phosphonate DETPMP and the phosphine-carboxylic acid (PPCA) scale inhibitor, with Lithium tracers included in the solution. At first, the cores were saturated with seawater, and the brine permeability was measured. Then the inhibitor slug with 50 ppm Li was injected with a stable flow rate using a Pharmacia P-500 high precision pump. The injection was carried out until 8-10 pore volume of inhibitor injection after the core achieved its saturation. At the end of the injection, the core was shut-in and heated to 70 °C. After 24 hours, the core was post flushed with seawater at different rate stages, i.e. 30, 5, 30, 300, and 5 ml/hr consecutively. The post flush was conducted until the inhibitor concentration had reached 1 to 2 ppm

---

active. At the end of the core flood, the brine permeability then was measured at room temperature and the effluent volume is measured using a fraction collection instrument, Pharmacia Frac-200. The effluent measured is from these following cases, i.e. results from the inhibitor injection stage, from the desorption/desolution of the early and the late stage. Since they assumed that the scaling inhibitor is retained in the rock formation with two mechanisms, i.e. adsorption and precipitation [119-121], they also displayed the comparison between the rate controlled precipitation and the rate controlled adsorption flood for both DETPMP and PPCA in the later post-flush duration.

From the experiment, they established a binary computer modelling based on the non-equilibrium adsorption in the variation of rates conducted. Firstly, they defined the dynamic of the non-equilibrium multicomponent system as the base principle for the isotherm and kinetic function. Then, they use a mathematical approach using the Freundlich model and rate expression to calculate the experimental inhibitor breakthrough curve. Freundlich model was selected rather than Langmuir, because the former appeared much better to represent the result from the experiment.

This work is utilised for validation in the simulator because the report provides one of the most complete laboratory and simulation result to be reproduced. The approach is, however, different. In their case, the investigation was conducted for a 13 cm core sample. In this case, the investigation is focusing more to the phenomena in pore channel itself. Certainly, the geometry needs to be scaled down to the one required in the study. The investigation is also focused on the distribution of the nanoparticles in solution in the micro-sized pore channel. The behaviour of the injected nanoparticles is assumed similar to the injected PPCA in the work of Zhang et. al. This is assumed valid because both are treated as a diluted species, because the size of the nanoparticles is much less than the magnitude of the micro-channel. Some other assumptions are also required to utilise in the simulation, i.e. no slip in the system, monolayer and multilayer adsorption according to the adsorption mechanism selection, isothermal, adsorption process without precipitation process, no interaction between particles, no chemical reaction, incompressible effect, no pH effect, and no agglomeration. All the assumptions refer to Chapter 4 in this thesis.

### 3.5 Simulation Procedure

The model is developed based on a core-flood laboratory experiment conducted by Zhang et.al. [221]. Two sets of equations for the 2D and the 3D axis symmetric geometry are derived.

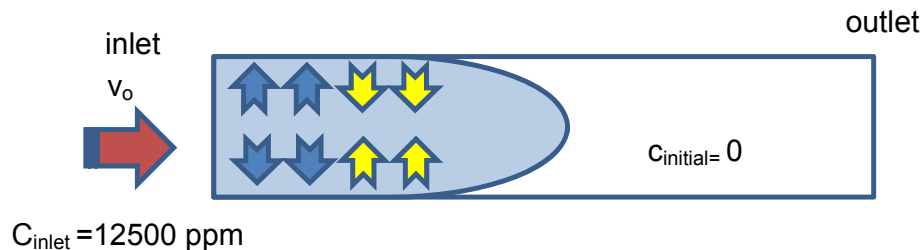


**Figure 3.9:** Illustration for the simulation procedure

A steady creeping flow is first solved, with fluid injected at the inlet. The velocity field from this calculation is then used in time dependent calculation of the concentration field by solving the advection dispersion equation. Hence, there is only one-way coupling and the presence of the nanoparticles is assumed not to affect the local fluid properties. Water is used for the fluid medium. The concentration of the injected nanoparticles is 12500 ppm, which number is selected based on the experiment conducted by Zhang et.al. [221]. This is illustrated in **Figure 3.9** where the red arrow is the inlet concentration, the blue arrows are the adsorption process, the yellow arrows are the desorption process, and the outlet is the right boundary of the microchannel.

There are two nanoparticle injection methods discussed in this study, i.e. (1) continuous injection along the simulation time and (2) discontinuous injection at the beginning of the simulation. These two injection methods have a different influence on the injected concentration distribution and adsorption/desorption profile in the system. The advection dispersion equation then is coupled with the adsorption isotherm equation that allows the concentration to be adsorbed on or desorbed from the channel wall governed by the concentration difference. By then the distribution of the particles concentration and the adsorption and desorption are investigated.

Most of the investigation in the study is plotted against the simulation time and the injection volume. Injection volume is measured in the number of pore volume. The number of pore volume is a dimensionless unit that is

measured by comparing the unit discharge over time and the volume of the domain. It follows the relationship below [222]:

$$V_{Injected} = \frac{v \cdot A \cdot t}{A \cdot L} \quad (3.42)$$

Removing the term  $A$ ,

$$V_{Injected} = \frac{v \cdot t}{L} \quad (3.43)$$

where  $v$  is the inlet velocity [ $m/s$ ],  $A$  is the cross sectional area of the microchannel [ $m^2$ ],  $t$  is the time interval [ $s$ ],  $L$  is the length of the microchannel [ $m$ ], and  $V_{Injected}$  is the injected volume which is measured in the number of the pore volume (unit in Pore Volume,  $PV$ ).

### 3.6 Computational Fluid Dynamic (CFD)

The simulation in this thesis is conducted by utilising Computation Fluid Dynamic (CFD). CFD is a branch of fluid mechanics engineering that predicts flow behaviour using mathematical physical problem formulation by solving partial differential equation system and algorithm that govern the fluid flow phenomenon. The process of CFD process is illustrated in **Figure 3.10**.

The knowledge of fluid mechanic is required to understand physic of fluid to solve a fluid problem. The physical properties of the fluid are described using mathematical equation, i.e. Navier-Stokes Equation as the governing equation of CFD, where partial differential equations (PDE) are included. For simple fluid problem, the equations can be solved analytically. However, for a complex CFD problem, the equations should be translated to discretized form, where the domain of the problem is divided into small parts (grid) where the discretization based on.

There some tools for the translation process, including Finite Difference method, Finite Volume method and Finite Element method. Discretization of fluid problem using Finite Difference Method is conducted by local approximation by utilising expression of differential operator on predefined grid points. The grid points are usually placed very regularly, where the governing equations are given in a discrete expression. Hence, in

this method, any reference to the association of physical quantities with geometric object other than points is not present. Therefore, this approach sometimes does not give consistent result with development of further analysis.

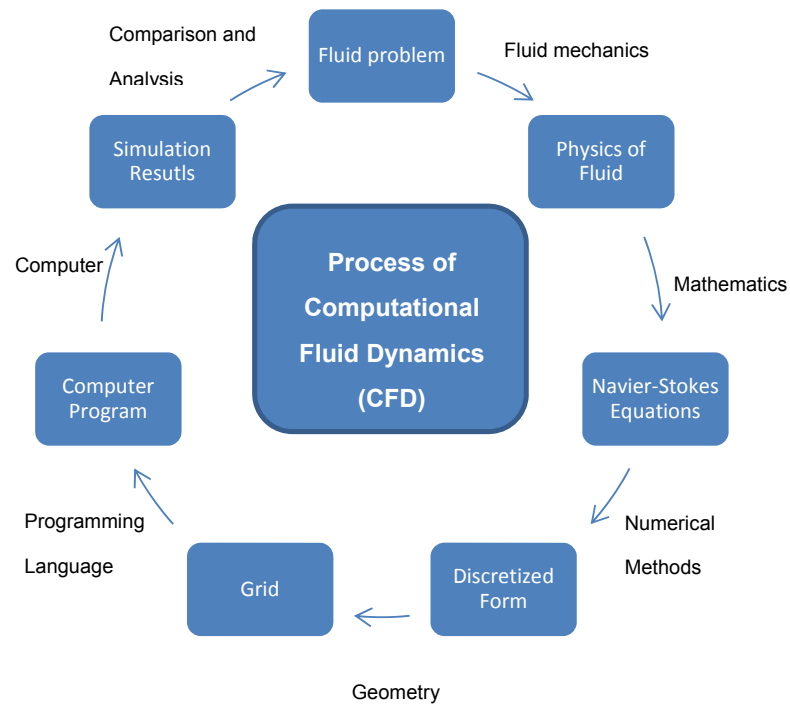


**Figure 3.10:** Process of computational fluid dynamics

Discretisation of the field equation using Finite Volume Method is conducted by subdivides the problem domain in cells and writes the field equation in integral form on these cells. However, the deployment of an integral approach alone does not guarantee that all the requirements of the physical approach to the discretization are recognized and implemented, and even sometimes missing its fundamental distinction. Moreover, usually the discretization produced by the integral statements of this method does not include time variable, which is alternatively subjected to a separate discretization. The separation discretization for the time variable with the integral statement might result the possibility of time-stepping formulas that cannot be derived in a natural way from a space-time co-boundary operator [223, 224]

The formulation in Finite Element Method is based on a direct physical approach that brings great geometrical flexibility with respect to the other

methods [223]. This feature is an important key benefit to use in this thesis because the study utilises microchannel domain with various surface and longitudinal geometries. It is the reason this method is selected to use in this thesis. The detail discussion for Finite Element Method is discussed in Section 3.7.

Computer program with programming language is used to solve the calculation of the discretized form by utilizing computers. When the simulation results are obtained, they are compared and analyse with experiments and real fluid problem. The process is repeated until the simulation results satisfy the experiment of the real fluid problem. In this thesis, COMSOL version 4.2a is used to conduct the FEM simulation. COMSOL enables the coupling of multiphysics into the flow very effectively.

CFD simulation has advantage over experiment to study fluid phenomenon. CFD is cheaper and faster to run compare to experiment. The study using CFD can be conducted to any scale, where the scale of experiment is limited. Information can be retrieved continuously along the domain and simulation time, however information from experiment can only be obtained from measurement point. CFD simulation is repeatable, but experiment sometimes not repeatable. CFD hardly has any negative effect to health and safety and experiment is sometime dangerous and unsafe for environment [225].

### **3.7 Finite Element Analysis (FEA)**

The Finite Element Analysis (FEA), or as well known as Finite Element Method, is a suitable numerical analysis method for solving computational problems over complicated domains. The solution of the problem involves solving the governing partial differential equations iteratively until the error falls below a specific tolerance. It is widely used for many areas of sciences, engineering, and applied mathematics i.e. solid mechanics, heat transfer, electromagnetism, fluid mechanics, etc.

Burnett [226] specified four concepts in understanding the FEA: system, domain, governing equation, and loading condition. The system is a physical object contained of different materials of solids and/or fluid. The domain is the spatial region or time occupied by the system. The governing equation is typically differential or integral equations expressing a conservation of some physical properties, which are considered in the system. The equations also include constitutive equations for the material,

e.g. physical constants from laboratory experiments. The last one, the loading condition, is the external forces subjected to the system. This load may present in the interior of the domain as a part of the governing equation. This load is known as the interior load. Or else, this load also may act on the boundary of the domain. This type of load presents in separate set of equations called the boundary condition. Loading condition corresponds to solid mechanics-property. In the fluid dynamics, this corresponds more to the boundary condition of the system (i.e. no slip condition and the inlet velocity).

The fundamental ideas of the FEA includes the discretisation, interpolation and minimising the error. Discretisation means that the domain of the model is divided into smaller regions of finite size. One small region is called an element and this is where the nomenclature of 'finite element analysis' comes from. The geometry of the finite element can be triangular, rectangular, tetrahedral, cubes, etc. The elements, which are also known as 'mesh', must cover the entire domain without overlapping with each other. The intersection of two elements is either on a common vertex or a common full edge. There also must not be any gap between two adjacent elements [227, 228].

Each element contains the governing equations where then is transformed into algebraic equations by approximation. Thus, the value in an arbitrary location within the elements can be computed, which is known as interpolation. The approximation has to be validated using an error function. By iteration, the error is minimised to obtained high accuracy result. The result obtained from simulation will be employed to understand the physics of the flow and particle distribution in the porous media. The simulation is conducted using fully implicit numerical method.

### 3.8 Model Overview

The model developed is versatile and provides flexibility of using different corresponding equations and approaches that are solved using Finite Element Method. Initially the geometry of the microchannel is specified whether it is a 2D channel or the 3D axis symmetrical channel geometry. The inlet of the microchannel and the outlet are then configured according the geometry used in the simulation, which refers to Section 3.3.2.

A certain concentration  $c = c_{in}$  is introduced from the inlet of the microchannel which normally located at the most left boundary of the

---

microchannel. There is initially no concentration in the microchannel and neither on the microchannel wall. The injected concentration propagation inside the microchannel is governed by the Equation **3.26** along with a steady creeping flow which governed by the Equation **3.23**. The steady state creeping flow follows the Newton linear direct solver.

The introduced concentration is given by two ways, i.e. continuously and discontinuously along the simulation time and for a fixed time length at the beginning of the simulation. The fluid used in the model is incompressible water. The effect of the diffusion is considered in the Equation **3.26**, which follows the Fick's law in Equation **3.24** that values are obtained from Equation **3.11**. During the propagation, some of the particles that located close to the microchannel wall are adsorbed to or desorbed from the channel wall, which is governed by the Equation **3.34**. The right hand side of the Equation **3.34** is the adsorption isotherm equation. The temperature of the system in the reservoir tends to be constant; thus, the simulation is conducted isothermally. Therefore, the adsorption isotherm equation selected is either the Langmuir equation (i.e. Equation **3.36**) or the Freundlich equation (i.e. Equation **3.41**). These two equations are selected due to the nature of the equation for the simplicity to define the aspect of the adsorption and desorption separately.

Both of Langmuir and Freundlich equations are investigated and one of them that provide the most satisfying results with experiment is selected to be utilised in the study. Since the advection at the outlet is assumed to be significantly, more dominant than the diffusion due to the nature of the magnitude, the diffusion in the adsorption boundary is neglected which is governed by Equation **3.29**. The full form of the governing equation for the outlet boundary follows Equation **3.30**.

The model validation is compared to a laboratory experiment results from Zhang et.al. [221] and the equations obtained are subjected to further studies. Thus, the movement of the concentration front is investigated in order to investigate the particle distribution. The outlet effluent concentration, the adsorbate mass, and the adsorbate concentration are also observed in order to study the effect of the adsorption and desorption process to the system. The profile of these parameters is obtained by averaging the magnitude along the corresponding boundaries in times.

The solution is obtained by using the Finite Element Analysis (FEA) method that utilises a commercial multiphysics software platform for

---

simulating physics-based problems, COMSOL version 4.2a. The domain of the system is expressed by a set of triangular grids. The solution for the parameters for each location in the grid are obtained using the governing partial differential equation introduced previously by iteration until the error falls below a specific tolerance. The transient simulation for the concentration flow and the adsorption-desorption process follows the Newton nonlinear solver with Jacobian numerical computation that is updated on every iteration.

The assessment of the mesh density needed to get grid independent result is important. Therefore, the mesh should be tested in order to get the most suitable mesh setting for an efficient simulation without sacrificing its accuracy. A systematic study is carried out by conducting several simulations using a typical problem. Each simulation uses different mesh setting. Then the results obtained from each model are compared to investigate the most suitable mesh setting for the simulator. The detail is referred to Section 4.4 in Chapter 4.

### **3.9 Summary**

This chapter presented the methodology of designing a simulator to study the distribution of the nanoparticles in porous media. The nanoparticles are treated as a concentration and the porous media is approached by introducing a single microchannel. The simulation is flexible where two types of geometry are considered, i.e. the 2D microchannel geometry and the 3D axisymmetric geometry. The former is subjected for modelling pore model that has longitudinal variance, i.e. microchannels with tortuosity difference. The latter is for modelling pore model that has variance in radial direction, i.e. microchannels with different roughnesses and microchannels with dead end regions. The detailed design is presented and explained with inclusion of the assumption and model simplification.

A finite element analysis is utilised to provide information for the analysis about the propagation of the nanoparticle concentration and the adsorption-desorption process in the microchannel.

## **Chapter 4**

### **Distribution of Nanoparticles in a Single Straight Microchannel**

#### **4.1 Introduction**

This chapter presents the development of a simulation for the distribution of nanoparticles in a single straight microchannel representing a pore throat within a rock formation. The purpose is to explore and validate a model linking bulk flow and surface adsorption/desorption using a simple geometry, before introducing more complicated geometry effects in later chapters.

Adsorption of the scale squeeze inhibitor is proportional to the surface area of the pore in the rock formation. Due to the magnitude of the size, nanoparticles have large specific surface area. Large surface area improves the frequency of any collision which results to a higher degree of adsorption [38]. Placing a layer of nanoparticles on the channel wall is one of the ways to increase the pore surface area [35]. This enhances the amount of the scale inhibitor adsorption on the rock surface and prolongs its lifetime.

It is important to understand the behaviour of the nanoparticles in the pore channel, i.e. the transportation, adsorption, desorption, etc. By understanding the behaviour, better prediction of the distribution and placement of the nanoparticles inside the rock will be easier. The behaviour of nanoparticles in porous media has been conducted for more than a decade [54, 171]. However, as far as the author is aware, there is no study or simulation that focuses specifically on the adsorption and desorption mechanisms inside the pore-channel itself. Therefore, the mechanisms are discussed in this study.

Nanotechnology is still quite a new thing in the oil and gas industry. Furthermore, there are Health, Safety, and Environment (HSE) concern that need to be considered [35]. It is important to understand the distribution and placement of the injected nanoparticles in porous media. Many studies have been conducted to investigate the behaviour of nanoparticles in porous media [54, 171]; however the studies were mostly conducted for a

---

macroscopic flow in a core-scale sample and there is none yet establish a simulation that focus specifically on the adsorption and desorption mechanism inside the pore-channel itself. Considering the magnitude and the size of the nanoparticles compare with the magnitude of the pores diameter, the nanoparticles can be modelled as a concentration field. Therefore, any chemical injection is potentially usable as a means for validation. However, specific chemistries will be important in different cases since it will influence the parameters used in the adsorption and desorption governing equations. In our study, any specific chemistry reaction in the system is not considered.

After a large number of literature reviews, the laboratory experiment results which conducted by Zhang et. al. [221] has been selected to explore and validate the model developed in the study. The experiment was conducted to investigate the adsorption of an injected solution through a core sample from a core flooding experiment of a scale squeeze treatment. In the experiment, 13 cm Clashach sandstone was flooded with each of a few solutions containing penta-phosphonate, Diethylenetriamine Penta Methylene Phosphonic acid (DETPMP) and phosphino-carboxylic acid (PPCA). In the study, only the injection of PPCA is to be investigated for a comparison for nanoparticles injection. PPCA is selected because this chemical is a common substance to use in the oil industry to treat the produced water because of its nature to have a strong inhibition capability [123]. The injected PPCA is treated as a concentration within the bulk fluid, which acts as the analogy for the nanoparticles concentration.

All the known and existing experiment data and result from Zhang's articles are considered in developing the simulation tool. Clashach-type sandstone is used as the sample of the porous media. The average size of this sandstone's pore-channel is 15  $\mu\text{m}$  [229]. Another source defined the typical pore throat diameter for a sandstone core is 20  $\mu\text{m}$  [53]. The magnitude of the pore channel size in the study is taken from the latter source.

Later on, the pore channel will be known as a term of 'microchannel'. Unfortunately, the complete raw input data of Zhang's experiment is not available. Therefore, some assumptions to simplify the model were used to convert the properties used in the core flood for the microchannel model in the simulator. The details of the assumption are discussed in Chapter 3. The simulator takes account the modelling of the fluid flow, particle-transport

within the flow, and the mechanism of particles' adsorption and desorption on the wall of the microchannel. The trends of the adsorption/desorption obtained from the simulation are compared with those from the laboratory experiment.

The tools developed comprise of two geometry configurations, i.e. the 2D and the 3D axis-symmetric geometry. The 2D geometry benefits the simulation for longitudinal geometry configuration, such as the microchannel with tortuosity, microchannel with the dead end regions, etc. The 3D axis-symmetric geometry benefits to approach the real micro pore-channel better.

## **4.2 Aims and Objectives**

In this chapter, a development of a conceptual model and simulator to model the transport of nanoparticles in a single straight microchannel is discussed. Injection of PPCA at a certain concentration is used for the equivalence of the nanoparticles concentration. PPCA is selected because this chemical is a type of nanoparticle and is commonly use in the oil industry to treat the produced water because of its nature to have a strong inhibition capability [123]. The model is validated with the results from a core flood experiment to test the performance of the model. This model will be used for the basis for further simulation of the nanoparticle transportation in microchannels.

## **4.3 Simulation Setup**

### **4.3.1 General Assumptions of the Simulation**

Some assumptions are utilised to simplify the mechanism of the transportation and adsorption/desorption process of the particles in the microchannel. The nanoparticles are small, inertless and dilute, and therefore treated as a concentration field that travels together in a carrier fluid under a steady creeping flow. The carrier fluid is water and assumed to be incompressible. There is no slip between the carrier fluid and the diluted nanoparticle concentration. Hence, the concentration field propagation is advected by the bulk flow. Diffusion of the nanoparticle concentration is also included, which is the function of the concentration difference in the system. There is no reaction between the nanoparticles in the concentration, which means that there is no process of agglomeration and/or repulsion between the nanoparticles considered in the model.

There is also no slip between the fluid and the microchannel wall, therefore the velocity at the wall is zero. The wall is incompressible and receives no deformation. The adsorption and desorption process happens only at the microchannel wall, following an adsorption isotherm mechanism which is influenced by a concentration difference between the fluid bulk and the wall. The effect of the temperature and pH effect is neglected. Further details of the assumptions are given in Chapter 3 section 3.3.

### 4.3.2 Geometry Configuration

Two geometries used for investigation, which are 2D and 3D axis symmetric geometry. The 2D geometry considers a micro-sized channel between two flat planes. This is used as the basis for further modelling which considers bends and dead-end regions in the microchannels. The illustration for the 2D model is shown by **Figure 4.1**, where the inlet of the microchannel is the left boundary and the outlet of the microchannel is the right boundary. The adsorption surfaces are the top and the bottom boundaries of the geometry.

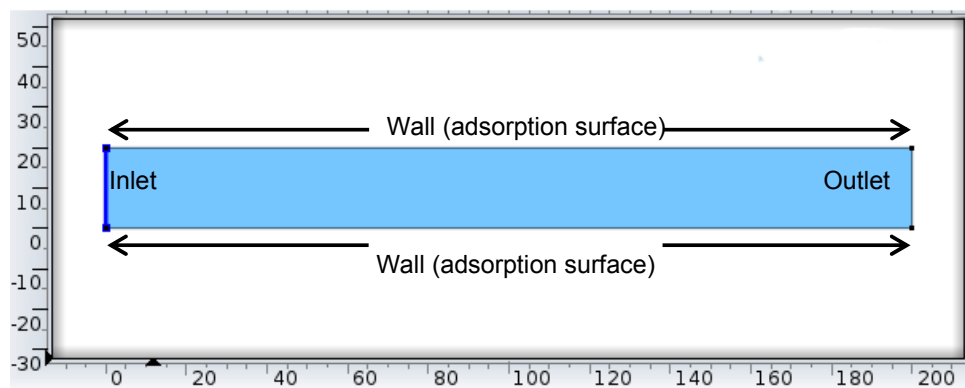


**Figure 4.1:** Geometry for the 2D model (units are  $\mu\text{m}$ )

The second geometry is a 3D axis symmetric. This geometry brings the model closer to a realistic 3D microchannel model. The illustration of this configuration that is utilised for the modelling is shown in **Figure 4.2 (left)**. The blue coloured boundary in this figure is the adsorption surface, and the boundary with the red-dotted-line is the axis symmetric of the geometry. The actual geometry in the simulation looks as it is shown in **Figure 4.2 (right)**.

Therefore, the model considers the effect of the actual cylindrical surface area geometry and not only in a two-dimensional geometry.

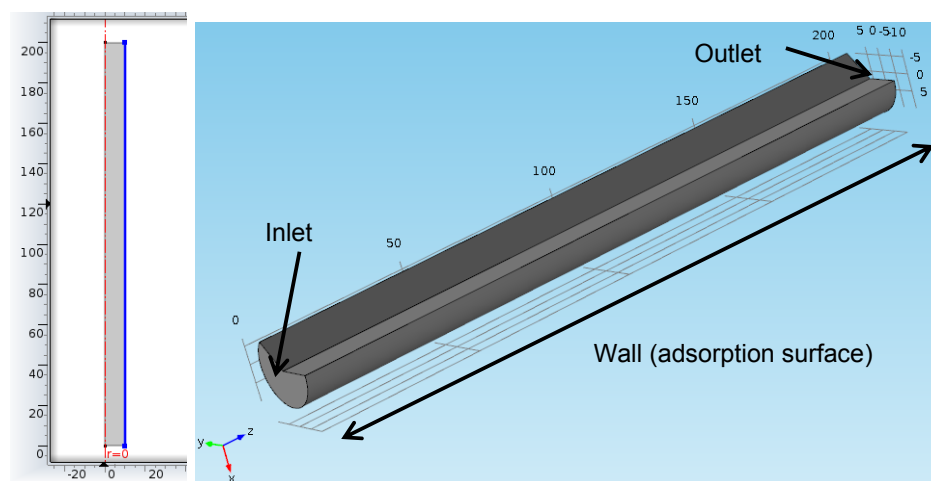


**Figure 4.2:** Geometry for the 2D axis symmetric model (left) and the corresponding 3D appearance (right)

### 4.3.3 Governing Equation for the Simulation

The governing equation of this simulation is divided into two sets of equations. The first set of equations describes the steady flow of the carrier fluid. The second equation is to solving the solid (nanoparticle concentration) transport. The adsorption and desorption happens at the boundary of the domain which follows adsorption isotherm mechanism. Langmuir and the Freundlich adsorption isotherm approaches are both initially investigated and compared to be utilised for further studies where selected laboratory experiment result used for validation. These two mechanisms are investigated because these two methods provide potential to easily understand the process of the adsorption and desorption in the system. The detail for the governing equation is discussed in Chapter 3 section 3.3.

### 4.3.4 Experiment Data and Result for Validation

The results from the core flood laboratory experiment conducted by Zhang et. al. [221] was used to validate the developed simulator. In the core flood experiment, a scale inhibitor slug was injected continuously to a 13 cm core until a full saturation condition was achieved. Then the core was flushed out with multiple flow rates of 30 ml/hr, 5 ml/hr, 30 ml/hr, 300 ml/hr,

and 5 ml/hr sequentially, until the concentration of the scale inhibitor in the effluent reached 1-2 ppm active.

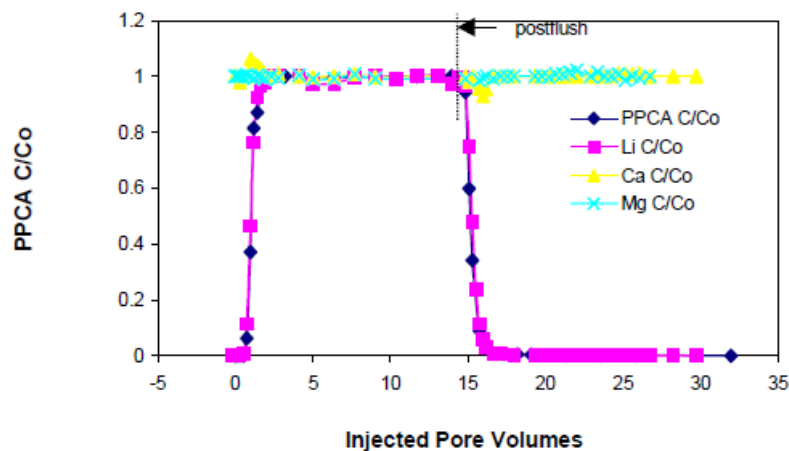


**Figure 4.3:** Injection and the early post flush stage for the PPCA concentration (reproduced from Zhang et. al. [221])

Two results from Zhang's experiment are used for the validation. The first result is the trend of the PPCA adsorption onto the porous media wall during the injection and the early post flush stage. It is important to note that a post flush stage in a scale squeeze injection treatment is where the scale inhibitor chemical is injected into the reservoir before the shut in stage. The injection and the early post flush stage included an injection of 12500-ppm concentration of PPCA until the core was fully saturated. Zhang conducted the experiment for four different injection substances, i.e. PPCA, Li, Ca, and Mg. The effluent profiles for these substances are shown in **Figure 4.4**. The effluent is characterised as a normalised effluent concentration, which is measured by dividing the effluent concentration by the initial injected concentration. The normalised effluent concentration is plotted against the injection volume, which the latter is measured as the number of volume of the pore space in the core. However, the trend of the PPCA effluent is the only one considered in our study because PPCA is a common substance to use in the oil industry to treat the produced water because of its nature to have a strong inhibition capability [123]. In the **Figure 4.4**, the trend of the PPCA is shown by a dark blue coloured profile. The PPCA is injected into the core until it reach saturation point after one pore volume. The injection is continued to 15 pore volume of the core to assure the system achieve the saturation. After 15 pore-volumes, post flush is then conducted. The trend of

the effluent obtained versus the injection volume from the simulation is compared to the one in this figure.

The second validation to compare the simulation result with the PPCA effluent profile from the post flush stage of injection. The original result taken from the lab experiment is shown in **Figure 4.4** where five sequential multi-rates injections were conducted. By default, the simulator developed measures effluent concentration in mol/m<sup>3</sup>. To convert this units to ppm, average molecular weight of PPCA is introduced, i.e. 3600 gr/mol [230, 231].

There are some challenges to simulate results from the laboratory experiment. In the original lab experiment, the sample was a core with arbitrary pores. The length of the sample was 13 cm with unknown diameter dimension. In order to establish a microchannel model, the dimension of the core diameter is important to know hence to be converted afterwards to the microchannel diameter. Therefore, a typical diameter of a core sample used in core flood experiment is used for the simulation, i.e. 1.50 inches ( $\approx 3.81$  cm) [232].

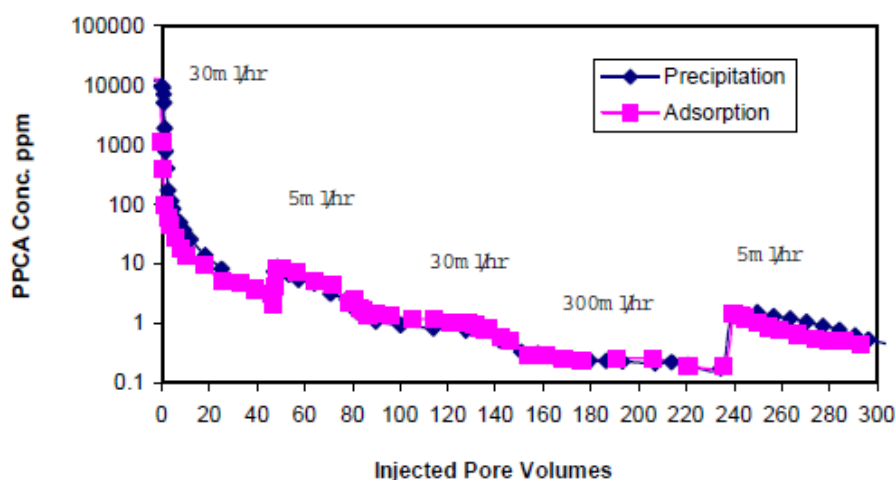


**Figure 4.4:** PPCA concentration in the effluent vs the injected pore volume (reproduced from Zhang et. al. [221])

The flow and adsorption/desorption process occurs in a pore in this core sample is used in the study. The pores are assumed a single microchannel as a simulation domain that provides access to investigate concentration flow, adsorption and desorption process mechanism for various microchannel surface and longitudinal geometry variation. Hence,

the property of the core sample is then “transferred” to this microchannel. A typical pore size diameter for the sandstone core is used, i.e. 20  $\mu\text{m}$  [53] and the length is taken based on the length of Zhang’s core sample, i.e. 13 cm. The detail for the model geometry is discussed in Chapter 3. Diffusion is considered in the study which diffusion coefficient follows Wilke-Chang method [193, 194] that is shown by Equation 3.26. This equation is suitable for the study since its valid for solvent in water. The data in the **Table 4.1** below is used in determining the diffusivity coefficient used in the study:

Parameter	Value	Units
$M_B$ , water molecular weight	18.015 [233]	<i>g/mol</i>
$T$ , absolute temperature	474.15	<i>K</i>
$\eta_B$ , viscosity of water	0.138 [233]	<i>cP</i>
$V_A$ , molar volume of PPCA = $M_B/\rho$	3537.32 [234]	<i>cm<sup>3</sup>/mol</i>
$\phi$ , association factor of solvent	2.6 [193]	<i>dimensionless</i>

**Table 4.1:** Data for calculating diffusivity coefficient

By introducing the values in **Table 4.1** into Equation 3.26, hence

$$D_{AB}^o = D_p = 7.4 \times 10^8 \frac{(2.6 \times 18.02)^{0.5} \times 474.15}{0.138 \times 3537.32^{0.6}}$$

$$D_p = 1.29 \times 10^{-5} \text{ cm}^2/\text{s}$$

Zhang et al [221] used Freundlich adsorption isotherm to calculate the adsorption. In the study, it is required to assess the adsorption and desorption mechanism separately to gain access for the thorough understanding of the process. Initially, Langmuir adsorption isotherm was selected to use as the governing equation for simulating the adsorption and desorption process. The adsorption and desorption mechanism in the Langmuir adsorption isotherm is easy to investigate since the term of the adsorption and desorption are separated with considering the available adsorption surface of the channel. However, it is normally difficult to satisfy results from a laboratory experiment with Langmuir adsorption due to the nature of the linear relationship in this approach.

Freundlich adsorption isotherm mechanism offers robustness more than the Langmuir adsorption isotherm mechanism to match results from the

laboratory experiment. However, the original Freundlich equation (Refer to Equation 3.38) is an empirical equation with limited ability to interpret the coefficient. In order to gain access for clear understanding of the adsorption and desorption process, the Freundlich adsorption isotherm method utilised the fractal reaction kinetics derived by Skopp [170] is used, where the term of adsorption and desorption are expressed separately similar with the Langmuir adsorption isotherm. The concentration profile in the simulation is plotted against the simulation duration and the injection volume. The injection volume is measured in the number of pore volume that follows Equation 3.39. There are four variables in this equation, i.e.  $k_{ads}$ ,  $n_{ads}$ ,  $k_{des}$ ,  $n_{des}$ , hence it will be more possible to match the results from the laboratory experiment. For detail of both methods refer to Chapter 3 and the simulation results for each method are discussed in Chapter 4.5.

#### 4.4 Mesh sensitivity Study

It is important to assess the mesh density needed to achieve grid independent result for the simulation. Therefore, a simple study was carried out by conducting simulation in various mesh settings.

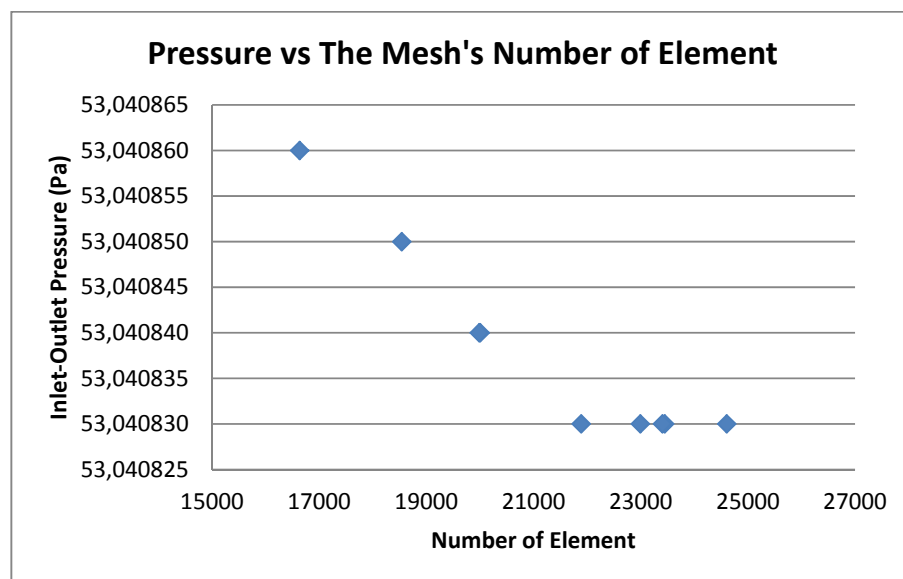


**Figure 4.5:** Results for the mesh sensitivity study

Number of element indicates the size of each mesh element and the density of the mesh. Since the domain of the microchannel is constant, high magnitude of mesh element means the mesh contains high density of small-size mesh elements. Inversely, low mesh element magnitude means the mesh contains low density of large-size mesh elements. Low number of

element offers quick simulation time but is low in accuracy. High number of element provides higher accuracy than the former, but the simulation time may take significantly long. The number of element in the mesh must not be too low to maintain the accuracy. However, it also must not be too high since the simulation becomes inefficient. Therefore, the number of element used in the mesh setting should be optimised.

A simple simulation for seven different mesh configurations was run under a constant injection velocity ( $v_0 = 8.08 \times 10^{-5}$  m/s) for a microchannel with diameter of  $20 \mu\text{m}$  and length  $200 \mu\text{m}$ . Since the simulation is run under a similar steady state velocity, maximum velocity contrast or magnitude of Reynold's number cannot be used for investigating the mesh size; therefore pressure difference between inlet and outlet of the microchannel is used for comparison. The small magnitude of the pressure difference presents due to the magnitude of the microchannel, however the results are still comparable.

The results for the mesh element investigation are shown in **Figure 4.5**, which is showing a plot between the inlet-outlet pressure differences for the model against the number of element of the mesh. It appears the simulation result is insensitive to the mesh for mesh's number of element is larger than 22000. Hence, number of mesh element 22000 is used then in the subsequence simulation in the study.

## 4.5 Comparison with Experiments

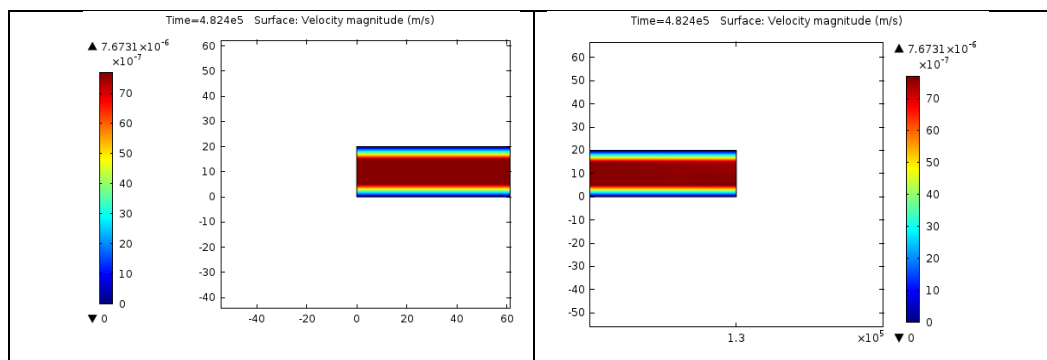


**Figure 4.6:** The typical profile of the velocity magnitude at the inlet (left) and at the outlet (right)

The simulation is conducted by injecting a certain concentration of particles through the left boundary of the microchannel. The injection happens under a steady state creeping velocity and constant pressure difference. The profile of the creeping flow velocity along the vertical axis follows a parabolic trend. The typical trend of the velocity magnitude at the

inlet and outlet are shown in **Figure 4.6 (left)** and **Figure 4.6. (right)** respectively. The highest velocity is at the middle of the microchannel and the lowest on each of the walls. Low velocity that occurs at the distant close to the microchannel walls allows the adsorption and desorption process to happen effectively in the area.

**Figure 4.7** shows the pressure profile at the inlet and the outlet of the microchannel. The pressure difference between the inlet and outlet boundaries observed is 26.6 Pa where the pressure alters gradually from the inlet boundary towards the outlet.

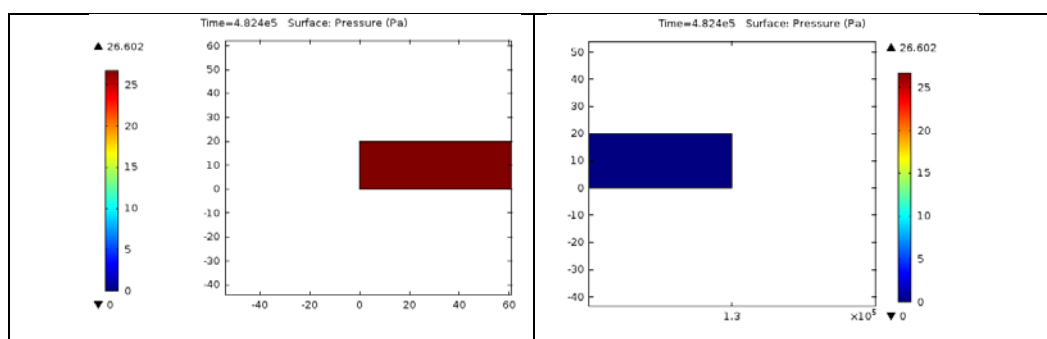


**Figure 4.7:** The typical profile of the pressure magnitude at the inlet (left) and at the outlet (right)

The rate of the injection and the initial early post flush stage are not clearly described in the original article. Therefore, the value of both is assumed to be similar to the first of the five injection rates in the post flush stage, i.e. 30 ml/hr. The complete multi injection rates used in the post flush stage is shown in **Figure 4.8**.

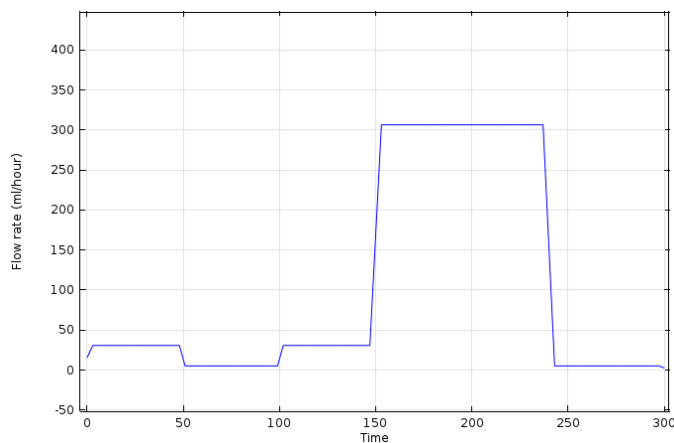


**Figure 4.8:** Flow rates at the post flush stage

### 4.5.1 Obtaining the Adsorption Parameters

In this study, both Langmuir and Freundlich adsorption isotherm mechanism are investigated to select the most suitable correlation to reproduce result from the laboratory experiment. The process of obtaining the adsorption parameters in the Langmuir adsorption isotherm and the Freundlich adsorption isotherm is discussed in this section. There are two experiment results to match for obtaining the adsorption isotherm parameters, i.e. (1) the trend of the effluent concentration for the injection and the early post flush stage and (2) the multirate post flush concentration injection. The parameters needs to be configured are the  $k_{ads}$  and  $k_{des}$  in the Equation 3.34 for Langmuir adsorption isotherm and  $k_{ads}$ ,  $k_{des}$ ,  $n_{ads}$  and  $n_{des}$  in the Equation 3.39 for Freundlich adsorption isotherm. Instead of using regression method, these parameters are obtained by trial and error method. This method allows investigation for the effect of the adsorption parameter to the concentration profile from the laboratory experiment, although this method seems more impractical than using a standard regression method, e.g. least square method.

Two geometry settings, i.e. 2D and 3D axisymmetric geometries are to be used for modelling. The model that is utilising these two geometry approaches can be scaled up accordingly to institute a more complex pore-network model to simulate the core behaviour (Refer to Chapter 3 for detail explanations). Effluent and adsorbate concentration on the corresponding boundaries are compared. Concentration profiles in the simulation are obtained by averaging the magnitudes along the boundaries during the simulation time or injection volume.

#### 4.5.1.1 2D Geometry - Langmuir Adsorption Isotherm

Many combinations of  $k_{ads}$  and  $k_{des}$  are examined in order to obtain suitable equations whose results fit the laboratory experiment. It is straightforward to match the trend for the effluent concentration for the injection and the early post flush stage. This happens because the advection dominantly contributes the process of the adsorption of the nanoparticles concentration on the microchannel wall during this stage. The typical comparison for the effluent concentration between the experimental result and the simulation is shown in **Figure 4.9**.

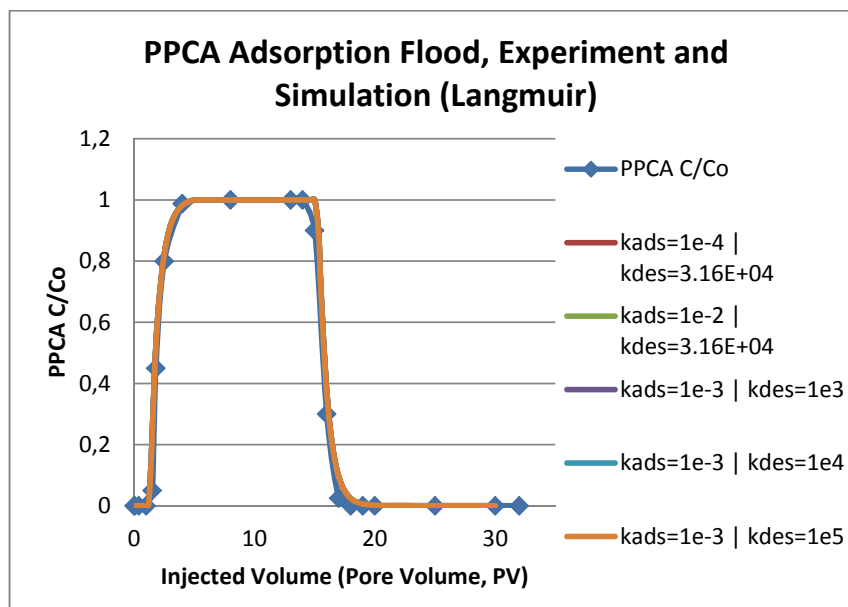


**Figure 4.9:** PPCA Average Effluent Concentration for the Injection and Early Post flush Stage: Experiment and Simulation (Langmuir)

However, it is another challenge to match the effluent concentration profile for the post flush stage due to inclusion of the various injection rates. After many trials, it is found that the Langmuir adsorption isotherm approach is not able to model the experiment fully with an acceptable degree of satisfaction. It happens due to the linear nature of this method that cannot reproduce the result from the laboratory experiment after numerous of regression processes. The comparison of the effluent concentration profile obtained from the simulation and the laboratory experiment is shown in **Figure 4.10**. (Note: only the profiles that is close enough to the match the experiment result is shown).

Although a well match is difficult to obtain, the Langmuir approach can still model the effect of different flow rates on the desorption mechanism. The effect of the low flow rates (in this case is 5 ml/hours) is less sensitive than the actual result from the experiment. One of the concentration profiles that represent this finding is displayed in **Figure 4.10**. The values of the  $k_{ads}$  and  $k_{des}$  for the trend in the figure are  $1 \times 10^{-3}$  m/s and  $3.16 \times 10^4$  mol/ (m<sup>2</sup>.s) respectively.

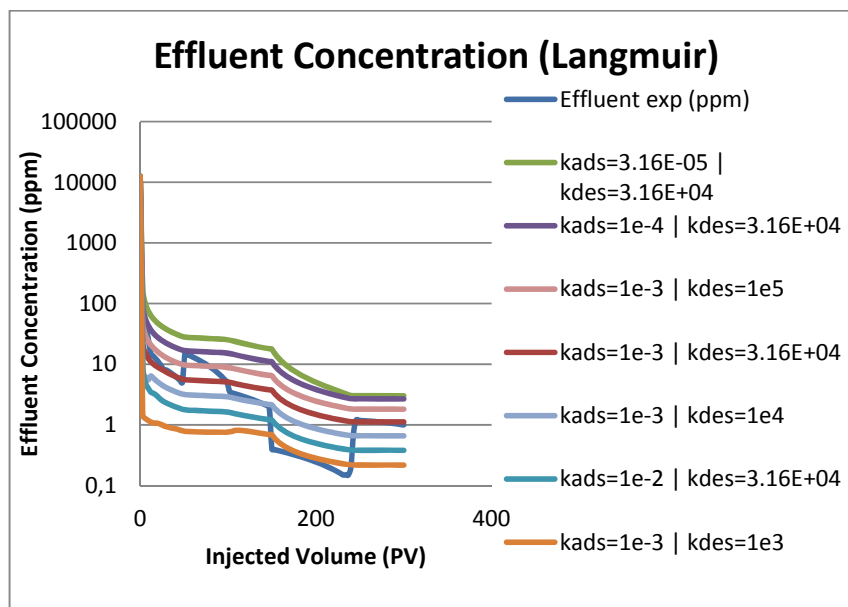


**Figure 4.10:** Post flush average effluent concentration vs pore volume (Langmuir Adsorption Isotherm)

#### 4.5.1.2 2D Geometry - Freundlich Adsorption Isotherm

The second adsorption equation to validate is the fractal Freundlich adsorption isotherm. It is discovered that this approach is suitable for modelling the experiment more than the Langmuir method. This discovery has a good agreement with Zhang's suggestion where Freundlich adsorption isotherm was used as the basis for the modelling for their experiment [221]. The utilisation of this approach does not consider the alteration of adsorption surface availability on the wall. Freundlich adsorption isotherm considers the adsorption and desorption mechanism as a function of concentration difference between the fluid bulk and the adsorption surface.

However, instead of using the conservative Freundlich adsorption isotherm approach, the Freundlich adsorption isotherm equation that derived by Skopp [170] is utilised where the forward and reverse adsorption are addressed separately [170] (Refer to Chapter 3 for the detail explanation.) There are four independent parameters that need to be included in this approach, i.e.  $k_{ads}$ ,  $n_{ads}$ ,  $k_{des}$ , and  $n_{des}$ . It is challenging and not simple to match a rate-dependent effluent concentration profile obtained from a laboratory experiment with an equation that considers four independent variables. Each of the variables should be adjusted from one and another to obtain a best-fit effluent concentration profile obtained from the experiment.

A study is conducted to investigate the effect of each parameter for the effluent concentration profile. Various set of  $k_{ads}$ ,  $n_{ads}$ ,  $k_{des}$ , and  $n_{des}$  combinations are simulated to establish an effluent concentration profile that is matched with the result from the experiment. The initial parameters used for the study are  $k_{ads} = 1 \times 10^{-2}$ ,  $n_{ads} = 0.5$ ,  $k_{des} = 1 \times 10^3$  and  $n_{des} = 0.5$ . Each value of the variables is updated and the simulation result is compared by the effluent concentration profile for the multirate post flush injection obtained from the experiment, which is called the base case. The results are numerous, however only a few representative trends are shown in this chapter.

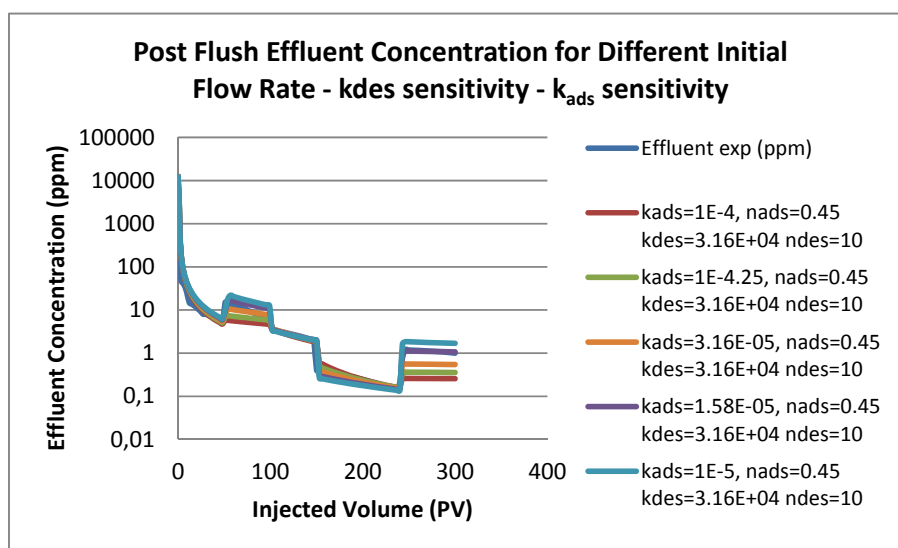


**Figure 4.11:** Preliminary study for the  $k_{ads}$  sensitivity - Average Post Flush Effluent Concentration (Freundlich Adsorption Isotherm)

At first, the effect of  $k_{ads}$  to the concentration profile is investigated. It appears that excessive  $k_{ads}$  significantly shifts and flatten the trend down. This means the  $k_{ads}$  value significantly influences the adsorption and reduces the desorption. Some of the trends obtained from the preliminary study are shown in **Figure 4.11**, which are for  $k_{ads}$  between  $10^{-5}$  and  $10^{-4}$  with predefined constant values of  $n_{ads} = 0.45$ ,  $k_{des} = 3.16 \times 10^4$ , and  $n_{des} = 10$ .

The second sensitivity study is to investigate the effect of the  $n_{ads}$  to the effluent concentration profile. It is discovered that this parameter should be low enough to maintain the shape of the concentration profile

proportional to the base case. It also found that the effect of  $n_{ads}$  differs more dominant for low injection rate. **Figure 4.12** shows the trend for the  $n_{ads}$  sensitivity that range sets between 0.3 and 0.5 with constants  $k_{ads} = 3.16 \times 10^{-5}$ ,  $k_{des} = 3.16 \times 10^4$ , and  $n_{des} = 5$ . High magnitude of  $n_{ads}$  flattens the concentration profile and decreases the magnitude of the effluent concentration.

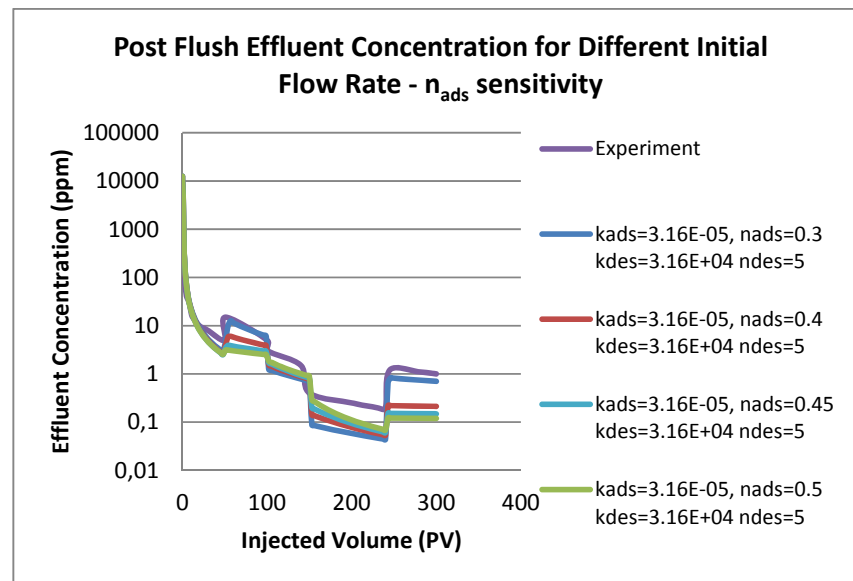


**Figure 4.12:** Preliminary study for the  $n_{ads}$  sensitivity - Average Post Flush Effluent Concentration (Freundlich Adsorption Isotherm)

Subsequently the effect of the  $k_{des}$  for the effluent concentration is investigated. It is discovered that the magnitude of the  $k_{des}$  balances the effect from  $k_{ads}$ . The effect of the  $k_{des}$  is somehow appears to be insignificant in this case, which is caused by the magnitude of the rest of the other Freundlich parameters. Some of the trends obtained from the preliminary study of the  $k_{des}$  between  $1 \times 10^4$  and  $1 \times 10^5$  is shown in **Figure 4.13** with predefined constant values of  $k_{ads} = 3.16 \times 10^{-5}$ ,  $n_{ads} = 0.45$ , and  $n_{des} = 10$ .

Finally, the preliminary study for the  $n_{des}$  is conducted. The magnitude of  $n_{des}$  gives influence to the magnitude of the effluent concentration. Low  $n_{des}$  decreases the effluent profile, which means less desorption. Inversely, high  $n_{des}$  increases the effluent profile, which means more desorption. Some of the trends obtained from the study are shown in **Figure 4.14** which  $n_{des}$  values are ranged between 5 and 15.

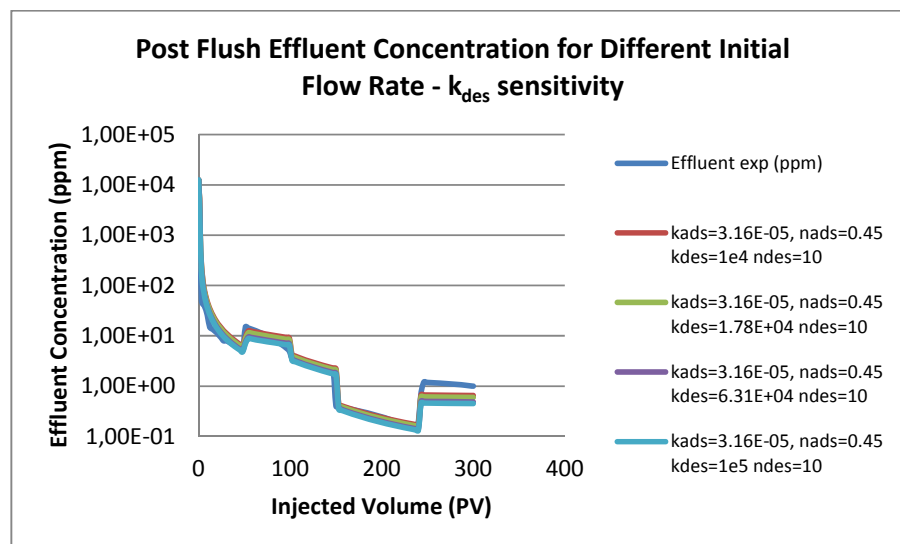


**Figure 4.13:** Preliminary study for the  $k_{des}$  sensitivity (Freundlich Adsorption Isotherm)

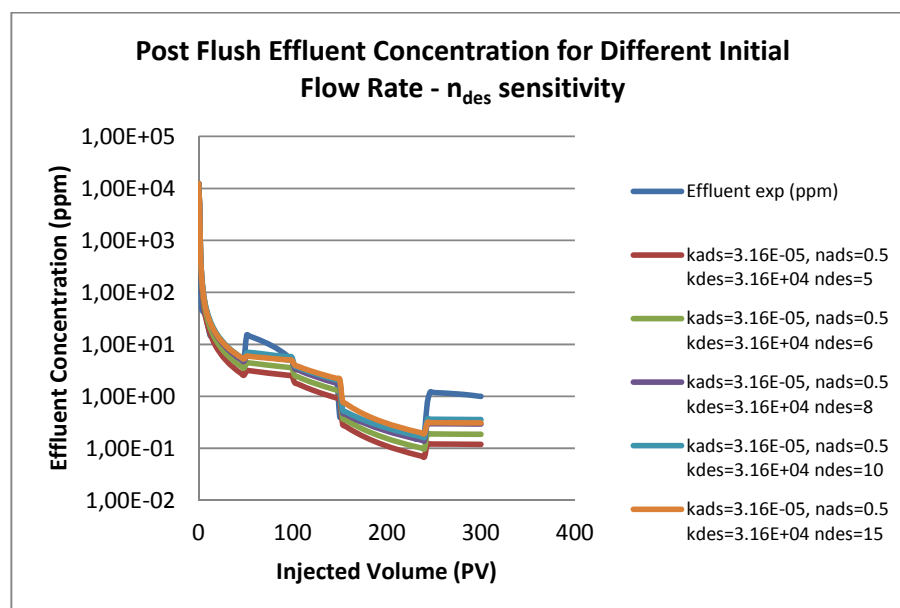


**Figure 4.14:** Preliminary study for the  $n_{des}$  sensitivity (Freundlich Adsorption Isotherm)

As it was discussed in chapter 3, some previous studies of the Freundlich adsorption isotherm equation found that the magnitude of the exponent should be between 0 and 1 [148], however there are also some discoveries that this parameter can exceed 1 [170, 219]. In this study, the consideration for the  $n_{des}$  follows that which may exceed the value of one. This is assumed valid recalling the objective of using the obtained equation

from the simulation is merely meant to be fitted with the experiment result. Moreover, there are many simplifications and assumptions utilised in the modelling compared to the real laboratory condition.

$k_{ads}$	$n_{ads}$	$k_{des}$	$n_{des}$	$R^2$
3.16E-05	0.5	3.16E+04	5	0.654265414
3.16E-05	0.5	3.16E+04	6	0.674565681
1.00E-04	0.45	3.16E+04	10	0.697871096
3.16E-05	0.5	3.16E+04	8	0.70112182
3.16E-05	0.5	3.16E+04	15	0.702596154
3.16E-05	0.5	3.16E+04	10	0.712681735
1.00E-05	0.45	3.16E+04	5	0.719696051
5.62E-05	0.45	3.16E+04	10	0.722595919
3.16E-05	0.45	1.00E+05	10	0.747840935
3.16E-05	0.45	6.31E+04	10	0.748801493
3.16E-05	0.45	3.16E+04	10	0.750713183
3.16E-05	0.45	1.78E+04	10	0.753924899
3.16E-05	0.45	1.00E+04	10	0.756082289
1.00E-05	0.45	3.16E+04	8	0.790336977
1.00E-05	0.45	3.16E+04	10	0.808668597
1.58E-05	0.45	3.16E+04	10	0.999826136

**Table 4.2:** Freundlich Adsorption Isotherm Investigation (2D geometry)

Further study of finding the combination of the four parameters is conducted to obtain the best-fit equation to model the lab experiment. The  $R^2$  of each equation is investigated and some of the results for this study are shown in **Table 4.2**. The detail figures of the results are found in the appendix. The parameter set with highest  $R^2$  ( $=0.99982$ ) is selected. For this selection,  $k_{ads} = 1.58 \times 10^{-5}$  [m/s],  $n_{ads} = 0.45$ ,  $k_{des} = 3.16 \times 10^4$  [mol/ (m<sup>2</sup>.s)], and  $n_{des} = 10$ .

**Figure 4.15** shows the comparison between the experiment result and the modelling where both appear to be in fairly good agreement. The trend of the effluent concentration decreases rapidly from the initial concentration at 12500 ppm. It follows the release of the concentration due to the 30 ml/h flow rate in the initial post flush duration. The effluent concentration increases slightly when the flow rate reduces to 5 ml/hr between the injection volume of 50 and 100 pore-volumes. Then the trend

falls from injection volume 100 to 150 pore volume due to the increase of the flow rate to 30 ml/hr. Afterwards, the concentration decreases more as the flow rate increase to 300 ml/h and finally rises again as the flow rate returns to 5 ml/ hr.

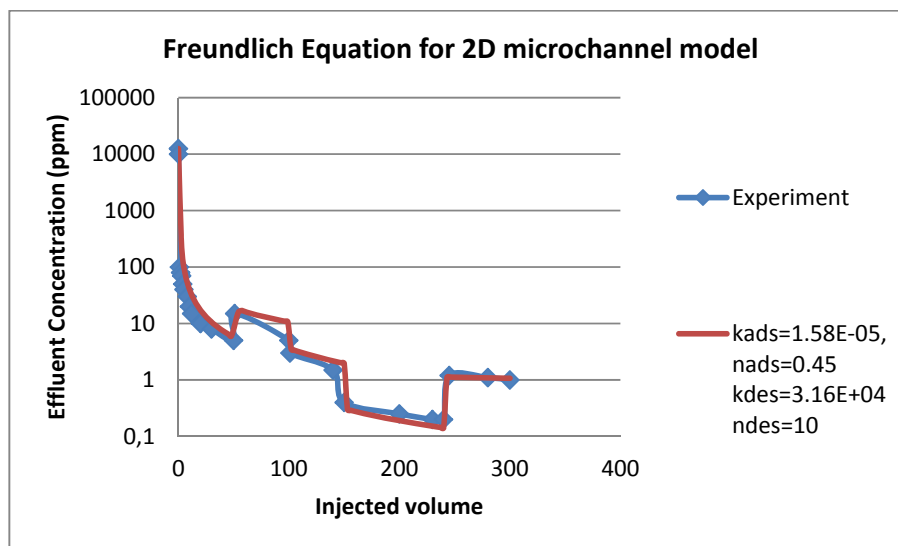


**Figure 4.15:** The Comparison of the Post Flush Effluent concentration for the experiment (blue line) and the 2D geometry (green line) - Freundlich Adsorption Isotherm

It is discovered that the post flush injection rate has a negative correlation with the effluent concentration. It is seen in **Figure 4.15** that low injection rate brings high effluent concentration. Inversely, high injection rate brings low effluent concentration. Since effluent concentration is proportional to the desorption, the post flush rate (advection) has a negative relation with the desorption rate. This shows that advection give more significant effect to adsorption than to desorption. Some errors between the simulation results and the experiment presents due to the limitation to gain access for the original experiment result. Simplification in the model also might give contribution to the difference. To improve the simulation, it is possible to establish a more complicated model that reproduce domain and condition that present in the laboratory experiment, however it needs more powerful computer source to construct and run. Complicated model is not necessarily required in this thesis since investigation for concentration profile, adsorption, and desorption in various longitudinal and surface geometry configuration.

### 4.5.1.3 3D Axis-symmetric Geometry - Freundlich Adsorption Isotherm

It is important to investigate the corresponding Freundlich adsorption isotherm equation for the 3D axis-symmetrical geometry because this geometry provides a more representative approximation to the geometry of an actual pore channel.

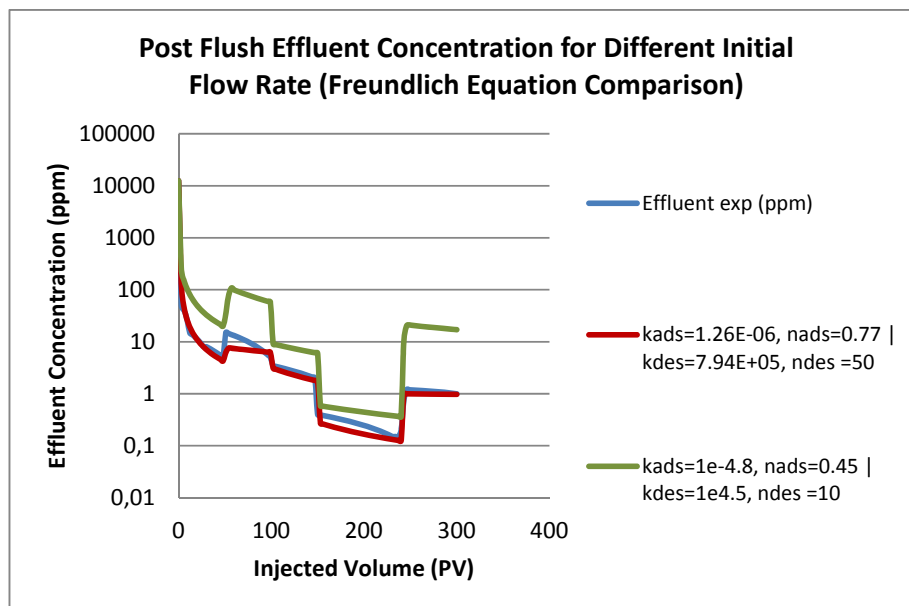


**Figure 4.16:** Comparison of the Post Flush Effluent concentration from the experiment (blue), 2D geometry simulation (green) and 3D axis-symmetric simulation (red) - Freundlich Adsorption Isotherm

At first, the Freundlich equation obtained from the 2D geometry is validated to reproduce the effluent concentration for the 3D axis-symmetrical geometry. However, the result of the simulation for 2D geometry is unmatched with the simulation with the 3D geometry where the profile is far below the one attained from the laboratory experiment. The comparison is shown in , where the result from the 2D geometry equation is the green-coloured line and lab experiment is the blue-coloured line. It is concluded that the equation obtained from the 2D geometry is no longer valid to use for the 3D axis symmetrical geometry. It is sensible since the adsorption surface areas for both geometry settings are different although the length and the diameter of both geometries remain the same. The adsorption surface area in the 2D geometry is the area of a double flat plane with a dimension of 1m

x 200  $\mu\text{m}$ . On the other hand, the adsorption surface area in the 3D axis-symmetric geometry follows the surface area of a cylindrical microchannel. This difference contributes a significant influence to the Freundlich parameters obtained.

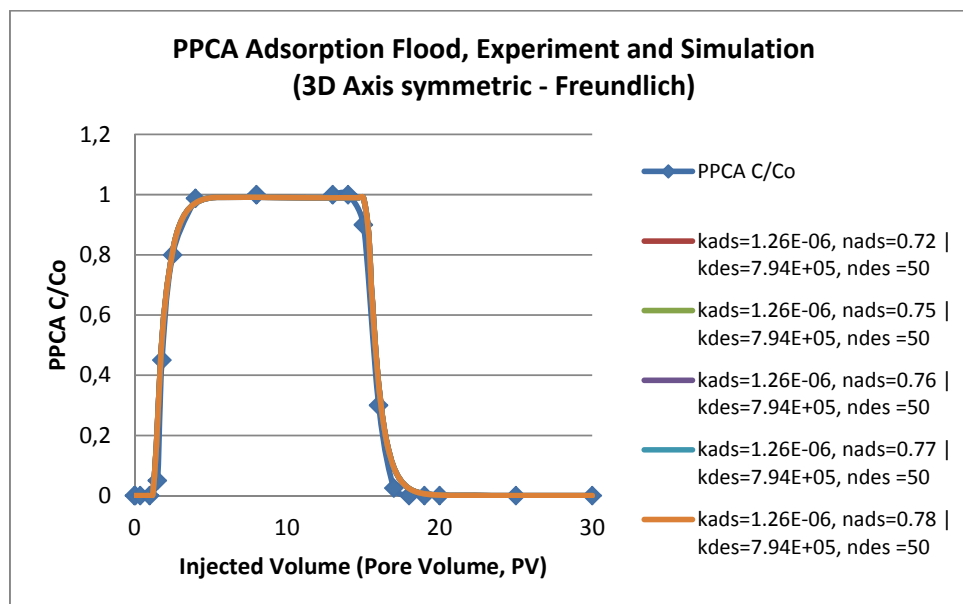


**Figure 4.17:** PPCA Effluent Concentration for the Injection and Early Post flush Stage: Experiment and Simulation (Freundlich)

Hence, another set of sensitivity study is conducted to find new Freundlich parameters that satisfy the 3D axis-symmetrical geometry configuration. First, the effluent concentration for the injection and early post flush stage is compared. Different parameter combinations are used and the results are compared. It is discovered that the concentration profile for injection and early post-flush stage for the various parameter combinations are in one alignment. This discovery is shown in **Figure 4.16**. In this case, the advection provides a dominant influence to the adsorption and desorption process, reducing the sensitivity effect of the equations used in modelling the system. Second, the effluent concentration for the post flush stage from the simulation is compared with the results obtained from the lab experiment. Many profiles were generated which the detail is displayed in the Appendix. The equation selection is based on the magnitude of the  $R^2$ . The highest  $R^2$  attained is for the parameter combination  $k_{ads} = 1.29 \times 10^{-6}$  m/s,  $n_{ads} = 0.77$ ,  $k_{des} = 7.94 \times 10^5$  mol/ (m<sup>2</sup>.s), and  $n_{des} = 50$ . The profile is

shown by the red colour in **Figure 4.16** and blue colour in the **Figure 4.17**. Both profiles have a good agreement with the results obtained from the laboratory experiment

## **4.6 The effect of velocity on the particle distribution in microchannel**

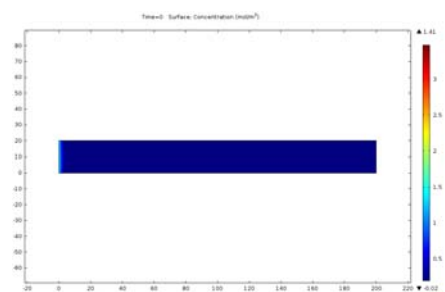
The effect of velocity on the particle distribution in microchannel is discussed in this section. Both correlations obtained for the 2D and the 3D axis-symmetrical geometries are utilised. In this case, the investigation is conducted for the injection-phase before the shut-in period process in the scale squeeze treatment. The effect of the advection and diffusion to the concentration distribution is considered in the study.

For sensitivity study, the effect of six various injection velocities on the nanoparticle concentration distribution is investigated and compared. It is assumed that there is no slip between the nanoparticles and the carrier fluid. The nanoparticles are treated as a concentration field that travel together with the carrier fluid. This assumption is valid since the nanoparticle is relatively small compare to the magnitude of the microchannel system. The nanoparticles are assumed free particles which physical movement is governed only by physical properties, e.g. velocity, pressure, simulation time, and injection volume.

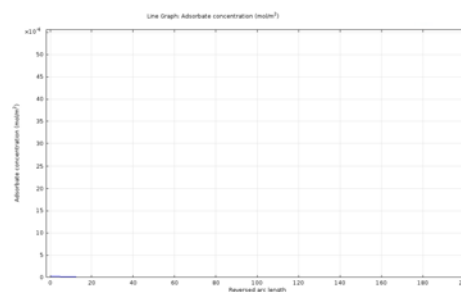
The discussion is divided into two cases, which are for continuous and discontinuous nanoparticles concentration injection. The trend of the effluent and the adsorbed concentration for each case, for different time and injection volume are discussed, whose magnitude is taken from the average values along the corresponding boundaries.

### **4.6.1 Continuous nanoparticle injection**

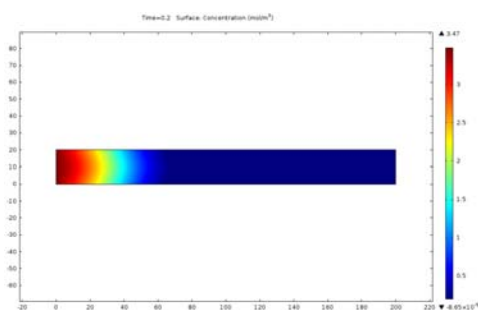
At the beginning the microchannel domain is unoccupied by the nanoparticles concentration. From the start of the simulation, 12000-ppm nanoparticle concentration is continuously injected from the inlet to the outlet of the microchannel under a steady creeping flow velocity. For the base case, average injection velocity ( $v_o$ ) for the injection is obtained from Equation **3.18**. Using the input data from Zhang's experiment [221], injection rate ( $Q$ ) = 30 ml/hr, injection volume ( $pv$ ) = 13,4 ml, and core length ( $L_{core}$ ) = 13 cm, hence the average injection velocity ( $v_o$ ) obtained is  $8.08 \times 10^{-5}$  m/s. This velocity is used for the base case for all simulation in the study.



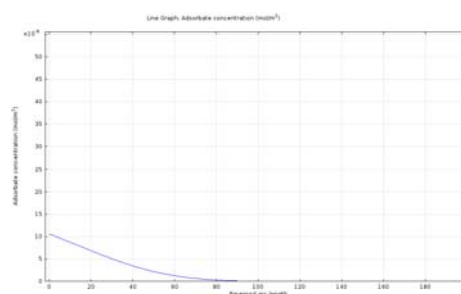
A1. Bulk Concentration profile at 0 s



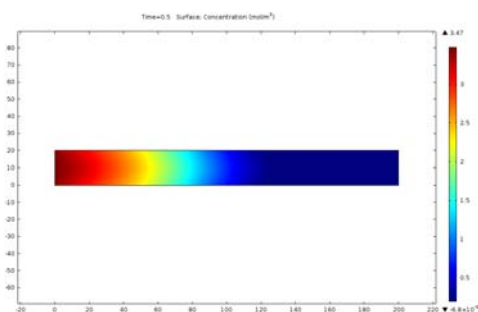
A2. Adsorbate Concentration profile at 0 s



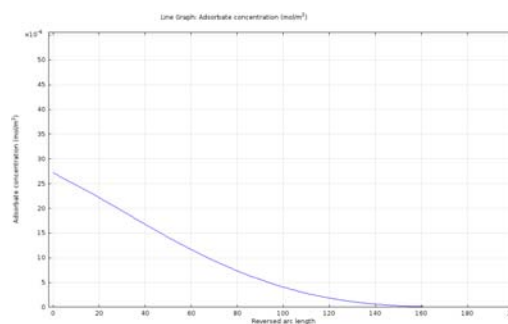
B1. Bulk Concentration profile at 0.2 s



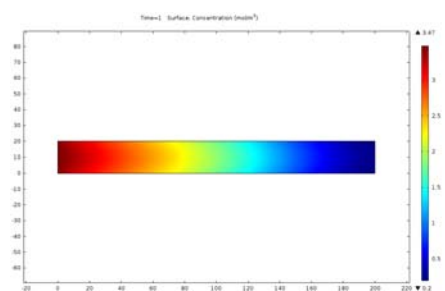
B2. Adsorbate Concentration profile at 0.2 s



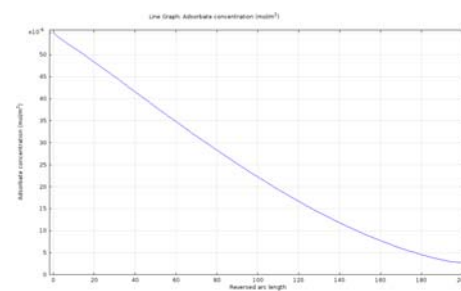
C1. Bulk Concentration profile at 0.5 s



C2. Adsorbate Concentration profile at 0.5 s



D1. Bulk Concentration profile at 1 s



D2. Adsorbate Concentration profile at 1 s

**Figure 4.18:** Bulk and adsorbate concentration for 0, 0.2, 0.5, and 1 second from 10 seconds simulation time length for a continuous injection with diffusion in various times for injection velocity  $v=2v_0$  and  $v_0=8.08 \times 10^{-5}$  m/s (base case)

Although the property of the flow is taken from 13 cm core length, the simulation only considers 200- $\mu\text{m}$  microchannel length as the domain for investigation. This number is taken arbitrarily as 10 times the magnitude of the microchannel diameter to gain adequate geometry for the simulation and to satisfy the computer resource available.

Without slip, the velocity of the injected nanoparticle concentration is similar with the velocity of the carrier fluid. In the study, the dimension of each nanoparticle diameter is relatively small ( $d_p = 80 \text{ nm}$ ) compare to the dimension of the microchannel diameter ( $d_{\text{channel}} = 20 \mu\text{m}$ ). The diameter of the nanoparticles is also homogenous and no agglomeration happens. Therefore, the adsorption of the nanoparticle concentration that occurs on the microchannel wall is assumed not to alter the diameter of the microchannel, even for the case of a multilayer adsorption. Particles will always be able to be adsorbed, as long the concentration of the particles in the fluid bulk is higher than on the wall. Inversely, the desorption happens if the nanoparticles concentration in the bulk is lower than the adsorbate concentration on the microchannel wall.

In this scenario, there is an unlimited supply of nanoparticle concentration from the inlet of the microchannel. This makes the particle concentration in the bulk to be always higher than the concentration on the microchannel wall. This condition allows the adsorption in the system happens all the time.

**Figure 4.18 (left)** shows the profile of the bulk concentration and **Figure 4.18 (right)** shown the adsorbate concentration for the corresponding time, which are 0, 0.2, 0.5, and 1 second from 10 seconds simulation time. Injection velocity utilised is  $v=2v_0$ , which  $v_0$  is  $8.08 \times 10^{-5} \text{ m/s}$  (base case). Initially, there is no concentration in the bulk and on the microchannel wall. This is shown in the **Figure 4.18 (A1)** and **Figure 4.18 (A2)**. At 0.2 seconds simulation time, the front of the concentration reaches one-fourth length of the microchannel. This is shown in the **Figure 4.18 (B1)** and **Figure 4.18 (B2)** where the adsorbate has built up until the corresponding length. Adsorption is observed further than the front of the concentration bulk due to the diffusion effect in the system. At 0.4 seconds, the front of the concentration bulk reaches the mid-length of the microchannel, shown in **Figure 4.18 (C1)**. At this time step, the adsorbate concentration accumulation has advanced towards the outlet boundary, shown in **Figure 4.18 (C2)**. At 1 second of simulation time, the front of the

concentration bulk propagates further, shown in **Figure 4.18 (D1)**. The adsorbate reaches the region near the outlet boundary, which is shown in **Figure 4.18 (D2)**.

#### 4.6.1.1 Continuous injection without diffusion

In this model, diffusion contributes a significant influence to the propagation of the nanoparticles concentration. To evaluate the hypothesis, the simulation for a continuous injection without diffusion is conducted. The profile of the average effluent concentration against the simulation time for different velocity profile is shown in **Figure 4.19**. The effluent concentration is measured at the outlet boundary where the breakthrough is indicated by the increase of the effluent concentration from zero magnitude.

The corresponding breakthrough time for the concentration with velocity  $0.1v_0$  is not available since the concentration profile is still far to reach the outlet boundary during the time of investigation. As the velocity gets higher, the time needed for the fluid to reach the boundary is decreased. This has a direct correlation with the assumption of no slip velocity consideration in the modelling. The breakthrough time for injection velocity,  $v=0.5v_0$  is 3.8 seconds,  $v=v_0$  is 1.8 seconds,  $v=1.5v_0$  is one second, and for  $v=2v_0$  is 0.8 seconds; where  $v_0$  is the base velocity  $8.08 \times 10^{-5}$  m/s.

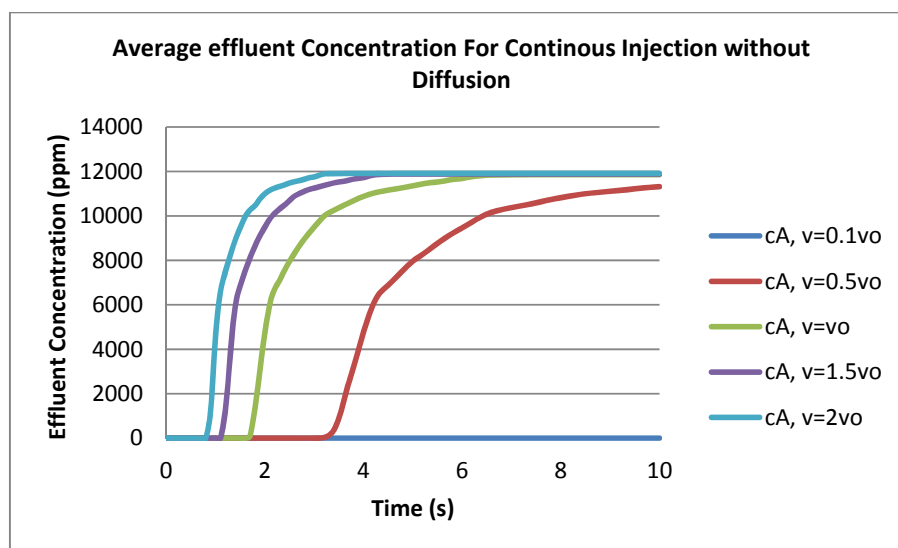


**Figure 4.19:** Average effluent concentration for various inlet velocity in continuous flow without diffusion against the simulation time interval,  $v_0=8.08 \times 10^{-5}$  m/s

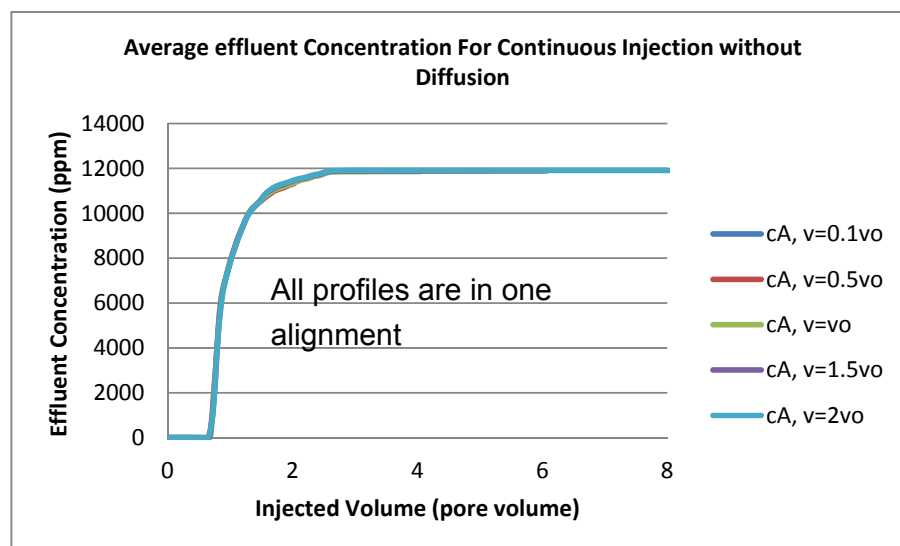


**Figure 4.20:** Average effluent concentration for various inlet velocity in continuous flow without diffusion against the injected volume,  $v_0=8.08 \times 10^{-5}$  m/s

The injection volume in the study is measured by the number of the pore-volume. The profile of the theoretical average effluent concentration against the injection volume for various continuous injection velocities without diffusion is shown in **Figure 4.20**. Without diffusion, each velocity case employs one pore volume to get the concentration breakthrough. This is shown in **Figure 4.20** where all the effluent concentrations profiles are situated in one alignment.

The profile of the average adsorbate concentration for various simulation time steps is shown in **Figure 4.21**. Since the surface area of the microchannel for all cases are similar, the adsorbate concentration corresponds linearly with the adsorbate mass. It is observed from **Figure 4.21** that the adsorption starts instantly from the beginning of the simulation. The rate of adsorption is indicated by the gradient of the profile, which magnitude is proportional with the injection velocity. It is also observed that there is a slight increase on the adsorbate concentration gradient as the simulation time increase, especially for the system with high velocity. An injection of a similar nanoparticles concentration with higher velocity causes higher particle flux that increases the effluent concentration at the outlet. Since there is no slip between the concentration and the carrier fluid assumed in the system, higher velocity brings higher amount of particles in a

given time. If there is more nanoparticles presence in the bulk, it will increase the chance of the nanoparticles to be adsorbed on the microchannel wall. Therefore, in a given injection time, higher injection velocity results in higher adsorption. Inversely, lower injection velocity results in lower adsorption. This observation is shown in **Figure 4.21**, which is displaying that the advection contributes a significant effect of the adsorption.

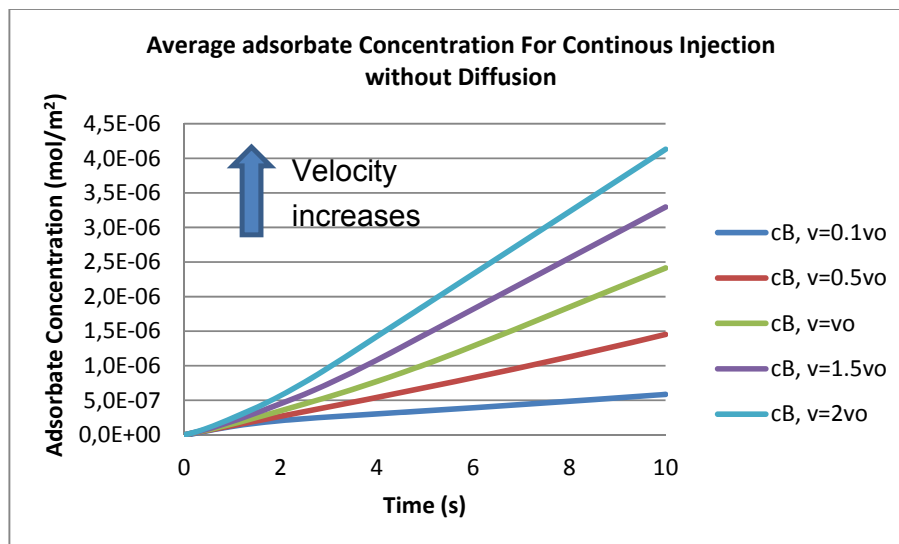


**Figure 4.21:** Average adsorbate concentration for various inlet velocity in a continuous flow without diffusion against the simulation time interval,  $v_0=8.08 \times 10^{-5}$  m/s

The comparison using the injection time is not really a fair comparison since the injected volume is not similar for each injection velocity. Since there is no slip assumed in the simulation, the injected volume propagation is governed by the injection velocity. The injection volume is measured in pore volume that follows the Equation 3.42. Low velocity needs higher time to inject a specific injection volume into the microchannel than with high velocity. The comparison of the adsorbate concentration for different injection volume is shown in **Figure 4.22**. It is observed that the magnitude of the adsorbed concentration varies inversely to the injection volume.

The comparison of the cumulative adsorbate mass for continuous nanoparticle injection for all injection velocity for 8 pore-volume injection is shown in **Figure 4.23**. It is shown that under a similar injection volume, more adsorption happens for a lower injection velocity than at a higher velocity.

This happens because, in a system with lower velocity, nanoparticles have more exposure time to the adjacent adsorption wall than in an environment with higher velocity. This allows more adsorption for the unlimited nanoparticles injection from the inlet boundary of the microchannel.

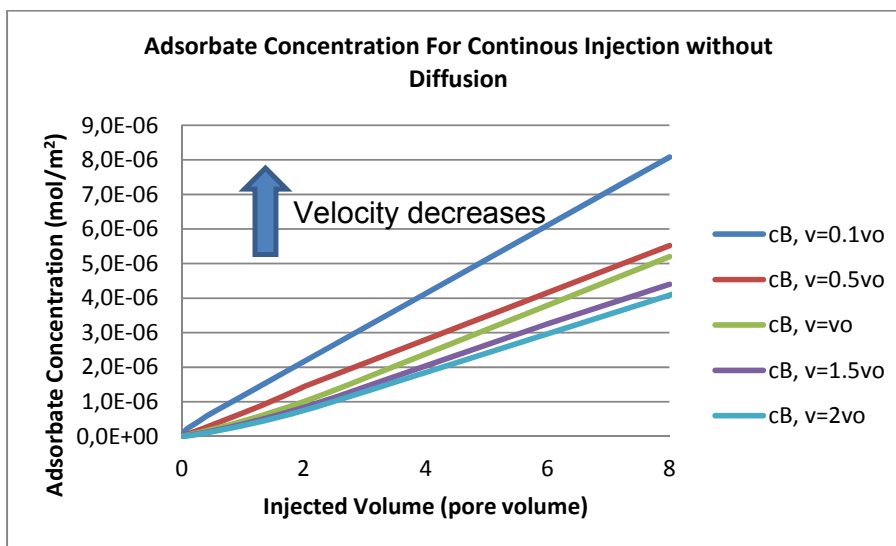


**Figure 4.22:** Average adsorbate concentration for various inlet velocity during an injection period in a continuous flow w/o diffusion against the injected volume,  $v_0=8.08 \times 10^{-5}$  m/s

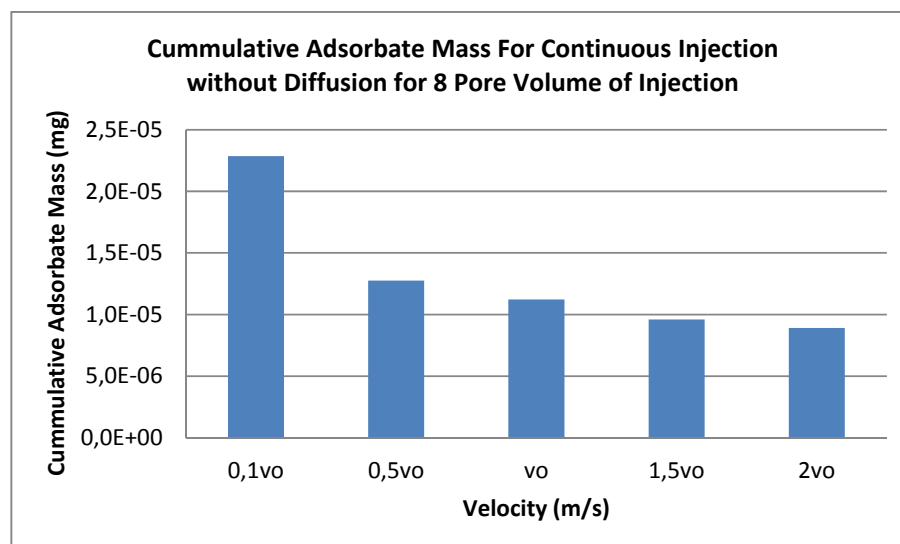


**Figure 4.23:** Cummulative adsorbate Mass for various inlet velocity during an injection period in a continuous flow w/o diffusion for 8 pore volume of injection,  $v_0=8.08 \times 10^{-5}$  m/s

#### 4.6.1.2 Continuous injection with diffusion

Simulation of nanoparticles injection is also conducted for a system with diffusion considered. **Figure 4.24** shows the trend of the effluent concentration for various velocities with diffusion against the injected volume. The injection volume in pore volume indicates the amount of injected fluid that measured by the volume of the microchannel system. 12500 ppm of nanoparticles is injected along with the fluid bulk continuously until eight times of the microchannel's volume. Generally, the concentration of the particle increases until it reaches a plateau. This plateau indicates the equilibrium condition of the system, where the rate of the adsorption is comparable with the rate of the desorption.

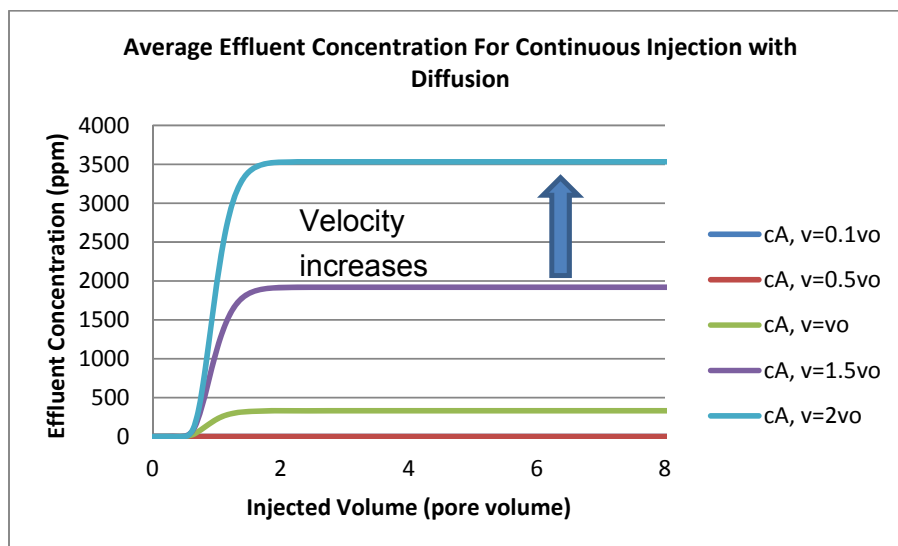


**Figure 4.24:** Average effluent concentration of various inlet velocities for continuous injection with diffusion in various pore volumes,  $v_o=8.08 \times 10^{-5}$  m/s. Effluent concentration profiles for  $(c_A, v=0.1v_o)$  and  $(c_A, v=0.5v_o)$  are on top of each other

It appears that each velocity has its own effluent profile for different pore volume. By common sense, higher velocity transport more volume for a given specific time. Therefore, the number of particles transported in the system is proportional to the injection velocity since the no-slip condition between the carrier fluid and the concentration introduced in the modelling. This phenomenon is shown in **Figure 4.24** where the highest equilibrium effluent concentration is at the highest injection velocity. In the high velocity injection for continuous injection, more particles are transported, more

particles adsorbed, and more particles are brought out the outlet. The equilibrium concentration does not reach similar magnitude because of the multilayer adsorption consider in the Freundlich adsorption isotherm mechanism utilised in the simulation. This means that each injection velocity corresponds to a specific adsorption rate, which relationship is proportional to each other. It also appears that all the equilibrium of the average effluent concentration do not reach the inlet concentration. This means that rate of the fluid flow due to the advection and diffusion is still less significant than the rate of the adsorption. The equilibrium effluent concentration increases proportionally with the magnitude of velocity for a constant diffusivity.

**Figure 4.25** shows the magnitude of the equilibrium effluent concentration for continuous injection with diffusion. The magnitude is taken from the plateau level in **Figure 4.24**. The trend of all the five data points does not follow standard regression line that perfectly satisfies all data. However, data points for  $v= v_0$ ,  $v=1.5v_0$ , and  $v=2v_0$  follows a linear regression that satisfies  $y=4 \times 10^{-7}x - 2873,5$  with  $R^2=1$ . Hence, balancing argument that satisfies all cases is not available, except for the cases higher than certain injection velocity, e.g. above  $v=v_0$  in this study.

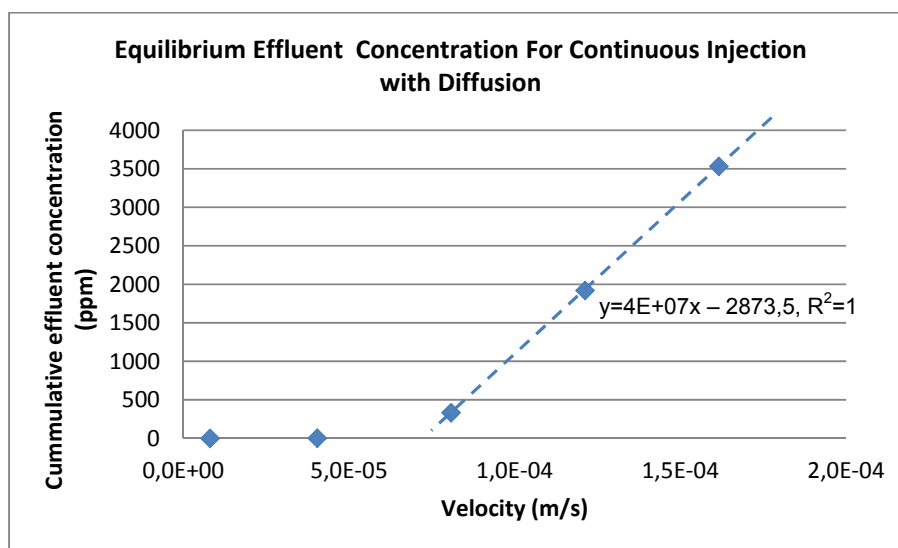


**Figure 4.25:** Equilibrium effluent concentration of various inlet velocities for continuous injection with diffusion in various pore volumes. Data points from left to right respectively are for injection velocity  $v=0,1v_0$ ,  $v=0,5v_0$ ,  $v=v_0$ ,  $v=1,5v_0$ , and  $v=2v_0$ .

The trend of the adsorbate concentration against the injection volume for various injection velocities is shown in **Figure 4.26**. In the simulation, the calculation was conducted based on the injection time. The injection is then later converted to the injection volume by considering the injection velocity and time. Therefore, not all the profile is continuous until 8 pore volume in **Figure 4.26**.

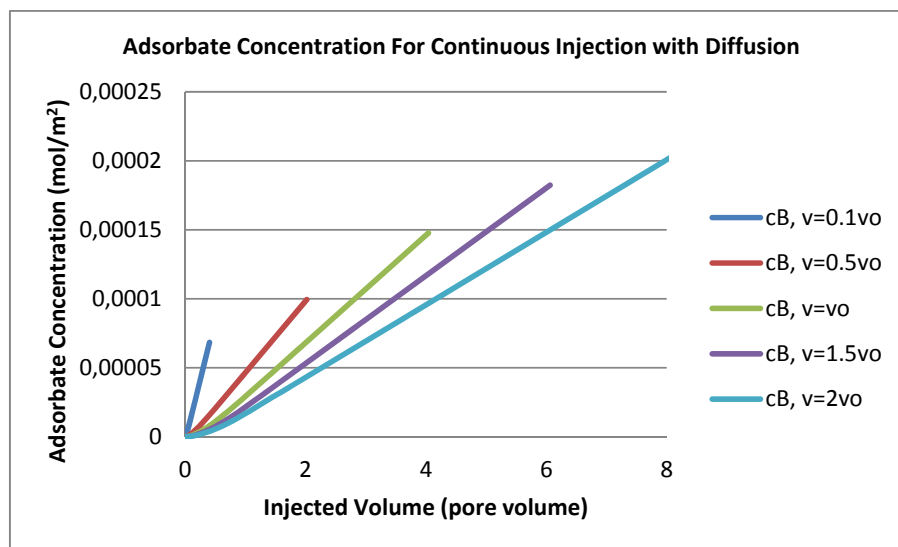


**Figure 4.26:** Average adsorbate concentration of various inlet velocities for continuous injection with diffusion against the injection volume,  $v_0=8.08 \times 10^{-5}$  m/s

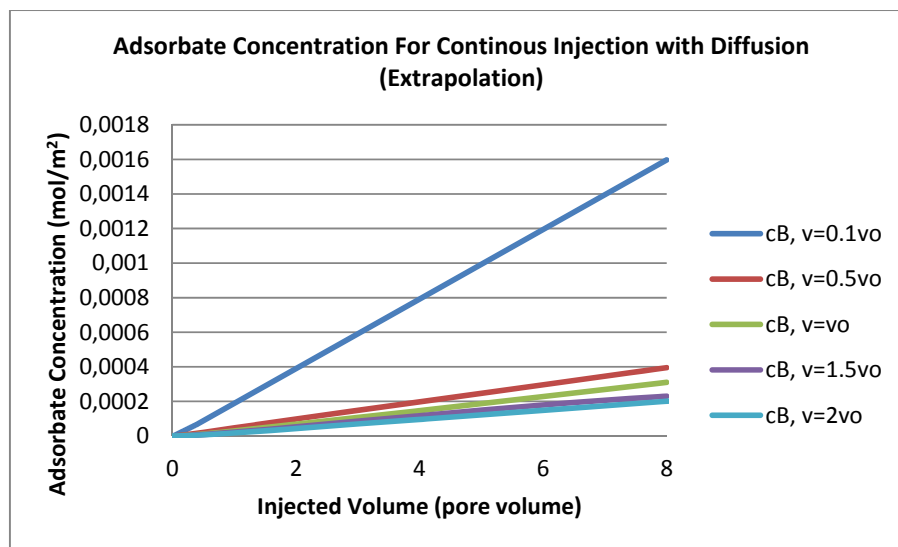


**Figure 4.27:** Average adsorbate concentration of various inlet velocities for continuous injection with diffusion against the injection volume (extrapolation),  $v_0=8.08 \times 10^{-5}$  m/s

Since the trend of the adsorbate concentration follows a linear relationship with the injection volume, the adsorbate concentration profile can be extrapolated. The result of the linear extrapolation for each of the adsorbate profiles for 8 pore volume is shown in **Figure 4.27**. It is discovered that the trend of the adsorbate concentration is proportional to the magnitude of the injection volume. However, the adsorbate concentration varies inversely to the magnitude of the injection velocity. This finding is in agreement with the previous finding in the discussion about the adsorption in the microchannel for the continuous injection without diffusion considered.

Comparing the trend of the adsorbate concentration in **Figure 4.27** with the effluent concentration profile in **Figure 4.24**, it seems that there is still a positive adsorption happens in the system although the effluent equilibrium concentration appears to be achieved already. The magnitude of the adsorbate concentration increase, however, is insignificant compare to the magnitude of the effluent concentration profile.

The cumulative adsorbate mass for the continuous nanoparticle concentration injection for 8 pore volume of injection is shown in **Figure 4.28**. For a similar injection volume, the adsorption is negatively associated with the injection velocity with a not easily defined correlation.

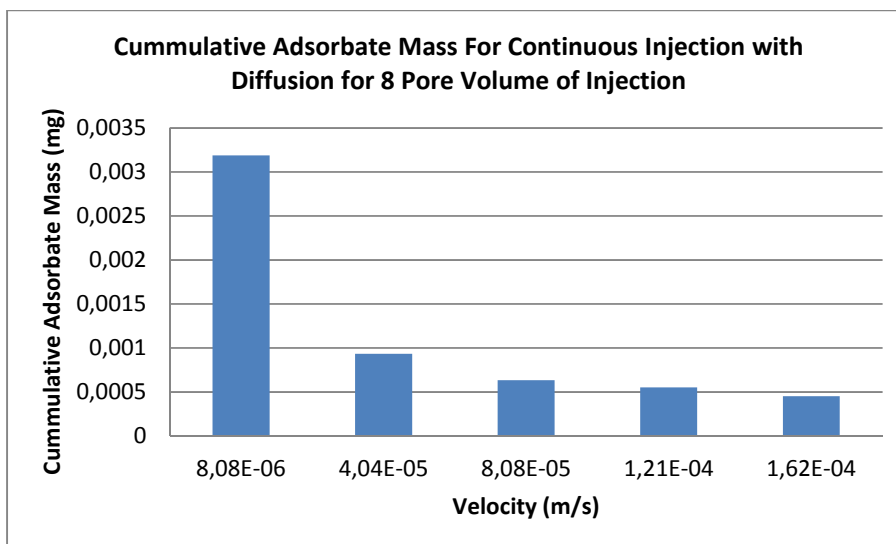


**Figure 4.28:** Cumulative adsorbate mass of various inlet velocities for continuous injection with diffusion for 8 pore volume of injection,  $v_0=8.08 \times 10^{-5}$  m/s

#### 4.6.2 Discontinuous nanoparticle injection

Discontinuous injection means the nanoparticles are injected for a finite period at the beginning of the simulation. In the simulation, the discontinuous nanoparticle injection is performed by setting a certain inlet concentration during time 0 second to time  $t_{\max}/1000$ , where  $t_{\max}$  is the maximum simulation time.  $t_{\max}$  is selected when the effluent concentration profile reaches its equilibrium condition. The equilibrium concentration is obtained by investigating the value of  $c_t$  when  $\frac{(c_t - c_{t+1})}{c_t} < 0.001\%$ . In this case,  $c_t$  (ppm) is the average effluent concentration at time  $t$ .

The amount of the nanoparticle injection is also normalised by the magnitude of the velocity to ensure similar concentration is injected to the microchannel regardless the magnitude of the injection velocity. After the period of concentration injection, the carrier fluid continues to flow in through the inlet at constant rate for the whole simulation duration. Following the previous study for the continuous injection, the velocity for the base case is selected  $v_0 = 8.08 \times 10^{-5}$  m/s. The diffusion coefficient of the concentration in the fluid used in the study is  $1.29 \times 10^{-5}$  cm<sup>2</sup>/s, which is defined by the utilisation of the values in Table 4.1 into Equation 3.26.

The typical profile of the bulk and the adsorbate concentration is shown in **Figure 4.29**. **Figure 4.29** A1, B1, C1, and D1 are the bulk concentration propagation for 0 seconds, 0.2 seconds, 0.5 seconds, and 1 second from 10 seconds simulation time. Injection velocity utilised is  $v=2v_0$ , which  $v_0$  is  $8.08 \times 10^{-5}$  m/s (base case). Blue colour indicates the lowest concentration is located and the red colour indicates the highest injected concentration. The adsorbate concentration that shows on **Figure 4.29** A2, B2, C2, and D2 corresponds to the propagation of the bulk concentration on **Figure 4.29** A1, B1, C1, and D1 respectively. There is no adsorption at the initial condition shown in **Figure 4.29** A1 and A2. At 0.2 seconds, the front of the main concentration body reaches the middle of the microchannel, which is shown by **Figure 4.29** B1. The corresponding profile of the adsorbate concentration is shown on **Figure 4.29** B2. It displays that the adsorption has been started and happens more at the location close to the inlet boundary, then decreases gradually towards the outlet. **Figure 4.29** C1 shows that at time 0.5 seconds the main concentration body has reached the outlet boundary. In this time, the adsorption on the microchannel wall has increased, which is shown by **Figure 4.29** C2..

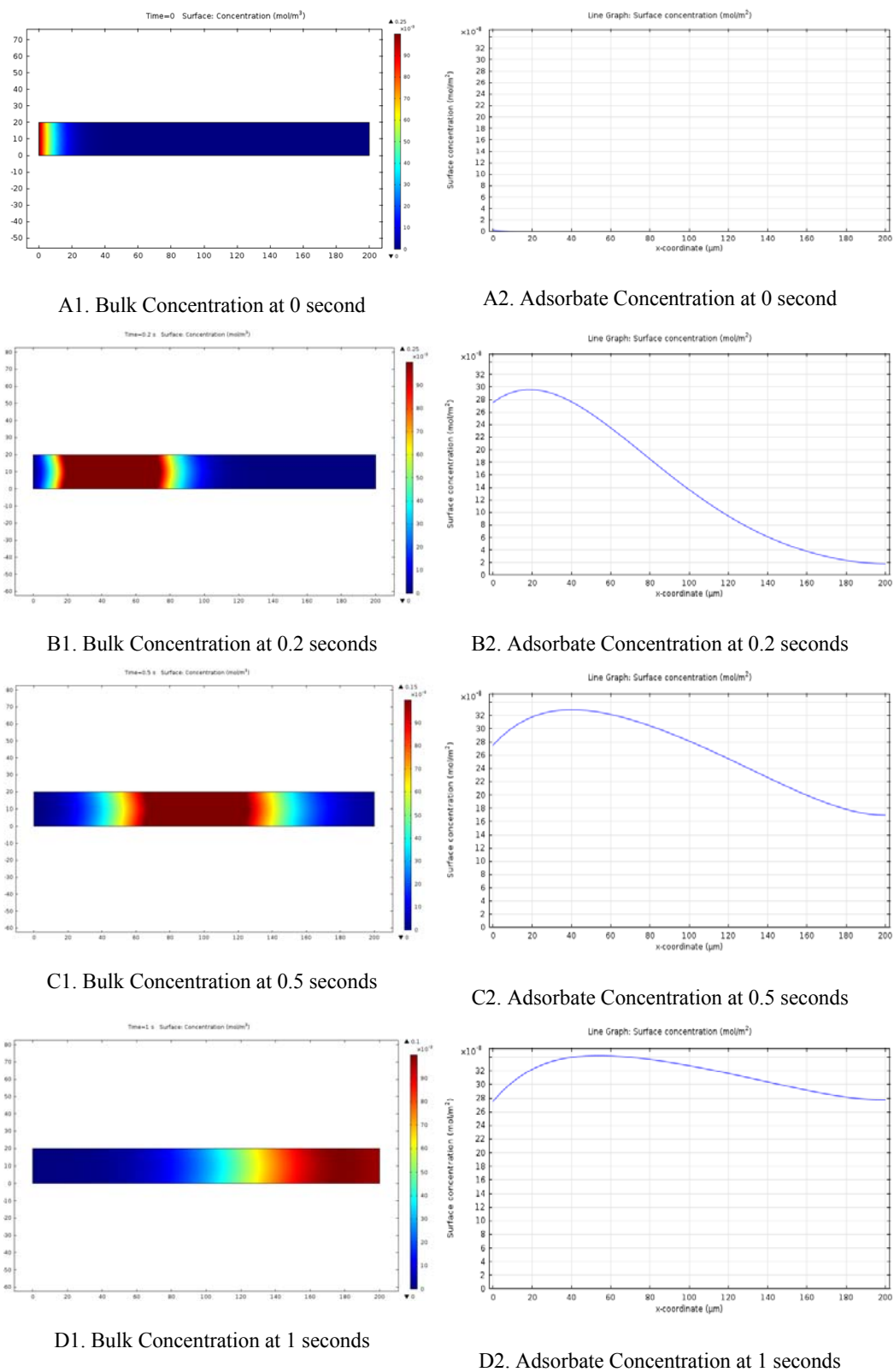


**Figure 4.29:** Bulk and adsorbate concentration for 0, 0.2, 0.5, and 1 seconds simulation time length for a discontinuous injection in various times for injection velocity  $v=2v_0$  and  $v_0=8.08 \times 10^{-5}$  m/s

On 1 second, the concentration main body is progressing to the outlet and the adsorption along the microchannel wall is now more even, shown by **Figure 4.29 D1** and **Figure 4.29 D2** respectively. In this case desorption is not observed since there is no reduction of adsorbate concentration on the microchannel wall during the simulation

#### 4.6.2.1 Discontinuous injection without diffusion

This section discusses the adsorption of the discontinuously injected nanoparticle excluding the effect of diffusion. **Figure 4.30** shows the trend of the effluent concentration for different injection velocity without diffusion against the simulation time. The effluent concentration is observed at the outlet boundary and it is observed that each reaches the outlet boundary at different time. This difference corresponds directly with the utilised injection velocity. Observing the profile of the effluent concentration, it typically increases at the beginning of the simulation until reaching a peak, and then it falls to zero with gradual gradient decrease. Without the diffusion, the concentration movement is governed by the advection. The speed and the observed effluent concentration magnitude are positively related with the injection velocity.

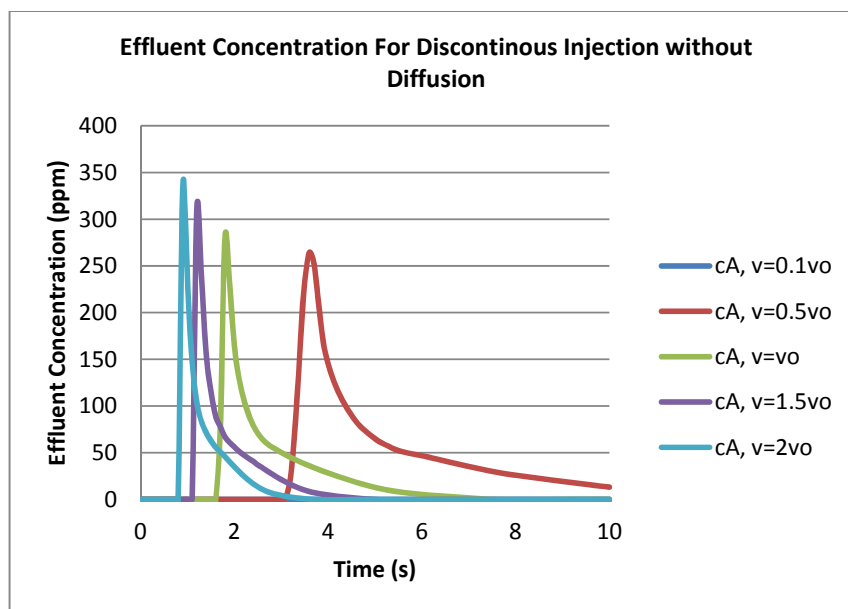


**Figure 4.30:** Effluent concentration of various inlet velocities for discontinuous injection without diffusion in various time,  $v_0=8.08 \times 10^{-5}$  m/s

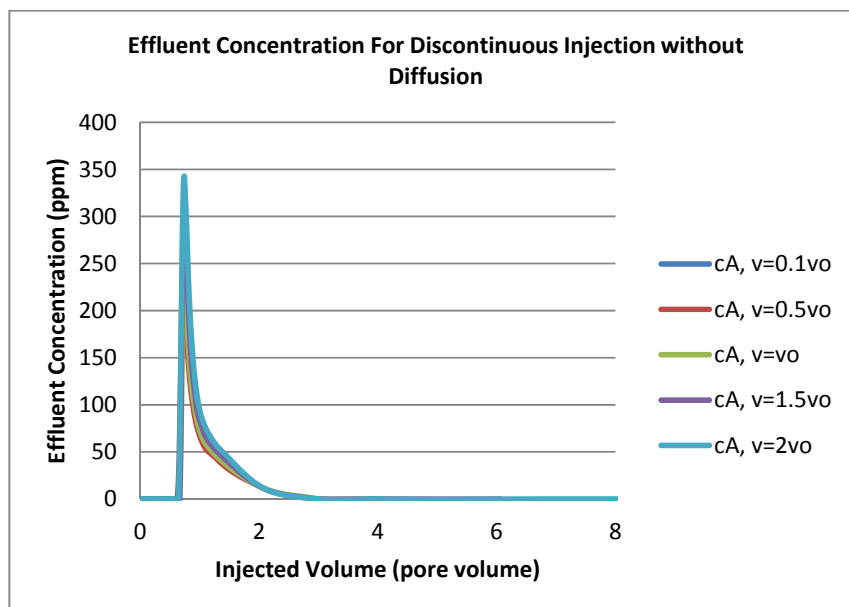


**Figure 4.31:** Effluent concentration of various inlet velocities for discontinuous injection without diffusion against the injected volume,  $v_0=8.08 \times 10^{-5}$  m/s

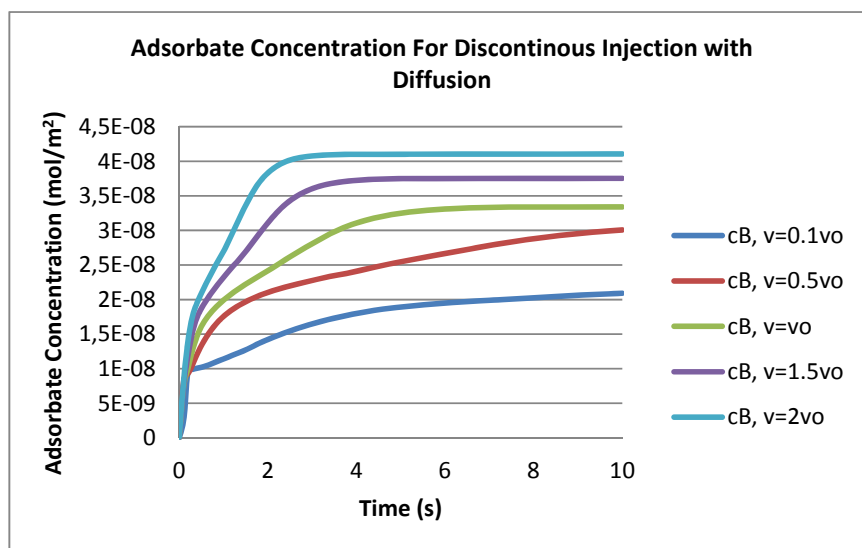


**Figure 4.32:** Adsorbate Concentration for various inlet velocities for discontinuous injection without diffusion against the injected time,  $v_0=8.08 \times 10^{-5}$  m/s

When the effluent profiles are plotted against the injection volume, each of them is situated in one alignment, which is shown in **Figure 4.31**. This indicates that all velocity cases require similar injection volume to reach

the outlet without the effect of diffusion, regardless of the time utilised in the injection. This shows that the profile observed on **Figure 4.30** is valid.

The adsorbate concentration for discontinuous injection for various injection velocities without diffusion is shown in **Figure 4.32**. It appears that the magnitude of the adsorbate concentration is proportional with the injection velocity. The equilibrium profile appear for the case  $v=2v_0$ ,  $v=1.5v_0$  and  $v=v_0$ , but not yet for  $v=0.5v_0$  and  $v=0.1v_0$ . The two latters require further observation with significantly longer simulation time to investigate the profile to reach the equilibriums.

#### 4.6.2.2 Discontinuous injection with diffusion

The final investigation in this chapter is for the discontinuous concentration injection with considering the effect of diffusion. The profile of the effluent concentration for various inlet velocities against simulation time for discontinuous concentration injection with diffusion is shown in **Figure 4.33**. In the figure, it is observed that the velocity has a positive relationship with the breakthrough time for the concentration reaching the outlet. The maximum concentration observed at the outlet is also proportional with the injection velocity, with anomaly for the lowest velocity. In the case of the lowest injection velocity, i.e.  $v=0.1v_0$ , the concentration movement is dominated by the effect from diffusion. The diffusion allows the concentration spread and remains at its position longer and this is the one detected at the outlet boundary. However, the case with diffusion domination has lower penetration than the case with advection domination, especially for longer microchannel. The concentration transport in the latter case with advection domination happens more towards downstream. On the other hand, the dispersion of the concentration due to diffusion goes in any direction regardless of the stream direction.

The effluent concentration for various velocities with diffusion against the injected volume is also investigated that is illustrated in **Figure 4.34**. In the discontinuous injection, the magnitude of the injected volume is independent to simulation time. In this figure, the effect of the injection velocity and diffusion is easier to observe. In this case, the effluent concentration breakthrough is detected before the injection reach 1 pore volume. This shows that diffusion contributes significant influence to the concentration transport in the system. All cases with advection domination, i.e.  $v=v_0$ ,  $v=1.5v_0$ , and  $v=2v_0$ , require similar injection volume to reach the

breakthrough at the outlet boundary. The required injection volume for the breakthrough decreases proportional with the velocity decrease, which indicates the increase of the diffusion domination. High effluent concentration is again detected for diffusion dominated case, i.e.  $v=0,1v_0$  relative to the case with  $v=0.5v_0$ . This happens because the concentration is dispersed by the diffusion in the system and some part of it remains for long at the outlet due to low injection velocity.

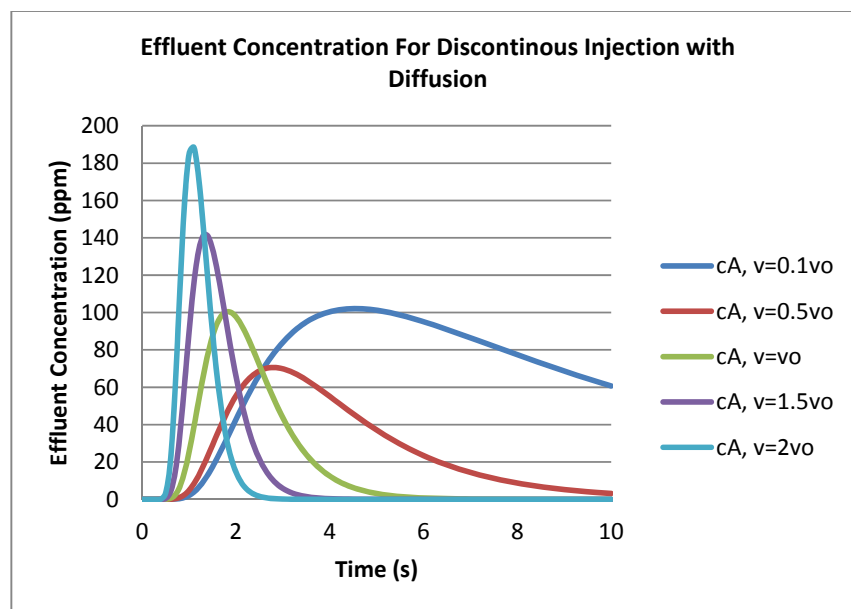


**Figure 4.33:** Effluent concentration of various inlet velocities for discontinuous injection with diffusion against the simulation time,  $v_0=8.08 \times 10^{-5}$  m/s

The trend of the effluent concentration increases and shifts to the right as the injection velocity increases. This indicates that the injection velocity affects the amount and the time needed for breakthrough. More and faster particles are transported further into the microchannel as the velocity increases and vice versa.

The decrease of the effluent concentration in **Figure 4.33** and **Figure 4.34** corresponds with the flushed particles out from the microchannel domain. The gradient decrease of the profile is also affected by desorption happens at the microchannel wall. Steep gradient decrease also indicates fast desorption. High injection velocity flushes the bulk concentration from the system faster than the case with lower injection velocity. Desorption is

enhanced as the wall and bulk concentration contrast becomes larger due to this flushing effect. Therefore, desorption happens faster in a system with higher injection velocity.

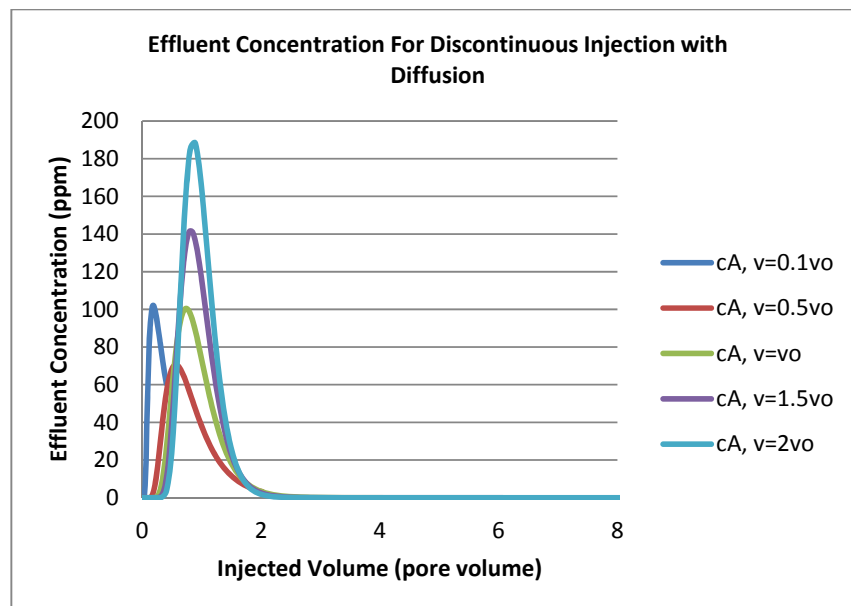


**Figure 4.34:** Effluent concentration of various inlet velocities for discontinuous injection with diffusion against the injected volume,  $v_0=8.08 \times 10^{-5}$  m/s

The trend of the adsorbate concentration for different time is shown in **Figure 4.35**. Each line shows that the concentration of the adsorbate along the microchannel increases until it reaches a plateau. The plateau shows the system has reached an equilibrium condition, which is where the adsorption rate equals the desorption rate. This equilibrium is achieved because there is no more nanoparticles supply from the inlet due to the concentration discontinuous injection. The figure shows that there is more adsorption happens for low injection velocity. The profile has a very slight negative gradient because of the slow desorption due to the concentration difference between the microchannel wall and the fluid bulk. The adsorption speed is indicated by the gradient increase of the profile. It seems that the adsorption speed varies inversely to the injection velocity. This happens because the concentration remains longer in a location in a low velocity environment and this enhance the possibility of the adsorption to happen due to diffusion.

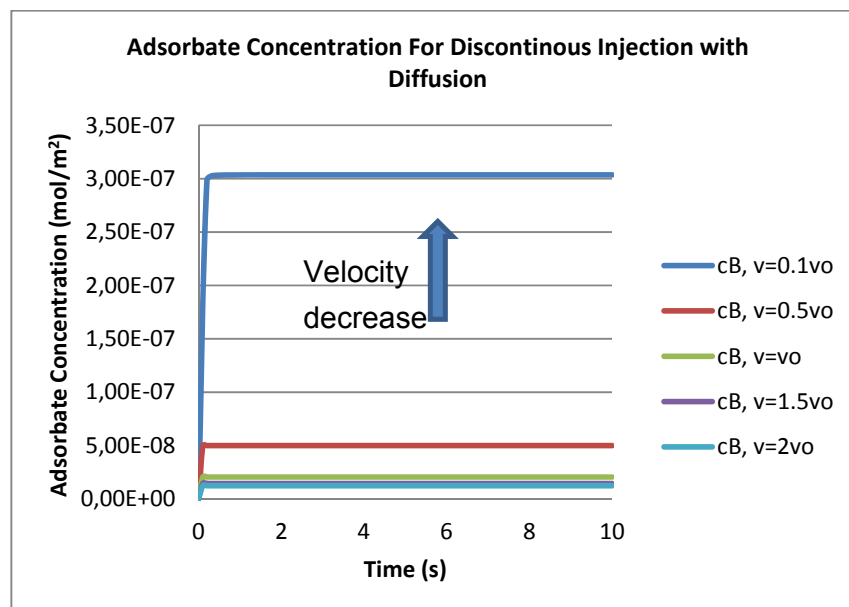


**Figure 4.35:** Average adsorbate concentration of various inlet velocities for discontinuous injection in various time,  $v_0=8.08 \times 10^{-5}$  m/s. Lines for  $c_B$ ,  $v=1,5v_0$  and  $c_B$ ,  $v=2v_0$  are on the top of each other.

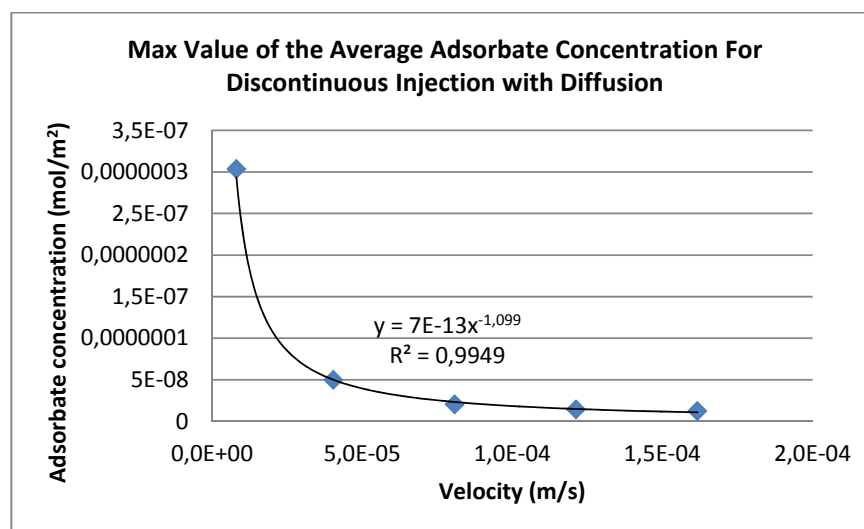


**Figure 4.36:** Maximum value of the average adsorbate concentration for various inlet velocities for discontinuous injection.

**Figure 4.36** shows the maximum value of the average adsorbate concentration for discontinuous injection with diffusion considered. The values are taken from the plateau profiles in Figure 4.35. That appears that the maximum value of the adsorbate concentration for discontinuous

injection with diffusion against the injection velocity follows Power Regression Model.

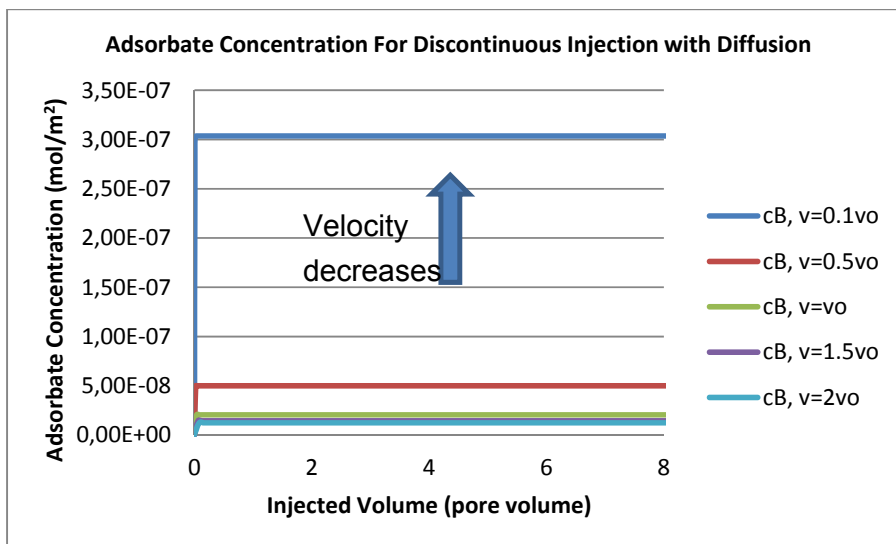


**Figure 4.37:** Adsorbed concentration of various inlet velocities for discontinuous injection in various pore volume,  $v_0=8.08 \times 10^{-5}$  m/s. Lines for  $c_B, v=1.5v_0$  and  $c_B, v=2v_0$  are on the top of each other.

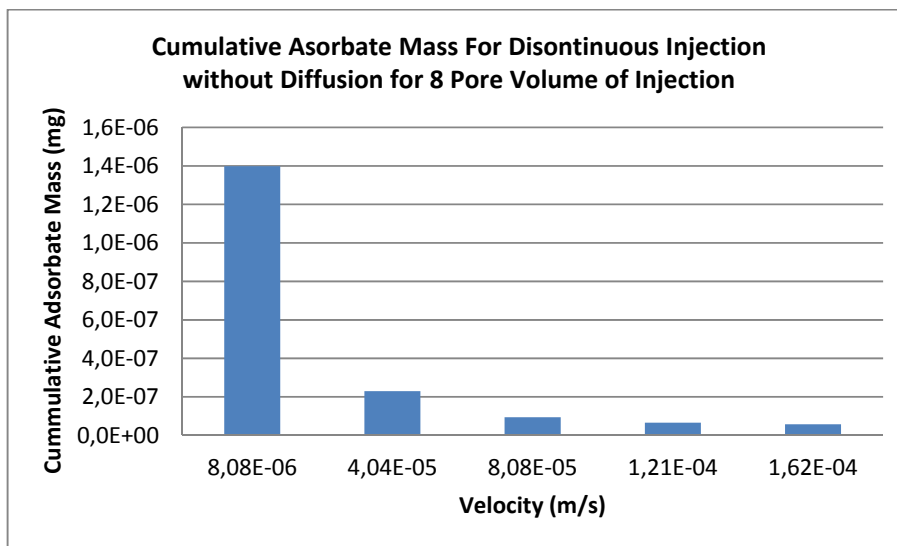


**Figure 4.38:** Cumulative adsorbed mass for various inlet velocities for discontinuous injection for 8 pore volume of injection,  $v_0=8.08 \times 10^{-5}$  m/s

**Figure 4.37** shows the trend of the cumulative adsorbate concentration for different injection volume. Generally, the adsorbed

---

concentration is increased and flattened until a certain point as the injection volume increases. This figure also shows that the adsorption happens instantly from the beginning of the simulation. The amount of the maximum adsorbate concentration varies inversely to the velocity. This is consistent with the investigation result from the previous section. The comparison of the cumulative adsorbate mass for different injection velocity with diffusion considered is shown in **Figure 4.38** where the result is in a good agreement with the previous observation discussed.

## 4.7 Summary and Conclusion

Nanoparticle technology is a new approach to extend lifetime of scale inhibitor attachment on the rock surface [35]. It is important to understand the distribution and placement of the injected nanoparticles in porous media. Many studies have been conducted to investigate the behaviour of nanoparticles in porous media [54, 171]; however the studies were mostly conducted for a macroscopic flow in a core-scale sample and there is none yet establish a simulation that focus specifically on the adsorption and desorption mechanism inside the pore-channel itself.

A conceptual numerical model for simulating the transport of nanoparticles in a single straight microchannel has been developed. In the study, nanoparticles are modelled as a concentration field with no specific chemistries involved. Therefore, any chemical injection is potentially usable as a means for validation; however, the rate constant obtained will not be universal. In the study, PPCA is used as an analogue for nanoparticles. Validation is conducted by comparing the effluent concentration that obtained from a core flood experiment conducted by Zhang et al [221].

The model is available for 2D and 3D axis-symmetric microchannel. Freundlich adsorption isotherm method appears to be more suitable as adsorption/desorption basic expressions for the modelling than Langmuir adsorption isotherm method. This follows Zhang's recommendation [221] to use Freundlich adsorption isotherm mechanism. However, the original Freundlich adsorption isotherm equation cannot clearly show the term of adsorption and desorption. Therefore, modified Freundlich equation conducted by Skopp [170] is used for the study. Skopp derived Freundlich adsorption isotherm equation by introducing term of adsorption and desorption separately, allowing to study adsorption and desorption process

more easily. The Freundlich equation follows the equation below and the corresponding parameters for both geometries are shown in **Table 4.3**.

$$r = k_{ads} \cdot c_A^{n_{ads}} - k_{des} \cdot c_B^{n_{des}}$$

$$\text{where } k_{ads} = k_f \text{ and } k_{des} = k_r$$

Geometry	$k_{ads}$ [m/s]	$n_{ads}$	$k_{des}$ [mol/(m <sup>2</sup> .s)]	$n_{des}$	$R^2$
2D	$1.58 \times 10^{-5}$	0.45	$3.16 \times 10^4$	10	0.99
3D axis symmetric	$1.29 \times 10^{-6}$	0.77	$7.94 \times 10^5$	50	0.99

**Table 4.3:** The parameters used for the Freundlich equation for the 2D and 3D axis-symmetric geometry

The Freundlich parameters obtained for these two geometry models are different because these two have different geometry assumptions that relates directly to the microchannel's adsorption surface area. The 2D model takes into account a concentration flow and adsorption/desorption mechanism in a micro-gap between two planes. This model is dedicated to investigate the effect of microchannel geometry with elongation variation. The 3D axis symmetric geometry takes into account configuration for cylindrical microchannel. This model is dedicated to investigate the effect of variation in wall configuration to the system. The Freundlich parameters obtained in this chapter, which are shown in **Table 4.3**, are only valid for the specific case, condition, and assumptions utilised in this thesis. Regression selection method is important to obtain the parameters.

In this chapter, the effect of fluid flow velocity is also investigated as a key preliminary study for understanding the transport and adsorption/desorption mechanism in a microchannel for continuous and discontinuous nanoparticle injection. The effect of diffusion and advection is discussed separately. Advection has a negative relation with the desorption rate, taken from the investigation of the post flush flow. Adsorption tends to happens more effectively in a low velocity environment.

Diffusion contributes highly to the effectiveness of the adsorption mechanism in the microchannel. Therefore, the shut in period in the scale

squeeze treatment is indeed important to allow placing the inhibitor on the wall of the rock efficiently. However, diffusion has lower penetration especially for longer microchannel.

The trend of the equilibrium effluent concentration for continuous injection with diffusion does not clearly follow any regression model when the low injection velocity is considered. However, the profile follows a linear regression model after the injection velocity above a certain level. It also found out that the maximum value of the adsorbate concentration for discontinuous injection with diffusion against the injection velocity follows Power Regression Model.

## Chapter 5

### Adsorption and Desorption in a Tortuous Microchannel

#### 5.1 Introduction

This chapter builds on the model described in Chapter 4 and explores the effect of the channel geometry on adsorption.

The transport of molecule particles in a pore structure is determined by structural parameters, fluid properties, and interaction between fluids and interfaces. The generally considered structural parameters are surface area, pore size distribution, and pore topology. The latter may be quantified by a parameter such as tortuosity [235, 236].

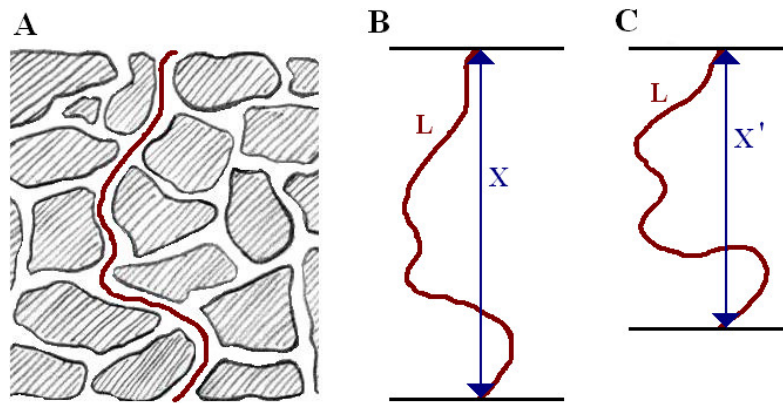


**Figure 5.1:** Determination of tortuosity through a porous material using the arc-chord ratio (after O'Connell et al., 2010)[237]

Tortuosity can be defined as an average elongation of fluid paths or as a retardation factor that measures the resistance of a porous medium to the flow. It reflects the efficiency of the transportation of a substance inside the respective material. In other words, tortuosity represents the degree of complexity of the channel configuration [238]. It can be defined as the ratio of specific surface of real porous media to an idealised capillary bundle [239]. It also can be described by a linear function of capillary diameter [240] or as function of porosity and characterized shape of the porous medium component [241]. In fluid mechanics of porous media, tortuosity is defined as the ratio between the length of the actual streamline and the straight-line

distance between two points [242]. This definition, which is illustrated in shown in **Figure 5.1** [237], is also commonly used in the oil and gas industry, especially in for rock formation evaluation, geology, drilling and reservoir characterisation. This definition is the one utilised in this chapter, where longitudinal geometrical variation of the microchannel domain is investigated. As it is illustrated in **Figure 5.1**, tortuosity is illustrated as a sinuous path in a porous media. The tortuosity of a path through a porous structure A is determined by the ratio of the pore length  $L$  and the displacement  $X$ . Picture B and C in **Figure 5.1** show that an equal pore length  $L$  may have different tortuosity since the displacement  $X$  and  $X'$  are different [237]. In this study, the 2D model built that was discussed in Chapter 4 is used for the investigation.

It is suggested that tortuosity should also consider an indication of more complex geometry parameter, such as the pore connectivity and the constrictivity of the pores [238]. However, the definition of the tortuosity selected in this chapter cannot be used to measure the complexity in a pore network, instead only the curvature complexity of microchannel. To measure the complexity of a pore network by tortuosity, it is defined by comparison of the specific conductivity of the electrolyte in the pore or derived from diffusion [243, 244] using Maxwell's equation [245]. Thus, an explicit relation as a function of total porosity, intraparticle tortuosity and intraparticle porosity was proposed to fit the experiment data for the whole porosity range. Matyka and Koza [246] discussed a possible method of numerical and experimental measurement of the tortuosity directly from the fluid velocity field. Tortuosity magnitude also can be approached by assessing diffusion and electrical measurement [247]. Transport properties in tortuous porous material has been researched for many areas, including study for fracture surface [248], lungs [249], metal foams[250], and aerogel [251, 252]. These studies discovered that geometrical structure of the pore has a significant influence to the flow easiness of the pore system. However, the investigation of porous media and the transport phenomena within has generally been limited to macroscopic measurement, which tells one little about the microscopic structure of these materials [252]. This chapter is a revisit to investigate the latter where microchannel with elongation variation (curvature) is considered as a contribution for study of transport in porous media.

---

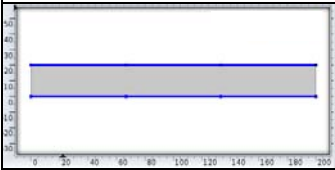
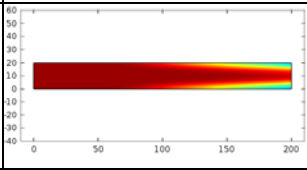
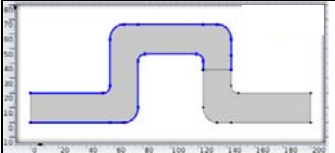
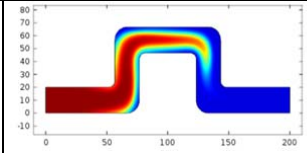
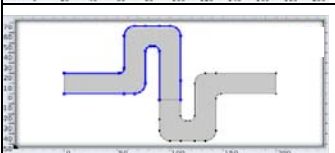
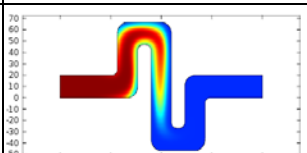
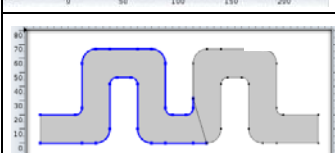
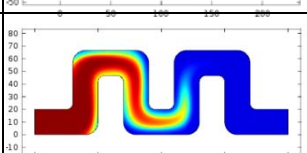
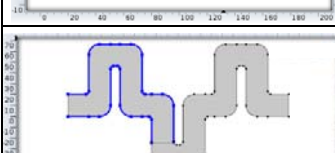
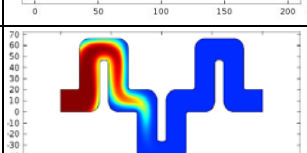
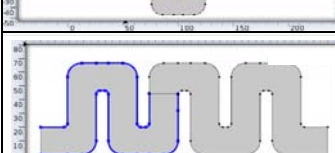
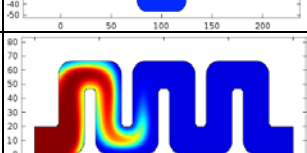
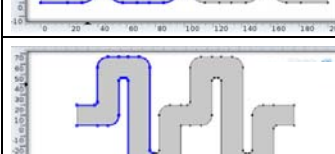
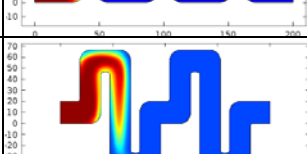
## 5.2 Aims and Objectives

The aim of the study in Chapter 5 is to investigate the effect of different channel geometry on the transportation and the adsorption of the nanoparticle in microchannel system. Numbers of bends and configurations in the channel are introduced, where channel with elongation variation (curvature) is represented tortuosity i.e. the ratio between the actual length and the distance between the inlet and outlet of the channel. The model extends that is described in Chapter 4. The concentration trend of the effluent and adsorbed nanoparticles is discussed which this ultimately allows a link to be made between the small-scale fluid behaviour and a macroscopic description of the rock such as tortuosity.

## 5.3 Simulation Setup

The simulation is addressed to study the transportation of nanoparticles in a tortuous 2D microchannel model. Nanoparticles are treated as concentration field that is transported with steady fluid flow without slip. The adsorption and desorption mechanism is governed by the Freundlich adsorption isotherm approach. A numerical simulation is used to solve sets of equations that consider the fluid and concentration flow in a microchannel and adsorption/desorption mechanism of the concentration with the microchannel wall. The details for the methodology and the detail validation are discussed in the Chapter 3 and 4 respectively.

Two investigations are conducted to investigate the nanoparticles' behaviour in the microchannel. The first investigation is to study the particle behaviour in the microchannel with identical channel length measured along the flow path. The adsorption surfaces for this study are shown by the blue-coloured boundaries at the microchannel in the geometry pictures under column "Active adsorption wall" in **Table 5.1**. The movement of the particles in the bulk was investigated by plotting the trend of the particles that transported through an imaginary 'outlet' at somewhere in the middle of the microchannel such that 200 $\mu\text{m}$  channel length from the inlet is measured. The second investigation is to study the particles behaviour in the channel with identical 200- $\mu\text{m}$  inlet-outlet of *distance* where various microchannel actual length and surface area are considered. It is important to conduct these two investigations separately since the way to acquire the tortuosity for both are different.

Geometry, L = 200 $\mu\text{m}$		Inlet-Outlet Distance from the inlet boundary (D, $\mu\text{m}$ )			
Active adsorption wall (blue lines)	Concentration flow that reach 200 $\mu\text{m}$ channel length	x	y	z	Tortuosity (L/D)
		200	0	200	1
		133.3	25.9	135.8	1.473
		114.8	5.85	114.9	1.740
		100	-16.35	101.33	1.974
		85.71	-34.67	92.46	2.163
		85.71	34.38	92.35	2.166
		57.92	-46.67	74.38	2.689

**Table 5.1 :** Simulation setup for the study of the effect of tortuosity to the particle distribution in microchannel

The fluid and concentration flow, adsorption and desorption parameters are the same as in Chapter 4. The simulation is conducted by injecting 12500 ppm of nanoparticle concentration into the microchannel. The investigation is performed for both continuous and discontinuously injection. Injection velocity for the base case is  $8.08 \times 10^{-5}$  m/s. Velocity sensitivity study is carried out for the base velocity, half and twice of the

base velocity. The trends of the adsorbed particles on the system on similar time length obtained from the breakthrough were also plotted for each study.

There are seven microchannels configurations with different tortuosity introduced in the study. The detail of the channel configurations is shown in **Table 5.1**, where the shapes are design accordingly with adding bends and curvature arbitrary with fixed inlet and outlet position. The first column in the **Table 5.1** displays the geometries used in the study. The distance in x-direction between the inlet and outlet boundaries of each microchannel is 200  $\mu\text{m}$ . The blue coloured wall at the channel boundary indicates the 200- $\mu\text{m}$  channel length measured from the inlet of the microchannel. The second column shows the front of the particles concentration reach the breakthrough at 200- $\mu\text{m}$  channel length at 0.2 seconds for both continuous and discontinuous injection. The concentration front is retarded near the walls due to no slip condition applied between the wall and the flowing fluids. It seems that the tortuosity affects to the propagation of the injection concentration in the microchannel. This will be discussed further in the next subchapters. The next column displays the distance in x and y direction of the outlet from the inlet of each geometry. z is the distance from the inlet to the outlet that is calculated using Pythagoras theorem from the value of the x and y. The last column shows the measured tortuosity of the associated geometry. The particles behaviour for both continuous and discontinuous particles injection is discussed in detail in the next subchapters. Note that the simulation considers the effect of diffusion, where the study of the effect of the diffusion is discussed in Chapter 4.

#### **5.4 Adsorption in Identical Length Tortuous Microchannel**

The transport, adsorption, and desorption of the nanoparticles in the identical length tortuous microchannel are discussed in this section. The effluent and the adsorbed particles concentration along the microchannel wall are investigated. The study is divided into the condition of continuous (Section 5.4.1) and discontinuous injection (Section 5.4.2). The investigation is conducted and the concentration profile is plotted against the injection volume. The concentration in the simulation is calculated by averaging the magnitude along the corresponding boundaries in times. The injection volume is measured by the equivalent volume of the microchannel, which also known by unit “pore volume”. The injection volume in pore volume unit is a function of injection velocity and simulation duration that is calculated

using the Equation 3.42. Plotting the concentration against the injection volume has advantage in order to gain a better view the relation of the concentration and the amount of the injected fluid. The injection volume is proportional to the simulation time as long as the injection flow rate, area, and the length of the microchannel remains constant. The detail for the injection volume is discussed in Chapter 3. Effluent and adsorbate concentration are investigated which values are obtained from the average along the corresponding boundaries in time.

#### 5.4.1 Continuous Injection in Identical Length Tortuous Microchannels

Initially there is no nanoparticle concentration in the microchannel domain. Then, a constant 12500 ppm of nanoparticles concentration is continuously injected with a steady  $8.08 \times 10^{-5}$  m/s velocity from the inlet of the microchannels. In this case, the outlet for all microchannels is measured at a location of 200- $\mu\text{m}$  lengths from the inlet. Therefore, the adsorption surface of each microchannel is comparable. After a short time, the front of the bulk concentration reaches the outlet. Some of the particles along the flow path are adsorbed on and desorbed from the wall of the channel due to difference in concentration between the surface and bulk. The adsorption and desorption mechanism follows Freundlich adsorption isotherm mechanism which is governed by the difference in between the fluid bulk and the adsorption surface.

**Figure 5.2** shows the profile of the effluent concentration against the injection volume. The profile is obtained from the average nanoparticle concentration measured at the outlet boundary of the microchannel during the simulation. The effluent profile increases rapidly at 0.32 pore volume, which equals to 0.8-second simulation time. A minor kink that is seen at the beginning of the breakthrough generated due to the smoothing mechanism in connecting the data obtained from the simulation.

In **Figure 5.2**, it appears that the effect of the diffusion remains for about 0.4 pore volume after the breakthrough discovered, which is shown by a flat effluent concentration profile between 0 and 0.4 pore volume. Then, after 0.75 pore volume, the gradient of the effluent concentration becomes precipitous. This is showing that the advection provides dominant effect to the effluent propagation in this period. After the main concentration body

reaches the outlet boundary, the effluent profile flattened steadily due to the continuous and unlimited supply of nanoparticle injection from the inlet.

As expected, in each case, the effluent concentration eventually reaches the inlet concentration, which is when the microchannel is saturated and the adsorption and desorption are in equilibrium. It is also discovered that the profile of the average effluent concentration slightly shifts to the right as the tortuosity increases. Since injected volume in this case is proportional with the injection duration, it means that the amount of the time and injected particles needed by the system to reach the equilibrium condition is proportional to the magnitude of the tortuosity.

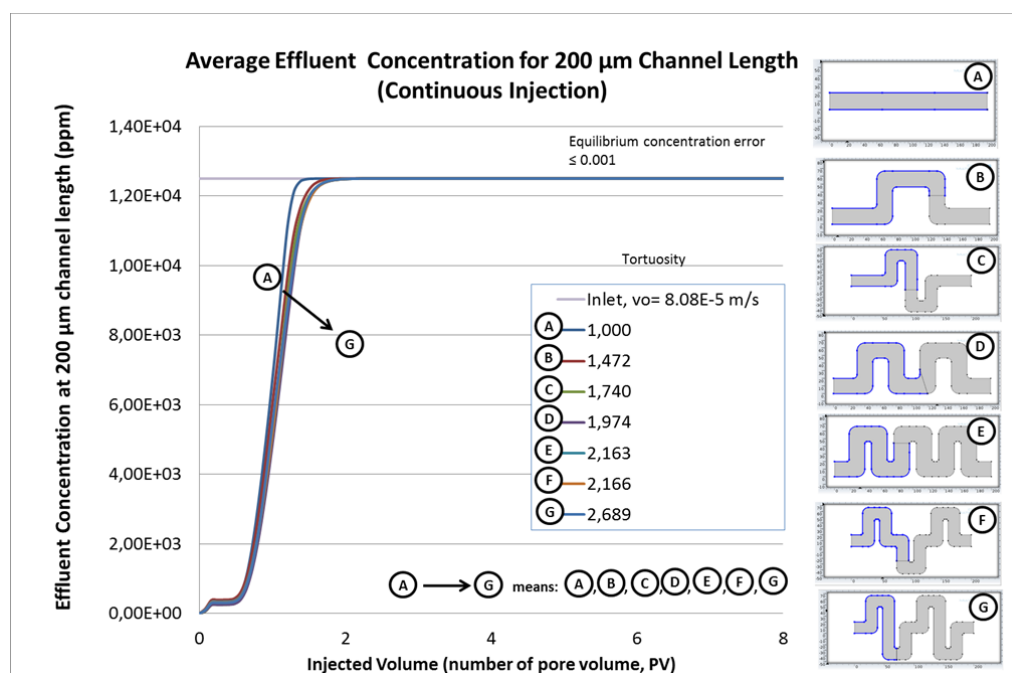


**Figure 5.2:** Bulk concentration vs. pore volume at the 200- $\mu\text{m}$  outlet boundaries for different tortuosity for continuous particles injection

**Figure 5.3** shows the profile of the average adsorbed concentration as a function of injected volume. This profile is measured by averaging the adsorbate concentration over walls of the whole microchannel. Initially, there is no adsorbate on the microchannel walls. The adsorbate concentration profile starts from a zero value at the beginning of the simulation and then increases until it reaches a constant value. The gradient of the adsorbate concentration profile in **Figure 5.3** indicates the rate of the

adsorption/desorption in the system. The rate of the adsorption for each tortuosity has a small difference. The gradient of the profile reaches a constant value at a similar injection volume as the one observed in the investigation of the effluent concentration. In this condition, the amount of the adsorbate on the wall is constant during the continuous injection. This is the equilibrium condition where the rate of adsorption equals the rate of desorption. The average adsorbate concentration has an affinity to inversely varies to the magnitude of the tortuosity. This is observed easier at the inset in the **Figure 5.3**, which shows the adsorbate concentration between injection volume 1 and 1.6 pore volume in a smaller scale. It indicates that a uniform adsorption tends to happen more efficiently on the wall of the less tortuous microchannel than on the wall of the microchannel with higher complexity. This is discussed shortly afterwards in the section of the discontinued injection in microchannels with identical length.

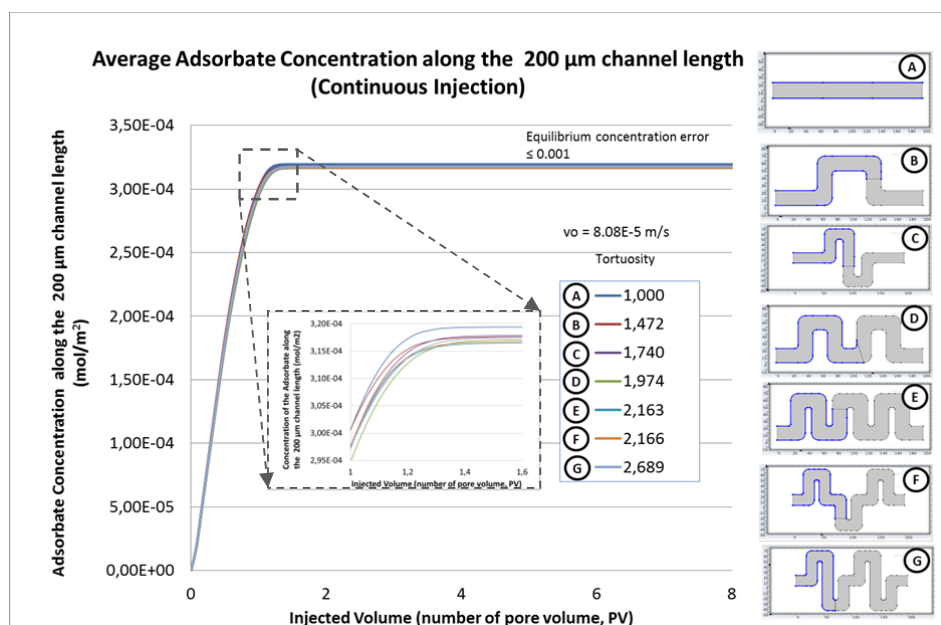


**Figure 5.3:** Adsorbed concentration against the injection volume for continuous concentration injection – Freundlich adsorption isotherm. The inset is the profile of the adsorbate concentration at the corner of the concentration profile change.

Although all microchannels in this study have a similar surface area, the access for interaction between the concentration and the microchannel wall is not similar. The access for interaction between the concentration and

the wall is higher in the microchannel system with low tortuosity. As an example, a snapshot for concentration propagation from two microchannels with different tortuosity magnitude is presented in **Figure 5.4**. **Figure 5.4 (left)** shows a snapshot of a concentration flow in a straight channel. **Figure 5.4 (right)** shows a snapshot of a concentration flow in a microchannel with two bends. In the figure, dashed-lines show the location of similar length measured from the inlet of the microchannel. Both snapshots are taken when the simulations are conducted for 0.8 seconds.

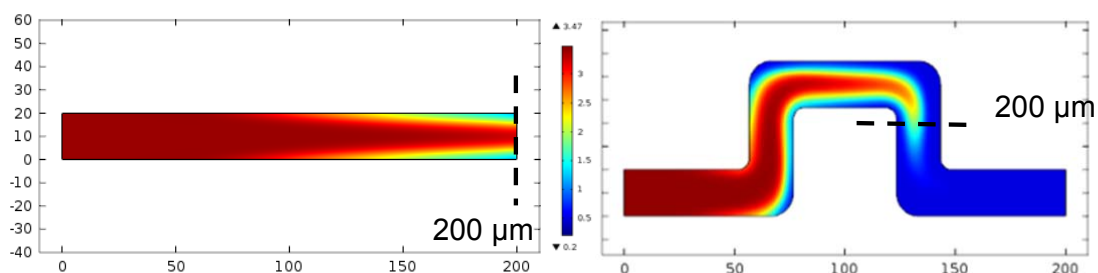


**Figure 5.4:** The concentration propagation of 2 different channel configuration i.e. with tortuosity=1 (left) and tortuosity=1.4724 (right) at 0.8 seconds. Recalled, the tortuosity is measured for similar microchannel length of 200  $\mu\text{m}$ .

In the figure of the straight microchannel (**Figure 5.4 (left)**), the surfaces of the walls are swept evenly with the concentration. In the curved microchannel (**Figure 5.4 (right)**), however, there are some parts in the area close to the bends where concentration is lower than the other parts of the channel wall. This indicates the interaction access between the concentration and the wall is not similar along the wall in microchannels with bends. This affects the effectiveness of the adsorption in the system. Bends in the channel therefore reduce the sweep efficiency of the bulk concentration along the channel wall at the bend. The condition reduces the impact of the particles and the channel wall, decreases the amount of particles adsorbed. Hence, the adsorption in a high tortuous microchannel is less uniform than the adsorption in a microchannel system with lower tortuosity. A further investigation about this finding is discussed in the section of adsorption in the microchannels with the dead ends in Chapter 6.

---

### 5.4.2 Discontinuous Injection in Identical Length Tortuous Microchannel

In this section, the investigation of the transportation and the adsorption/desorption of the discontinuous injected concentration is discussed. The configuration of the simulation for this case is similar with the study for the continuous particles injection. A 20  $\mu\text{m}$  diameter and 200  $\mu\text{m}$  length microchannel is the domain of the simulation. Initially, the microchannel is empty and with no nanoparticle concentration adsorbed on the walls. 12500 ppm of nanoparticles concentration is injected discontinuously for 5 pore volume of the microchannel from the inlet boundary with an  $8.08 \times 10^{-5}$  m/s steady creeping velocity. After the period of concentration injection, the carrier fluid continues to flow in through the inlet at constant rate for the whole simulation duration.

There are seven different tortuous microchannels with equal length being investigated in the study. The adsorption and desorption mechanism follows Freundlich adsorption isotherm mechanism which is governed by the concentration difference between the fluid bulk and the adsorption surface. The trend of the effluent and the adsorbate concentration is investigated.

For visualization, concentration flow sequence for the tortuosity in microchannel with geometry E for 0, 0.3, 0.6, and 0.9 seconds is shown in **Table 5.2**. Please note that the investigation is conducted for a 200- $\mu\text{m}$  microchannel length, which is marked by the straight line in the microchannel. The left column shows the concentration profile inside the microchannel for a specified simulation time step. The right column shows the adsorbate concentration for the corresponding time. At 0.05 seconds, some of the particles have started to flow into the microchannel. Due to the diffusion, some of the injected concentration has been transported further and desorbed. This is indicated by the corresponding adsorbate concentration profile that is shown in Figure (B2) in the **Table 5.2**. The adsorbate starts at  $20 \times 10^{-8}$  mol/m<sup>2</sup> and increases until  $24 \times 10^{-8}$  mol/m<sup>2</sup> at 40  $\mu\text{m}$ . This is where the first bend is located.

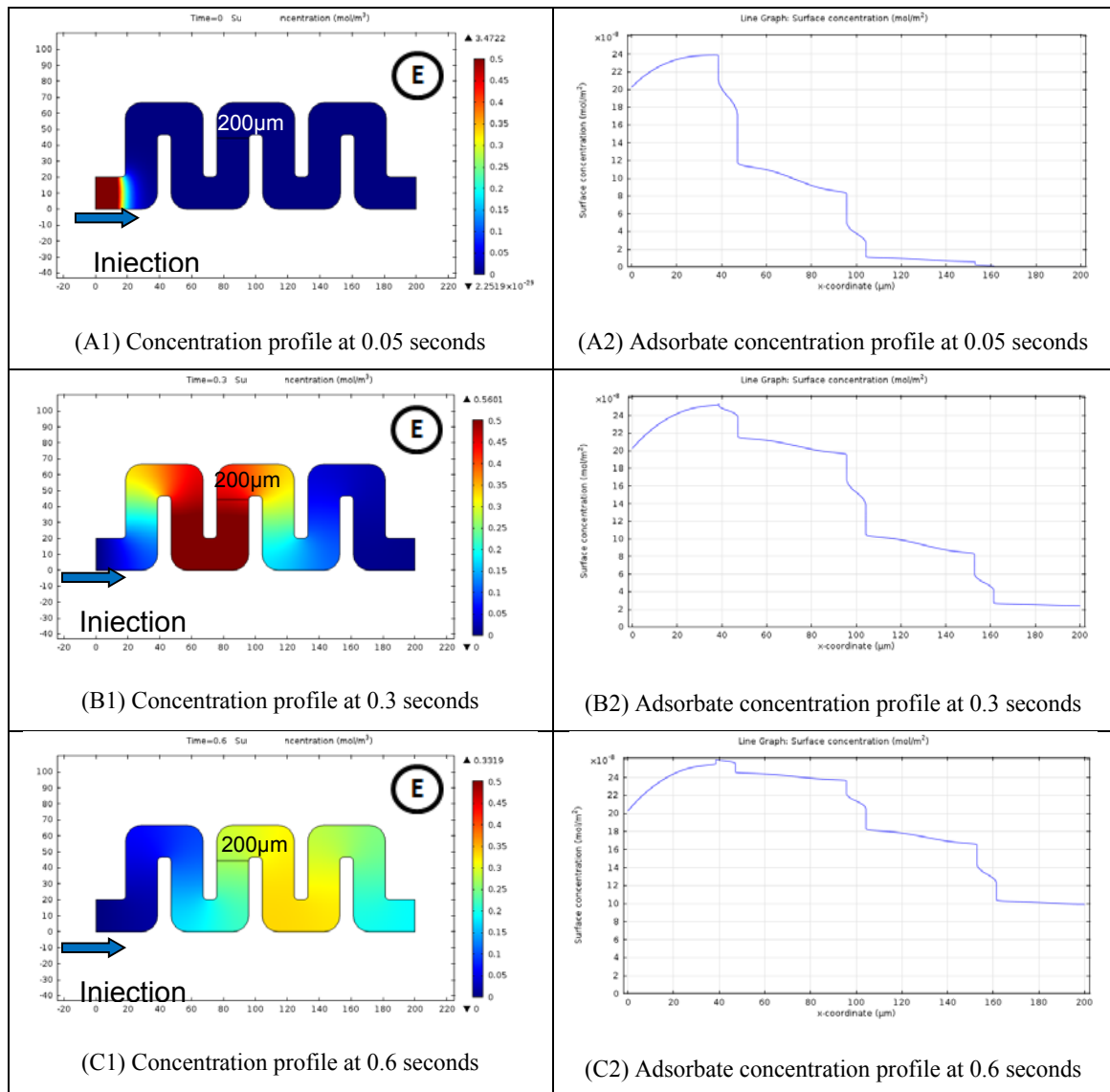


**Table 5.2 :** Flow sequence of the concentration flow and the corresponding adsorbate concentration profile for geometry E for a discontinuous injection. Units for the x-axis is in  $\mu\text{m}$

The magnitude of the adsorbate at the wall after the first junction also is observed in **Table 5.2**. Between 50-90  $\mu\text{m}$  lengths, the adsorbate is flattened. This is where the wall between the 2<sup>nd</sup> and 3<sup>rd</sup> bend is stationed. After 90  $\mu\text{m}$  the adsorbate decreases, and between 110 and 155  $\mu\text{m}$  the profile is flattened. On time 0.3 seconds in Figure (B1), the concentration bulk is located between the second and the eighth bends. The degradation of concentration shown in (B1) happens due to the effect of diffusion. From (B2), more adsorption is observed with typical profile follows (A2). At

simulation time 0.6, the concentration has been transported further and diffused inside the microchannel. The amount of the adsorbate is also increased and the shape of the profile is affected by the configuration of the geometry of the microchannel. It seems that the adsorption at the bends after the first one always decreases, and then flattened after the corresponding bend. It means that there is less adsorption at the bends than at the wall after the bend, where this particular wall is perpendicular to the direction of the concentration flow.

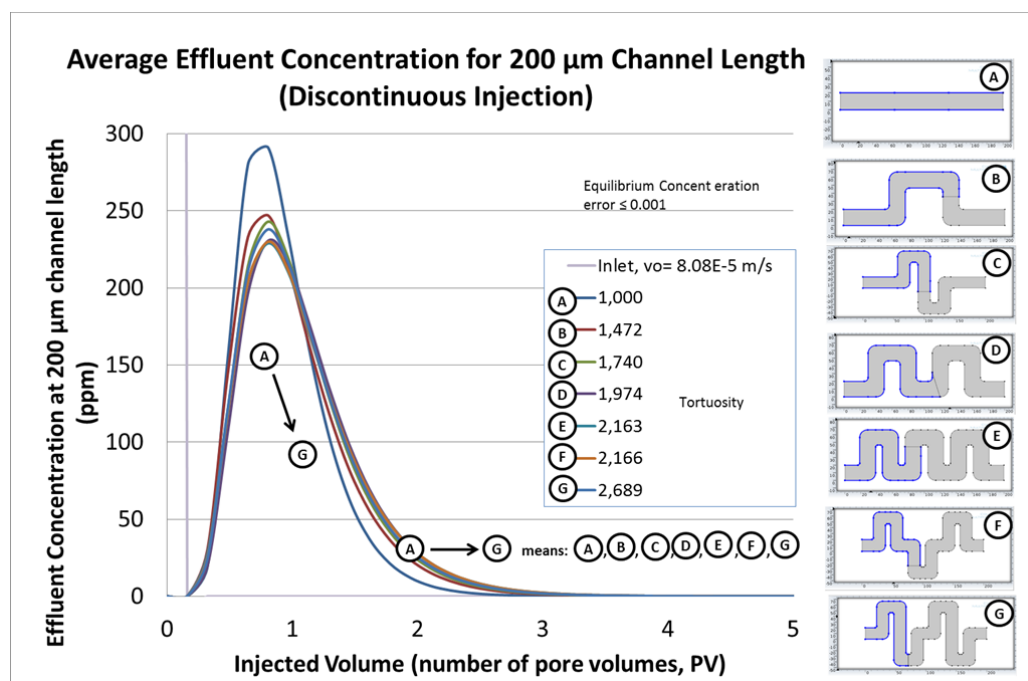


**Figure 5.5:** Effluent concentration vs. injection volume at the 200- $\mu\text{m}$  outlet boundary for discontinuous injection for different tortuosity

The profile of the effluent concentration against the injection volume is shown in **Figure 5.5**. This profile is obtained from the average effluent concentration measured at the outlet boundary of the microchannel during the simulation. The profile of the effluent concentration in the discontinuous injection is different from the effluent concentration for the continuous concentration injection. The increase of the effluent profile in **Figure 5.5** indicates the breakthrough that occurs at the outlet. It is important to restate that the length all tortuosity channel is identical, i.e. 200  $\mu\text{m}$ . It is observed that the profile increase for all tortuosity cases happens at the same injection

volume. Since the injection volume is proportional with the injection time, and since the investigation is conducted under a similar injection velocity and microchannel length, it means that the breakthrough of all cases happen roughly in the same time.

Typically, the average effluent concentration increases rapidly until attaining a maximum value and then decreases until reaching an asymptotic profile to a zero value. The effluent concentration increase shows a build-up concentration at the outlet as the front of the main concentration passes the corresponding boundary. The gradient of the effluent concentration varies inversely to the magnitude of the tortuosity. It means that less injection volume is required to transport similar amount of nanoparticle to the same distance in a microchannel with less tortuosity than in the higher one. This is also in agreement with the magnitude of the maximum value of the effluent concentration in **Figure 5.5**. Briefly, this means that the injected particles move easier the microchannel with simple configuration than in the microchannel with higher degree of complexity.

The effluent concentration measured at the outlet is the concentration of the injected nanoparticles that is transported without sustaining any adsorption. Some of the injected nanoparticle is adsorbed on the microchannel wall due to the concentration difference between the bulk and the microchannel wall. Meanwhile, the rest of the injected nanoparticles that remains in the main bulk pass through the outlet. After the main bulk passes through the system, the concentration inside the channel is less than the concentration on the microchannel wall. This is when the desorption mainly happens. Since the nanoparticles are treated as a dilute species, only those adsorbed to the wall will be left behind. The concentration difference between the fluid bulk and the microchannel wall is wider as more concentration flushed out from the system. This difference initiates and enhance the desorption mechanism, transporting the previously adsorbed nanoparticles back to the fluid in the microchannel. The tail observed in the effluent concentration reach the maximum value indicate the desorption.

The magnitude of the gradient decrease and the length of the concentration tail is not the same for all case of tortuosity. Steeper gradient decrease is observed in **Figure 5.5** for the microchannel with low tortuosity. Steep gradient downwards after the maximum concentration value indicates that the concentration difference between the wall and the fluid bulk decrease rapidly. This concentration difference enhances the desorption

mechanism. The concentration profile gradually decreases after roughly 1 pore volume, and then follows an asymptotic line in the end of the profile, indicating the process of desorption happens in the system.

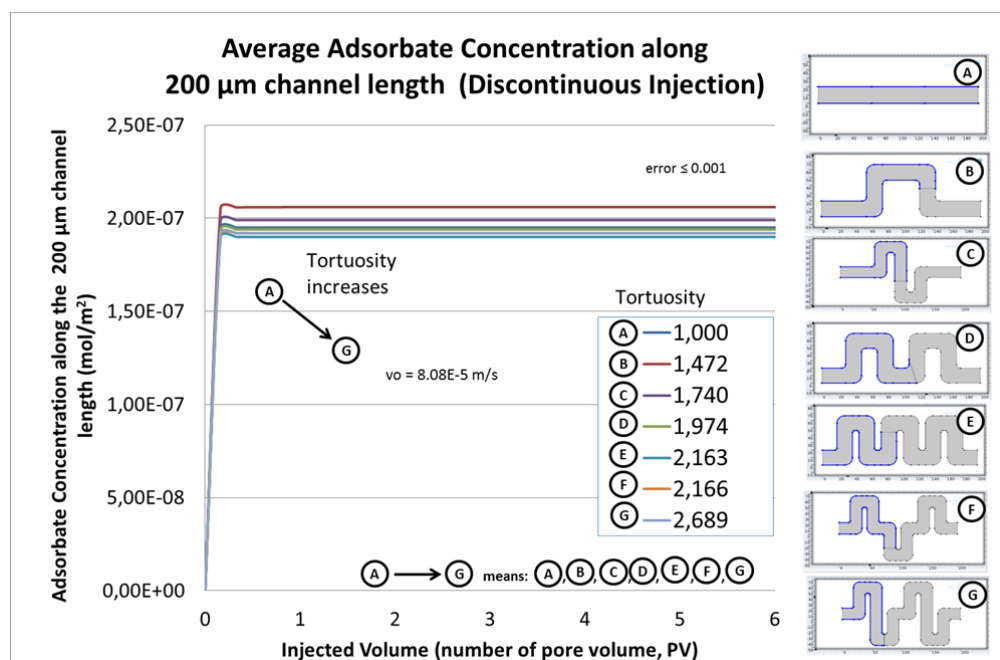


**Figure 5.6:** Adsorbed concentration of the nanoparticles vs. injection volume at the 200  $\mu\text{m}$  outlet boundary for discontinuous concentration injection

**Figure 5.6** shows the trend of the average adsorbate concentration on the microchannel for a discontinuous injection concentration against different injection volume. In this case, the concentration is measured on a similar adsorption surface area for all tortuous microchannels. It is observed that the adsorbate concentration starts instantaneously at the beginning of the simulation. During the simulation, the adsorbate concentration increase until reaching a profile with a zero or a very small gradient, indicating no or very little desorption. Some particles (adsorbate) remains on the walls even after inlet concentration reduced to zero. The magnitude of the adsorbate concentration in the case of discontinuous injection is much smaller than the system with continuous nanoparticles injection. This happens because the latter has unlimited nanoparticles supply from the inlet boundary during the simulation.

A short and curvy profile is observed just before the profile is flattened. In the duration, some of the particles are adsorbed on the microchannel wall at the beginning. As the injection continuous, some of the injected particles are desorbed back into the channel. This feature happens because at the beginning the effect of diffusion transports some of the nanoparticle concentration upfront the main bulk towards the outlet boundary. Some of these nanoparticles are adsorbed on the microchannel wall. The main nanoparticles concentration follows and more adsorption happens due to the effect from the advection. However, the system tries to reach its equilibrium condition. Hence, some of the adsorbed nanoparticles are desorbed back into the channel to balance the concentration between the wall and the internal of the microchannel.

The average adsorbate concentration appears to vary inversely to the magnitude of the tortuosity. This is shown in **Figure 5.6** that high adsorbate concentration is found in the microchannel with simpler configuration than the more complex one. This happens because the interaction access between the injected nanoparticle concentration and the wall is more efficient in the microchannels without bends. This finding has a good agreement with the one discovered previously in the system with continuous nanoparticle concentration injection. The detail explanation refers back to Section 5.4.1.

Velocity magnitude and a typical streamlines at a corner of a microchannel bend is shown in **Figure 5.7**. The surface represents the velocity field in the system and the dark lines represent the streamlines of the injected concentration. The streamlines at the bend are not visible where the magnitude is very low compare to the ones in the centre of the microchannel. There are likely eddy currents [253] happens in the bend that reduces contact between the concentration and the microchannel wall. This is discussed further in Chapter 6 for the concentration distribution in microchannels with dead end.

Injection volume is proportional to the duration of the injection. Therefore, the gradient of the adsorbate concentration also shows the rate of the adsorption on the microchannel wall. It appears that the system in a microchannel with high tortuosity needs longer time to reach the equilibrium condition compare to the system with simpler microchannel configuration.

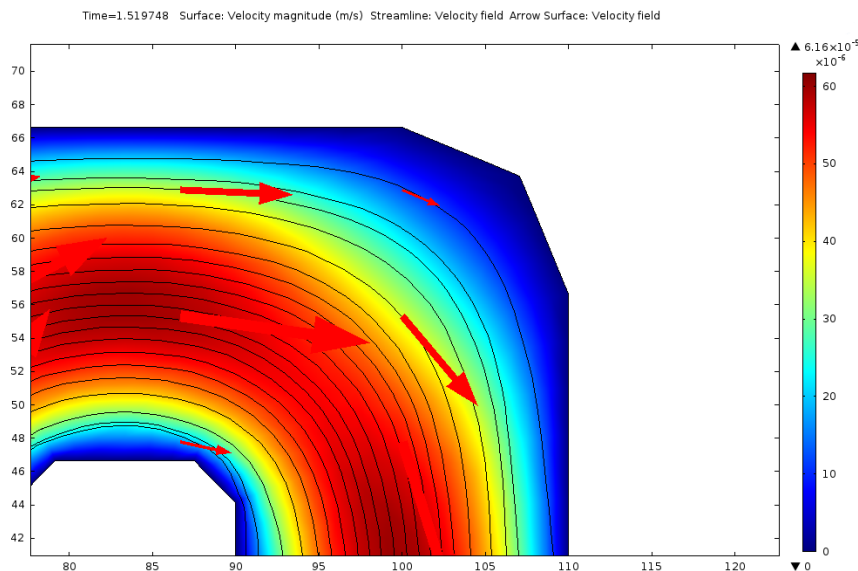


**Figure 5.7** Velocity field magnitude and a typical streamlines at a corner in a microchannel bend. Taken one of the bends at microchannel C at simulation time 1.52 seconds.

### 5.4.3 The Relation between the Adsorption and the Tortuosity for Microchannel System with Similar Microchannel Length

The relation between the adsorption and the tortuosity for different injection velocity is investigated. Similar with the simulation conducted in the previous section in this chapter, empty microchannels with different tortuosity configurations are prepared. All microchannels in the simulation have a similar length, i.e.  $200 \mu\text{m}$ .  $12500 \text{ ppm}$  of nanoparticle concentration is injected from the inlet boundary of the microchannel until its equilibrium condition achieved. The equilibrium adsorbate concentration is retrieved from the value of the adsorbate concentration in the equilibrium condition. The equilibrium condition is when the rate of adsorption equals the rate of the desorption. This condition is, for example shown the plateau of the adsorbate concentration profile in **Figure 5.6**. In the simulation, the plateau is accepted as the equilibrium condition when the difference of the current and the concentration magnitude after the previous time step is less than  $0.01\%$ . This percentage is simply known as the error. For sensitivity study, the simulation is conducted under three different constant injection velocity, i.e.  $v_0 = 8.08 \times 10^{-5} \text{ m/s}$ ,  $v = 0.5v_0$ , and  $v = 2v_0$ . The adsorption and desorption mechanism follows Freundlich adsorption isotherm mechanism which is governed by the concentration difference between the fluid bulk and the

adsorption surface. Hence, the equilibrium adsorbate concentration and the corresponding tortuosity is plotted and investigated.

The situation in the discontinuous injection is different from the continuous injection. Except what is desorbed from the wall, there is no more bulk concentration after the main concentration leaves the domain. As there appears to be no desorption, there must be no adsorption either. The equilibrium average adsorbate concentration is therefore the 'final' adsorbate concentration.

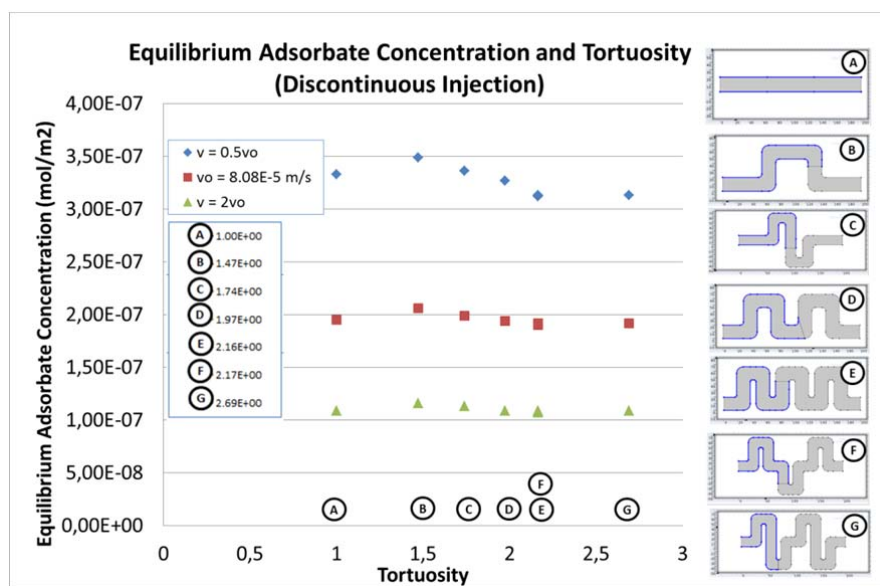


**Figure 5.8:** The equilibrium adsorption and desorption concentration for similar length

In this study, it is discovered that the advection kinetic contributes more dominant effects to the adsorption than the tortuosity. The plot of the final concentration and the corresponding tortuosity is found in **Figure 5.8**. In the figure, high injection velocity is specified by the green colour marks, the medium injection velocity is specified by the red coloured marks, and the high velocity is specified by the blue coloured marks. In the system with high velocity, the final adsorbate concentration is comparable. It is shown by the green marks whose trend is situated linearly. When the injection velocity is lessening, the tortuosity starts to give more effect to the adsorption. This is shown by the trend of the red and the blue marks that indicates the velocity increase correspondingly.



boundary of each microchannel under three different steady velocities, i.e.  $v_0 = 8.08 \times 10^{-5}$  m/s,  $0.5v_0$  and  $2v_0$ . The adsorption and desorption mechanism follows Freundlich adsorption isotherm mechanism which is governed by the difference in concentration between the fluid bulk and the wall of the microchannel.

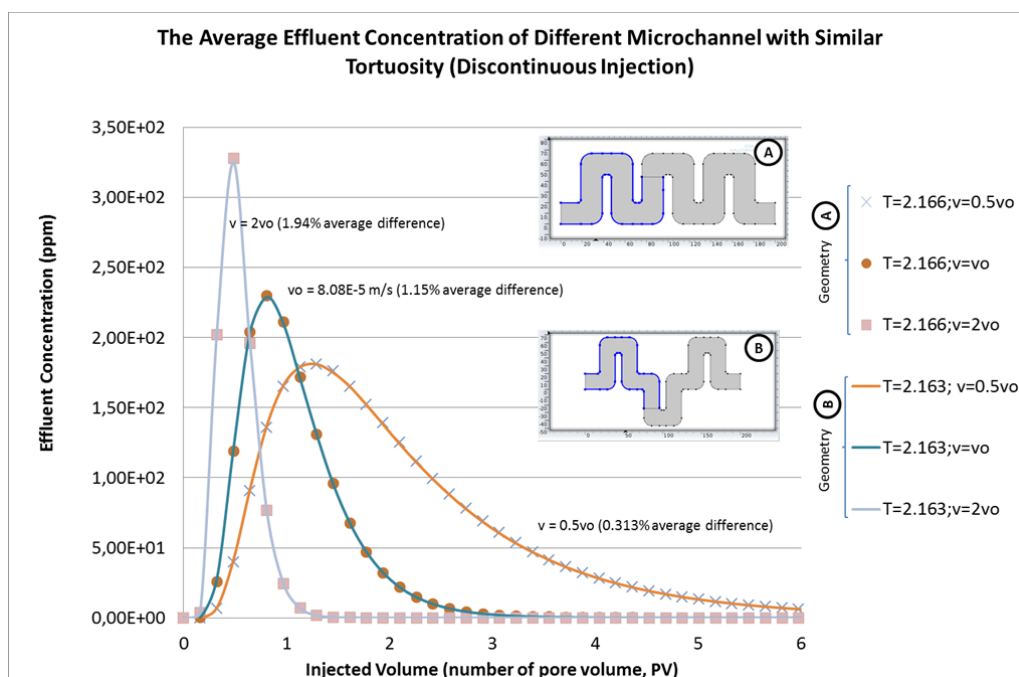


**Figure 5.10:** The effluent concentration of different microchannel with similar tortuosity.

The trend of the outlet effluent concentration for each case is plotted against the injection volume (measured in pore volumes) and results are shown in **Figure 5.10**. It is observed that the effluent concentration for similar tortuosity align to each other in a relatively high precision.

The effluent concentration for every simulation time step for both tortuosity configurations is compared. The comparison follows  $(c_{T=2.166} - c_{T=2.163})/c_{T=2.166}$ , where  $c_{T=2.166}$  is the effluent concentration that is observed at the outlet boundary for geometry A and  $c_{T=2.163}$  is for geometry B. The averages of the comparison are calculated by dividing the sum of all comparison measurements by the number of measurements. This parameter is known as average difference in this study. The average difference for  $v=0.5v_0$  is 0.313%, for  $v=v_0$  is 1.15%, and  $v=2v_0$  is 1.94%.

These errors are relatively small and can be neglected. Therefore, it is possible to utilise the tortuosity as a key parameter to indicate channel complexity. In addition, the influence of the velocity to the effluent concentration can be observed easily.

Higher injection velocity transports more particles to the outlet in less time than the low velocity does. Therefore, the magnitude of the maximum effluent concentration is large for high injection velocity. The high injection velocity transports the fluid bulk altogether, leaving a short tail behind that shown by the rapid decrease of the concentration line after reaching the peak. The tail shows the concentration flow that was left behind due to the diffusion.

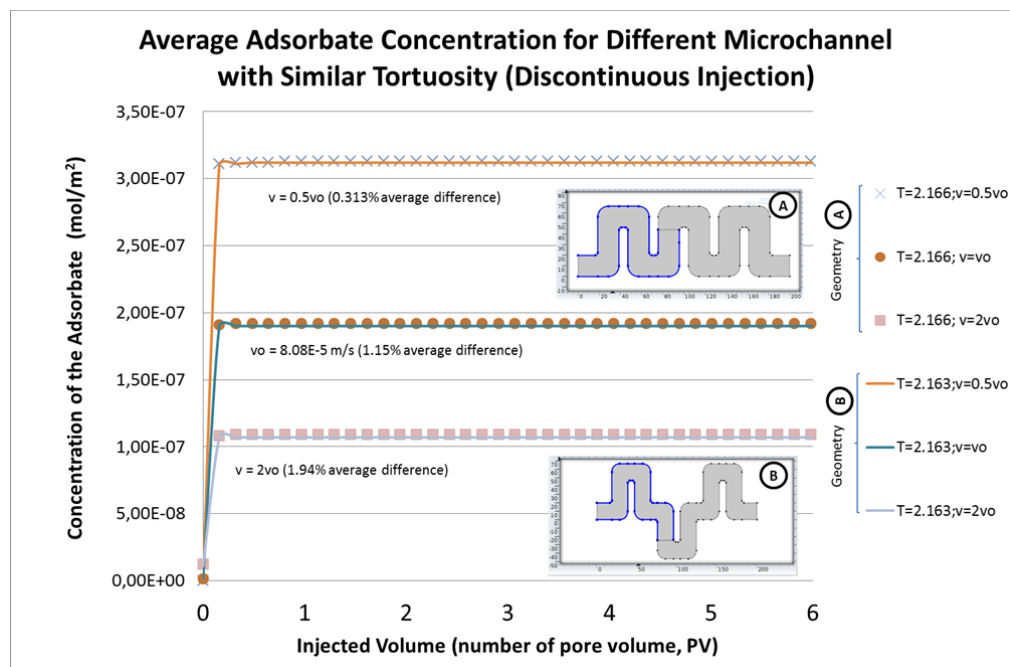


**Figure 5.11:** The concentration of the adsorbate for different microchannel with similar tortuosity.

The trend of the adsorbate concentration versus injection volume is shown in **Figure 5.11**. The profile of the adsorbate concentration increases rapidly at the beginning of the simulation and then is flattened after a certain injection volume. It is again discovered that the amount of injection to convey the system into equilibrium is affected by the injection velocity. Fluid flow with lower injection velocity allows a better contact between the

concentration in the fluid bulk and the microchannel wall. Hence high injection velocity encourages the concentration adsorption onto the microchannel wall. This is shown in **Figure 5.9**, where the system with the lowest injection velocity has the largest concentration plateau of all.

Again, it is also observed that there is a slight curve at the adsorbate profile just before it reaches its equilibrium concentration. After adsorption that occurs at the beginning, some of the adsorbed nanoparticles are desorbed back into the microchannel. The higher adsorption happens at the beginning occurs due to the influence of the diffusion that diffuse the concentration in front of the main bulk. When the main concentration bulk comes, some of the adsorbed concentrations are desorbed back to the channel to balance the concentration between the wall and the microchannel wall.

The adsorbed concentration for every simulation time step for both tortuosity configurations is also compared. The comparison follows  $(c_{B_{T=2.166}} - c_{B_{T=2.163}})/c_{B_{T=2.166}}$ , where  $c_{B_{T=2.166}}$  is the adsorbate concentration that is observed at the outlet boundary for geometry A and  $c_{B_{T=2.163}}$  is for geometry B. The averages of the comparison are calculated by dividing the sum of all comparison measurements by the number of measurements. In this study, this parameter is known as average difference. The average difference for  $v=0.5 v_0$  is 0.313%, for  $v=v_0$  is 1.15%, and  $v=2v_0$  is 1.94%, which are similar to the comparison which derived from the effluent concentration.

It appears that the channel geometry does not give much adsorption difference for the two geometries. The adsorption differences for both channel geometry are relatively small. It means that the adsorption can be related directly to the magnitude of the tortuosity.

## 5.5 Adsorption in Identical Inlet-Outlet Distance Tortuous Microchannel

The second study is to investigate the behaviour of the concentration that flows inside various tortuous microchannels with equal inlet-outlet distance. The surface area of the microchannel with equal inlet-outlet *distance* is not always similar with the one with equal inlet-outlet *length*. For a constant diameter, microchannels with equal inlet-outlet length always

---

have similar surface area. However, it is not always the same with microchannels with equal inlet-outlet distance. The latter is very dependant to the configuration of the microchannel, i.e. tortuosity. The microchannel with higher tortuosity has greater surface area than the microchannel with lower tortuosity. Since the surface area of the microchannel depends on the tortuosity, adsorbate mass is considered to use for comparison instead of using adsorbate concentration, since using the latter does not give a fair result.

In this study, the configuration of the microchannels follows the one used previously for the microchannel with identical length; however, the full length of microchannel is now considered. There are two injection types used in the system, i.e. continuous and discontinuous particles injection. The particles are transported along a steady state flow field inside the microchannel. The injection volume is linearly proportional to the simulation time because the concentration flows under a steady injection velocity. Effluent concentration, adsorbate concentration and adsorbate mass are investigated which values are obtained from the average along the corresponding boundaries.

### **5.5.1 Continuous Injection in Tortuous Microchannels with Identical Length in Identical Inlet-Outlet Distance**

In this study, seven tortuous microchannels with diameter of 20  $\mu\text{m}$  and 200- $\mu\text{m}$  inlet-outlet distance are prepared. The elongation shape of each microchannel is not similar; therefore, the corresponding tortuosity is also different. Initially, each microchannel is empty from any nanoparticles concentration. 12500 ppm of nanoparticle concentration is then injected continuously from the left boundary of the microchannel with a constant injection velocity of  $8.08 \times 10^{-5}$  m/s. Some of the particles are adsorbed on the microchannel wall until the system reaches its equilibrium condition. The adsorption and desorption mechanism follows Freundlich adsorption isotherm mechanism which is governed by the concentration difference between the fluid bulk and the adsorption surface.

The relation between the effluent concentration and the injection volume for nanoparticle continuous injection is shown in **Figure 5.12**. In this study, the injection volume is proportional to the simulation time. The injection volume is specific for each case because it utilises relevant pore

volume for each channel configuration. The effluent concentration rises at the beginning of the simulation and then gradually flattens. It is discovered that the required injected volume for the breakthrough is inversely varies with the magnitude of tortuosity. In other words, the tortuosity delays the breakthrough. This occurrence indicates that the concentration moves easier in the less tortuous microchannel. This means the effect of flow and diffusion is more dominant for the concentration transport for microchannel with less tortuosity.

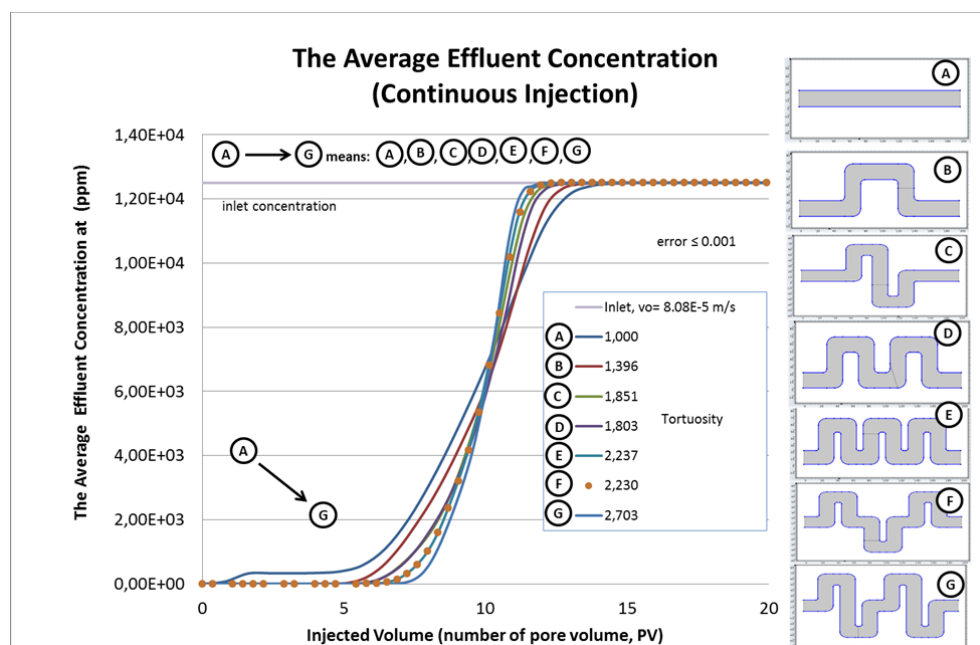


**Figure 5.12:** Effluent concentration at 200  $\mu\text{m}$  channel length for continuous PPCA injection (ppm)

According to expectation, the magnitude of the effluent concentration in every case eventually reaches the inlet concentration. This is when the microchannel is saturated with the concentration and the adsorption and desorption are in equilibrium. In this steady state condition, the concentration difference between the fluid bulk and the microchannel wall remains constant due to comparable adsorption and desorption rate in the system. Hence, the concentration detected at the outlet is similar with the injected concentration at the inlet.

The trend of the adsorbate concentration is shown in **Figure 5.13**. The concentration of the adsorbate increases due to the unlimited supply of the particles in the fluid bulk. The rate of the adsorption is shown by the gradient increase of the adsorbate concentration. The rate of the adsorption appears to be comparable for all cases. This happens because the adsorption and desorption parameter used for all cases in the simulations are the same. The profile of the adsorbate concentration of all cases is also in one alignment, which shows equilibrium condition for the adsorption-desorption on the area of each microchannel has been comparably achieved.

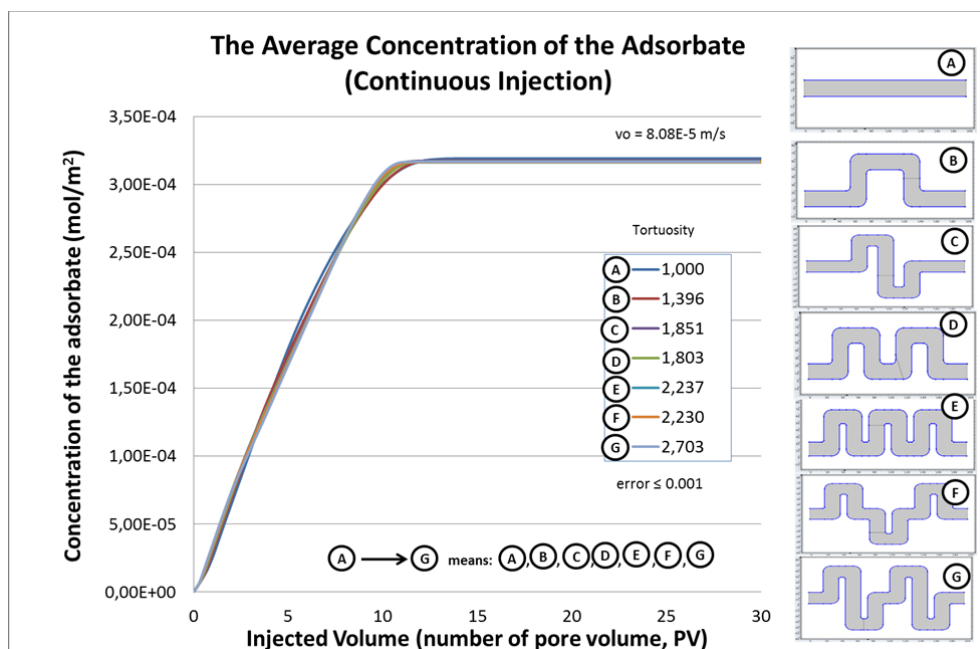


**Figure 5.13:** Effluent concentration at 200  $\mu\text{m}$  channel length for continuous PPCA injection (ppm)

In this study, each microchannel has its own specific surface area due to the corresponding shape and tortuosity. Therefore, the amount of the adsorbate on the microchannel wall is not comparable using the concentration since the magnitude of this parameter is normalised to the corresponding microchannel surface area. The mass of the adsorbate is then used for investigation because this parameter indicates the actual amount of the adsorbate on the wall. The profile of the adsorbate mass for different tortuosity is shown in **Figure 5.14**. The adsorbate mass profile in

this figure is plotted against the injection volume, which is independent to the simulation time. Observing the trend, there are more mass of particles adsorbed in the microchannel with higher tortuosity. There are two reasons for this. The first one, the microchannel with higher tortuosity has larger surface area than the lower one, allowing more adsorption happens on to it. The second one is due to the bends that happens in the system. The bends alter how the wall of the microchannel situated relatively to the direction of the flow. The possibility for nanoparticles to be adsorbed on the wall is increased when the wall is facing the direction of the concentration flow. This is validated with investigating the profile of the concentration on the microchannel, which is shown in Table 5.2.

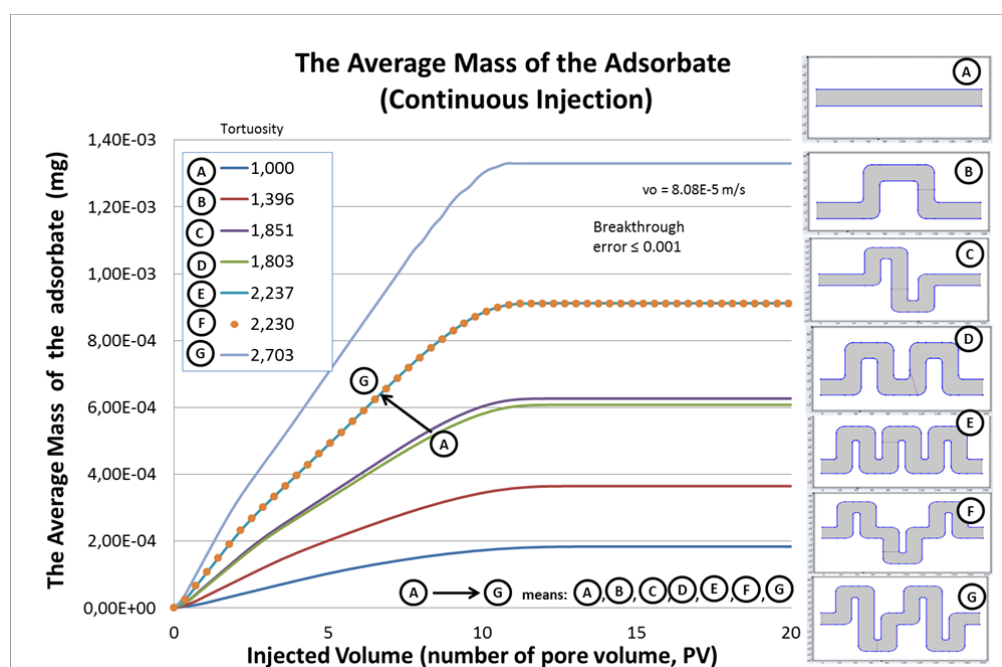


**Figure 5.14:** Effluent concentration at 200  $\mu\text{m}$  channel length for continuous PPCA injection (ppm)

**Table 5.3.** shows the comparison of the distribution profile of the injected nanoparticle and the corresponding adsorbate concentration for continuous injection for geometry A, B, and E. The first column shows the nanoparticles concentration distribution in the microchannel (units in  $\text{mol}/\text{m}^3$ ) and the second column shows the corresponding adsorbate concentration for each geometry ( $\text{mol}/\text{m}^2$ ). The data are obtained from the average value

of the specific location in the microchannel after the injection is conducted for 2 seconds.

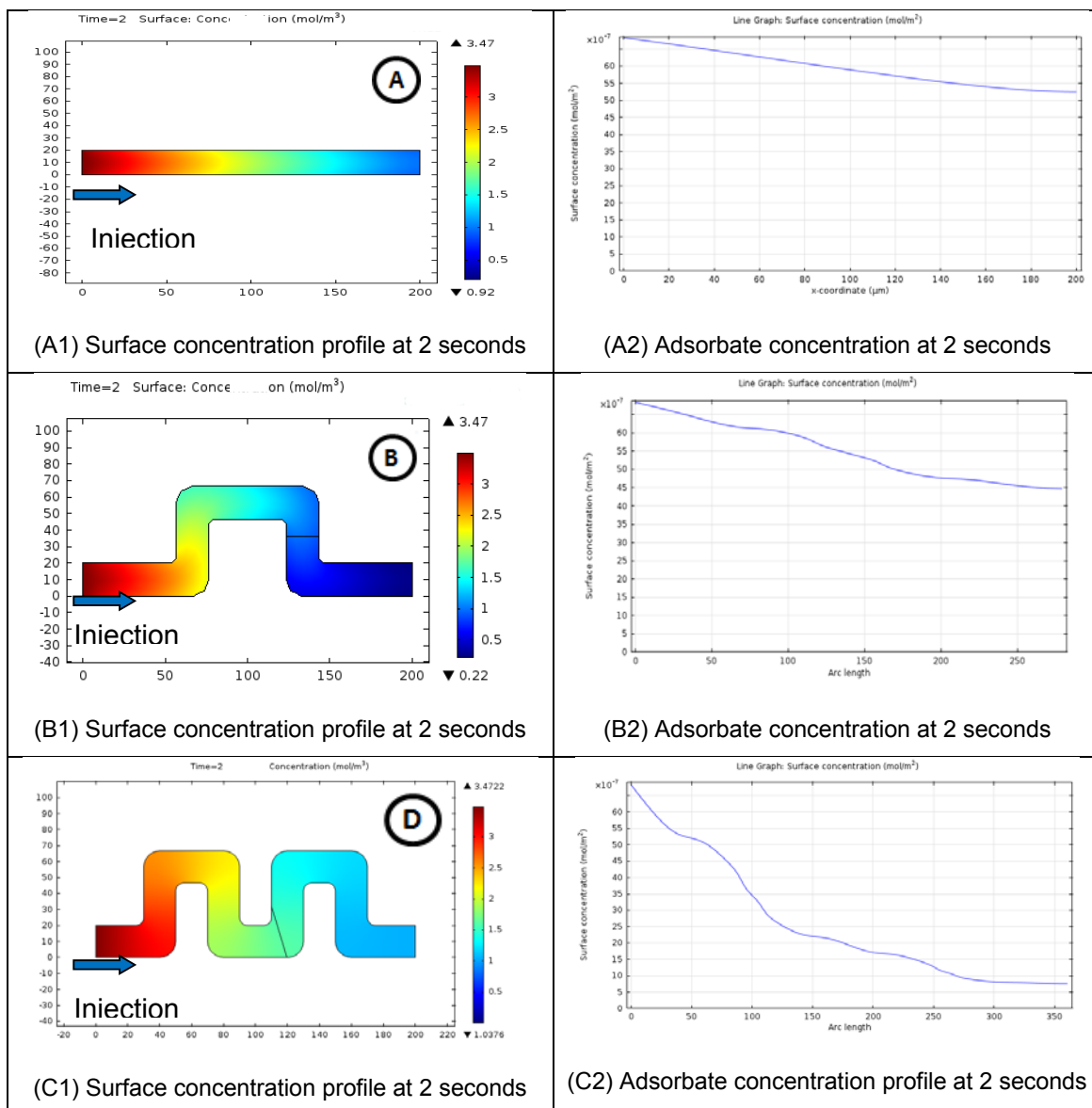


**Table 5.3 :** Distribution profile of the injected nanoparticle and the corresponding adsorbate concentration on the wall for geometry A, B, and D for continuous injection. The unit in x-axis is in  $\mu\text{m}$ .

Looking at the nanoparticle concentration profile in the first column in **Table 5.3** figure (A1), (A2) and (A3), it seems that at this time step the microchannel has been filled with comparable nanoparticles concentration.

For this moment, the concentration at the inlet of all the microchannel is similar, i.e.  $70 \times 10^{-7} \text{ mol/m}^3$ . However, the adsorbate distribution along the wall is not similar for each geometry. This is shown by the adsorbate concentration profile in the second column. The adsorbate concentration in (A2) shows a linear profile. The adsorbate concentration in (B2) and (B3) shows some undulations profile that corresponds with the bends in the microchannel. Adsorbate concentration is always reduced at the bends; however, it increases on the surface wall after the bends that perpendicular to the direction of the injection fluid flow-path. The figure for the distribution for surface concentration and the adsorbate concentration for all microchannel configurations in different simulation time is shown in Appendix C-1.

### 5.5.2 Discontinuous Injection in Tortuous Microchannels with Identical Length in Identical Inlet-Outlet Distance

In this section, the investigation is conducted to discuss the behaviour of the concentration that is discontinuously injected at the beginning of the simulation. Similar with the previous study,  $20 \mu\text{m}$  diameter with  $200 \mu\text{m}$  length microchannel is used as the domain in the study. Seven microchannels with different tortuosity are used for the sensitivity study. The microchannels are initially empty with no concentration accumulation on the walls. Then, 12500 ppm of nanoparticles concentration is injected into the microchannel from the inlet boundary between 0 to  $t_{\text{max}}/1000$  seconds, where  $t_{\text{max}}$  is the maximum simulation duration time.  $t_{\text{max}}$  is selected when the effluent concentration profile reaches its equilibrium condition. The equilibrium concentration is obtained by investigating the value of  $c_t$  when  $\frac{(c_t - c_{t+1})}{c_t} < 0.001\%$ . In this case,  $c_t$  (ppm) is the average effluent concentration at time  $t$ . After the period of concentration injection, the carrier fluid continues to flow in through the inlet at constant rate for the whole simulation duration. A mechanism of adsorption and desorption is expected to happens on the microchannel wall that follows the Freundlich adsorption isotherm mechanism. The mechanism is governed by the difference in concentration between the fluid bulk and the surface of the microchannel. The trend of the effluent concentration, mass and the concentration of the adsorbate are discussed.

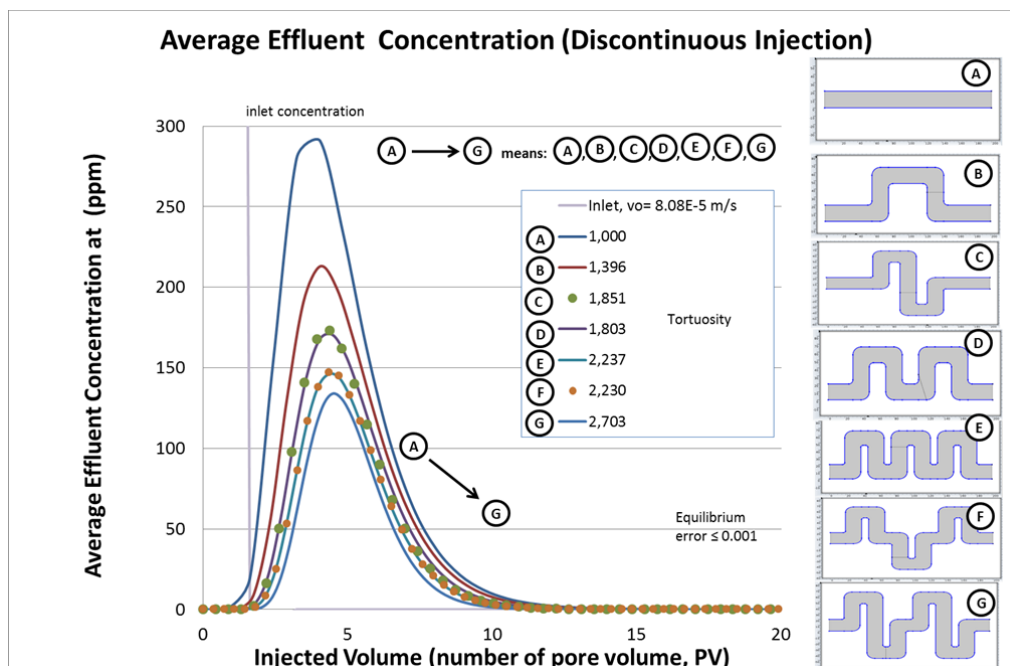


**Figure 5.15:** Average effluent concentration for discontinuous particles injection

The profiles of the average effluent concentration measured at the outlet boundary of the microchannels are shown in **Figure 5.15**. The magnitude of the concentration is much less than the one measured in the continuous injection (i.e. **Figure 5.12**). In this case, the amount of injected nanoparticles is limited due to the discontinuous concentration injection applied in the system. Not all of the injected nanoparticles transport out of the microchannel because some of them are adsorbed onto the microchannel wall. It is again observed that the required injection volume is proportional to the magnitude of the tortuosity. This indicates that concentration transport is easier in the least tortuous microchannel. The magnitude of the average effluent concentration is the highest for the least tortuous microchannel. Inversely, the magnitude of the average effluent concentration is the least for the most tortuous microchannel. This shows that the magnitude of the average effluent concentration varies inversely to the magnitude of the tortuosity. It means that there are more nanoparticles adsorbed as the tortuosity of the microchannel increases. This observation has a good agreement with the one discovered in the study with the continuous injection.

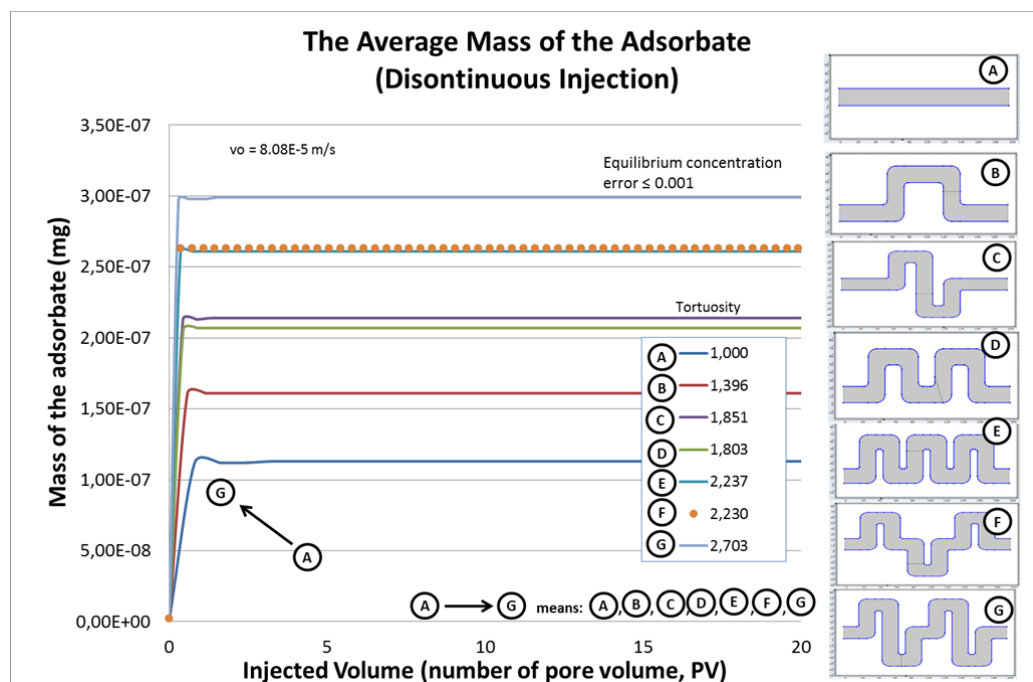


**Figure 5.16:** Mass of the adsorbate for discontinuous particles injection

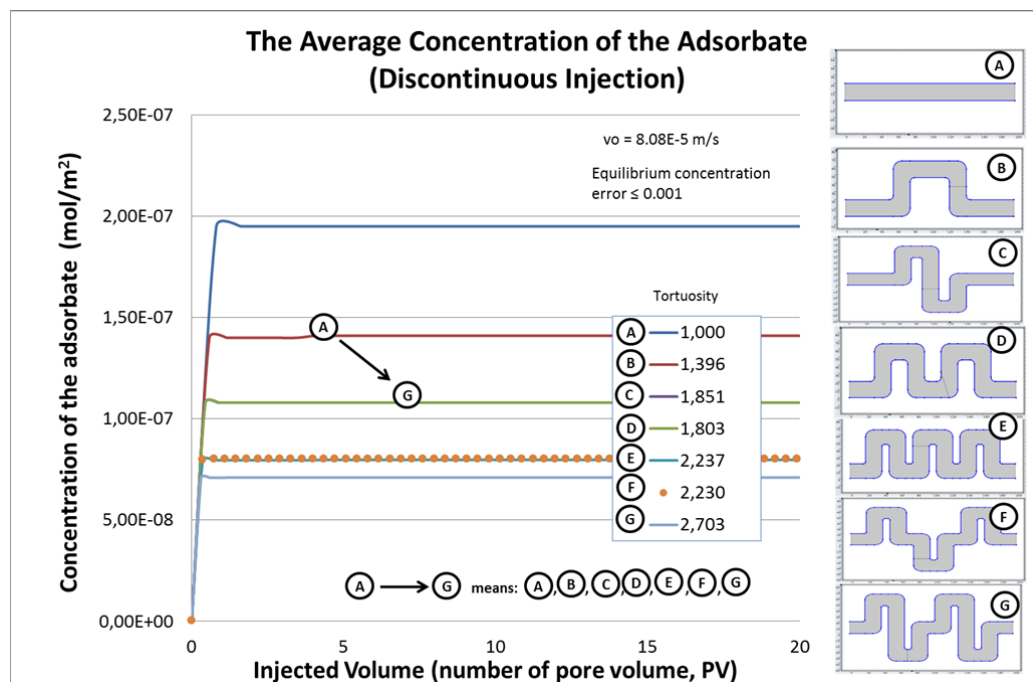


**Figure 5.17:** Concentration of the adsorbate for discontinuous particles injection

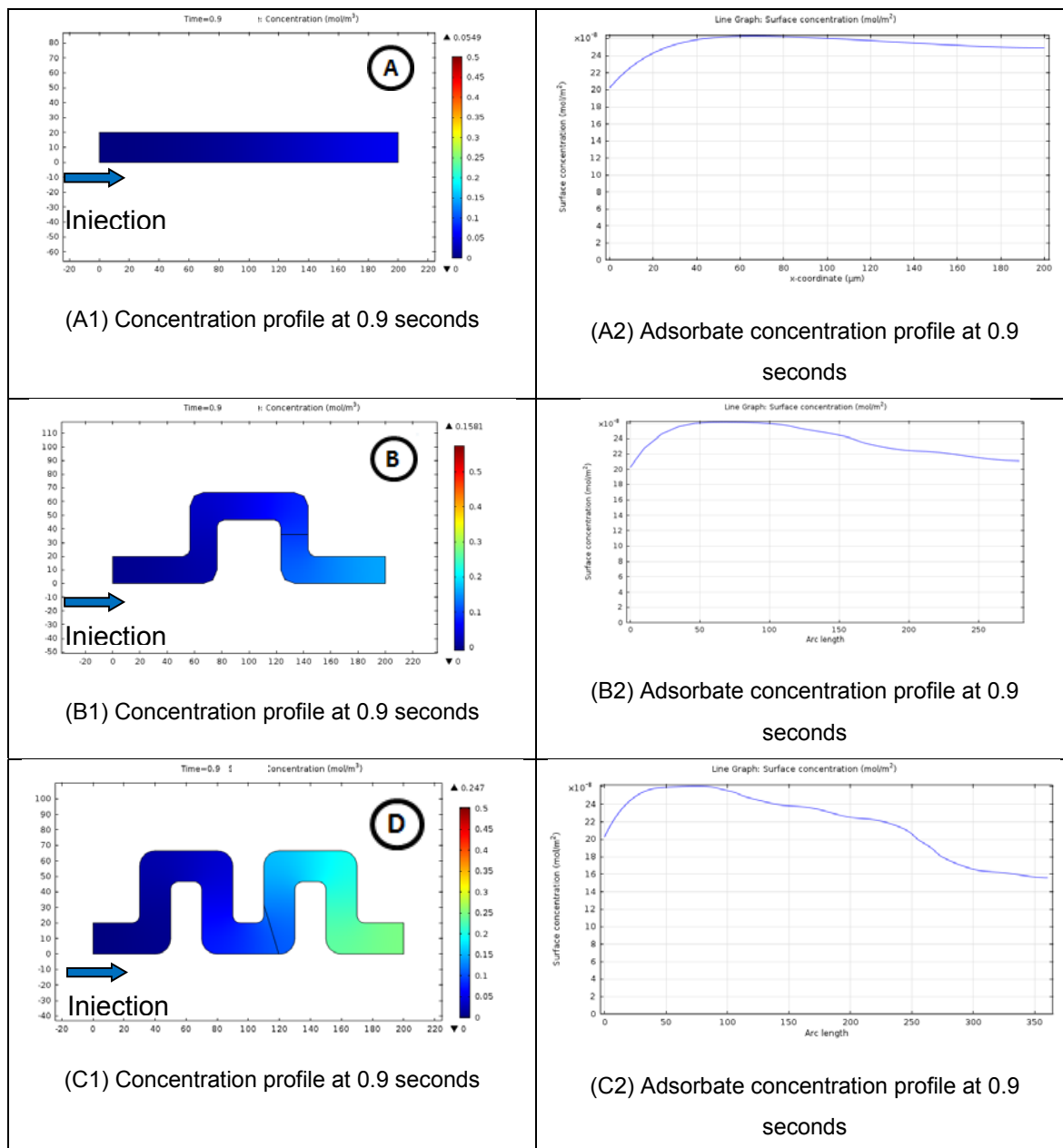


**Table 5.4 :** Distribution profile of the injected nanoparticle and the corresponding adsorbate concentration on the wall for geometry A, B, and D for discontinuous injection. The unit in x-axis is in  $\mu\text{m}$ .

The profile of the average adsorbate mass for different injected volume is shown in **Figure 5.16**. For each case, it is discovered that there is a short kink in the adsorbate mass profile at the beginning of the breakthrough. This is seen only because of the smoothing mechanism of the profile connecting the data obtained from the simulation.

---

The trend of the adsorbate concentration is, however, inversely correlated with the tortuosity since it takes into account the surface area of the microchannel. However, the result using adsorbate profile is incomparable because the surface area for each case is not similar. The profile of the adsorbate concentration and the injection volume is shown in **Figure 5.17**.

**Table 5.4** shows the comparison of the distribution profile of the injected nanoparticle and the corresponding adsorbate concentration for discontinuous injection for geometry A, B, and E after 0.9 seconds. In this timestep the main bulk concentration ( $\text{mol/m}^3$ ) has left the microchannel that is shown by the low magnitude of nanoparticles concentration in the left column in **Table 5.4**. The adsorbate concentration ( $\text{mol/m}^2$ ) is shown on the right column in the table.

The distribution of the adsorbed particles on the walls is not the same for each geometry. The adsorbate concentration on the wall of the microchannel A is smooth, starting from  $20 \times 10^{-4} \text{ mol/m}^2$ , and it increases up to  $27 \times 10^{-4} \text{ mol/m}^2$  at the length of 60-80  $\mu\text{m}$ , then it decrease towards the outlet. In microchannel B, concentration at the inlet is also  $20 \times 10^{-4} \text{ mol/m}^2$ , then it builds up until 50  $\mu\text{m}$ . It is at its maximum value between 50 and 90  $\mu\text{m}$ , where it is located at the surface after the bend. After 100  $\mu\text{m}$ , the profile decreases steeper than in microchannel A.

In microchannel D, the effect of tortuosity looks more obvious. The adsorbate concentration starts at  $20 \times 10^{-4} \text{ mol/m}^2$ , then it increase until the first bend at 40  $\mu\text{m}$ . The adsorbate keeps high until the second bend at 80  $\mu\text{m}$ , then decrease all the way until the outlet. The decrease is steeper than the other two geometries with a few undulation that corresponds with the bends in the channel. The adsorbate concentration on the bends is slightly lower than in the adjacent straight wall at its surrounding location.

### **5.5.3 The Relation between the Effluent Concentration and the Tortuosity for Microchannel System with Equal Inlet-Outlet Distance**

In this part, the relation between the effluent concentration and the tortuosity for microchannel system with equal inlet-outlet distance is discussed. Data for the investigation is taken from the simulation results

conducted in Section 5.5.2. However, the simulation was conducted under three different velocities, i.e.  $v_0=8.08 \times 10^{-5}$  m/s,  $v=0.5v_0$ , and  $v=2v_0$ .

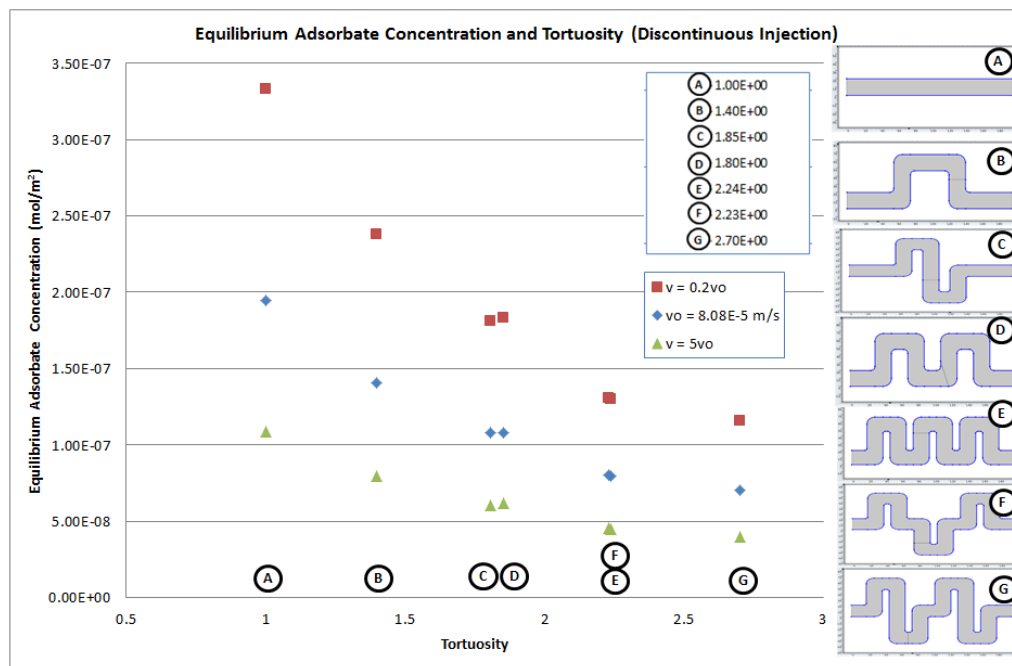


**Figure 5.18:** Adsorbate concentration for discontinuous particles injection for 3 difference velocities, i.e.  $v_0$ ,  $0.5x v_0$ , and  $2x v_0$ , where  $v_0=8.08 \times 10^{-5}$  m/s

The profile of the equilibrium adsorbate concentration versus the tortuosity is shown in **Figure 5.18**. The equilibrium adsorbate concentration is taken from the result in Section 5.5.2 on the value of  $c_t$  when  $\frac{(c_t \times c_{t+1})}{c_t} < 0.001\%$ . In this case,  $c_t$  (mol/m<sup>2</sup>) is the adsorbate concentration at time  $t$ . The magnitude of the adsorbate concentration varies inversely to the injection velocity. This is consistent with the observation from the previous results i.e. the study for the case with the continuous injection. However, it is more obvious to discover that the adsorption concentration is influenced by the tortuosity of the microchannel by conducting the simulation for the discontinuous particles injection than the continuous injection.

The concentration of the adsorbate varies inversely with the magnitude of the tortuosity. The effect of tortuosity to the adsorbate concentration is more remarkable for the microchannel system with higher injection velocity than the lower one. Adsorbate concentration is the highest

for the microchannel system with the lowest tortuosity and the highest injection velocity. Inversely, the lowest adsorbate concentration is observed for a microchannel system with highest tortuosity and the lowest injection velocity. This resembles one of the previous results that investigates the relation between tortuosity and the fractal filling fraction [252], where the fractal filling fraction is represented as adsorbate concentration in this case. However, it is not fair to use adsorbate concentration for comparison since these parameters consider the corresponding adsorption area in the microchannel that is not similar from one to another. It is important to investigate the adsorbate mass since this parameter indicates the actual adsorption on the surface excluding the area consideration.

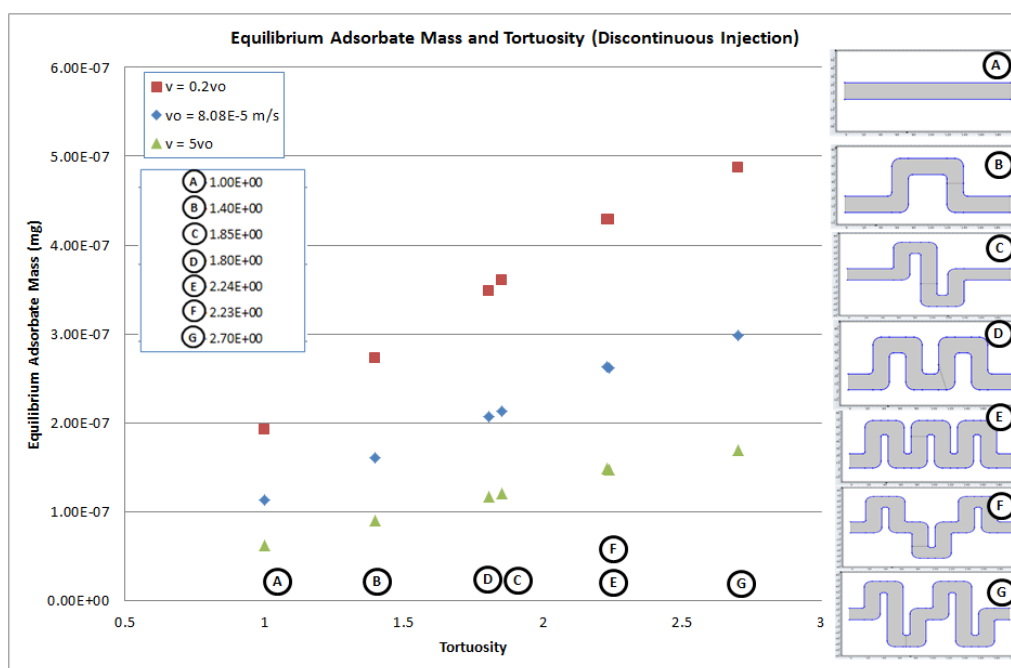


**Figure 5.19:** Mass of the adsorbate for discontinuous particles injection for 3 difference velocities, i.e.  $v_0$ ,  $0.5x v_0$ , and  $2x v_0$ , where  $v_0=8.08 \times 10^{-5}$  m/s

The trend of the equilibrium adsorbate mass against the magnitude of the tortuosity is shown in **Figure 5.19**. The equilibrium adsorbate mass is taken from the result in Section 5.5.2 on the value of  $m_t$  when  $\frac{(m_t \times m_{t+1})}{m_t} < 0.001\%$ . In this case  $m_t$  (mg) is the adsorbate mass at time  $t$ . Investigating the equilibrium adsorbate mass in the microchannel system, it is discovered that the adsorbate mass is discovered the highest for the system with lowest

velocity in the most tortuous microchannel. On the other hand, the least adsorbate mass is found in the system with the highest velocity in the least tortuous microchannel. It is important to state that the amount of the injected nanoparticles is the same for all cases.

Difference in the discovery between the profile of the adsorbate concentration and the adsorbate mass occurs because the adsorption happens on the microchannel wall is not even. The adsorption at the bends tends to smaller than the wall after the bends when it is perpendicular to the direction of the flow. Reducing the injection velocity increases the interaction efficiency of the particles and the channel wall, resulting in more adsorption. However, the total adsorbate mass is found to be higher in the microchannel with higher tortuosity because, in this case, higher tortuosity means larger microchannel surface area.

## **5.6 Summary and Conclusion**

Investigation for the effect of microchannel complexity to the adsorption mechanism on to the microchannel wall is discussed in this chapter. The channel complexity is represented by the tortuosity [238], which is the ratio of the distance of two points with the actual length. Complexity in pore's geometrical structure has a significant influence to the flow easiness of the pore system. Transport properties in tortuous porous material has been investigated in many areas, e.g. fracture surface [248], lungs [249], metal foams[250], and aerogel [251, 252]. However, the investigation of porous media and the transport phenomena within has generally been limited to macroscopic measurement, which discussion for the microscopic pore structure has not been much covered [252]. This chapter is a revisit to investigate the latter as a contribution for study of transport in porous media. In this chapter, investigation for the effect of the complexity of the microchannel with the flow and adsorption/desorption process of the nanoparticle in the system is conducted.

The simulation was developed based on the 2D microchannel model in Chapter 4. Seven microchannel geometries with different tortuosity are utilised where two of them have similar tortuosity with different configuration. There are two conditions to be investigated, i.e. tortuous microchannel with similar length and tortuous microchannel with similar outlet-inlet distance. The first condition considers only the aspect of the complexity of the

---

microchannel. The second condition considers the aspect of microchannel complexity and the corresponding surface area. Both cases have different implication to the microchannel adsorption surface area. In the microchannels with equal length, the adsorption area for all microchannels are comparable. In the cases of microchannel with equal inlet-outlet distance, the surface area of the microchannel is proportional to the corresponding tortuosity magnitude. The simulation for both configuration is carried out under continuous and discontinuous nanoparticles injection. The investigation then is conducted by studying the effluent concentration, the adsorbate concentration, and the adsorbate mass for both continuous and discontinuous concentration injection. Then, for comparing the adsorption process, adsorbate concentration is used for investigation conducted for sensitivity study for microchannels with similar surface area. On the other hand, adsorbate mass can be used for investigation conducted for microchannels with various surface area. It is because the magnitude of adsorbate mass is not “normalised” by surface area of the domain.

For the case of the microchannel with equal length, tortuosity means the complexity of the channel. It is discovered that the magnitude of the channel tortuosity is proportional to the amount of the time and injected concentration needed by the system to reach the steady state condition. The steady state condition of the effluent concentration is the maximum effluent concentration whose value is similar to the injected concentration. This also indicates the equilibrium condition where the rates of adsorption and desorption are comparable. Microchannel system with a highly tortuous microchannel needs more time to reach the equilibrium concentration compare to the system with simpler microchannel configuration. The effect of microchannel complexity (tortuosity) for these parameter is more dominant when the tortuosity also represents the effective length of the microchannel.

The adsorption process happen more smooth and uniform on the microchannel with low tortuosity than the ones with more complex configuration. Adsorbate concentration is always reduced at the bends. Bends in the channel somehow reduce the sweep efficiency between the bend wall and the concentration in the fluid bulk. This phenomenon is related to the profile of velocity field in the region which is lower than its surrounding. However, the adsorbate increases on the surface wall after the bends that is located perpendicular to the direction of the injection fluid flow

---

path. The bends alter how the wall of the microchannel situated relatively to the direction of the flow. The possibility for nanoparticles to be adsorbed on the wall is increased when the wall is facing the direction of the concentration flow. This causes the overall adsorption is less dense for the microchannel with high tortuosity, which is confirmed by investigating the concentration of the adsorbate on the microchannel wall. It is also discovered that the advection kinetic contributes more dominant effects to the adsorption than the tortuosity. This is shown by plotting the adsorbate concentration and mass against the tortuosity magnitude for different injection velocity.

For the case of the microchannel with the same inlet-outlet distance, tortuosity means both microchannel complexity and the surface area of the microchannel. Increase tortuosity means increase in complexity, as well as the increase of the microchannel surface area. Therefore, instead of only investigating the concentration behaviour, the mass of the adsorbate nanoparticle is as well discussed. Using mass of the adsorbate gives more understanding and overview to the actual adsorption than investigating the adsorbate concentration for tortuous microchannels with various surface area. This is because the magnitude of the adsorbate mass is not 'normalised' with the surface area as the adsorbate concentration is.

The concentration of the adsorbate varies inversely to the tortuosity, which is in agreement with the previous study [252]. However, the mass of the adsorbate is positively correlated with the tortuosity. In the study, these are shown by the comparison of the concentration and mass of the adsorbate for different tortuous microchannel. There are two reasons for this. The first one, the microchannel with higher tortuosity has larger surface area, allowing more mass adsorbed on to it. The second one, the bends introduce perpendicular walls against the direction of the concentration flow, increasing the chance for the particles to be adsorbed on these walls. The adsorption on the bend itself, however, is less than the surrounding surfaces. This happens because the advection effect in this location is low, reducing the sweep efficiency of the concentration bulk and the microchannel wall.

The average adsorbate concentration measured is less for microchannel system with high complexity for the system with equal inlet-outlet distance. The complexity, in this case, is indicated by the magnitude of tortuosity. The effect of the tortuosity to the adsorption process is more

significant as the injection velocity decreases. In this condition, the effect of the tortuosity is more dominating to the adsorption than the advection. However, although the microchannel with high tortuosity has a lower adsorbate concentration compared to the microchannel with low tortuosity, the mass is higher for the former. The equilibrium (final) mass of the adsorbate is typically increased along with the tortuosity magnitude. The trend of the increase is relatively linear for higher injection velocity, but rises more as the injection velocity reduces. It is also observed that the tortuosity has a negative correlation with the desorption rate.

## Chapter 6

### Distribution of Nanoparticles in a Single Rough Surface Microchannel

#### 6.1 Introduction

This chapter presents a study of the effect of the wall roughness on the adsorption of the injected nanoparticle in the microchannel system. The model builds on that developed in Chapter 4.

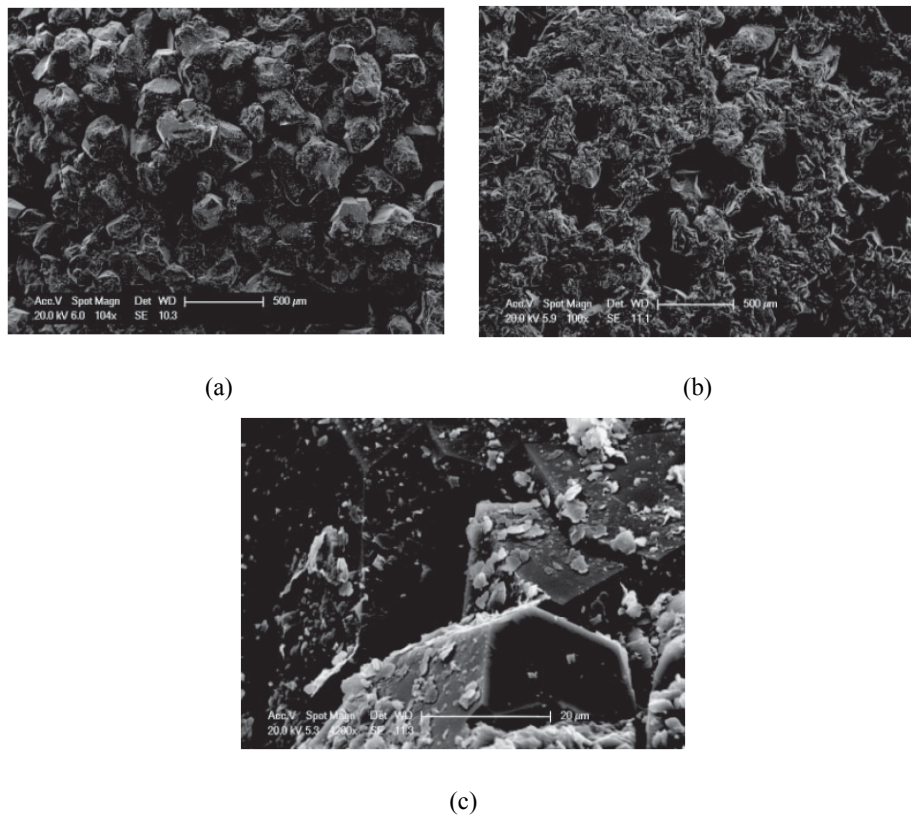


**Figure 6.1:** (a) Grains of the clashash sample before injection that dominantly consist of quartz grains with open pore, (b) Post-test sample of the injection face of the core plug showing the occurrence of a very thin filter cake of particles but with large, open pores. (c) Post-test sample showing that the scattered kaolinite platelets on quartz grains are still held in place after successive treatments. (After Fleming et al[114])

---

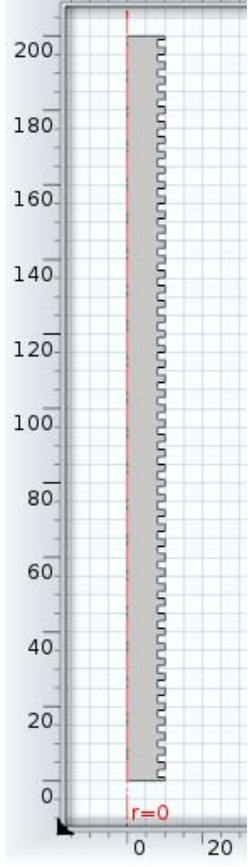
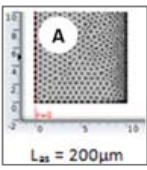
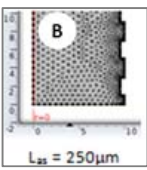
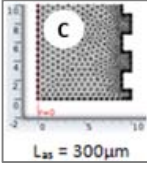
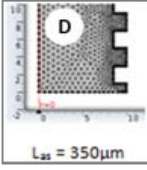
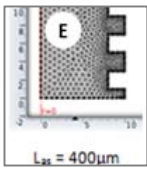
This study is initiated by an investigation conducted by Fleming et al [103, 113]. They studied the alteration of the formation properties as a result of injecting a low concentration kaolinite and organosilane into the reservoir. This produces an increase in the rock formation surface area which enhances the adsorption of the scale inhibitor in the scale squeeze treatment. In the scale squeeze treatment, the kaolinite and calcium carbonate particles are injected along the preflush fluid and subsequently followed by the injection of the scale inhibitor and the organosilane in the main treatment. The kaolinite particles are retained in the near-wellbore region by the organosilane and enhance the number of potential adsorption sites for scale inhibitor. The investigation was conducted by injecting a clashash core sample with kaolinite. The condition of the core sample before injection is shown in **Figure 6.1**. **Figure 6.1a** shows the surface of the rock sample grain before the injection which is still clean from the kaolinites. **Figure 6.1a** and **Figure 6.1b** shows the condition of the rock grains after the injection. In the later figures, It is observed that a thin layer cake of kaolinite is formed on the surface of the rock grains which increases the total surface area of the grains.

In this study, the heterogenous site surface of the microchannel is simplified and modelled by introducing an array of regular rectangles at the side-wall boundary. This array modifies the length of the microchannel and adjusts its corresponding surface area. The detail is discussed later in Section 6.3.

## 6.2 Aims and Objectives

Rough surface improves the adsorption mechanism, however the detail investigation of the adsorption profile on the wall's asperition is not yet much uncovered by the previous studies [254-258], especially for an injected nanoparticle concentration. Therefore, this study is conducted to investigate the adsorption and desorption profile of nanoparticles on the asperition of the microchannel wall surface. In this study, the wall roughness is an analogue of a microchannel wall surface alteration due to significant nanoparticle adsorption that significantly modify the internal configuration of the microchannel. The objective in this chapter is to investigate the concentration profile of the effluent and the adsorbed particles for different wall roughness for continuous and discontinuous concentration injection.

### 6.3 Simulation Setup

Illustration	Surface variation	Actual surface length, $L_{as}$ ( $\mu\text{m}$ )	Average roughness ( $R_a$ , $\mu\text{m}$ )	Surface area ( $\mu\text{m}^2$ )
		200 (reference)	$R_a = 0$	12566.37
		250	$R_a = 0.25$	15707.96
		300	$R_a = 0.5$	18849.56
		350	$R_a = 0.75$	21991.15
		400	$R_a = 1$	25132.74

**Table 6.1: The geometry of the simulation setup**

A 3D axis-symmetrical single and straight microchannel geometry model is used in the study. The simulation is developed based on the approach discussed in Chapter 4. To model the surface variation, an array

of regular-shaped rectangles is introduced along the channel wall as the equivalent of the wall roughness. The dimension of each rectangle is modified proportionally to simulate the change of the microchannel's roughness due to the particles adsorption on to it. This subsequently increases the surface area of the microchannel where the outer diameter of the microchannel remains constant.

In the study, the roughness is measured using average surface roughness ( $R_a$ ), which is the industry standard term for surface roughness. The magnitude of the average surface roughness follows equation 6.1 below:

$$R_a = \frac{1}{l} \int_0^l |f(x)| dl \quad (6.1)$$

where  $R_a$  is the average surface roughness ( $\mu\text{m}$ ),  $l$  is the length of the microchannel surface (dimensionless), and  $f(x)$  is the vertical surface position measured from the average surface height ( $\mu\text{m}$ ). The illustration of the average surface roughness is shown in the figure below.

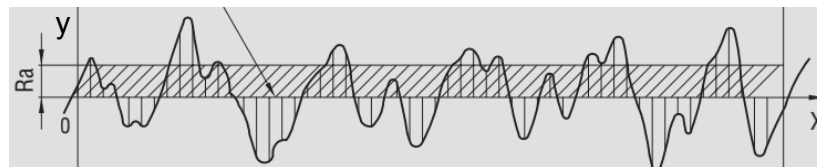


**Figure 6.2** Illustration of the average surface roughness

The average surface roughness parameter used in this simulation is  $0 \mu\text{m}$ ,  $0.25 \mu\text{m}$ ,  $0.5 \mu\text{m}$ ,  $0.75 \mu\text{m}$ , and  $1 \mu\text{m}$  where it is also shown in the fourth column in **Table 6.1**. The first column in **Table 6.1** shows an illustration of a 3D axis-symmetric microchannel with a rough wall. The roughness of the wall is established by an arrangement of regular and comparable-sized rectangles that is located at one sidewall boundary. The other sidewall of the geometry is marked with red line indicated the symmetry of the geometry. The second column shows the geometrical illustration for the wall roughness due to the rectangle's size alteration. Four microchannel scenarios with different surface roughness that are simulated in this study. From top to bottom, the roughness of the channel wall is increased which surface length is shown in the third column. The corresponded cylindrical surface area for each value of  $R_{dim}$  is shown in the fifth column. The illustration for one

microchannel geometry with  $R_a = 1 \mu\text{m}$  used in the study is shown in **Figure 6.3**.

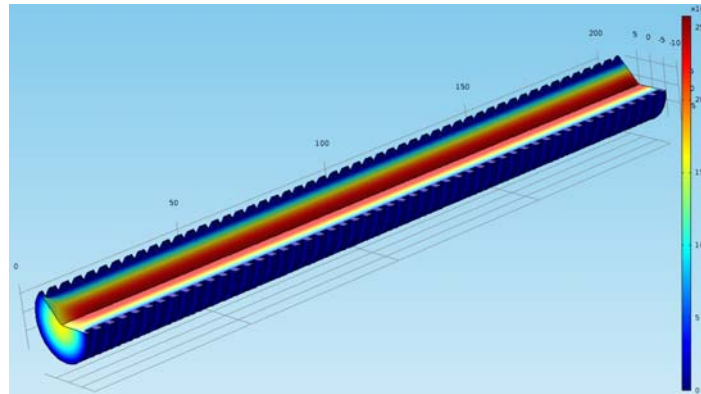


**Figure 6.3** Illustration of the microchannel geometry with the velocity fields. Taken from the microchannel in this study for  $R_a = 1 \mu\text{m}$

The study is focused on the transportation, adsorption, and desorption of the injected nanoparticles that is injected along a steady flow. The transportation, adsorption and desorption of the particles are investigated for the continuous and discontinuous injection. The trend of the effluent concentration, and mass and the concentration of the adsorbed particles are discussed. The properties of the injected particles are taken based on the discussion in Chapter 4. The investigations for the continuous and discontinuous particle injection are conducted. Both investigations are subjected to a steady creeping flow  $v_0 = 8.08 \times 10^{-5} \text{ m/s}$ , thus injection volume is linearly proportional to the injection simulation time. The profile of the concentration and mass are investigated against the arc length of the microchannel wall surface. The profile of the concentration and mass are not plotted against the distance from inlet so then the actual adsorption can be observed and compared easier.

#### **6.4 The Effect of the Wall Roughness to the Particle Transportation and Adsorption**

In this section, nanoparticles concentration is continuously injected into the microchannel. It is important to state that the simulation in this study is conducted under an identical steady state injection velocity, therefore the injection time length is proportional to the injection pore volume.

---

The trend of the adsorbate mass on the microchannel wall with different roughness is investigated. The adsorbate mass in this simulation is obtained by averaging the magnitude along the corresponding boundaries in time. The roughness is simulated by modifying the microchannel wall by introducing a set of asperities with even size along the wall. Sensitivity study for the concentration distribution also is conducted on various sizes of asperities.

The mass of the adsorbate for wall roughness is plotted and compared against the arc length of the channel surface. Refer to Chapter 5 that it is more suitable to use adsorbate mass than the adsorbate concentration for comparing the adsorption on the microchannels with different adsorption surface areas. The mass of the adsorbate is obtained from the average of the cumulative mass on the surface of the microchannel domain at a specific time with axis-symmetric nature considered. Arc length is used instead of the distance from the inlet boundary of the microchannel to justify the surface area of the microchannel. The reason for the utilisation is that the former is more suitable to compare the adsorption on different adsorption areas for various roughnesses.

#### **6.4.1 Model Geometry Selection**

A preliminary study was conducted to select the type of geometry that is suitable for the modelling. Since the objective is to investigate the effect of the variety at the microchannel circumference on the concentration distribution, a preliminary study dedicated to compare actual 3D geometry and 3D symmetric axis geometry model behave similarly. Simulation using the actual 3D microchannel geometry is more accurate than the 3D symmetric axis geometry. However, the simulation time needed for it is much larger for the former than the latter.

For the investigation, both geometries have similar diameter and length are prepared, i.e. 20 $\mu$ m and 200 $\mu$ m respectively. The average surface-roughness parameter ( $R_a$ ) for both geometry configurations is 0. As initial condition, both geometries are empty from any nanoparticle concentration. 12500 ppm of nanoparticles concentration is injected into the inlet of the geometries with a constant and continuous velocity  $v_0=8.08\times 10^{-5}$  m/s. The simulation is conducted from 0 to 10 seconds. The average adsorbate mass along the wall for both 3D geometry channel and 3D symmetric axis

geometry are plotted and investigated. The adsorbate mass is obtained from the average of the nanoparticle mass accumulation on the wall at a specific time with axis symmetry is properly accounted.

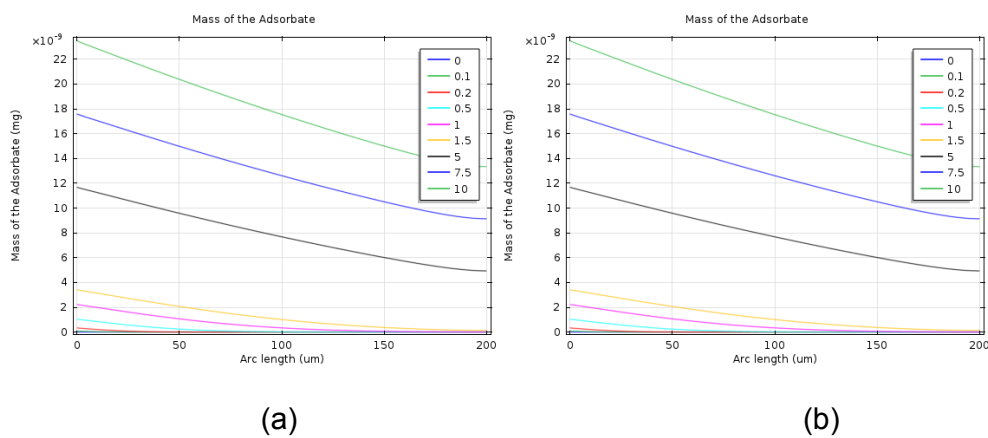


**Figure 6.4:** Mass of the adsorbate for different time steps (in seconds) for continuous particles injection for (a) actual 3D microchannel geometry and (b) 3D symmetric axis geometry for  $R_a = 0 \mu\text{m}$

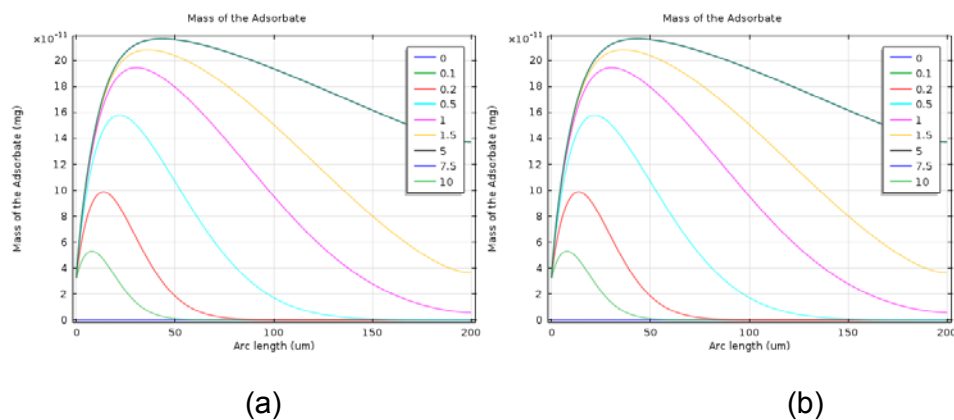


**Figure 6.5:** Mass of the adsorbate for different simulation time (s) for discontinuous particles injection for (a) 3D microchannel geometry and (b) 3D axis symmetric geometry for  $R_a = 1 \mu\text{m}$

**Figure 6.4** shows side-by-side the profile of adsorbate mass that is measured along the arc length of a microchannel for the actual 3D microchannel geometry and the 3D symmetric axis microchannel geometry. It is discovered that the profile of the adsorbate mass for both geometry configurations is in good agreements.

---

The validation is also conducted for the discontinuous injection. 12500 ppm of nanoparticle concentration is injected from 0 to 1/200 seconds with a constant injection velocity  $v_0=8.08 \times 10^{-5}$  m/s. The adsorbate mass is plotted against the microchannel arc length for various injection time step which is shown in **Figure 6.5**. It appears that the adsorbate mass profile for the 3D channel model and the 3D axis symmetric have a good agreement with each other.

Therefore, it is deduced that the simulation conducted in the 3D symmetry axis geometry is comparable to the actual 3D geometry. This finding is important since using the 3D symmetry axis geometry reduces the simulation time significantly compare with modelling with the actual 3D microchannel geometry. Therefore, the 3D symmetry axis will be used for the rest of the study in this chapter.

#### 6.4.2 Continuous Injection Flow

The effect of the wall roughness to the distribution and adsorption/desorption process of a continuously injected nanoparticle concentration on the microchannel is investigated. The roughness is simulated by modifying the surface of the microchannel by changing the size of the asperities on the wall. A parameter used for defining the roughness is the ratio between the actual surface are of the microchannel with the surface area of the base case, which is called the average surface roughness( $R_a$ ). The  $R_a$  selected are 0  $\mu\text{m}$ , 0.25  $\mu\text{m}$ , 0.5  $\mu\text{m}$ , 0.75  $\mu\text{m}$ , and 1  $\mu\text{m}$ . The illustration for all geometry configurations is shown in **Table 6.1**.

The adsorbate mass for different time steps are plotted and compared against the corresponding microchannel arc length. The profile is shown in **Figure 6.6**. The adsorbate mass are plotted for a few simulation time steps i.e. 0, 0.1, 0.2, 0.5, 1, 1.5, 5, 7.5, and 10 seconds. It is found that the adsorbate mass increases proportionally with the injection time. The adsorption profile is high at the region that is close to the inlet boundary, and then decreases gradually towards the outlet. The shape of the trend is also affected by the roughness of the microchannel wall. As it is observed that the profiles are altered with steps that correspond with the asperities on the wall.

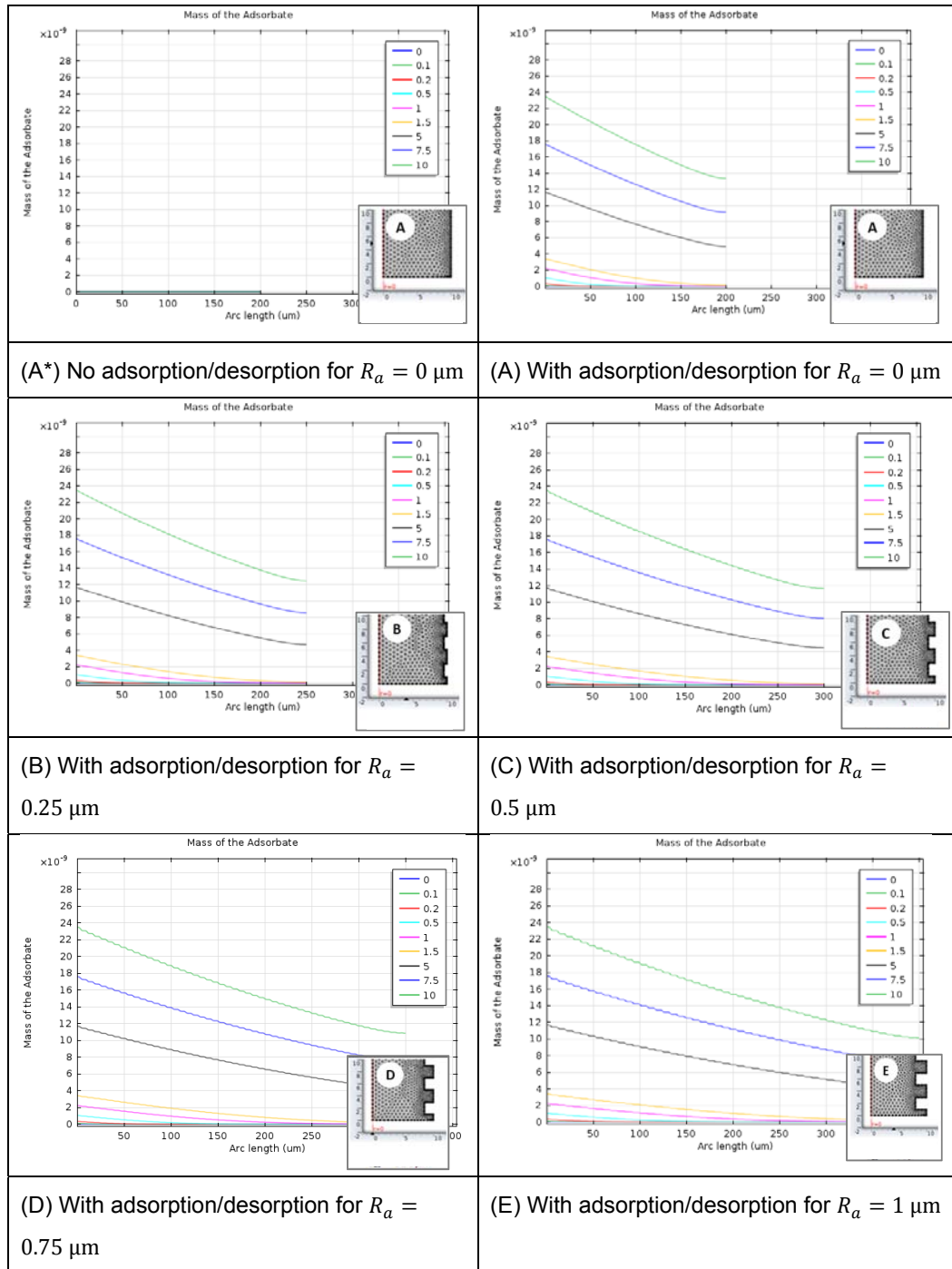


**Figure 6.6:** Adsorbate mass for different time steps (0 - 10 seconds) for continuous particles injection for various average surface roughness ( $R_a$ )

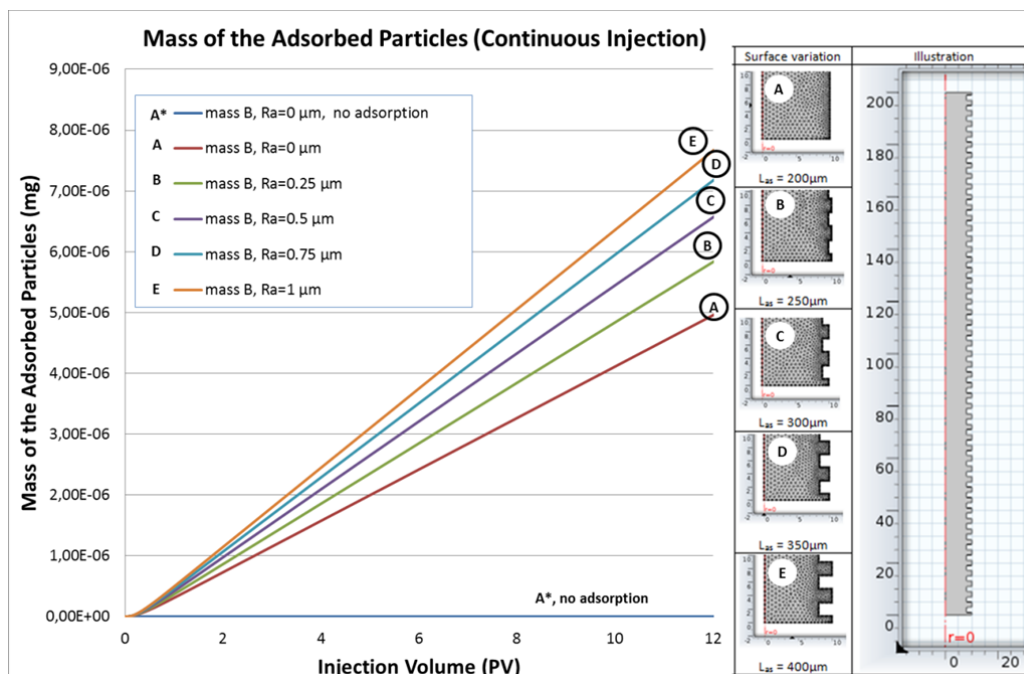


**Figure 6.7:** Adsorbate mass on the channel wall for continuous particles injection for against the injection volume for various average surface roughness ( $R_a$ )

**Figure 6.7** shows the profile of the adsorbate mass against the injection volume. Additional profile with index A\* is the result for simulation without adsorption process, used for validation for the developed model. There is no mass build up in the A\* system. This is shown by flat trend of the adsorbate mass regardless of the injection pore volume.

It is discovered that roughness of the wall gives positively correlates with the amount of particles adsorbed. Microchannel with rougher surface has larger surface area than the microchannel with less roughness. Nanoparticles have more opportunity to be adsorbed on the microchannel wall with large surface area. As it is shown in **Figure 6.7**, the mass of the adsorbed concentration for B, C, D, and E microchannel compared with microchannel A are increased for 18.2%, 34.07%, 47.96% and 60.05% as the area of the adsorption surface are increases for 25%, 50%, 75% and 100%. Hence the increase of the adsorption is positively correlated with the increase of the adsorption surface area, however the increase magnitude is not similar.

The effluent concentration measured at the microchannels' outlet boundary is also investigated. **Figure 6.8** shows the plot of the effluent concentration versus the corresponding injection volume for microchannels with various roughnesses. The effluent concentration increases together with the increase of injection volume. After 2 pore volume of injection, each of the effluent profile achieves the equilibrium condition. In the equilibrium, the magnitude of the effluent concentration is constant regardless the amount of the injected concentration.

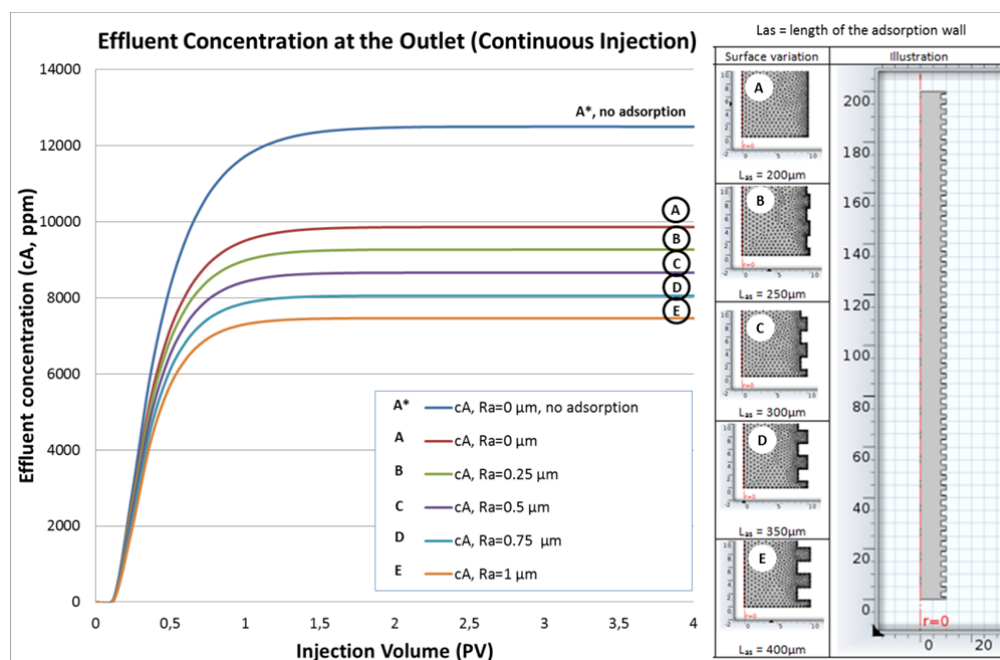


**Figure 6.8:** Effluent concentration at the outlet for continuous particles injection for different pore volume

The magnitude of the equilibrium concentration in **Figure 6.8** is not similar due to multi-layered adsorption that is considered in the Freundlich adsorption isotherm mechanism assumed in the simulation. This is also confirmed by the discussion in Section 4.6.1.1 in Chapter 4. The equilibrium effluent concentration of the system that takes into account the effect of desorption is less than the case without adsorption (A\*). The equilibrium effluent concentration for the case A\* is similar to the concentration of the initial injection.

---

Equilibrium concentration of the system decreases as the roughness of the wall increase. This shows that there is more adsorption happen in the wall with rougher surface. This indication is valid because the magnitude of the effluent concentration varies inversely with the amount of adsorbed particles on the microchannel wall. Comparing the flat surface with and without adsorption, the effluent concentration alters 21.11%. Furthermore, by increasing the length of adsorption wall by 25%, 50%, 75% and 100%, the equilibrium concentration decreases 9.83%, 18.61%, 26.38%, and 33.25% for B, C, D, and E microchannel compared with microchannel A respectively. These values are in agreement with those obtained from the investigation of the adsorbate mass. Thus, it is deduced that the equilibrium adsorption concentration is inversely correlated with the surface roughness of the microchannel.

The alteration of the profile's gradient from the increase and the plateau indicates the injection required by the system to transport the concentration bulk to the outlet boundary. The injection needed to take the concentration bulk to the outlet boundary is similar for all roughness cases. The magnitude is similar because the distance between the outlet and the inlet for all cases are also similar, although the roughness and surface length of each are different. This indicates that the effect of the surface roughness does not significantly affect the movement of the concentration bulk, as long as the concentration is introduced to the system continuously.

### 6.4.3 Discontinuous Injection Flow

The effect of wall roughness to the distribution of the injected nanoparticles is discussed in this section. Five microchannels configurations with the ones in Section 6.4.1 are used for the investigation. At the beginning of the simulation, the microchannels are empty from nanoparticle concentration. 12500 ppm of nanoparticles concentration is injected to the inlet boundary of the microchannels from 0 to 1/200 seconds. The concentration is injected along with a constant  $8.08 \times 10^{-5}$  m/s fluid velocity from 0 to 10 seconds of simulation duration. After the period of concentration injection, the carrier fluid continues to flow in through the inlet at constant rate for the whole simulation duration.

**Figure 6.9** shows the profiles of the adsorbate mass on the channel wall for all microchannels with different roughness for various time steps.

The adsorbate mass is measured from the average cumulative nanoparticle mass on the microchannel wall by properly considering the axis symmetry of the geometry. The case for nanoparticle distribution in a microchannel without adsorption/desorption is also shown by the mass of adsorbate in **Figure 6.9 A\*** for validation.

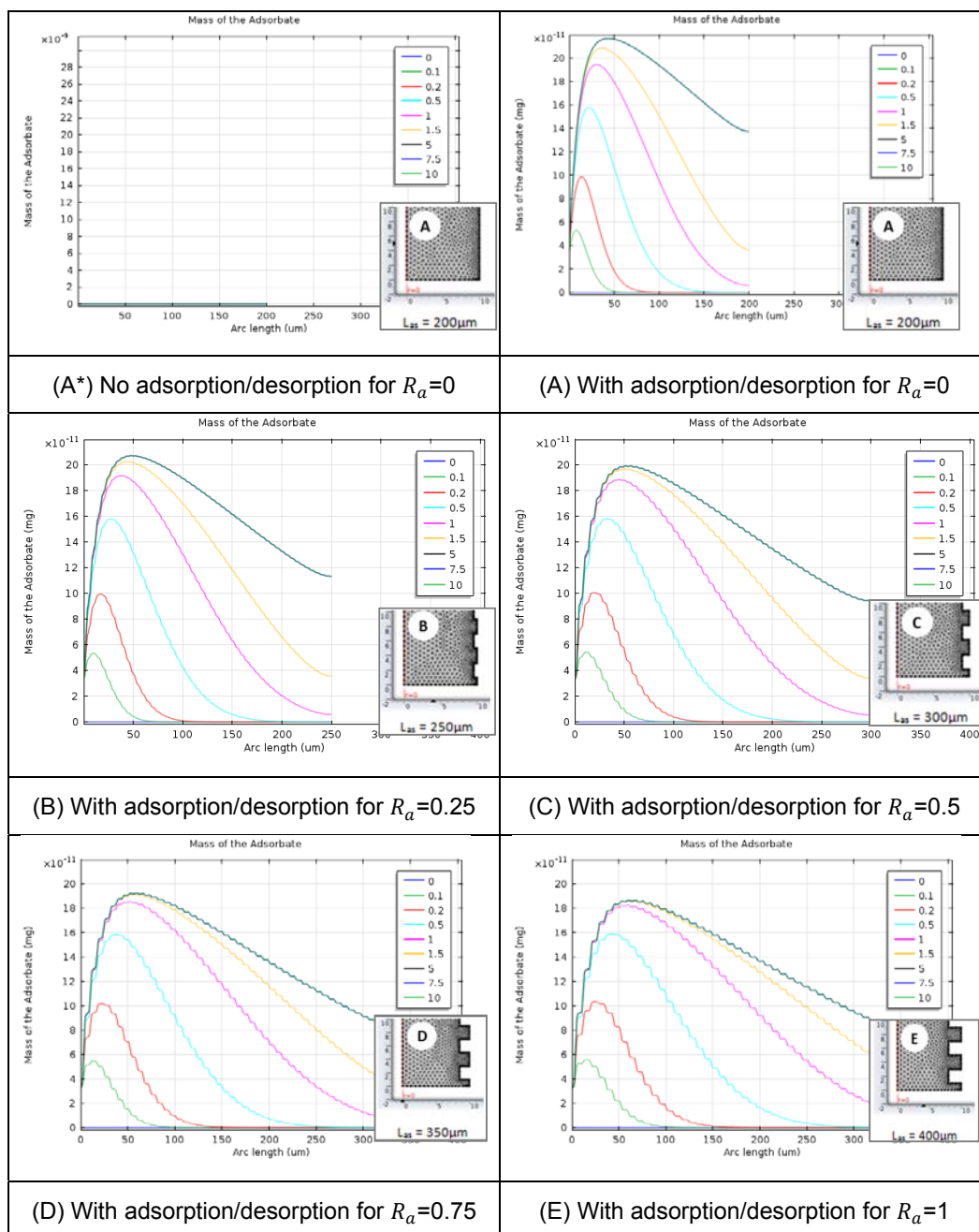


**Figure 6.9:** Adsorbate mass for different simulation time (0-10 seconds) for discontinuous particles injection particles injection for various average surface roughness ( $R_a$ )

---

Observing the trend of the adsorbate mass on the microchannel wall in **Figure 6.9**, at the beginning there is no nanoparticle mass on the microchannel wall. This, which is shown by the zero adsorption at 0 seconds. At time 0.005 seconds, adsorbate starts to build up at the region close to the inlet boundary, but decrease gradually towards the outlet. Maximum value of the adsorbate concentration in the microchannel surface increases (shown in arc length in the figure) proportional with the injection time. The maximum value of the adsorbate also shifts to the right showing the nanoparticle coverage on the wall becomes larger as the injection time increase. This shows that the advection affects the placement of the adsorbate on the microchannel wall. This also the reason for maximum value of the adsorbate mass is not in the region that is close to the inlet. It is also observed that at the profiles of adsorbate mass for simulation time 5 – 10 seconds align to each other. This means that the system has reach its equilibrium condition, where the rate of adsorption equals the desorption. The roughness of the channel affects the profile distribution of the adsorbate mass. The trend of the adsorbate is smooth for the smooth channel wall (i.e. case A). As the wall roughness increases, the profile of the adsorbate mass becomes rougher following the profile of the wall roughness

The effect of different roughness to the adsorption mass is also investigated by comparing the profile development of the adsorbate mass against the injection volume in **Figure 6.10**. The mass of the adsorbate escalates as the injection increases. This escalation, however, is not unlimited as it is in the case of the continuous injection. The injection volume is proportional to the injection time length because the system is subjected to a constant advection velocity. When the injection volume equals to 1 pore volume, the main bulk mass of the injected nanoparticle leaves the outlet boundary of the microchannel. Because the nanoparticle is injected only at the beginning of the simulation with no slip condition, there is no more nanoparticle supply in the channel at this moment. The system reaches the equilibrium condition where the rate of the adsorption equals the desorption which is shown as a flat adsorption profile in the **Figure 6.10**. It is also observed that the adsorbate mass correlates positively to the magnitude of the wall roughness. For similar microchannel length, rougher surface increases the adsorption surface area on the microchannel wall. Larger surface area enhances the possibility for more adsorption of the injected nanoparticle.

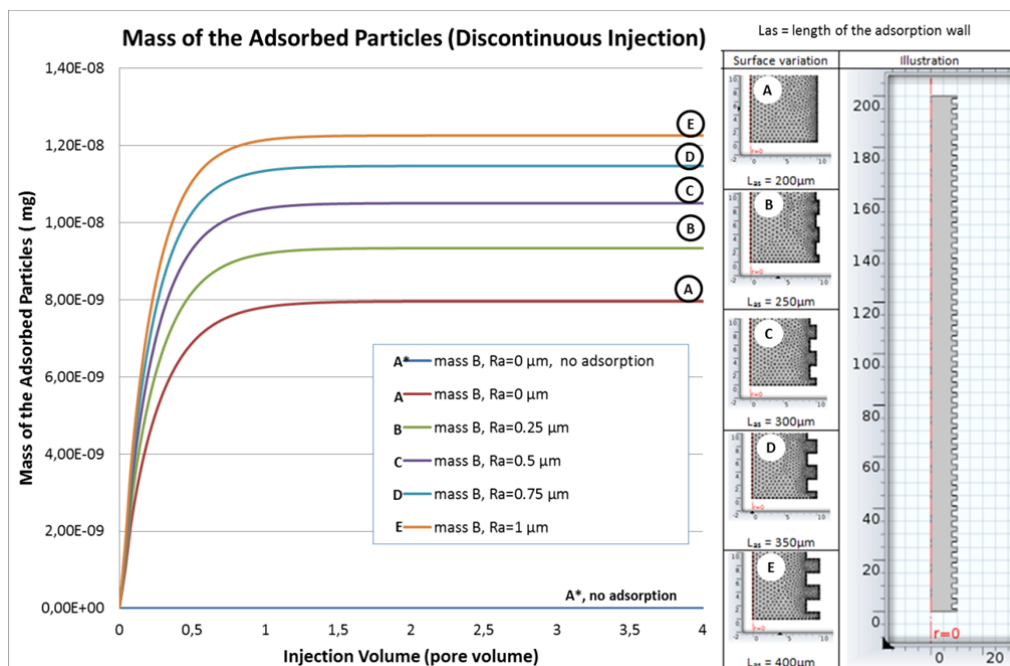


**Figure 6.10:** Mass of the adsorbed particles on the channel wall for discontinuous injection as a function of injection volume for various average surface roughness ( $R_a$ )

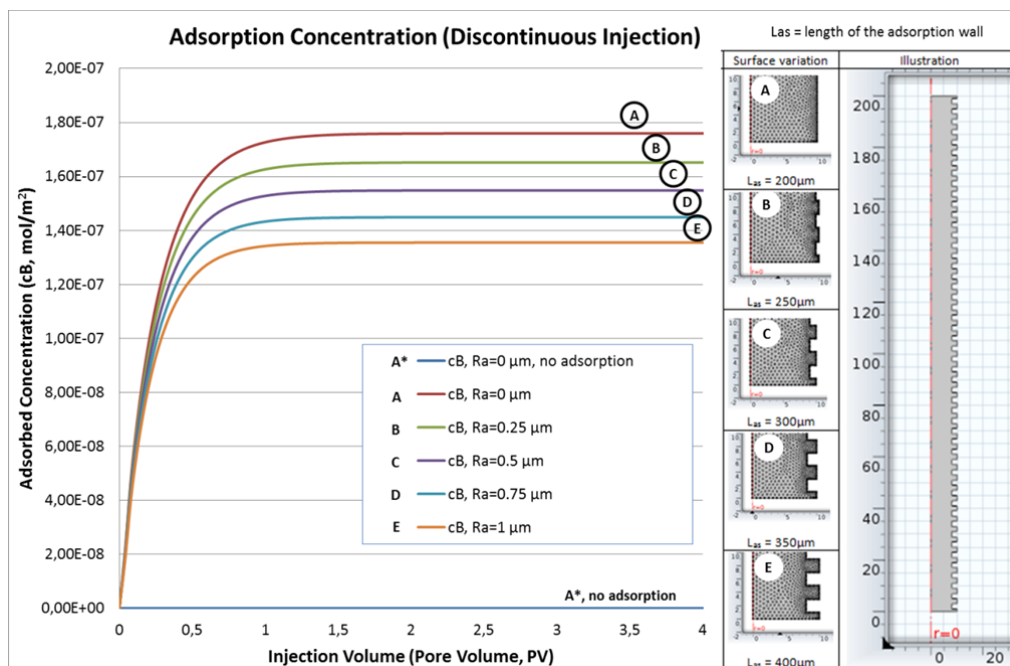


**Figure 6.11:** Concentration of the adsorbed particles on the channel wall for discontinuous injection as a function of injection volume for various average surface roughness ( $R_a$ )

The concentration of the adsorbate for discontinuous injection is shown in **Figure 6.11**. The trend follows the profile of the adsorbate mass; however, the magnitude of the adsorbate mass is the inverse against the wall roughness. The adsorbate concentration varies inversely to the wall roughness magnitude. This shows the density of the adsorbed particle on the rougher wall is less than on the smoother one. The former has larger adsorbate because it has a larger surface area than the former.

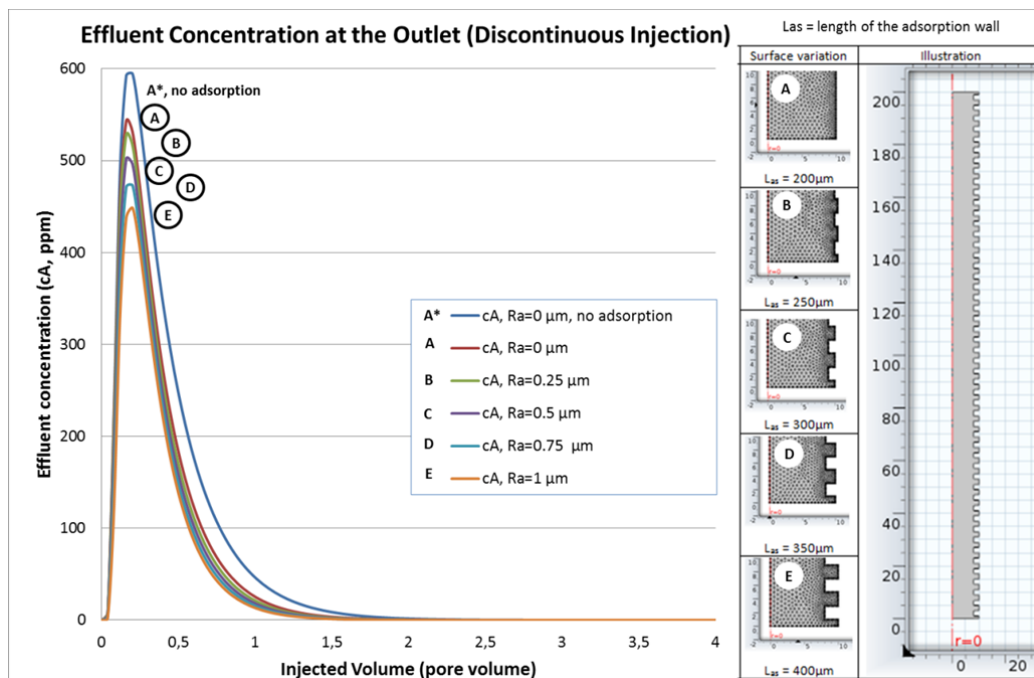


**Figure 6.12:** Effluent concentration at the outlet for discontinuous particles injection as a function of injection volume for various average surface roughness ( $R_a$ )

**Figure 6.12** shows the trend of the effluent concentration for the discontinuous injection as a function of the injection volume. The start of the profile-increase indicates the breakthrough of the injected particles at the outlet boundary of the microchannel. The required injection for the front of the concentration bulk reaches the outlet is comparable for all roughness cases. Since the injection volume is linearly proportional with the injection time, this also means that the breakthrough time for all roughness case is comparable. The maximum value of the effluent concentration is, however, not similar for all cases. The value varies inversely to the roughness of the microchannel wall. This is shown in **Figure 6.12** where the highest

maximum effluent concentration presents at the least rough channel (A), then it is followed by B, C, and D as the roughness increases. This is physically acceptable because adsorption occur higher on the microchannel wall with rougher surface than the smoother one due to the different in the magnitude of the surface are. This finding is in a good agreement with the investigation of the adsorbate mass previously.

#### 6.4.4 Effect of Wall Roughness to the Change in the Concentration Distribution and Adsorption in a Microchannel for Continuous and Discontinuous Nanoparticle Injection

In this section, the effect of the wall roughness to the change in the concentration distribution and adsorption in a microchannel for continuous and discontinuous nanoparticle injection are discussed. The methodology is to investigate the deviation the effluent concentration ( $c_A$ , mol/m<sup>3</sup>), adsorbate concentration ( $c_B$ , mol/m<sup>2</sup>), adsorbate mol ( $n_B$ , mol), and adsorbate mass ( $m_B$ , mg) of different wall roughness. Base case for the study is the geometry is the microchannel with diameter roughness parameter ( $R_a$ ) = 0  $\mu m$ , which is the microchannel with smooth wall surface.

The deviation of each parameters  $c_A$ ,  $c_B$ ,  $n_B$ , and  $m_B$  for each  $R_{dim}$  is shown in **Table 6.2**. The deviations shows in the columns in the table are the magnitude of the corresponding parameters compared with the base case. The increase of the wall roughness is indicated by the increase in  $R_{dim}$ . Effluent concentration ( $c_A$ ), adsorbate concentration ( $c_B$ ), adsorbate mol ( $n_B$ ), and adsorbate mass ( $m_B$ ) of different wall roughness are obtained from both cases of the continuous and discontinuous injection when the corresponding system reaches the equilibrium condition. Equilibrium condition for the case with continuous nanoparticle injection is indicated by zero gradient profile for the effluent concentration. Equilibrium condition for the case with discontinuous nanoparticle injection is indicated by zero gradient profile for the adsorbate concentration. The equilibrium concentration is obtained by investigating the value of  $c_t$  when  $\frac{(c_t - c_{t+1})}{c_t} < 0.001\%$ . In this case,  $c_t$  is the corresponding average concentration for each injection case at time  $t$ .

$R_a$ ( $\mu\text{m}$ )	cA Deviation		cB Deviation		nB Deviation		mB Deviation	
	Cont. Inj.	Discont. Inj.						
0	0,00 %	0,00 %	0,00 %	0,00 %	0,00 %	0,00 %	0,00 %	0,00 %
0.25	-6,00 %	-54,83 %	-5,88 %	-6,12 %	17,65 %	17,35 %	17,65 %	17,35 %
0.5	-12,17 %	-76,90 %	-11,70 %	-12,01 %	32,45 %	31,98 %	32,45 %	31,98 %
0.75	-18,31 %	-88,35 %	-17,33 %	-17,65 %	44,67 %	44,11 %	44,67 %	44,11 %
1	-24,32 %	-94,40 %	-22,72 %	-22,99 %	54,57 %	54,01 %	54,57 %	54,01 %

Note:

(-) sign: decrease in the value deviation compared to the L-Equivalent  $200 \mu\text{m}$  ( $R_a = 0 \mu\text{m}$ )

(+) sign: increase in the value deviation compared to the L-Equivalent  $200 \mu\text{m}$  ( $R_a = 0 \mu\text{m}$ )

**Table 6.2:** Comparison for the deviation of the outlet effluent concentration (cA,  $\text{mol}/\text{m}^3$ ), concentration of the adsorbate (cB,  $\text{mol}/\text{m}^2$ ), mol of the adsorbate (nB, mol) and the mass of the adsorbate (mB, mg) for different wall roughness.

Each of the deviations is plotted against the dimensionless roughness parameter of the microchannel wall. The plot is shown in **Figure 6.13** and **Figure 6.14** for continuous and discontinuous injection respectively. The value on the y-axis on the left shows the deviation of the effluent concentration and the adsorbate concentration (cB). The y-axis on the right shows the adsorbate mol and mass

For both continuous and discontinuous injection, the deviation of the effluent concentration and the adsorbate concentration varies inversely with the microchannel roughness. On the other hand, the magnitude of adsorbate mol and mass are proportional with the roughness. The magnitude change for effluent concentration, adsorbate mol and adsorbate mass for both continuous and discontinuous nanoparticle injection are comparable.

The alteration of the adsorbate concentration, mol, and mass for both continuous and discontinuous injection are comparable. The alteration of the effluent concentration for the increase of wall roughness is different between the continuous and discontinuous injection. This happens because the concentration for the former is unlimited and those in the latter are limited.

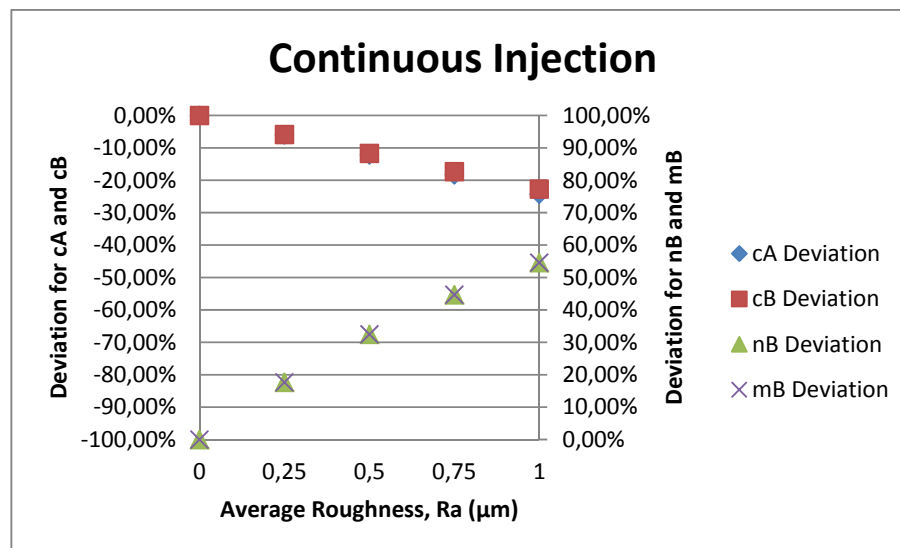


**Figure 6.13:** Comparison for the deviation of the outlet effluent concentration ( $cA$ ,  $\text{mol}/\text{m}^3$ ), adsorbate concentration ( $cB$ ,  $\text{mol}/\text{m}^2$ ), adsorbate mol ( $nB$ ,  $\text{mol}$ ) and adsorbate mass ( $mB$ ,  $\text{mg}$ ) for different wall roughness – continuous injection.

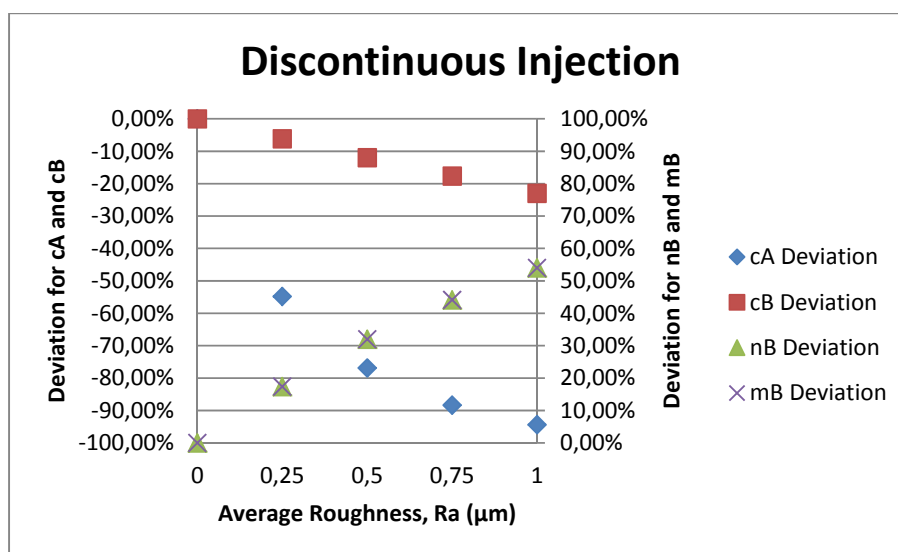


**Figure 6.14:** Comparison for the deviation of the outlet effluent concentration ( $cA$ ,  $\text{mol}/\text{m}^3$ ), adsorbate concentration ( $cB$ ,  $\text{mol}/\text{m}^2$ ), adsorbate mol ( $nB$ ,  $\text{mol}$ ) and adsorbate mass ( $mB$ ,  $\text{mg}$ ) for different wall roughness – discontinuous injection

### 6.4.5 Adsorption on the Asperities of the Rough Microchannel Wall

The adsorption of the nanoparticles on the asperities of the rough microchannel wall is investigated closer in this section. The parameter used for the investigation is the mass of the adsorbate that obtained from the located at the wall whose value is around maximum. The adsorbate mass is measured from the cumulative average of the adsorbate mass on a specific simulation time step where the axis symmetry of the microchannel is considered properly. The typical trend of the adsorbed mass on the roughness asperities is shown in **Figure 6.15 (left)**. The corresponding surface for the adsorbate mass is shown in **Figure 6.15 (right)**. Inset I and Inset II display the position of the arc length that corresponds to the asperities in a larger resolution.

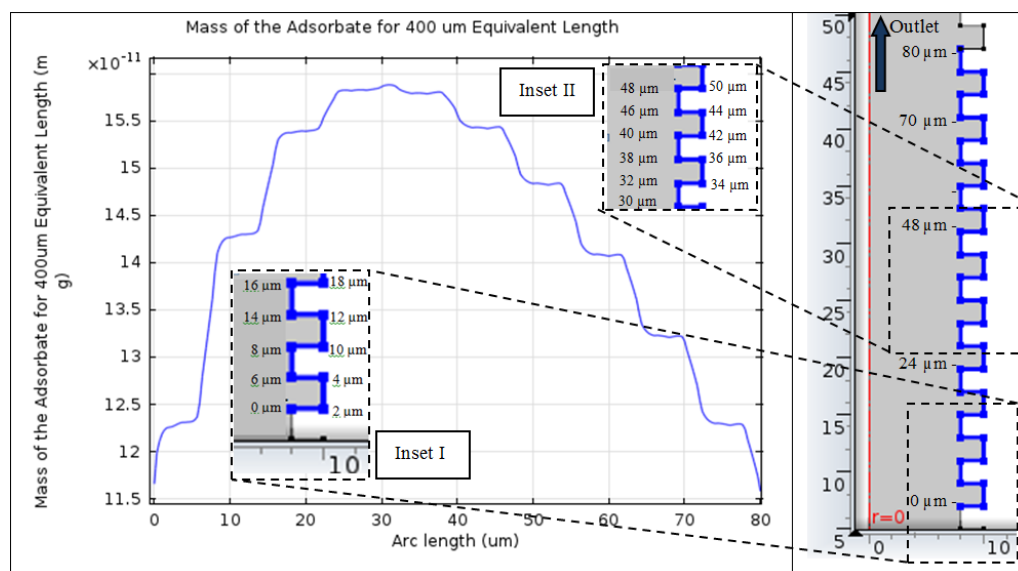


**Figure 6.15:** The peak of the adsorbate mass distribution of the adsorbate for microchannel with  $R_a = 1$  for 0.5 seconds simulation

The adsorbate mass profile is taken from the cumulative of the average adsorbate where the maximum value presents on the surface of a microchannel with  $R_{dim} = 2$  (microchannel E) at 0.5 seconds simulation time. The arc length is the normalised to the section of interest that corresponds to the microchannel roughness illustrated on **Figure 6.15 (right)**. Inset I in **Figure 6.15 (left)** shows the corresponding surface

between 0  $\mu\text{m}$  to 18  $\mu\text{m}$ , where the profile of the adsorption increases. From arc length datum 0  $\mu\text{m}$  to 2  $\mu\text{m}$ , the adsorbate mass increase in steps from roughly  $11.8 \times 10^{-11}$  mg to  $12.3 \times 10^{-11}$  mg. From 2  $\mu\text{m}$  to 6  $\mu\text{m}$  the increase of the adsorbate mass reduced, which is from  $12.3 \times 10^{-11}$  mg to  $12.35 \times 10^{-11}$  mg. 2  $\mu\text{m}$  to 6  $\mu\text{m}$  is the location inside the cavity in the asperities measured from the centre of the channel. The adsorption happens in this section is the least of all. From 6 to 8  $\mu\text{m}$ , the adsorbate mass increases from  $12.35 \times 10^{-11}$  mg to  $14.35 \times 10^{-11}$  mg. This is the location for the wall closest to the centre of the microchannel. In this location, the adsorption is the highest of all. Then the trend is repeated with reduce magnitude until the maximum adsorbate mass reach at 30  $\mu\text{m}$ . Inset II in **Figure 6.15 (left)** shows the corresponding surface between 30  $\mu\text{m}$  to 48  $\mu\text{m}$ , where the profile of the adsorption decreases. From 30 to 32  $\mu\text{m}$ , the adsorbate mass in the system is the highest, i.e.  $15.8 \times 10^{-11}$  mg. it decreases slightly to  $15.75 \times 10^{-11}$  mg from 32 to 36  $\mu\text{m}$ . The profile of the adsorbate mass increases slightly to  $15.8 \times 10^{-11}$  mg from 36 to 38  $\mu\text{m}$ . The profile then it reduced to  $15.45 \times 10^{-11}$  mg between 38 to 40  $\mu\text{m}$ , which is the surface segment that is closest to the internal of the microchannel. Segment 40 to 42  $\mu\text{m}$  the profile decreases, and then becomes relatively constant between 42 to 46  $\mu\text{m}$  whose segment is the furthest from the internal of the microchannel. The profile decrease again from 46 to 48  $\mu\text{m}$  which located on surface closest to the internal of the microchannel. The decrease in adsorption happens in this step continuously until the end of the arc length. It seems adsorption increase and decrease happen the most on the surface area that is the closest to the internal of the microchannel. Inversely, the adsorption happens the least on the surface that has the furthest distance from the internal of the microchannel.

#### **6.4.6 Investigation of the Dead End Region in the Microchannel**

The configuration of the asperities in this study is also an analogue for a system with dead end regions. As it was observed in section 6.4.4, the adsorption happens the most at the roughness surface that closest to the inner of the microchannel and the least at the furthest surface. Many studies have been conducted to investigate the flow in a grooved microchannel. In 2002, Stroock et. al. studied a simple analytical description to measure transversal flow component at the grooved microchannel surface by pressure-driven fluid flow [259]. A few years after, the utilisation of CFD modelling using this approach then was started to implement in designing a

---

micromixer [260]. The modification of the groove is later modified to optimize the functionality of the micromixer [261-263].

In this study, the investigation is demonstrated by assessing the influence of advection to the concentration transport at the region close to the wall asperities. The geometry of the wall asperities is modelled by introducing a cavity on the wall channel. The transportation of the particle is mainly influenced by the advection because there is no slip between the fluid and particles. In this study, the wall roughness is introduced by placing “rectangles” of asperities to establish cavities that decrease the inner cross-section area of the microchannel. The asperities are placed regularly to model roughness on the microchannel wall. Detail explanation for the geometry is discussed in Section 6.3. There is a dead region between two asperities whose concentration flow and adsorption upon it are investigated. The dead end region hinders the effect from advection to transport the concentration inside. The amplitude of the dead end region is small compared to the size of the main channel in this case. In this condition, a transverse pressure gradient build up to drive a necessary circulation of the fluid in the groove. This discovery confirms the finding report earlier by Stroock et.al. [259]. The magnitude of the circulation, however, is weak comparing to the magnitude of the fluid movement in the main channel.

There are streamlines that represent the flow in this region that move spaced out. The rainbow colour is the streamlines of the velocity profile, which blue is the lowest and red is the highest. The red arrows show the direction of the flow velocity. The length of each arrow is not proportional to the magnitude since the velocity in dead end is significantly smaller than in the bulk. As seen in **Figure 6.16**, the crenelated structure of the wall introduces corner eddies [253] which are separated from the main flow. As the amplitude of the surface features is increases, the corner eddies merge (see schematic in **Figure 6.17**) to produce a recirculating region separated from the bulk by separating streamline. This is well known from studies of cavity flows [264, 265]. Since flow cannot cross a streamline, it is impossible to transport the concentration inside the main bulk into the dead end region by the advection. This shape induces flow effectively in lateral direction without assistance from any external energy sources [262]. Instead, the transportation of the particle between the main channel region and the dead end region is likely happened due to the diffusion. The particles that are ‘trapped’ inside the dead end are then be adsorbed on the wall. Some other

particles remain in the dead-end due to the velocity vortex and might be released back to the inner channel due to the diffusion.

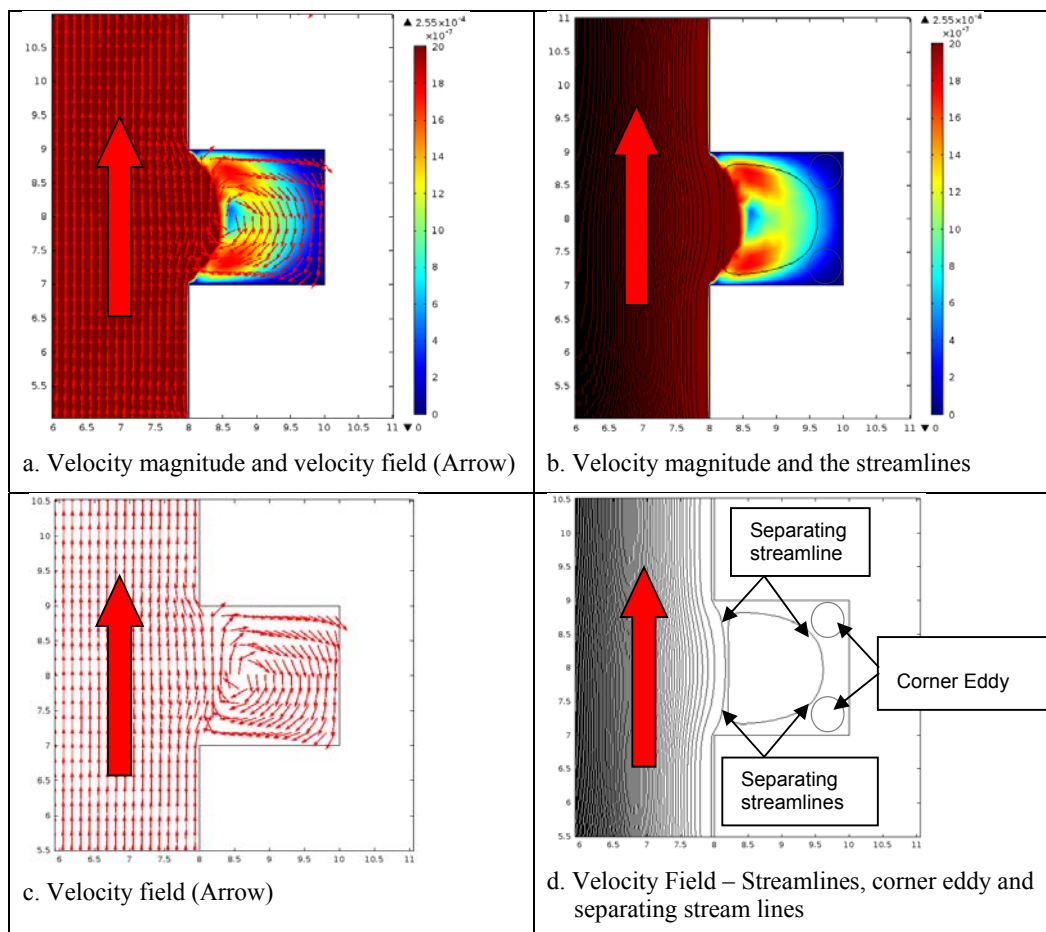


**Figure 6.16:** Velocity magnitude, velocity field, streamlines in one of the cavity on the wall in this study. Red arrow is the direction of the flow

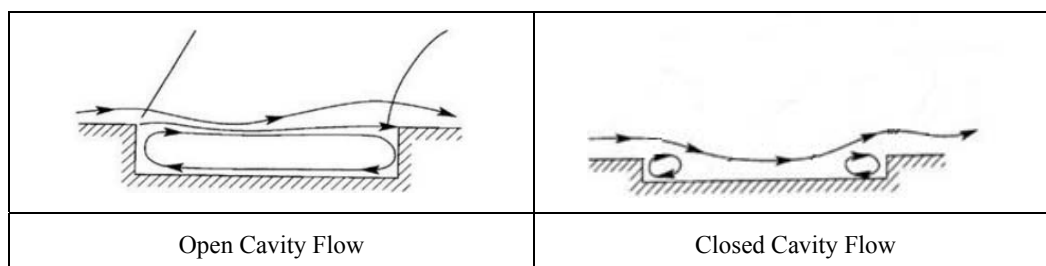


**Figure 6.17:** Flow schematic for open and cavity flow (Reproduced from Plentovich, 1993[264])

**Figure 6.17** to **Figure 6.21** shows the velocity profile and direction that occurs in the microchannels A, B, C, D, and Velocity stream lines magnitude at the location close to the wall of the smooth microchannel ( $R_a = 0 \mu m$ ) between 5 and 11  $\mu m$  are shown in **Figure 6.18 (left)**. The velocity at the wall is very low and it increases towards the centre of the microchannel. The profile of the adsorbate mass on the microchannel wall follows a smooth trend and increases upwards.

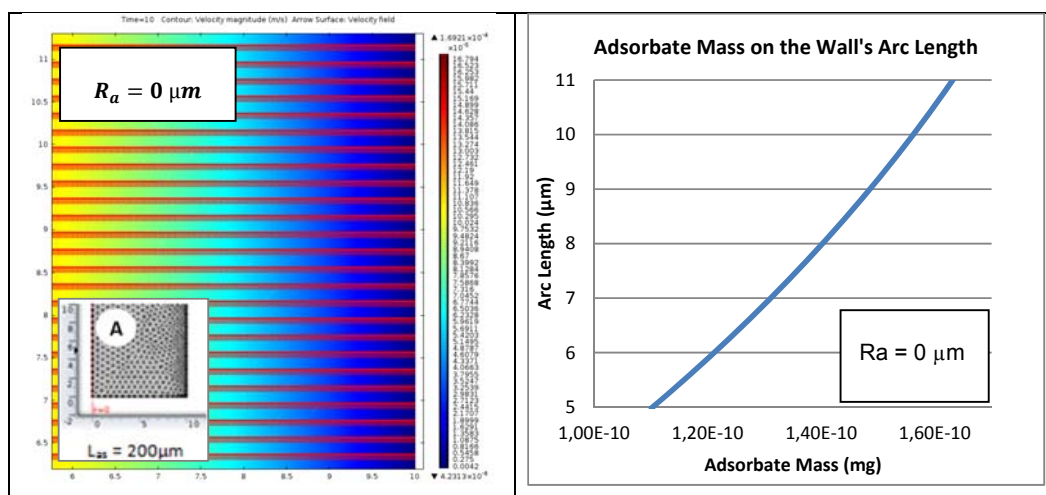


**Figure 6.18:** Velocity streamlines magnitude at a cavity on the wall (left) and the corresponding adsorbate mass (right) for microchannel with  $R_a = 0 \mu m$

Velocity magnitude and streamlines at the cavity that is located between 5 and 11  $\mu m$  for microchannel with  $R_a = 0.25 \mu m$  is shown in **Figure 6.19 (left)**. Small cavity is introduced at the wall where some of the streamlines flows into it. It seems that the corners of the cavity are not covered by the streamlines. The profile of the adsorbate mass on the wall is shown in **Figure 6.19 (right)** where the profile of the cavity influence the distribution. Highest increase for the adsorbate mass presents on the wall (2) and (3). However, the amount of adsorbed particles is more on wall (1) and (5). The least adsorbate mass increase is on wall (3).

Velocity streamlines magnitude at the cavity for microchannel with  $R_a = 0.25 \mu m$  is shown in **Figure 6.20 (left)**. The cavity is larger than the one in **Figure 6.19 (left)** and less streamlines observed in it. The profile of the adsorbate mass on the cavity wall is shown in **Figure 6.20 (right)**. The profile follows the trend previously discussed for the microchannel with  $R_a = 0.25 \mu m$ , however with less adsorption on wall (3).

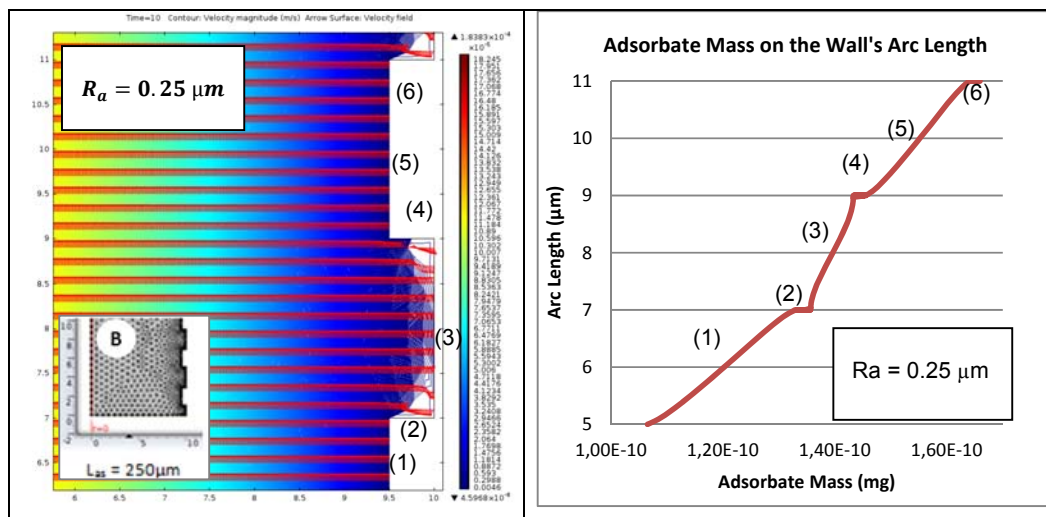


**Figure 6.19:** Velocity streamlines magnitude at a cavity on the wall (left) and the corresponding adsorbate mass (right) for microchannel with  $R_a = 0.25 \mu m$

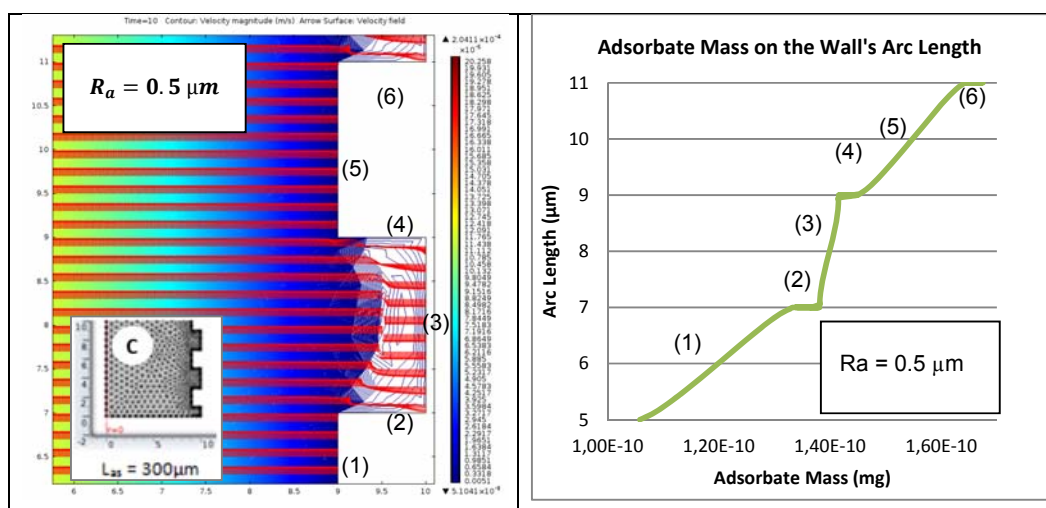


**Figure 6.20:** Velocity magnitude and stream lines at a cavity on the wall (left) and the corresponding adsorbate mass (right) for microchannel with  $R_a = 0.5 \mu m$

The cavity at the microchannel wall is increased more for D and E geometries which is shown in **Figure 6.21** and **Figure 6.22** respectively for  $R_a = 0.75 \mu m$  and  $R_a = 1 \mu m$ . Less streamlines discovered in the cavity and less adsorbate distribution on the wall (3).

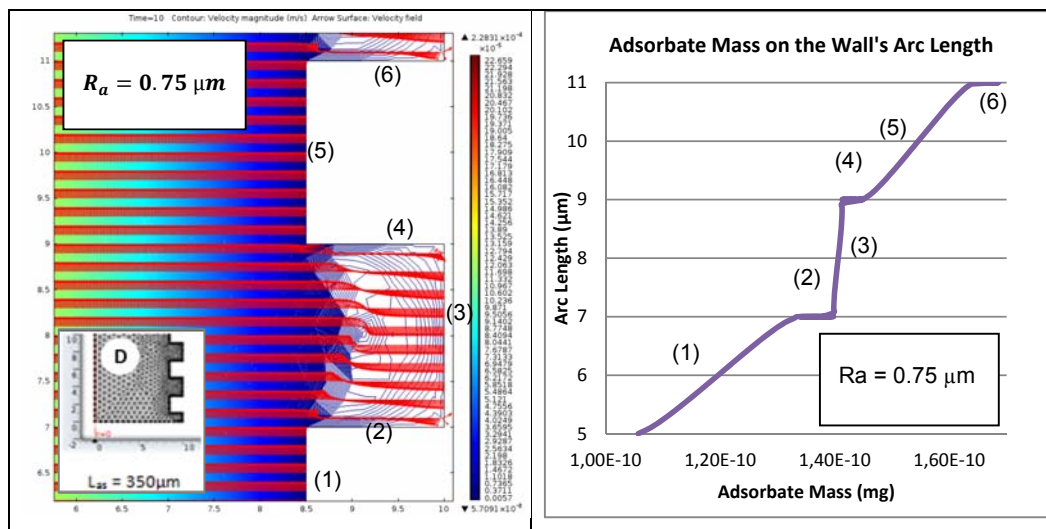


**Figure 6.21:** Velocity magnitude and stream lines at a cavity on the wall (left) and the corresponding adsorbate mass (right) for microchannel with  $R_a = 0.75 \mu m$

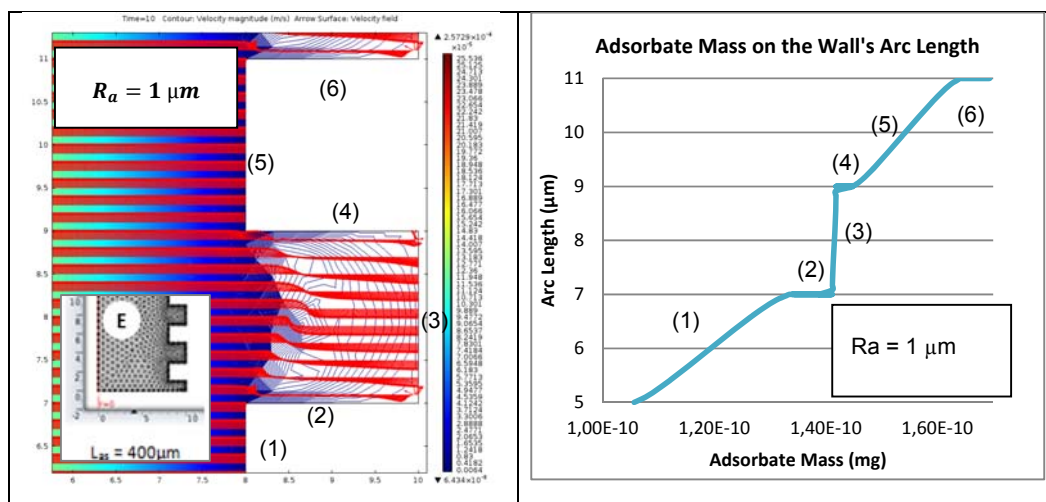


**Figure 6.22:** Velocity magnitude and stream lines at a cavity on the wall (left) and the corresponding adsorbate mass (right) for microchannel with  $R_a = 1 \mu m$

The comparison of the adsorbate mass on the cavity wall of the microchannel with different roughness is shown in **Figure 6.23**. It appears that alteration in the wall profile influences the distribution of the adsorbate mass on the wall. As the cavity becomes larger, less adsorbate is observed on the inner wall of the cavity. This finding is in a good agreement with the previous investigation that is shown in **Figure 6.15**.

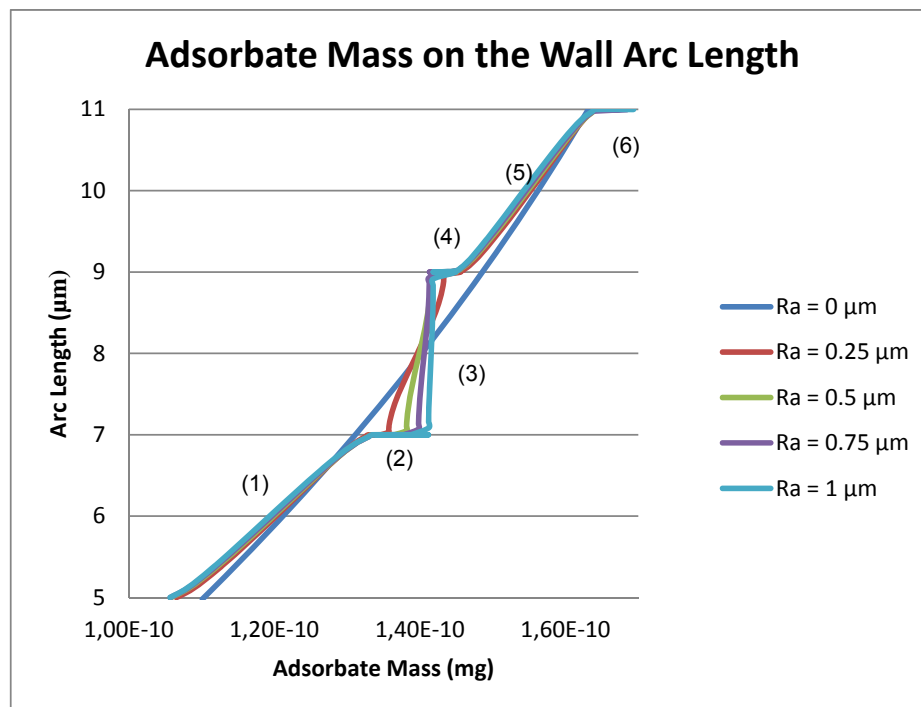


**Figure 6.23:** Adsorbate mass on the arc-length of the microchannel wall

## 6.5 Summary and Conclusion

This chapter discussed about the study for the effect of the wall roughness on the adsorption of the particle in the microchannel system. The idea is initiated by the study conducted by Fleming et al (2009a, b and 2010) that discover the enhancement of the adsorption of the scale inhibitor on the rock surface by injection the kaolinite and organosilane. The substances that attached on the rock grains increase the capability of the grain to adsorb the injected PPCA. Many studies have been carried out to investigate the adsorption on a wall with roughness [254-258]. However, study of the detail adsorption profile on the asperities is not yet much visited; hence, this study is conducted to contribute in filling this gap. In addition, study for adsorption in a dead end region in the microchannel is also visited.

A model of a 3D axis symmetrical microchannel based on the model discussed in chapter 4 is used in the study. A number of regular-shaped of squares along the channel wall are introduced to model the surface variation. The dimension of each square is then increased to simulate the enhancement of the surface area of the channel.

The study is focused on the transportation, adsorption, and desorption of the particles that is injected along a steady flow inside microchannels with different roughness. The transportation, adsorption and desorption of the particles is investigated for the continuous and discontinuous injection. The trend of the effluent concentration and the adsorbate particle mass and concentration is discussed.

It is observed that the wall surface roughness does not significantly affect the movement of the injected concentration front. However, it is discovered that the adsorption is positively correlated to the roughness of the microchannel. This is shown by the profile of the effluent concentration and the adsorbate mass on the wall's asperities. Focusing at the asperities of the channel's wall roughness, the adsorption happen the least at the surface that is the furthest from the centre of the microchannel and the highest on the surface that is closest from the centre of the microchannel. This findings confirms the study conducted by Fleming et al [103, 113] that the adsorption on the rock surface can be enhanced by increasing the surface are of the wall, e.g. by increasing the roughness of the rock's wall surface.

It is also found that diffusion is the main driving mechanism to transport the particles into the dead end region at the channel. Advection vortex and eddies also present at corner of the dead end region that hinders the particles to return to the channel after trapped inside the dead end. The profile of the cavity that presents on the microchannel wall influences the distribution of the adsorbed particle. It is impossible to transport the concentration inside the main bulk into the dead end region by the advection since flow cannot cross a streamline. This is in agreement with the theory of cavity flow [264, 265].

## Chapter 7

### Study of the Network Model

#### 7.1 Introduction

A development of a pore-channel network model based on the study in the previous chapters is discussed in this chapter. This study establishes to construct an alternative pathway to understand the distribution and adsorption-desorption mechanism in microchannel in porous media, where the previous studies [104, 117-119, 121] were mostly conducted for a macro-scale pore model.

The pore network is characterized by combination of several basic microchannel segments. Several basic microchannel segment configurations are developed that can be arranged to construct a more complex microchannel network model which represents a porous media. The transport, distribution and adsorption/desorption behaviour of an injected nanoparticle concentration are investigated.

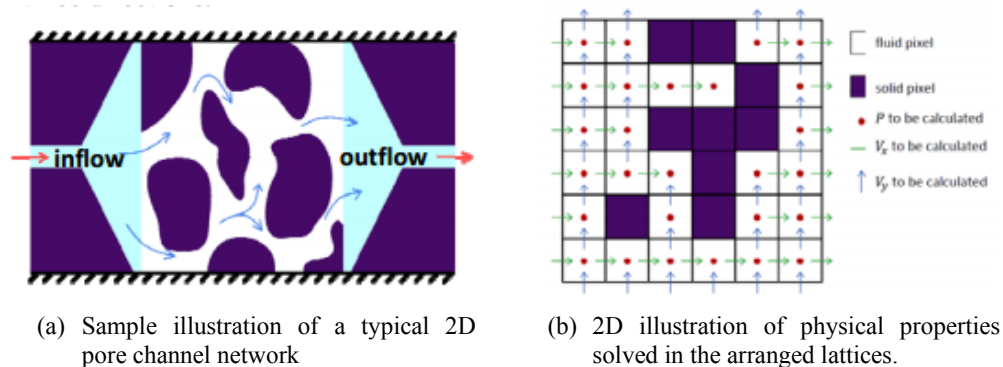


**Figure 7.1** Illustration of a pore channel network characterisation  
(Reproduced from Zhang et.al, 2011 [266])

The illustration of a pore-channel network characterisation is shown by **Figure 7.1**. **Figure 7.1a** shows a sample illustration of a typical 2D pore channel network and **Figure 7.1b** displays the corresponding 2D physical properties solved that represent in arranged lattices. These figures are taken from a study conducted to capture images of a nano-scale pore channel

---

network [266]. Instead of only capturing the pore channel image, this study investigates more thoroughly the transport and distribution of injected nanoparticles for each microchannel segment in the lattices. This will ultimately allow making a link between the properties in the microchannel segment and a more complex and established pore channel network.

## 7.2 Aims and Objectives

The aim is to develop an alternative tool to flexibly create typical network of pore channels where the transport and distribution of injected nanoparticle concentration within can be investigate. The objective is to establish investigation for microchannel segmentation that can be arranged flexibly to construct a more complex typical microchannel network model. Flow direction, pressure drop, and adsorption behaviour for each microchannel segment is also studied.

## 7.3 Methodology

Four simple channel-segment configurations were created in 3x3 units lattice with adaptable shapes to establish channel-networks with further complexity. In total, there are seven various flow patterns can be modelled in these five microchannel configurations. The patterns include flow in (1) a straight channel, (2) channel with bend to the left, (3) channel with bend to the right, (4) T junction that branches in the middle, (5) T junction that branches to the right, (6) T junction that branches to the left, and (7) a cross junction. The illustration for these channel segment configurations are shown in **Figure 7.2**.

The left boundary of each segment is the inlet of each microchannel, which inflows are illustrated by arrows with red coloured boundary in **Figure 7.2**. The outlet boundaries are the other end(s) of the microchannel boundary, which are illustrated according to the end direction of the arrows in the figure. In the simulation, the diameter of the microchannel segment presents in the lattice is 20  $\mu\text{m}$ , which remains similar as the dimension used in Chapter 4, 5, and 6.

The investigation is conducted for two geometry studies according to the magnitude of the corresponding lattice configuration. The first study is the preliminary investigation conducted for microchannels segment with similar surface area. The difference in size of the lattice is not considered in

this study. This preliminary study is to investigate the effect of segment's geometry configuration to the concentration distribution. The second is the main study, which is investigation for microchannel segment with similar magnitude lattice dimension. This configuration benefits the study because the microchannel segment inside the lattice can be arranged easily for constructing microchannel network. Each of the channel segments is stationed in a 3x3 unit's lattice that has similar length of magnitude. The corresponding length for the lattices is 200x200  $\mu\text{m}$ . The lattice can flexibly be arranged with each other at the corresponding boundaries to developing any complex microchannel network-model. The illustration of one of the possible arrangements for the lattices with similar dimension is displayed in **Figure 7.3**.

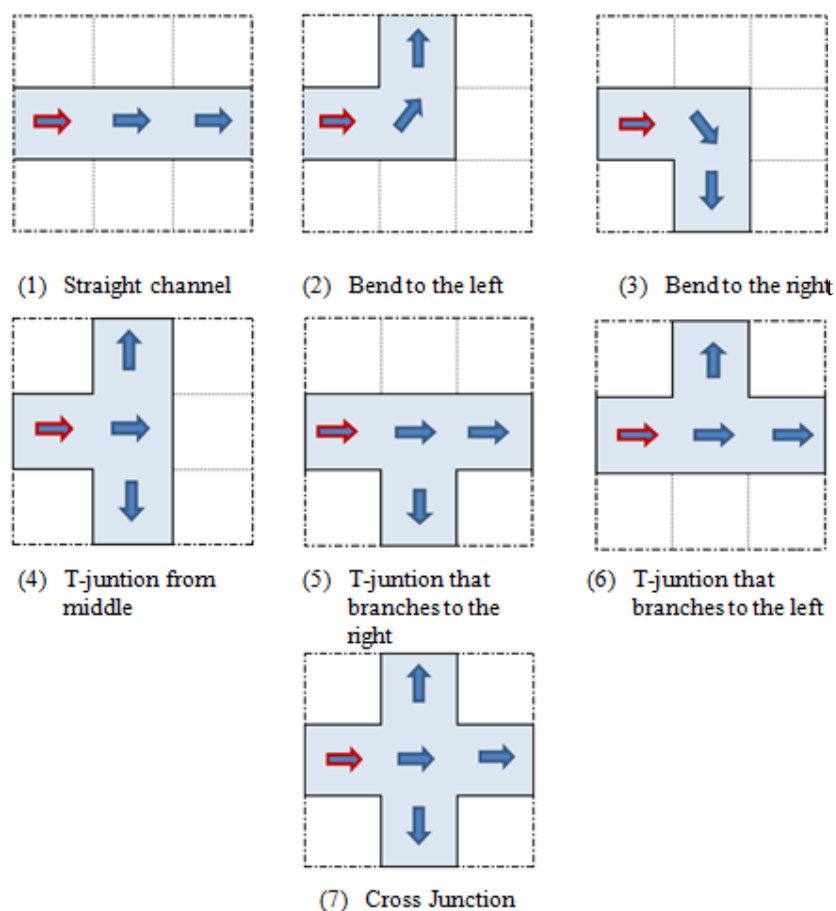


**Figure 7.2:** Channel geometry with similar adsorption surface area. Redlined arrow is indicates the inlet of the channel segment with 3x3 units lattice magnitude.

The segment is initially empty at the beginning of the simulation from any nanoparticle concentration. There is also no adsorbate present on the microchannel wall. 12500 ppm of particles is introduced at the inlet boundary for a fixed time length between 0 and 0.001 seconds. Each simulation is conducted for 10 seconds of simulation time. The injected concentration follows a constant and developed creeping velocity  $v=8.08 \times 10^{-5}$  m/s that satisfies Stokes Law applied in the simulation. The steady creeping flow establishes to a constant pressure difference between the inlet and the outlet of each segment. This also works in the other way around in the study, i.e. constant pressure applied provides a steady creeping flow for the microchannel. The simulator is flexible to run either under a constant creeping flow or under constant inlet-outlet pressure difference, hence the particles concentration distribution and adsorption can be investigated. After the injection at concentration  $C_{inj}$ , the inlet concentration is reduced to zero, but the flow continues. Diffusion is also considered in the system by introducing diffusion coefficient  $D_p = 1.29 \times 10^{-5}$   $\text{sm}^2/\text{s}$  whose value is obtained from Equation 3.26.

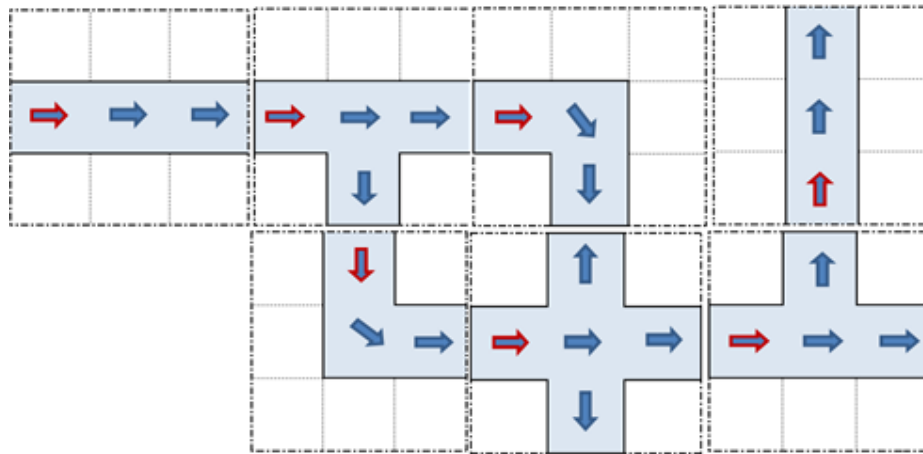


**Figure 7.3:** Illustration of the lattice arrangement for the study with similar lattice magnitude dimension

There are two types of concentration transport mechanisms in the system. The first is the concentration movement with the flow of the fluid bulk in the microchannel domain. This movement is governed by advection and diffusion. The second transport mechanism is the concentration movement between the fluid bulk and the channel wall due to concentration difference that triggers the adsorption and desorption process. Instead of using Langmuir isotherm adsorption [267], in this study the adsorption and

desorption mechanism follows the modified Freundlich isotherm adsorption that was derived by Skopp [170]. This method is valid to use in the study because the system is in reservoir condition where the temperature is constant and the pressure difference between each rock pores is relatively low.

In the study, the profile of the effluent concentration, adsorbate mass and adsorbate concentration against the injection volume are investigated. The relation between the adsorption with the corresponding pressure-difference between the inlet and outlet of the segment is also evaluated. The amount of the adsorbate for the latter is reflected in the term of adsorbate mass of the adsorbent at a certain concentration magnitude ( $x$ ) per unit mass of the adsorbent ( $m$ ). This parameter follows the Freundlich relationship below

$$\frac{x}{m} = kp^{1/n}$$

alternatively, in logarithmic form this equation becomes

$$\log x/m = \log k + 1/n \log p$$

where  $x$  is the weight of the adsorbate by mass of the adsorbent at a certain pressure  $p$ . Therefore,  $\frac{x}{m}$  represents the amount of adsorbate by the adsorbents per unit mass.  $k$  and  $n$  are constants at a particular temperature and for a particular amount of adsorbate and adsorbent. In this equation,  $n$  is always greater than one, indicating that the amount of the adsorbate does not alter as rapidly as the pressure.

The illustration of the Freundlich adsorption isotherm is shown in **Figure 7.4** i.e. plot for the adsorbate against the pressure (**Figure 7.4a**) and the plot  $\log \frac{x}{m}$  against the  $\log p$  for the adsorbate (**Figure 7.4b**). In this study, the mass of the adsorbent is unknown. Hence,  $\frac{x}{m}$  is approached by the adsorbate concentration which magnitude has already considered the surface area of the channel segment.

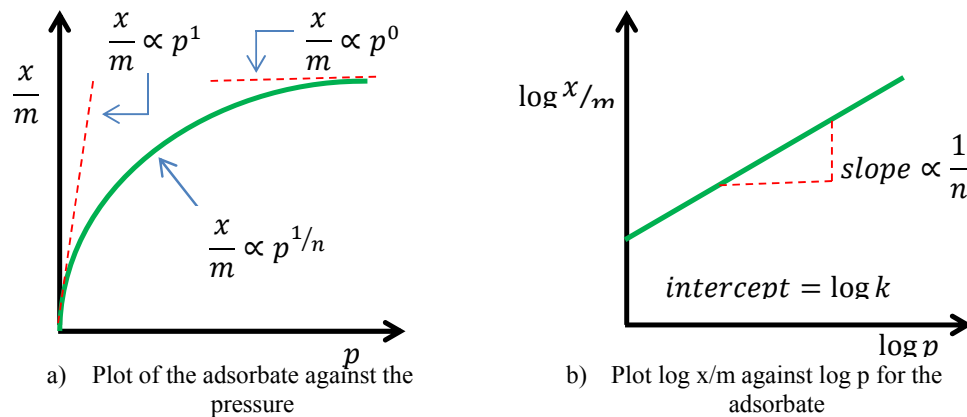


**Figure 7.4:** Freundlich adsorption isotherm

## 7.4 Microchannel segments with similar surface area

This section discusses variation of concentration distribution in the microchannel segments with similar surface. The surface area of each microchannel is fixed i.e.  $1.26 \times 10^{-8} \text{ m}^2$ . A similar volume of 12500 ppm of nanoparticles concentration is injected at the beginning of the simulation until 0.001 seconds from the inlet boundary of each segment. The injected concentration is transported along a constant creeping flow velocity. The velocity for the base case is  $v_0 = 8.08 \times 10^{-5} \text{ m/s}$  with constant pressure at the outlet boundaries, 0 Pa. The simulation for each case is conducted for 10 seconds.

Generally, velocity profile of a creeping flow inside a microchannel follows a parabolic profile. Parabolic profile means the highest velocity presents at the middle of the channel and the least velocity at the region close to the wall boundary of the channel. This general profile deviates a little from this feature when bends are encountered, as seen in **Figure 7.5**. The base case in the study is the straight channel (A), which velocity follows the parabolic profile evenly in the microchannel. In the curved microchannel (B) and (C), the velocity parabolic profile is uneven that there is a more noticeable section with low velocity at the bend than then section with uncurved channel. In the microchannel with the T-junction that branches from the middle, the flow is divided evenly to the left and to the right direction. A noticeable area with low velocity is observed at the junction of the segment (D). In the microchannels with T-junction that branch to the left

and right i.e. segment (E) and (F) respectively, the velocity parabolic profile directs to the middle of the junction and divided to the branches. The velocity profile in the cross-junctional geometry (G) is dispersed at the middle of the junction and the flow is divided into three directions towards the outlets.

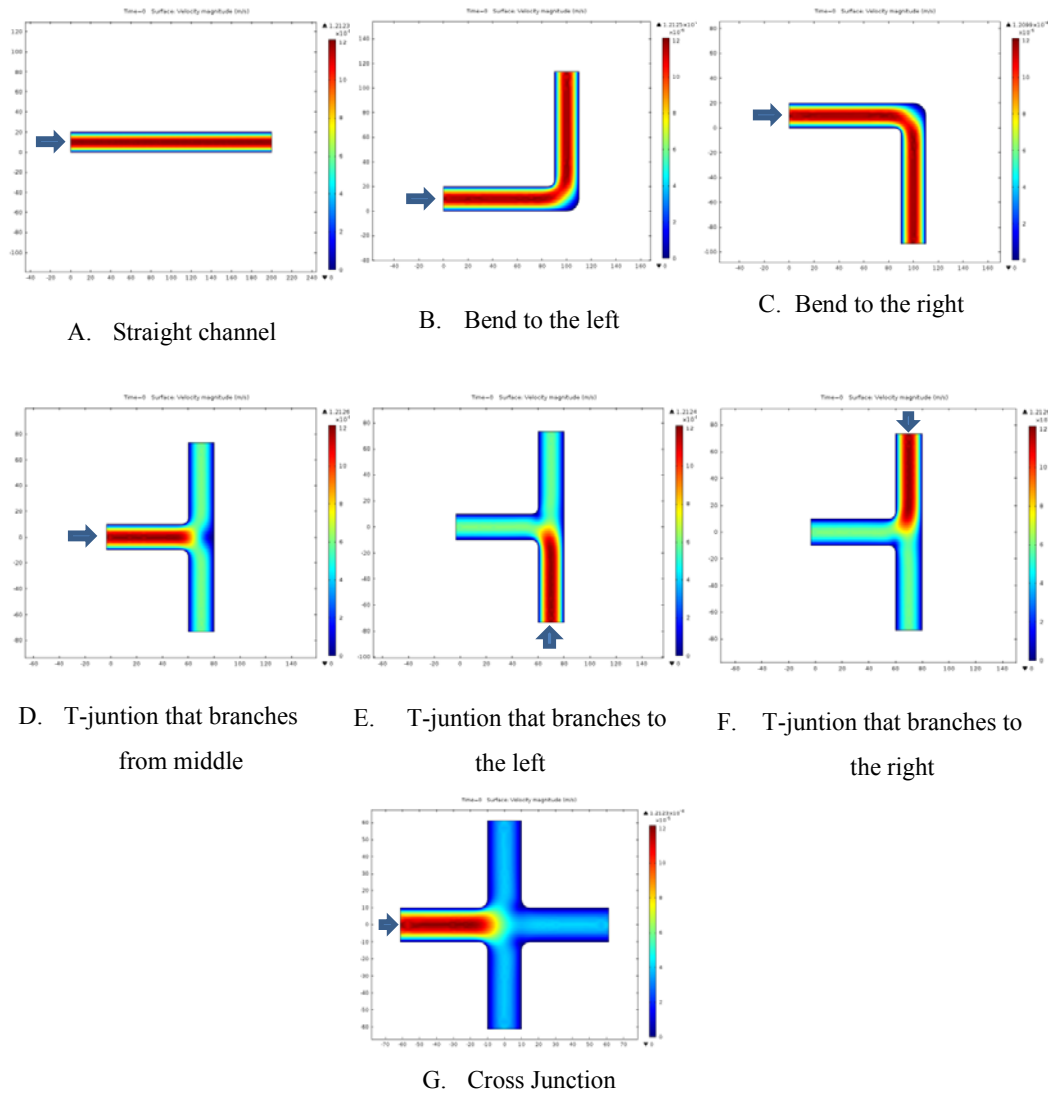


**Figure 7.5:** Contours of velocity magnitude for the microchannel segment geometry with similar adsorption surface area

**Figure 7.6** shows the pressure distribution for each geometry segment. It appears that the number of outlet boundary influences the pressure distribution in the segment. The pressure distribution for the

straight channel (A), channel with bend to the left (B), and the channel with bend the right (C) is equivalent. The pressure distribution for the T-junction branch microchannel segments (D, E, and F) is comparable. The pressure profile for the cross-junction microchannel segment (G) is slightly different from the T-junctions where the pressure drops is higher for the former at the location before the junction.

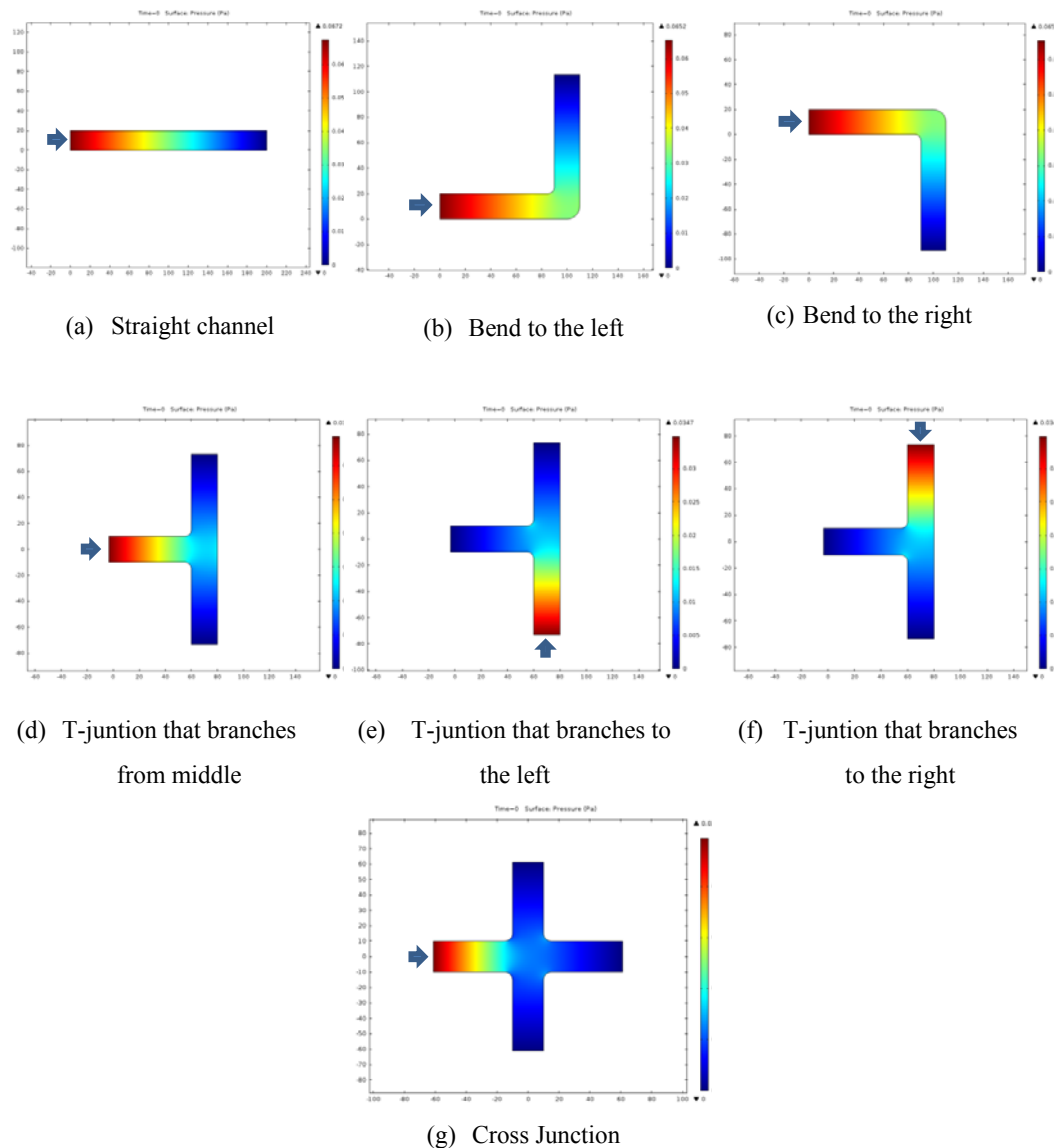


**Figure 7.6:** Pressure profile for the microchannel segment geometry with similar adsorption surface area

**Figure 7.7** shows the profile of (a) inlet-outlet pressure difference, (b) average effluent concentration, (c) total adsorbate concentration, and the (d) total adsorbate mass for the microchannel segment geometry with similar adsorption surface area. The profile is taken by averaging the magnitude of each parameter for each injection volume over the corresponding area.

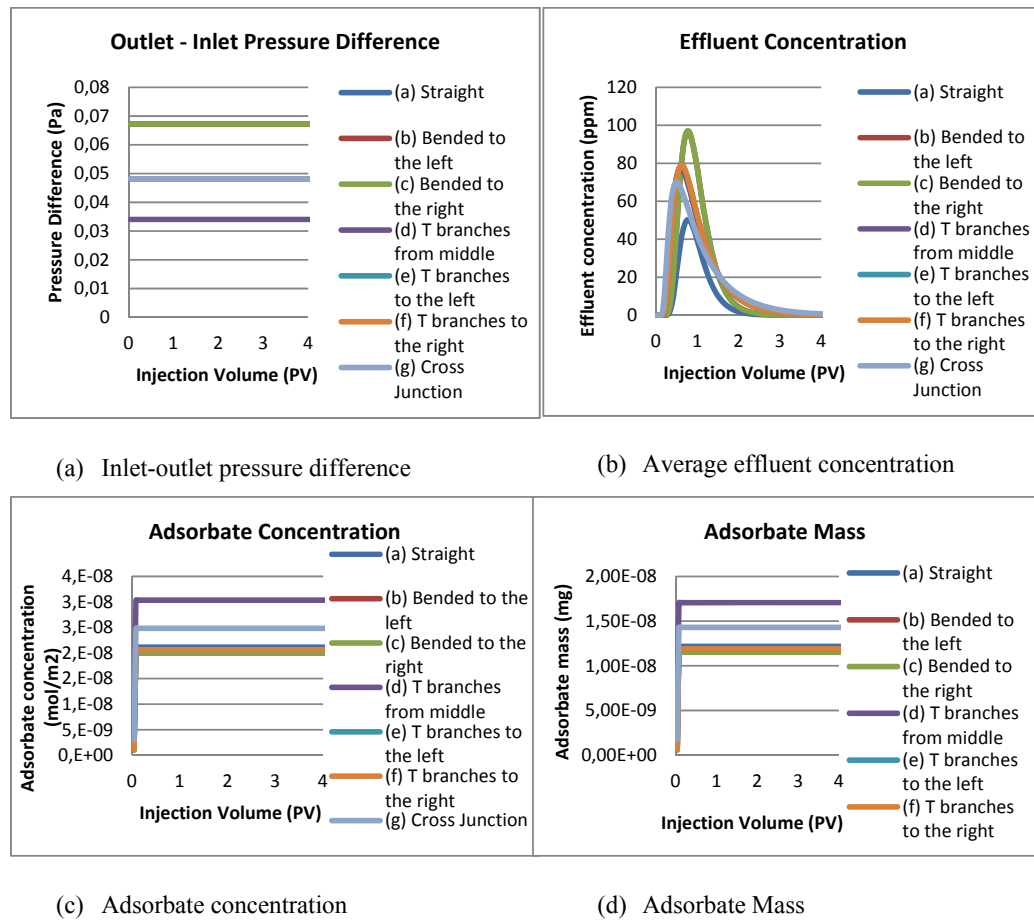


**Figure 7.7:** The profile of (a) inlet-outlet pressure difference, (b) effluent concentration, (c) adsorbate concentration, and the (d) adsorbate mass for microchannel segment geometries with similar adsorption surface area

In **Figure 7.7a**, it is observed that the inlet-outlet pressure difference for the straight microchannel segment (a) and the segments with one bend (b and c) are fairly similar, which is in the magnitude of 0.067 Pa. This value is higher than the outlet-inlet pressure difference for segment (d), (e), (f) and (g). The inlet-outlet pressure difference segment (d) is 0.034 and for segment (e), (f) and (g) is 0.048. Segment (d), (e) and (f) has similar

geometry, i.e. the T-junction. However, the inlet for segment (d) is at the middle, and the rest is from the other end of the geometry. The pressure difference for the segment (e) and (f) is similar to segment (g) although the geometry configuration is not similar.

The profile of the average effluent concentration for different microchannel segment geometry is shown in **Figure 7.7b**. The lowest to the maximum average effluent concentration is observed for the straight microchannel (line a), then the microchannel segment with cross-junction (line g), then the T branch-segments (line d, e, f), and the highest for the bended segments (b and c). The trend of the effluent concentration tends to be the inverse of the adsorbate concentration and mass, which are shown in **Figure 7.7c** and **Figure 7.7d** respectively. This observation shows that the configuration of the microchannel segment influence the concentration transport and adsorption in the microchannel. This is shown by the profile variation in the effluent concentration and the adsorbate concentration and mass in the system with similar adsorption surface area.

Microchannel segment geometry	Adsorption equivalent length ( $\mu\text{m}$ )	Inlet-Outlet Pressure difference (Pa)	Average Effluent Concentration (ppm)	Average Adsorbate Concentration ( $\text{mol}/\text{m}^2$ )	Average Adsorbate Mass (mg)
(A) Straight	400	0.0673	935.21	2.11E-08	1.22E-08
(B) Bended to the left	400	0.0673	1869.70	2.00E-08	1.15E-08
(C) Bended to the right	400	0.0673	1869.70	2.00E-08	1.15E-08
(D) T branches (L/R)	400	0.0340	1847.93	3.00E-08	1.73E-08
(E) T branches to the left	400	0.0482	1868.79	2.07E-08	1.19E-08
(F) T branches to the right	400	0.0482	1868.79	2.07E-08	1.19E-08
(G) Cross Junction	400	0.0482	1850.25	2.48E-08	1.43E-08

**Table 7.1:** The magnitude of (a) inlet-outlet pressure difference, (b) average effluent concentration, (c) average adsorbate concentration, and the (d) average adsorbate mass for the microchannel segment geometry with similar adsorption surface area

The detail for the deviation for the inlet-outlet pressure, effluent concentration, adsorbate mass and the adsorbate concentration is shown in **Table 7.1**. The values are obtained from similar injected pore volume of each microchannel segment when the effluent concentration has reached its equilibrium condition. The equilibrium concentration is obtained by

investigating the value of  $c_t$  when  $\frac{(c_t - c_{t+1})}{c_t} < 0.001\%$ . In this case,  $c_t$  (ppm) is the average effluent concentration at time  $t$ . The magnitude of each parameter for every microchannel segment is plotted. The inlet-outlet pressure difference for each segment is shown in **Figure 7.8**, the effluent concentration for each segment is in **Figure 7.9**, the adsorbate concentration is in **Figure 7.10**, the adsorbate mass is in **Figure 7.11**.

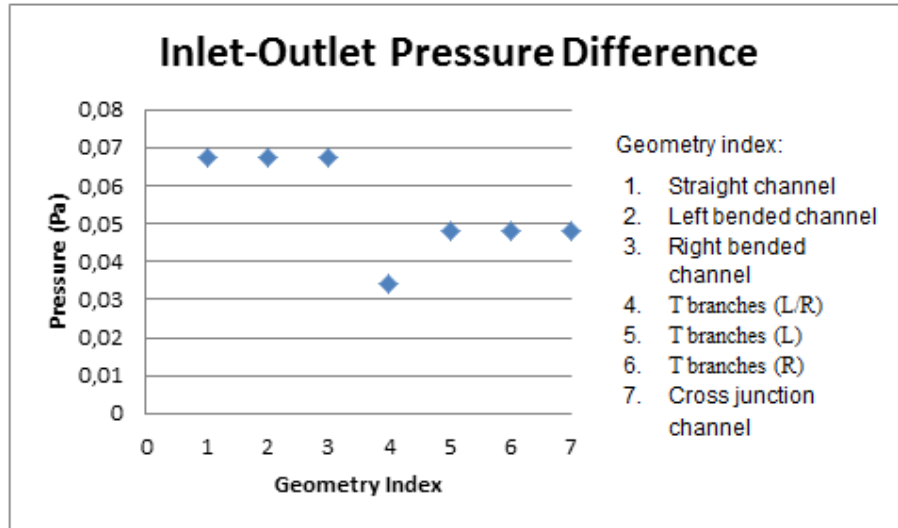


**Figure 7.8:** Inlet-Outlet Pressure Difference for different geometry with similar total adsorption surface area

**Figure 7.8** shows the plot of the inlet-outlet pressure difference for different segment geometry. The pressure difference for the straight microchannel (index 1) and the bended microchannel segments (index 2 and 3) is comparable. The magnitude of the pressure difference of these three cases is the highest of all, which means the flow restriction for this microchannel segment is the greatest. Particular characteristic for index 1, 2, 3 is these three has only 1 outlet boundary, and outlet is positioned furthest from the inlet boundary. The T-junction microchannel segment (index 4) which stream-flow directs from the middle has the least inlet-outlet pressure of all. However, the T-junction that stream flows from the other ends (index 5 and 6) has larger pressure difference than index 4, although the shape of the segment is similar. The microchannel with index 4 has a lower pressure difference than microchannels with index 5 and 6 because the flow for the former is divided 90 degrees into two directions. The pressure different of the cross-junction microchannel (index 7) is comparable with the

microchannel with index 5 and 6 although the configuration and the number of the outlet boundary are different. This indicates that both the number and the position of the outlet from the inlet of the segment configuration influence the pressure difference between the inlet and the outlet.

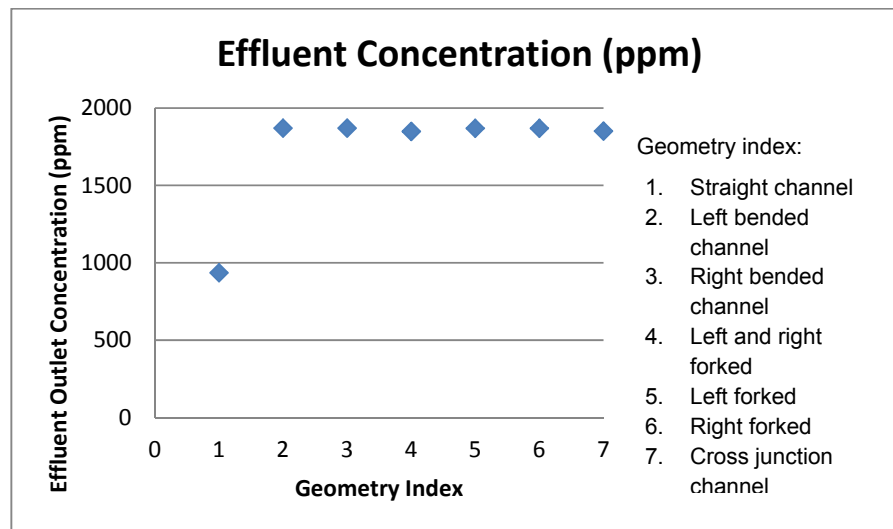


**Figure 7.9:** Effluent concentration for different geometry with similar total adsorption surface area

The comparison for the average effluent concentration of each microchannel segment is shown in **Figure 7.9**. The magnitude of the total effluent concentration for index 1 is the lowest of all, i.e. 935.2 ppm. The magnitude of the other cases is comparable with a slight low value for the index 4. The comparison of the average adsorbate concentration for each microchannel segment is shown in **Figure 7.10**. Basically, the difference of the average adsorbate concentration of each microchannel segment is small. However, the discussion is carried on for further investigation. Here it is observed that the adsorbate concentration for T-branched microchannel with middle inlet (index 4) is the highest of all, follows by the cross-junction segment (index 7), the single straight microchannel (index 1), the T-branches microchannel whose inlet from the side boundary (index 5 and 6), and the least is the bended microchannel segments (index 2 and 3). The correlation between the amount of the adsorption and the geometry configuration might be affected greatly by the pressure difference and the configuration of the corresponding microchannel segments. The adsorption is especially high in segment 4 because there is a section of the microchannel wall that facing the direction of the flow. Since the surface

areas of all microchannel segments are similar, the magnitude of the total adsorbate concentration is comparable with the total adsorbate mass which is shown in **Figure 7.11**. Thus, it is deduced that the complexity of the microchannel geometry influences the amount of adsorption and does not correlate straightforwardly with the amount of the outlets.

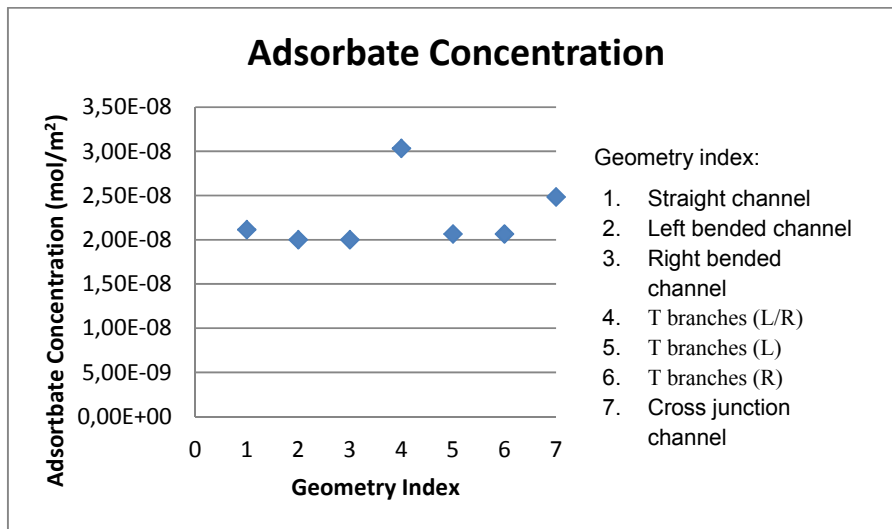


**Figure 7.10:** Adsorbate concentration for different geometry with similar total adsorption surface area

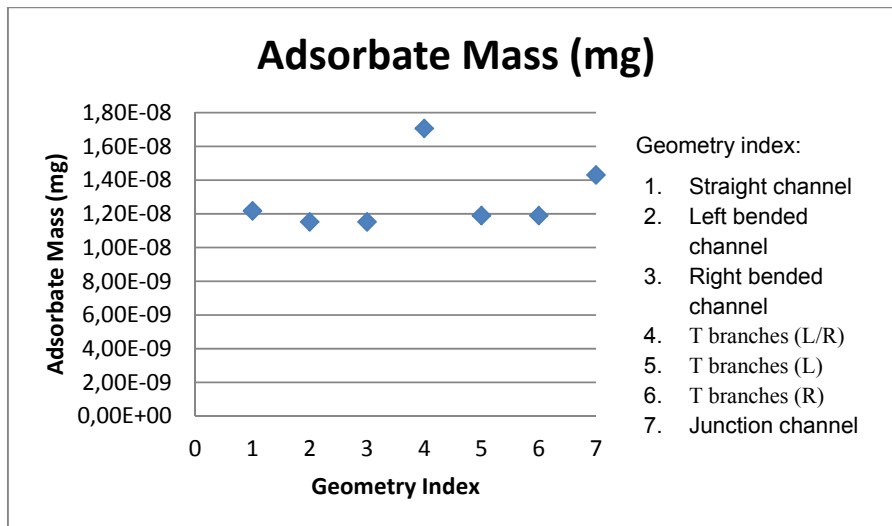


**Figure 7.11:** Total adsorbate mass for different geometry with similar total adsorption surface area

## 7.5 Microchannel segments with similar lattice dimension

In the case of microchannel with similar lattice dimension, the surface area of each microchannel segments is different from one to another. Besides using index, each surface area of the microchannel segment is represented by the ratio of the corresponding surface area compare to the surface area of the straight channel. This is named *equivalent surface area ratio*. The equivalent surface area ratio for the straight channel is 1, for the channels with one bend is 0.98, for the T shaped channels is 1.39, and for the cross junction channel is 1.82  $\mu\text{m}$ .

Similar with the case of continuous injection, initially the segments are empty from any nanoparticle concentration. 12500 ppm concentration is injected for a fixed time length between 0 and 0.001 seconds through the inlet boundary into the microchannel along with a constant inlet velocity  $v=8.08 \times 10^{-5}$  m/s. Some of the injected concentration is adsorbed to and desorbed from the wall of the domain due to concentration difference. The outlet of each segment is set for 0 Pa pressure, allowing a constant steady state pressure difference and velocity between the inlet and outlet boundaries. The simulation is conducted for 10 seconds period.

The difference of the inlet and the outlet pressure as the result of the constant injection velocity for each segment is shown in **Figure 7.12**. The magnitude of the pressure difference is different from one of another. The inlet pressure for the straight channel (index a) is the highest i.e. 0.068 Pa. The second highest of all is the microchannel with one bend (index b and c), i.e. 0.064 Pa. The third highest pressure difference is the microchannel with T branches i.e. around 0.048 Pa. There are three segments with T branches configuration, i.e. the one that flow begins from the middle section of the branch and then divided into two outlets, one that flows branches to the left, and the last one is the flows that branches to the right. The inlet pressure from the T branch with flow from the middle has slightly less inlet pressure than the two others, i.e. 0.047 Pa. The least inlet pressure is observed for the microchannel with a cross junction; however the amount of the outlet boundary is the most of all. This is interesting to discover that geometry index (a), (b), and (c) have larger pressure differences than the rest although the formers have less surface area than the latters do. It is then again deduced that the number of the outlet boundary affects the pressure difference for the microchannel segment.

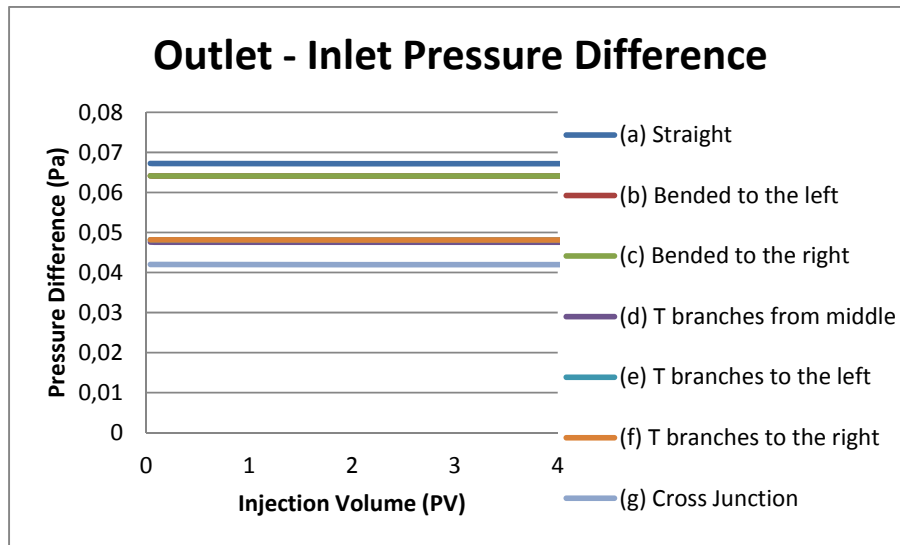


**Figure 7.12:** The difference of the inlet and the outlet pressure for different channel segment geometries with similar channel lattice dimension

The pressure distribution along each microchannel segment is displayed in **Figure 7.13**. The pressure distribution for the segments with one outlet is relatively similar. This is shown in **Figure 7.13** index (a), (b), and (c) where the green colour legend is at the middle of the microchannel is used for comparison. The pressure distribution decreases more rapidly as the number of the segment's outlet boundary increases. This is shown in **Figure 7.13** (d), (e), (f), and (g) where the green colour legend moved closer to the inlet boundary.

The distribution of the corresponding flow velocity for each microchannel segments is shown by **Figure 7.14**. The axial velocity in the microchannel follows a parabolic distribution, with zero velocity at the wall and maximum at the middle of the channel. The low velocity region is shown with the blue colour. The low velocity region is also observed at the middle part of the branch of the T-junction in **Figure 7.14** (d). The low velocity region in geometry (e) and (f) is less discovered than in geometry (d). At the junction of geometry (d), (e), and (f), the stream is divided into two directions with each velocity is half of its initial. In the cross junction (g), the velocity is divided into three different flow directions, with velocity magnitude of each direction is one-third of the initial magnitude.

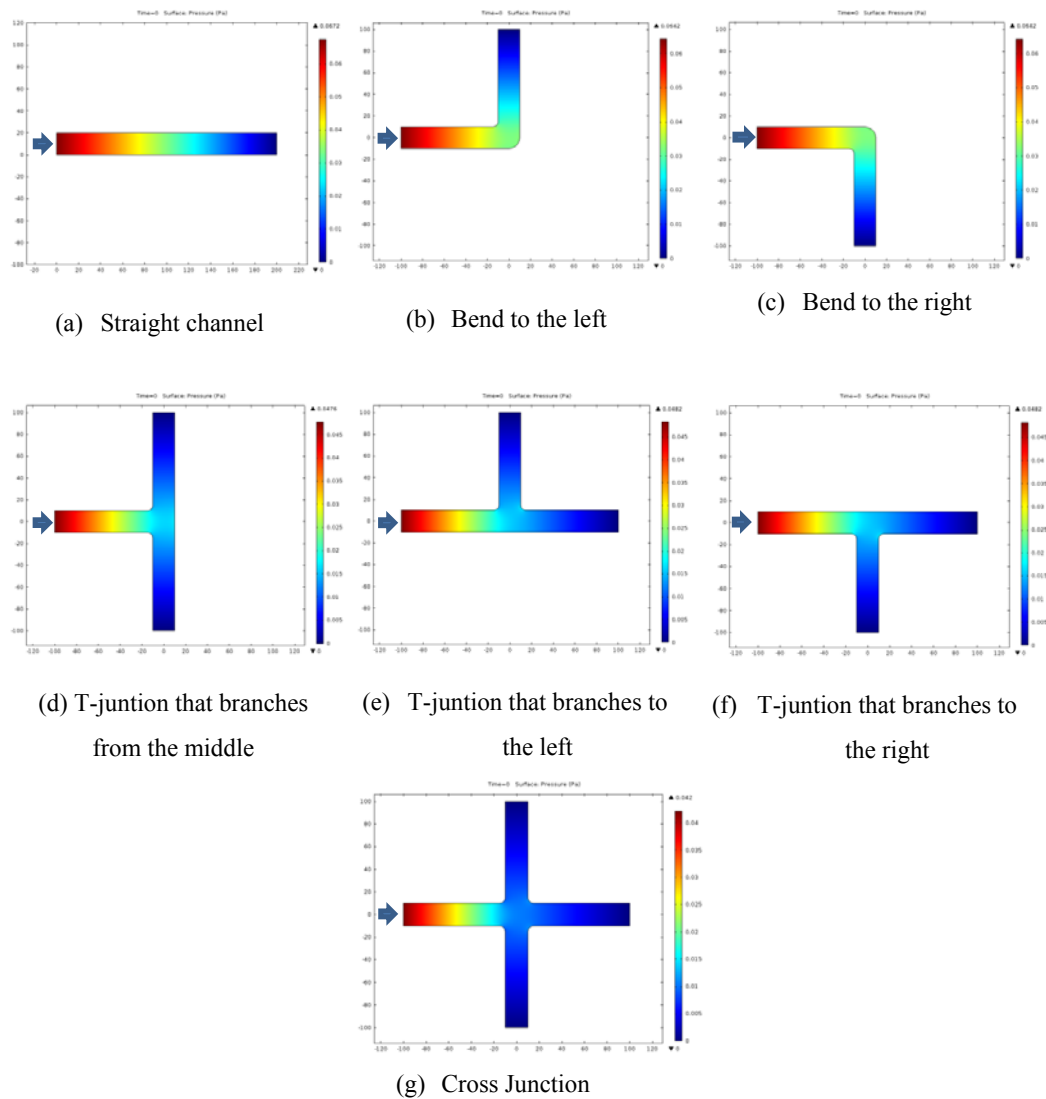


**Figure 7.13:** Pressure distribution for different channel segment geometries with similar channel lattice dimension

The profile of the effluent concentration for each microchannel segment is investigated. Since the nanoparticle is injected discontinuously, the effluent concentration also indicates the amount of the particle adsorbed on the wall of microchannel segment by subtracting the effluent from the initial injected concentration. On the other word, high effluent concentration is an indication of low adsorption, and inversely low effluent concentration indicates a high magnitude of adsorption. However, this observation will not be valid for a continuous concentration injection because eventually the effluent concentration will match the inlet concentration when the adsorption

and desorption rate balance and the channel is saturated. Thus, the time evolution of the inlet and effluent concentration difference is needed to deduce the total amount adsorbed.

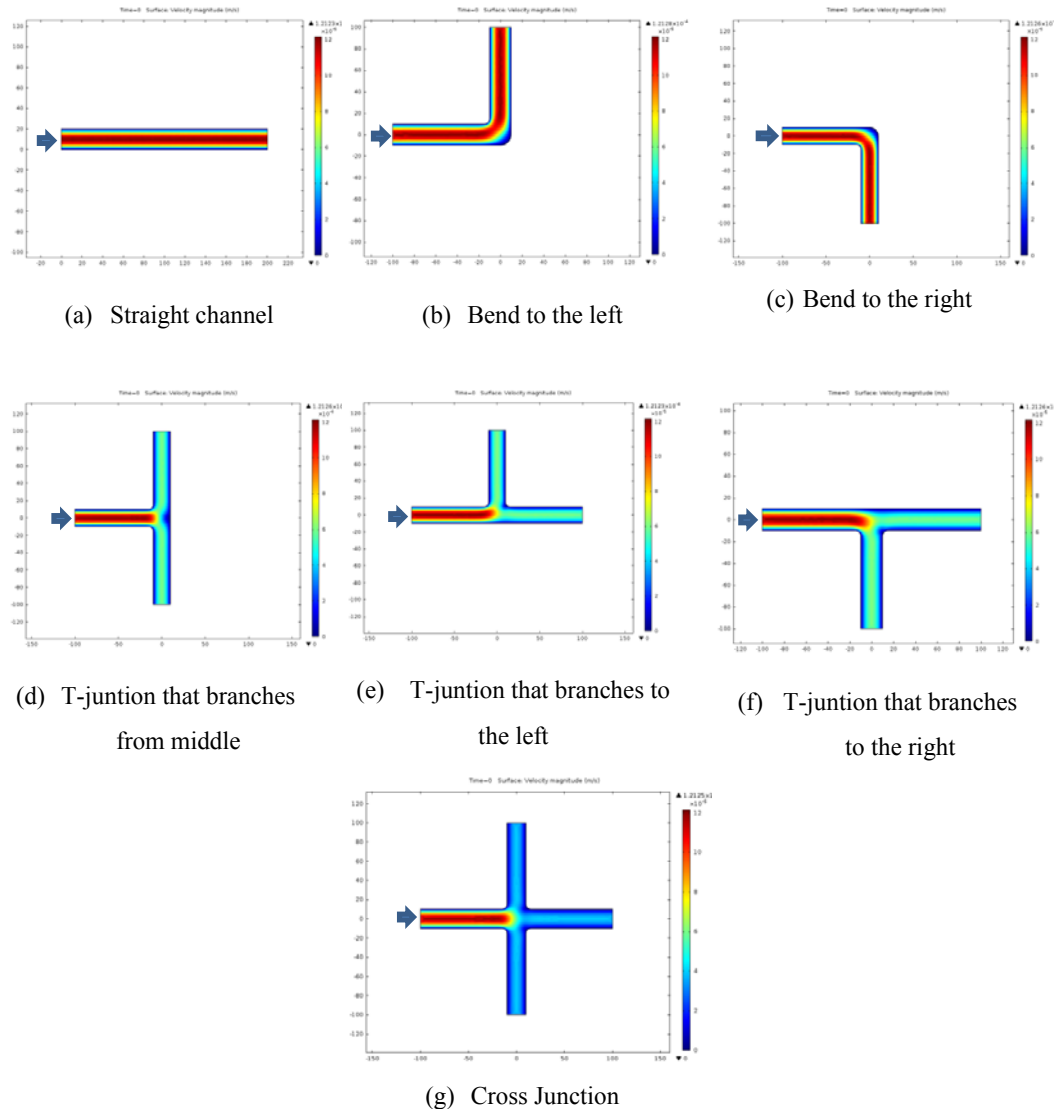


**Figure 7.14:** Velocity profile for different channel segment geometries with similar channel lattice dimension

**Figure 7.15** shows the profile of the effluent concentration for each microchannel segment. The largest peak of effluent concentration is found for the bended segment (b and c), where the magnitude is similar for the two. The next highest peak is the channel segment with a cross junction (g). The third largest peak of the effluent concentration is all segment with T

junctions i.e. microchannel segment with branches from the middle (d), the microchannel segment with T junction that branches to the left (e) and also right (f). The least effluent concentration is observed at the straight microchannel segment (a).

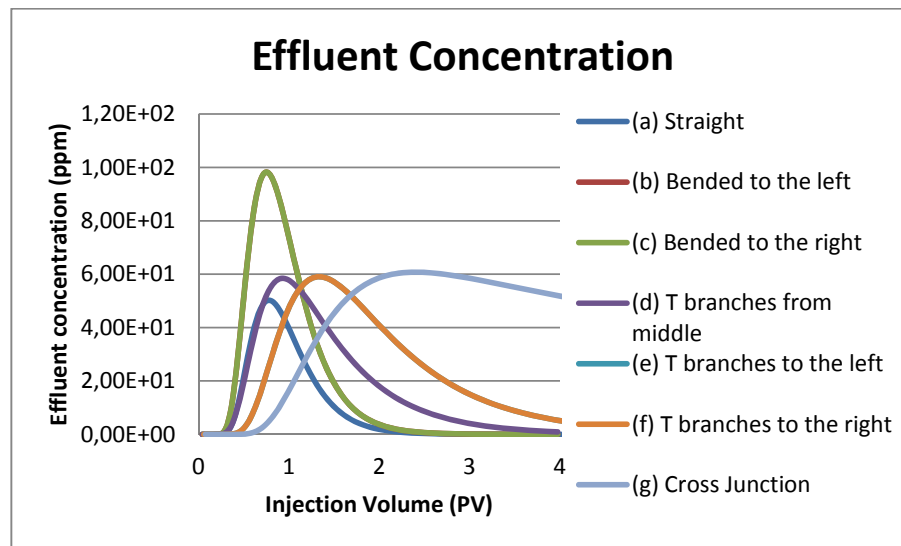


**Figure 7.15:** Effluent concentration for different channel segment geometries with similar channel lattice dimension

The decrease of the trend shows the desorption of the particles from the channel wall. The decrease profile of the segment with cross-junction (g) is however different from the rest of the profile where the concentration is still found in the boundary after 4 PV (pore volume) injection. The desorption happens during the longest simulation time for the cross-junction segment (g). This is indicated by the lowest inclination of the grey line in the **Figure 7.15**. This means the geometry complexity of the channel affects the desorption in the system.

The amount of the adsorbate is investigated by observing the trend of the adsorbate mass, which is shown in **Figure 7.16**. The trend shows the mass of the adsorbed particles builds up until reaching a constant magnitude. The build-up very early showing that the adsorption happens promptly after the injection. The profile increase before the flattening shows the process for the system reaching its equilibrium condition between the adsorption and desorption. The constant profile magnitude of the effluent concentration when it reaches plateau shows the condition of equilibrium for

the adsorption system where the rate of the adsorption and desorption are comparable. The highest magnitude of the adsorbate concentration profile observed presents for the cross-junction microchannel (g). This indicates the adsorption happen the most at this microchannel segment compared to the others. The second largest adsorbate mass plateau belongs to all the channels with the T branches (d,e,and f). The lowest adsorption occurs at the straight and bended microchannel (a, b, c). It appears the amount of the adsorbate mass is proportional to the number of the outlet boundary. Since in the study the number of the outlet boundary reflects the magnitude of the microchannel's surface area, hence, it is deduced that the amount of adsorbate mass is proportional to the magnitude of the surface area of the microchannel.

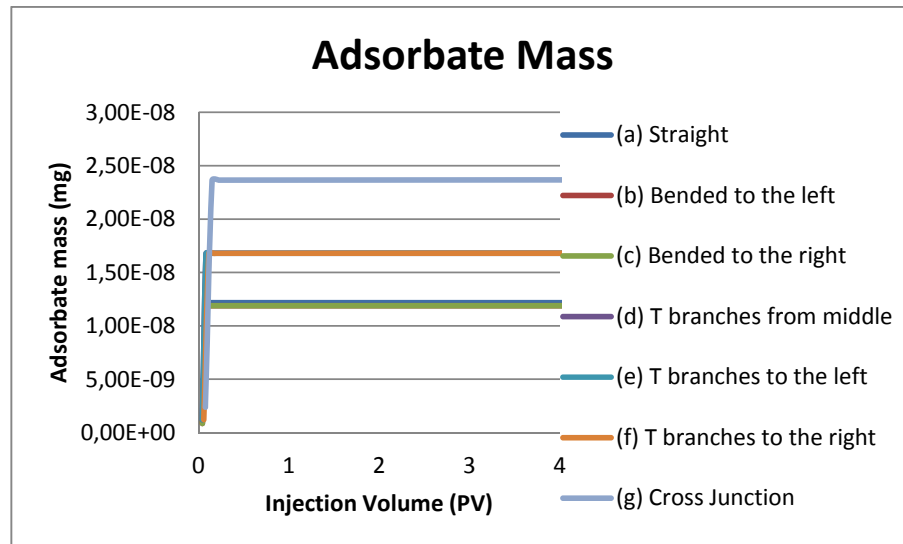


**Figure 7.16:** Adsorbate mass for different channel segment geometries with similar channel lattice dimension

The profile of the adsorbate concentration is also investigated which is shown in **Figure 7.17**. The adsorbate concentration for the straight and the bended microchannel (a, b, c) have the highest adsorbate concentration. The cause for these segments have similar adsorption concentration is because of their surface area is comparable. The second largest adsorption concentration is observed on the microchannel segments with T-junction (d, e, and f). The magnitude of the adsorption for all the T-junction segments are also in one alignment, which also happens because each of them has similar surface area. The least adsorption concentration is found for the

microchannel segments with cross-junction (g). The trend of the adsorbate concentration is the inverse of the adsorbate mass profile. This means that the alteration of the adsorption mechanism is incomparable with the alteration of the dimension of the segments in the study. This condition causes the concentration of the adsorbate in the microchannel with less surface area is denser than in the microchannel with larger surface area.

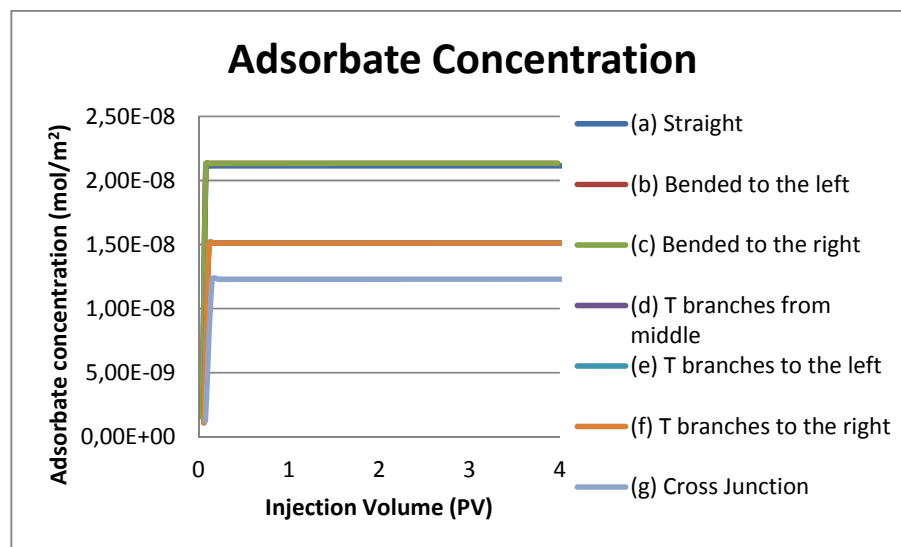


**Figure 7.17:** Adsorbate concentration for different channel segment geometries with similar channel lattice dimension

**Table 7.2** shows the summary for the values of the adsorption equivalent ratio, the inlet-outlet pressure difference, the effluent concentration, the total adsorbate mass and the adsorbate concentration. The first column displays the basic segment geometries used in this study. The segment geometries are represented by the geometry index i.e. geometry (1) for the straight channel, geometry (2) for the segment which bended to the left, geometry (3) for the segment which bended to the right, geometry (4) for the T-branch segment which stream flows from the middle, geometry (5) for the T-branch segment which stream flows to the left branch, geometry (6) for the T-branch segment which stream flows to the right branch, and the geometry (7) for the cross junction microchannel segment. These basic segment geometries can be combined to create a network of pores.

Microchannel segment geometry	Adsorption surface equivalent ratio	Inlet-Outlet Pressure difference (Pa)	Effluent Concentration (ppm)	Adsorbate Mass (mg)	Adsorbate Concentration (mol/m <sup>2</sup> )
(1) Straight	1	0.0673	935.21	2.11E-08	1.22E-08
(2) Bended to the left	0.98	0.0642	1870.47	2.13E-08	1.19E-08
(3) Bended to the right	0.98	0.0642	1870.47	2.13E-08	1.19E-08
(4) T branches from middle	1.39	0.0476	1855.48	1.51E-08	1.68E-08
(5) T branches to the left	1.39	0.0482	1857.24	1.51E-08	1.68E-08
(6) T branches to the right	1.39	0.0482	1857.24	1.51E-08	1.68E-08
(7) Cross Junction	1.82	0.0420	4187.41	1.23E-08	2.37E-08

**Table 7.2:** Summary for the similar lattice dimension

The geometries are created based on similar lattice dimension, the adsorption equivalent length different from one to the others. The second column shows various adsorption surface of each microchannel that is indicated by the adsorption surface equivalent dimensionless ratio. This ratio is calculated by comparing the surface area of particular segment with the base case segment (the straight channel segment). It is observed that there are 4 groups of adsorption surface equivalent ratio, which are 1 for the straight channel, 0.98 for the channel with one bend, 1.39 for the microchannel with T branch, and 1.82 for the microchannel with the cross junction. The straight microchannel and the ones with one bend have comparable magnitude.

The third column shows the inlet-outlet pressure difference of each corresponding segment. For all segment geometry, these pressure differences are measured based on similar inlet velocity and 0 Pa outlet pressure. The fourth column shows the total effluent outlet concentration for each segment. The fifth column shows the adsorbate mass and the last one shows the adsorbate concentration. All data are measured for 4 pore volumes to be comparable with the study of the case of similar adsorption surface in section 7.3.

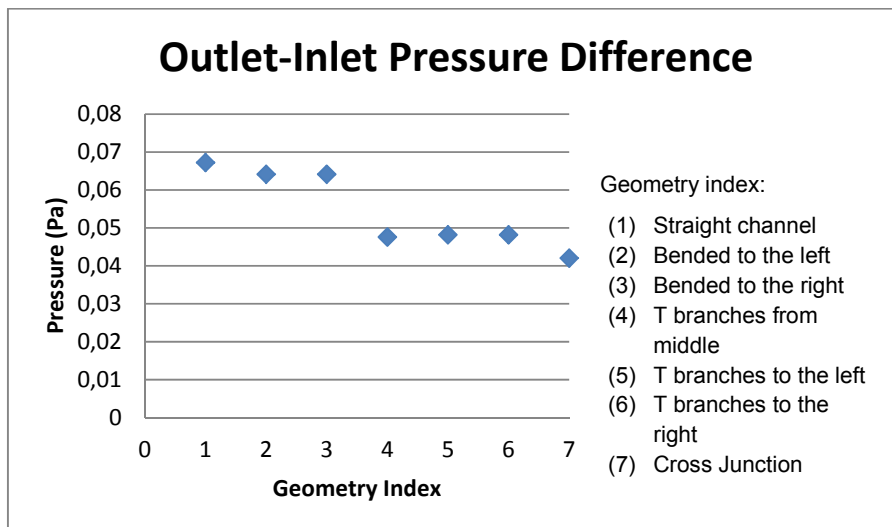


**Figure 7.18:** Inlet-Outlet pressure for different channel segment geometries under a constant inlet velocity for similar channel lattice dimension

**Figure 7.18** shows the plot between the inlet-outlet pressure difference and the microchannel segment geometry for a constant inlet velocity. The geometry of the segment influences the system's inlet-outlet pressure difference. The highest inlet-outlet pressure presents in the straight microchannel. The pressure difference for the bended microchannels is slightly lower than the pressure difference in the straight microchannel system. The pressures of the microchannels with T branches are lower than the straight microchannel. The pressure different for the cross-junction is the lowest of all. The variation in the pressure difference is proportionally affected by the complexity, the surface area, and the amount of the outlets of the microchannel.

The trend of the final effluent concentration against the geometry index is also investigated which results are shown in **Figure 7.19**. The effluent is measured by averaging the magnitude at the outlet boundaries of each corresponding microchannel segment when the system reaches equilibrium. It is important to recall that the surface area of each segment is different, therefore the effluent concentration measured is only shows the qualitative value of the adsorption, and might not be comparable in quantity. It is observed that the magnitude of the effluent concentration for the straight microchannels is the lowest of all, i.e. 935 ppm. On the other hand, the effluent concentration observed for the cross junction microchannel is the

highest of all, i.e. 4187 ppm. The rest of the microchannel segments have comparable effluent concentration, i.e. around 1860 ppm.

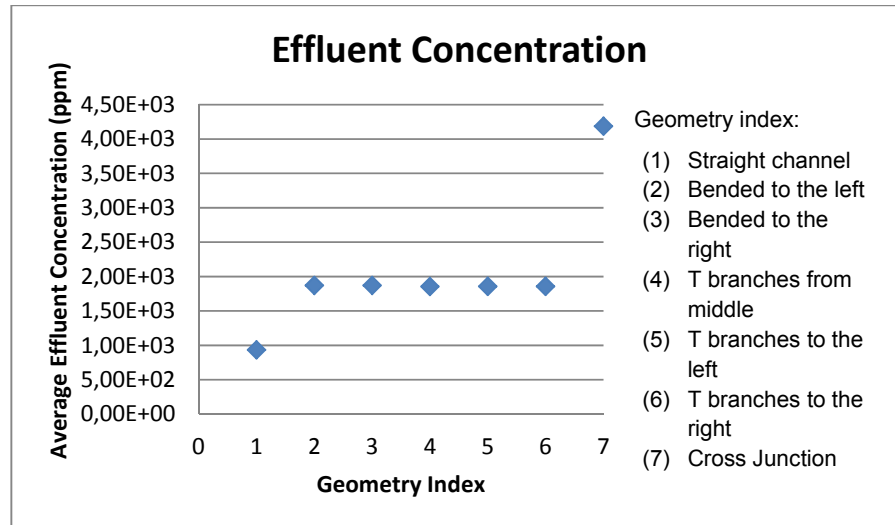


**Figure 7.19:** Final effluent outlet concentration for different channel segment geometries for similar channel lattice dimension

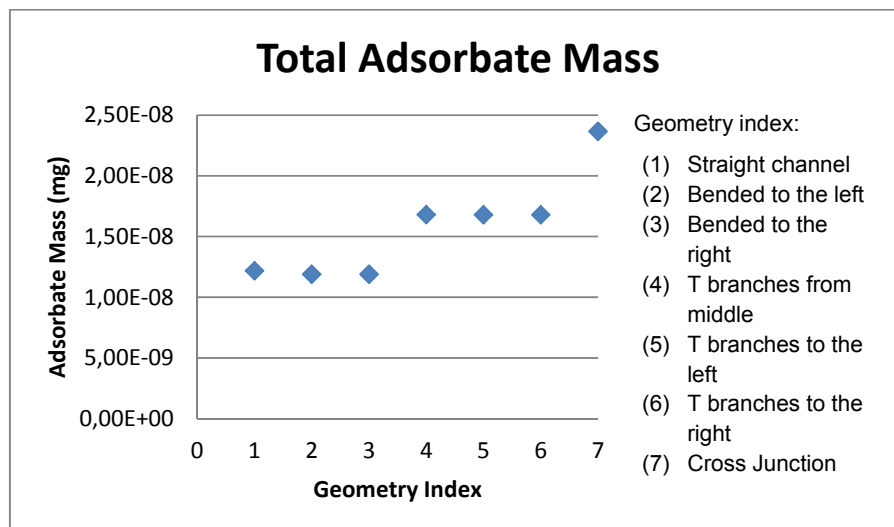


**Figure 7.20:** Total adsorbate mass for different channel segment geometries with similar channel lattice dimension

The plot of the average adsorbate mass for different microchannel segment geometry is shown in **Figure 7.20**. The straight channel and the bended channel have approximately similar total adsorbate mass that values

are the least of all. The total mass adsorption on T branches is the second largest and the total adsorbate mass of the cross-junction microchannel is the largest of all. The adsorbate mass is closely related to the surface adsorption area of the microchannel. Larger surface area allows more particles adsorbed onto the wall. In this study, large adsorbate mass does not always indicate a high packed particles on the surface. This is shown in **Figure 7.21** where the adsorbate concentration of the straight and the bended microchannels are the highest of all. The least packed surface is observed for the microchannel with T branch that flow injected from the rear inlets. The concentration of the adsorbate for the cross junction is less than the concentration on the T-branches because the amount of the mass adsorbed over per surface area on the latter is lower.

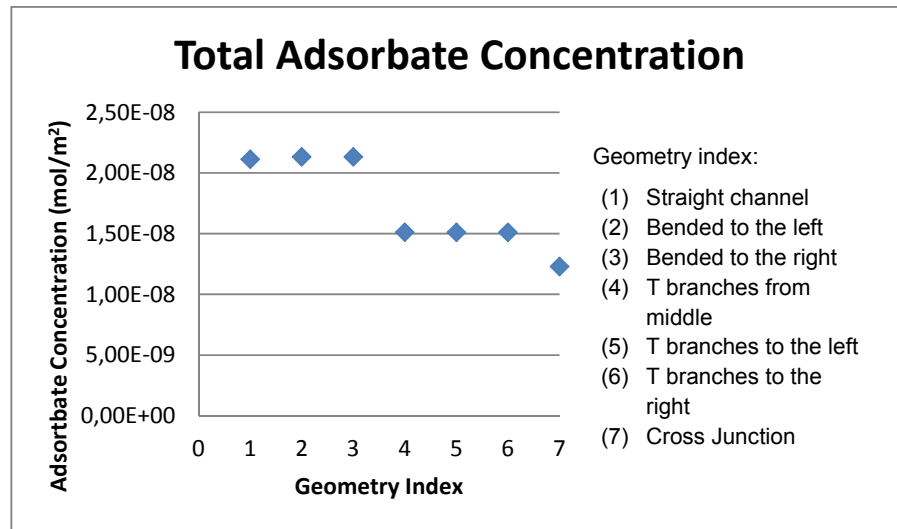


**Figure 7.21:** Total adsorbate concentration for different channel segment geometries with similar channel lattice dimension

## 7.6 Finding correlations for the concentration profiles and pressure difference for the microchannel segments

This section investigates if there is any direct connection between the inlet-outlet pressure differences and adsorption of the nanoparticle transport for the introduced microchannel segment. By correlating the pressure difference and the amount of the adsorption for each segment, the end boundaries of each segment can be represented as nodes. Each node

represents the junction between two microchannel segment that accommodates pressure and concentration profile at a specific time. By introducing the nodes, establishing a complex microchannel model will be more efficient and easier to study.

In the study the effluent concentration is a function of concentration, pressure and time at the inlet and the inlet of the microchannel, it is illustrated in

**Figure 7.22** where  $p$  is the pressure,  $c$  is the concentration and  $t$  is the time. The illustration uses the geometry of a cylindrical microchannel. The effluent concentration  $c_2$  is measurable if the pressure of the inlet and outlet ( $p_1, p_2$ ), the inlet concentration ( $c_1$ ) under a specific simulation time ( $t$ ) are known. In mathematical form, this is written as follows:

$$c_2 = f(p_1, p_2, c_1, t_o, t)$$

where index 1 is position 1 and index 2 is position 2. Index o shows the initial value. By integrating overtime, the difference between  $c_1$  and  $c_2$  is assumed to be the concentration of the adsorbate in the channel. This follows the common measurement assumption used in adsorption laboratory experiment [268]. The simulation is conducted for the system with finite injection. This is because the assumption stated will not be valid for continuous concentration injection. In the system with continuous injection, the difference between the effluent and the injected concentration will be zero once the segment is eventually saturated. It will be impossible to correlate the adsorption and the inlet-outlet concentration difference. The actual adsorbate concentration (cB) and mass (mB) are also calculated based on the method explain in Chapter 3.



**Figure 7.22:** Effluent outlet concentration for different channel segment geometries with similar channel lattice.

Two types of channel segment configurations are investigated for the current study, i.e. (1) the simple straight channel and (2) the single 90 degrees bended channel. These two were selected because both have the comparable adsorption length and similar number of outlet boundary (see **Table 7.2**).

A certain concentration ( $c_{inj}$ ) is injected for a fixed period at the beginning of the simulation with a steady creeping flow speed  $v_o$  at the boundary of the microchannel. There is no concentration in the microchannel or on the microchannel wall at the initial condition of the simulation. In the simulation, some of the concentration in the fluid bulk and the channel wall experiences the mechanism of adsorption and desorption due to a concentration difference between the two locations. After the concentration of  $C_{inj}$  is injected, the inlet concentration is reduced to zero, but the flow continuous.

Sensitivity	Base	Multiplier for Sensitivity Study
Initial inlet concentration	$c_{inj} = 12500 \text{ ppm}$	0.5, 1, 2
Inlet velocity (related linearly with the pressure difference, dP)	$v_o = 8.085 \times 10^{-5} \text{ m/s}$	0.5, 1, 2, 5, 10, and 15

**Table 7.3:** Sensitivity study configuration to find correlation for the concentration and pressure difference for the microchannel segments

Two sets of sensitivity studies are based on the inlet velocity and the inlet concentration are used. The detail configuration of the sensitivity study is listed in the **Table 7.3**. The creeping velocity at the inlet is linearly proportional to the inlet-outlet pressure difference present at the microchannel.

A preliminary study to investigate if the inlet-outlet pressure is proportional with the injection is conducted. The simulation is carried out for a system of single straight microchannel until the equilibrium system is achieved. The equilibrium is obtained by investigating the value of  $c_t$  when  $\frac{(c_t - c_{t+1})}{c_t} < 0.001\%$ . In this case,  $c_t$  (ppm) is the average effluent concentration at time  $t$ . The simulation is run under different velocities based

on the magnitude in **Table 7.3**. The time length for this condition is 10 seconds that equals to 4.04 pore volume. The base case for the injection concentration is  $c_{inj} = 12500 \text{ ppm}$ . Two injection concentration multipliers used the sensitivity study, i.e. 0.5 and 2 times the base case. Sensitivity study for injection inlet velocity is also conducted. The study hence is continued to investigate the trend of the actual adsorbate concentration ( $c_B$ ,  $\text{mol/m}^2$ ), the actual adsorbate mass ( $m_B$ ,  $\text{mg}$ ), the effluent concentration ( $c_A$ ,  $\text{ppm}$ ), and the difference between effluent and the injected concentration ( $dc_A$ ,  $\text{ppm}$ ) for different inlet-outlet pressure difference. The relation between the inlet-outlet pressure difference and injection velocity for various the injected volume is shown in **Figure 7.23**. The profile is a straight line, showing the two are proportional. Therefore, the injection velocity is interchangeable with the inlet-outlet pressure difference.

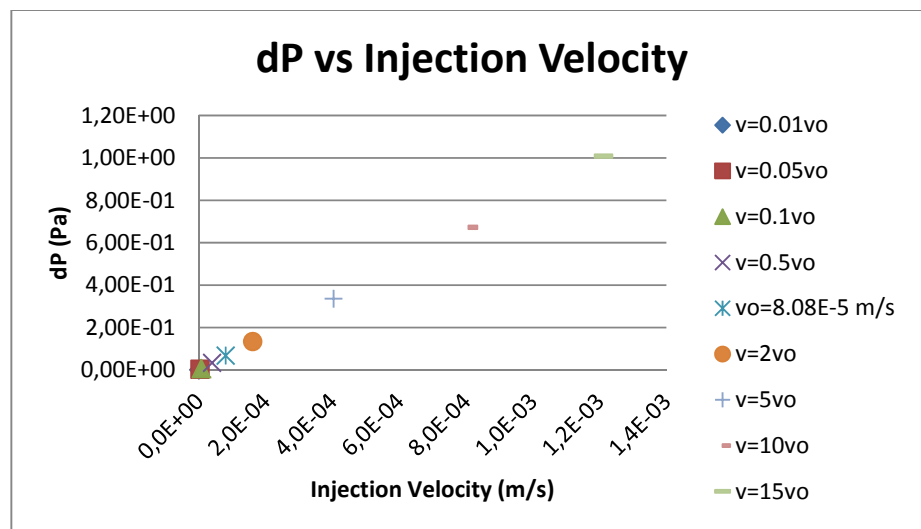


**Figure 7.23:** Effluent outlet concentration for different channel segment geometries with similar channel lattice dimension

### 7.6.1 Concentration profile for single straight microchannel segment

The first study is the simulation that is conducted for the straight microchannel segment. Discontinuous nanoparticle injection is utilised to correlate the difference between the injected and the effluent concentration with the adsorption. At the beginning of the simulation, the segment is empty from any nanoparticle concentration. Certain concentration based on the values in **Table 7.3** is injected for a fixed period from 0 to 0.001 seconds into

the microchannel at the beginning of the simulation. **Figure 7.24** shows the illustration for the flow direction for the straight microchannel segment (left) and velocity profile of the system after 10 seconds of the simulation time (right). The concentration flow is directed from the inlet boundary which is indicated by the red arrow on the left figure in **Figure 7.24**. The velocity profile follows the parabolic profile that is in agreement with the investigation in the previous section. The amount of the adsorption is investigated by evaluating the profile of the mass and the concentration of the adsorbate against the simulation time length.

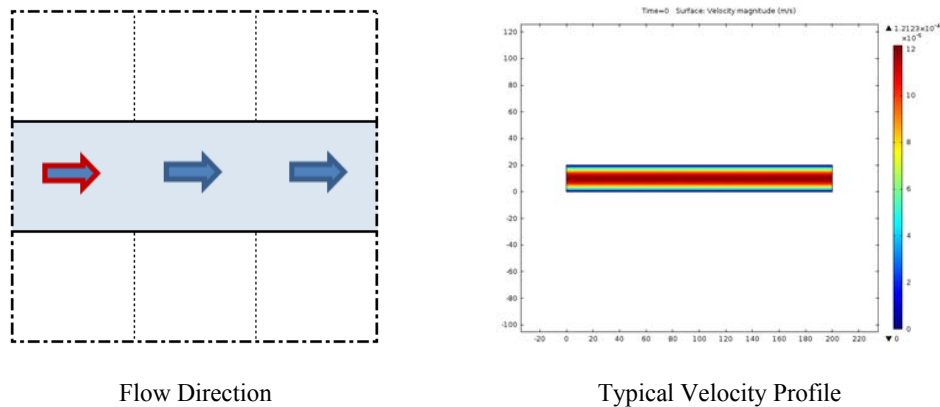


**Figure 7.24:** The illustration for the flow direction for the straight microchannel segment (left) and velocity profile of the system after 10 seconds of the simulation time (right)

The effect of the magnitude of concentration injection on magnitude of effluent concentration is investigated. The effluent concentration for different inlet injection concentration and velocity is plotted against the simulation time. The results displayed in **Figure 7.25**. The breakthrough of the main body of the injected concentration is indicated by the increase of the concentration profile in **Figure 7.25 (left)**. The front of each concentration bulk reaches the outlet boundary on the same time, which is indicated by the starting point of the concentration profile increase. The magnitude of the maximum fluid bulk concentration is proportional to the injected concentration. For similar injection velocity and similar injection time length, the carrier fluid transports more concentration for larger concentration injection than the lower one. The peak of the effluent is also correlated positively with the injected concentration. The peak for the effluent concentration for the base case  $c_{inj} = 12500$  is 50.2 ppm, for  $c_{inj} =$

62500 is 25.4 ppm, and for  $C_{inj} = 25000$  is 93.6 ppm. After reaching the peak value, the concentration decreases to minimum. The gradient decrease for each case is not comparable. This happens due to the different of the concentration magnitude that is injected in the system. High magnitude of the injected concentration results the system requires long time for the tail profile reaches zero value. This is shown in **Figure 7.25 (left)** that the green profile requires longer time to reach zero value compare to the other profiles.

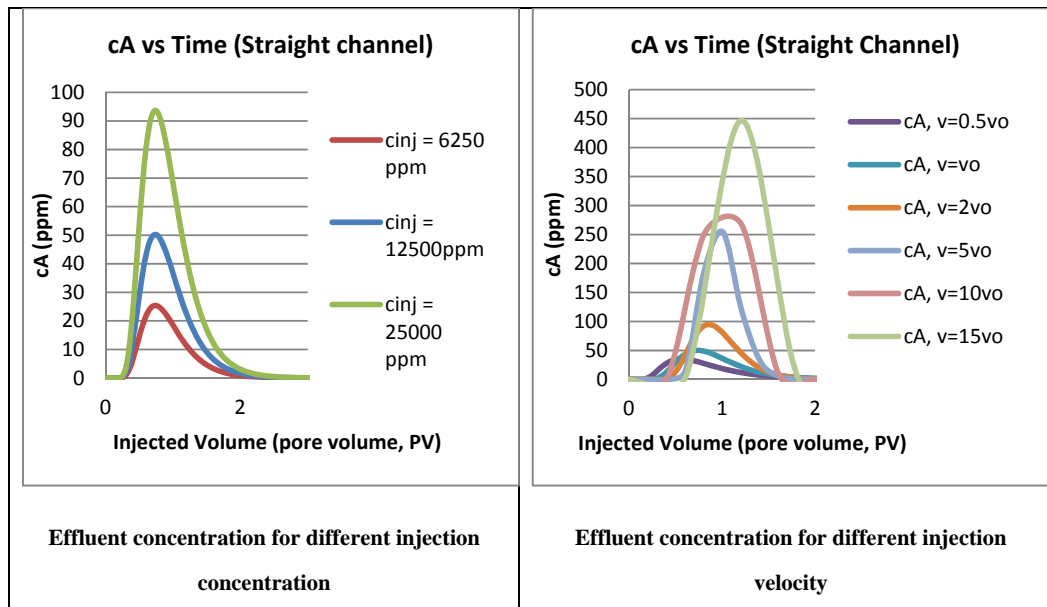


**Figure 7.25:** The plot of the effluent concentration against the simulation time for different injection concentration (left) and injection velocity (right) for the straight microchannel.

**Figure 7.25 (right)** shows the effluent concentration profile for different injection velocities against the injected volume. It is observed that the peak value of the effluent concentration profile is proportional with the injection velocity. For  $v_0 = 8.085 \times 10^{-5}$ , the peak velocity for  $v = 0.5v_0$  is 35.26 ppm, for  $v = v_0$  is 50.2, for  $v = 2v_0$  is 94.13 ppm, for  $v = 5v_0$  is 254.3 ppm, for  $v = 10v_0$  is 266.8 ppm, and for  $v = 15v_0$  is 446.9 ppm. Under a no slip condition, high injection velocity has more flux that transports more particles from the inlet to the outlet more than the system with low injection velocity. In the case of low injection velocity, i.e. at  $v = 0.5v_0$ , the required injection volume for the breakthrough is less than the system with larger injection velocity. This happens because, in the low injection velocity, the diffusion dominates the system more than the advection. Diffusion effect extends the

concentration to the region close to the outlet boundary quickly. However, the penetration is short due to the nature of the diffusion. The diffusion dominance is reduced as the velocity increases. When the velocity is more dominant than the diffusion the effluent concentration measured at the outlet boundary is proportional to the velocity magnitude. This shows that there is a competition between the effect of the advection and diffusion in the system with regards of the concentration transportation. .

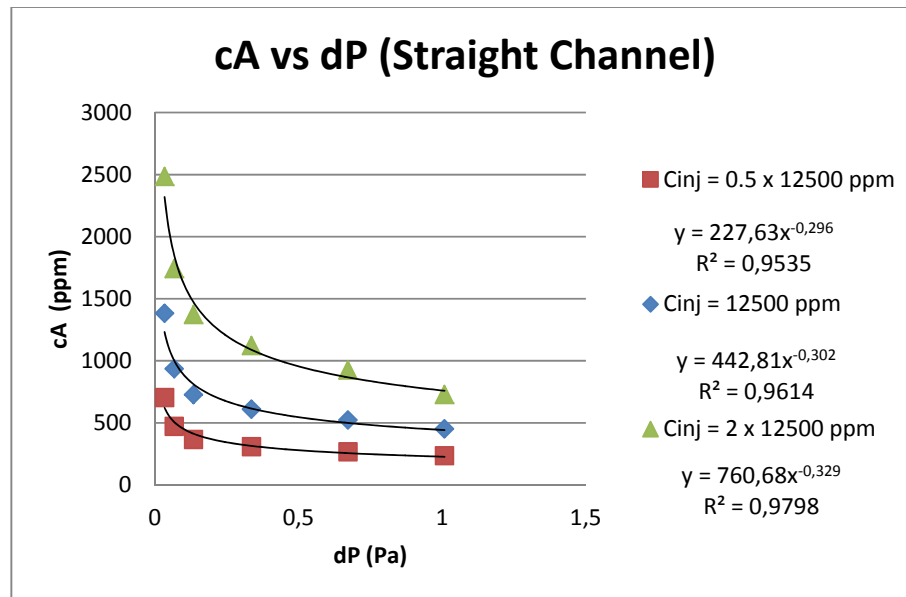


**Figure 7.26:** The plot of the effluent concentration against the inlet outlet pressure difference for various case of injection concentration

The effluent concentration and the inlet-outlet pressure for all cases are plotted in **Figure 7.26**. It is discovered that the effluent concentration varies inversely with the inlet-outlet pressure difference. This result is consistent with the investigation of **Figure 7.25** because the inlet-outlet pressure difference is linearly proportional to the injection velocity. Trend lines for each concentration injection case against the inlet-outlet pressure difference are established. The trend lines follow power regression profile. The regression equation for the effluent concentration for  $c_{inj} = 12500 \text{ ppm}$  is  $y = 443x^{-0.302}$  with  $R^2=0.9614$ . The regression equation for  $c_{inj} = 0.5 * 12500 \text{ ppm}$  is  $y = 228x^{-0.296}$  with  $R^2=0.9535$ . The regression equation for  $c_{inj} = 2 * 12500 \text{ ppm}$  is  $y = 761x^{-0.329}$  with  $R^2=0.9798$ . Comparing to the base case of  $c_{inj} = 12500 \text{ ppm}$ , the equation multiplier for the  $c_{inj} = 6250 \text{ ppm}$  is roughly 0.5 and for the  $c_{inj} = 25000 \text{ ppm}$  is roughly 1.7 times higher

than the base case. It is discovered that the equation multiplier is linearly correlated with the magnitude of the injected concentration.

The profile of the adsorbate mass against the simulation time for different injection concentration and different injection velocity are shown in **Figure 7.27 (left)** and **Figure 7.27 (right)** respectively. The amount of the adsorbate mass is proportional to the level of the injected concentration. The higher the concentration in the system, the more adsorption will happen due to the concentration difference between the fluid bulk and the microchannel wall. The adsorption is also detected to happen early as the simulation started, which is shown by the increase of the profile that happens early at 0 pore volume.

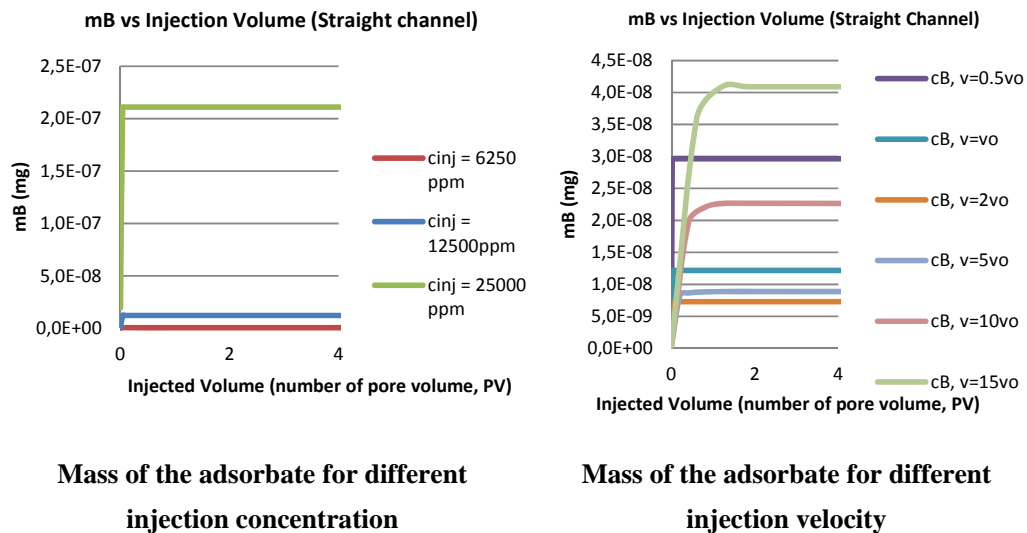


**Figure 7.27:** The mass of the adsorbate for different injection concentration (left) and velocity (right) for the straight microchannel segment.

The injection velocity influences the adsorption behaviour on the microchannel wall. This is shown by the different magnitude of the equilibrium adsorbate mass in **Figure 7.27 (right)**. The equilibrium adsorbate mass in this figure is shown by the flat mass profile against the injected volume. A high magnitude of equilibrium adsorbate mass presents for  $v=15v_0$  i.e.  $4.09 \times 10^{-8}$  mg, then the equilibrium mass reduced to  $2.26 \times 10^{-8}$  mg for  $v=10v_0$ . The equilibrium mass remain reduces to  $8.87 \times 10^{-9}$  mg for  $v=5v_0$  and reaches the minimum at  $7.3 \times 10^{-9}$  for  $v=2v_0$ . The magnitude of the adsorbate mass increase to  $1.22 \times 10^{-8}$  and  $2.69 \times 10^{-8}$  for  $v=v_0$  and  $v=0.5v_0$

respectively. As it was discussed previously; there is a competition between the diffusion and advection that influence the process of adsorption.

For the case of high velocity injection, it seems the system requires more injection to trigger high adsorption. This is shown by the increase profile for the case of  $v=10v_0$  and  $v=15v_0$  where the required injection for the system reaches the equilibrium is after 1.5 pore volume injection. Therefore, it is deduced that the adsorption is more efficient to be happen in an environment with low injection velocity. In low velocity, the concentration field has longer time to be in contact with the channel wall that enhances the possibility for adsorption process.

The adsorbate mass is plotted against the pressure difference for various injection concentrations which is shown in **Figure 7.28**. There is an interesting finding where there is an injection velocity that causes minimum adsorption in the system. It seems that the profile of the mass adsorbate is difficult to regress, hence more study is needed.

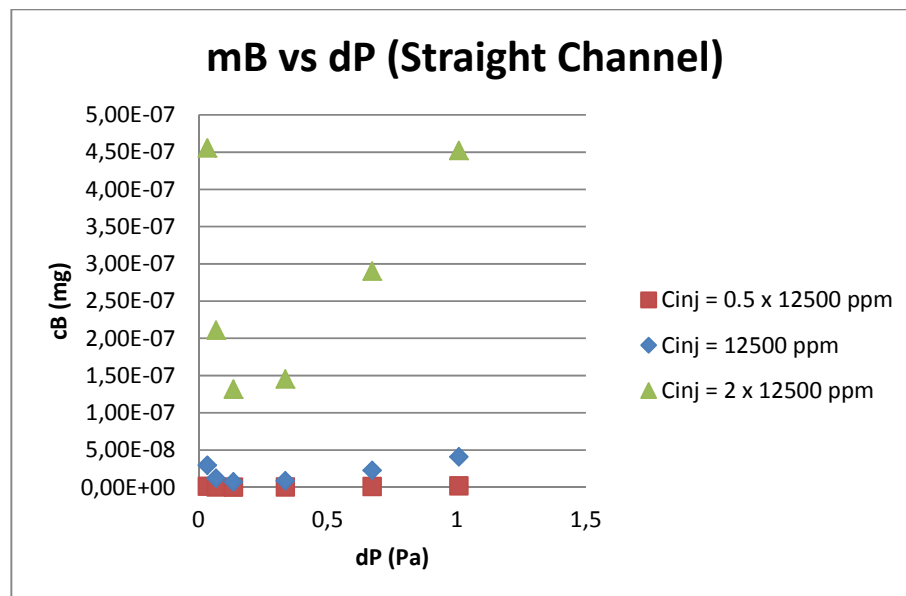


**Figure 7.28:** The plot of the adsorbate mass against the inlet and outlet pressure difference for various case of injection concentration

With similar methodology, the adsorbate concentration is also investigated. Since the surface of the microchannel is constant, the trend of the adsorbate mass and concentration are comparable. This finding is shown in **Figure 7.29** which values are taken from the average of the adsorbate concentration on the microchannel wall for various injection

volumes. The magnitude of the adsorbate concentration is different from the profile of the adsorbate mass because the simulation of the adsorbate concentration considers the surface area of the system. The adsorbate concentration for all cases then is plotted with the inlet-outlet pressure difference. The results in detail are shown in **Figure 7.30**, which again, the profile is difficult to regress.

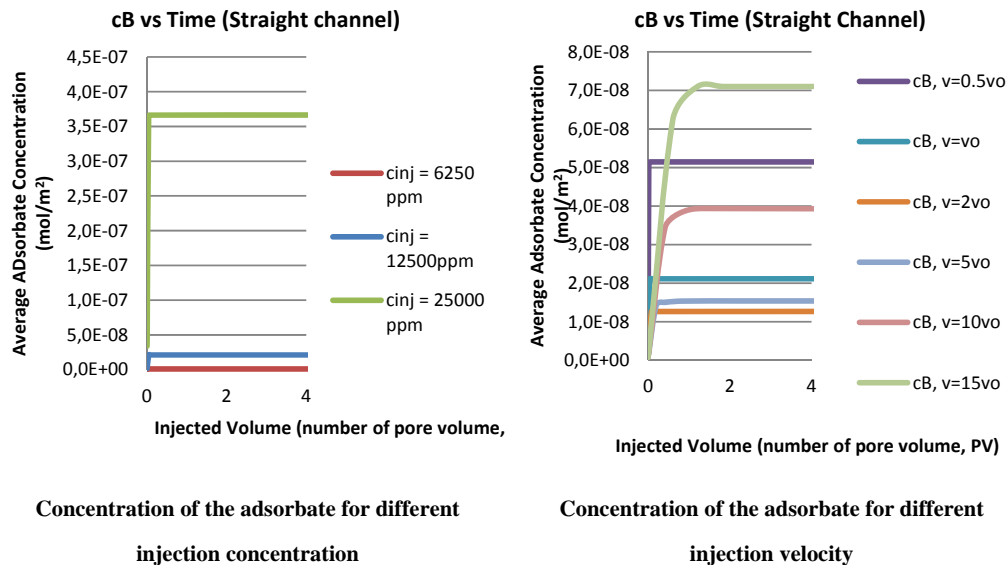


**Figure 7.29:** The plot of the adsorbate concentration against the simulation time for the straight microchannel segment

The original Freundlich adsorption methodology proposes to plot the amount of adsorbate by the adsorbents per unit mass ( $x/m$ ) for the investigation. In this study, the  $x/m$  is approached by the amount of adsorbate concentration on the microchannel, assuming the adsorption wall has a constant mass. The first reason is because the microchannel segment is incompressible, and the second reason is the adsorption does not change the property of the adsorption wall. The adsorbate concentration ( $dcA$ ) is measured by the difference between the injected concentration and the effluent concentration. This approach has a limitation, because  $dcA$  hypothetically includes both the amount of particles adsorbed and those that are still in the fluid bulk due to desorption.

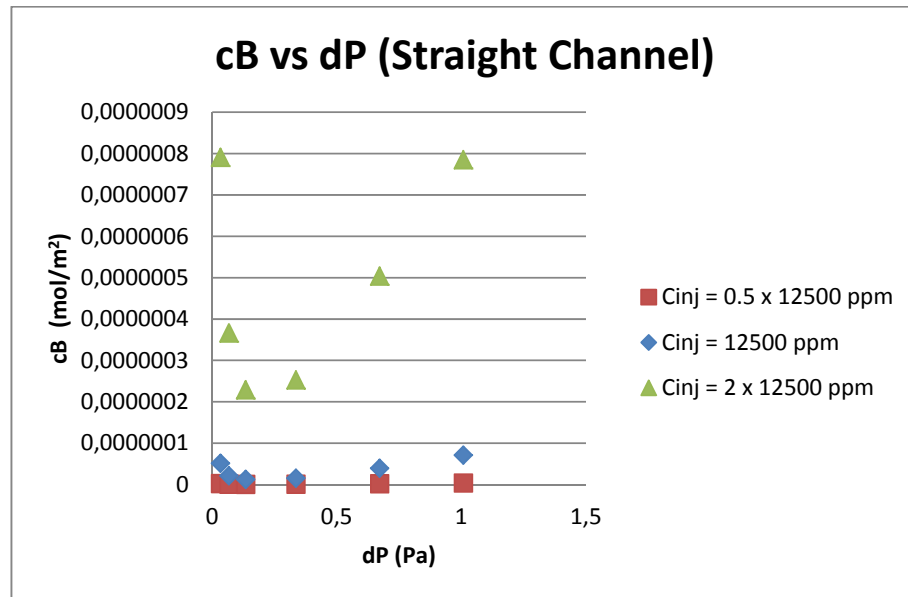


**Figure 7.30:** The plot of the adsorbate concentration against the inlet outlet pressure difference for various case of injection concentration

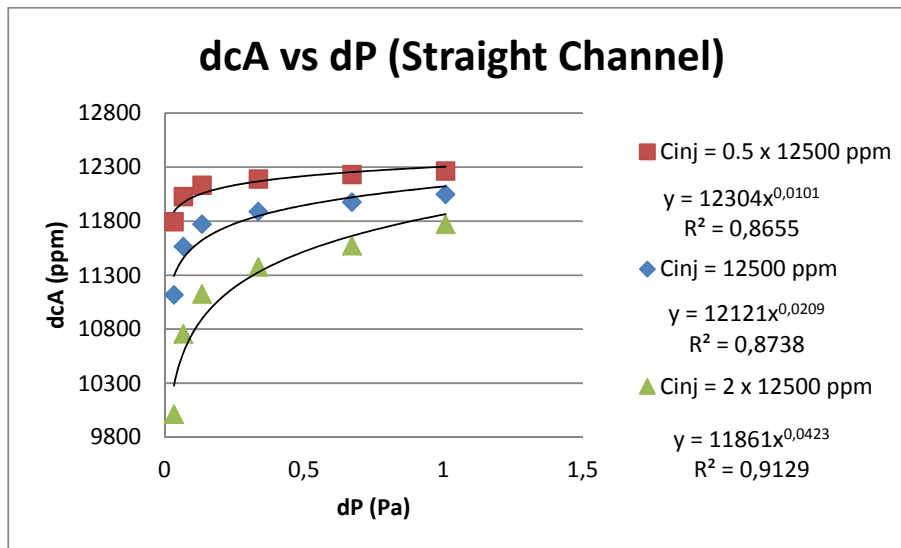


**Figure 7.31:** Freundlich plot of the straight microchannel segment

The adsorbate concentration ( $dcA$ ) then is plotted against the inlet-outlet pressure difference, which is shown in **Figure 7.31**. Each trend, which is based on the magnitude of the injection concentration, is regressed using power trend line. The regression equation for the  $dcA$  obtained is  $y = 12121x^{0.0209}$  with  $R^2 = 0.8738$  for the base case  $c_{inj} = 12500$  ppm. The regression equation for the case of  $c_{inj} = 6250$  ppm is  $y = 12304x^{0.0101}$  with

$R^2 = 0.8655$  and for the case of  $c_{inj} = 25000$  ppm is  $y = 11861x^{0.4235}$  with  $R^2 = 0.9129$ .

It is discovered that the profile of the effluent concentration can also be related to the inlet-outlet pressure difference which is proportional to the injected concentration. However, this discovery does not apply for the profile of the adsorption.

### 7.6.2 Concentration profile for single bended microchannel segment

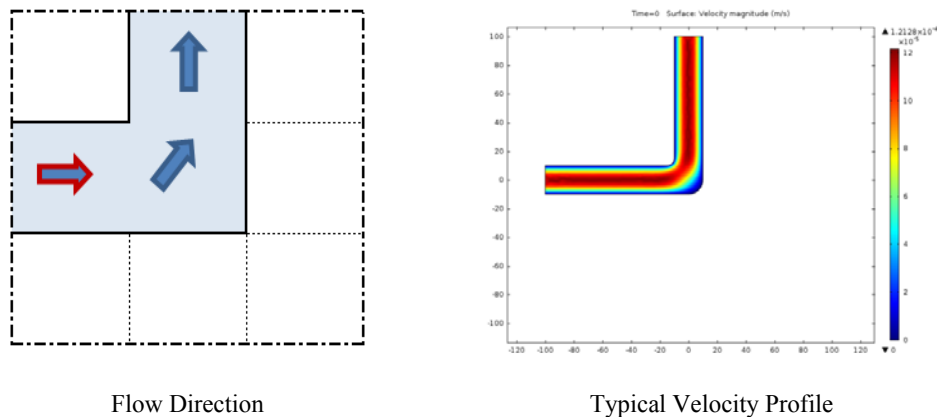


**Figure 7.32:** The illustration for the flow direction for the bended microchannel segment (left) and velocity distribution (right) of the system after 10 seconds of the simulation time

The second investigation is conducted to investigate the concentration profiles and the inlet-outlet pressure difference in a single bended microchannel segment. This study is intended to clarify if the Freundlich equation behaves similarly as in the straight microchannel segment. The adsorption surface equivalent ratio of the bended microchannel segment is 0.98. As in the simulation for the straight microchannel segment, 12500 ppm of nanoparticle concentration is injected for a fixed period 0 to 0.001 seconds along with a constant creeping velocity at the beginning of the simulation into the inlet boundary of the bended microchannel segment. Some of the concentration is expected to be adsorbed onto and desorbed from the microchannel wall. The illustration of the flow direction and velocity profile for this simulation is shown in **Figure 7.32**.

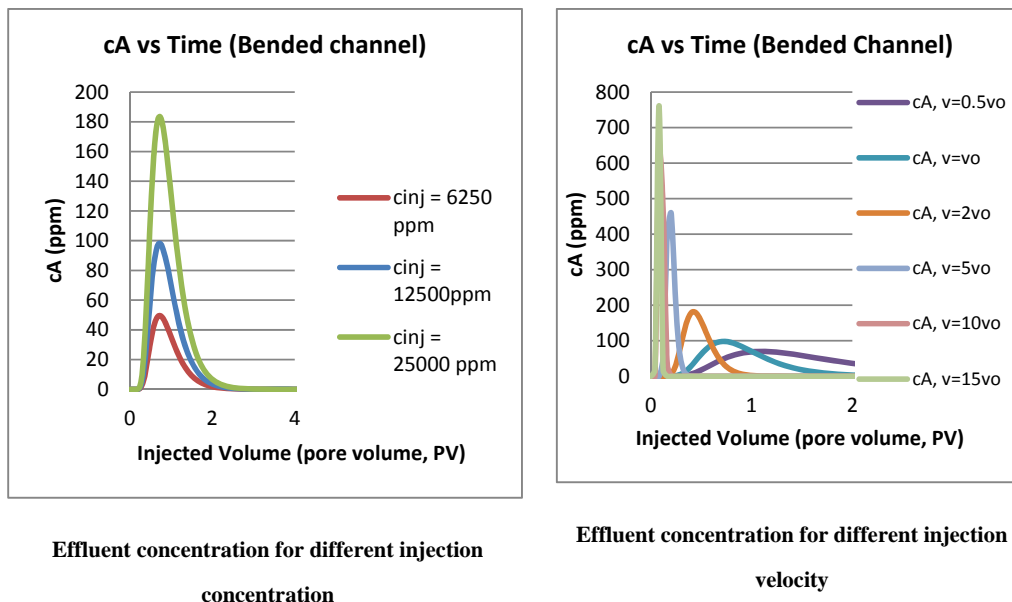


**Figure 7.33:** The illustration for the flow direction for the bended microchannel segment (left) and velocity profile of the system after 10 seconds of the simulation time (right)

The profile of the effluent concentration against the simulation time is shown in **Figure 7.33**. **Figure 7.33 (left)** shows the effluent concentration profile for different injection concentration and **Figure 7.33 (right)** shows the effluent concentration for different injection velocity. It is again observed that the magnitude of the effluent concentration is proportional to injection concentration as the implication of the mass balance in the system. In agreement with the straight microchannel, the effluent concentration is proportional with the injection velocity. This happens because higher velocity induces more mass flux than in the system with low velocity, transporting more particles to the outlet.

In the case of the system with low injection velocity, the diffusion effect is more dominant than the advection (refer to Section 4.6.2.2). However, the effect of diffusion for transporting the particle in this bended segment is less than in the straight segment; although both cases have similar diffusion constant. The diffusion effect to the nanoparticle transport is reduced by to the increase of the channel complexity. The increase of velocity reduces the diffusion dominance for the concentration movement, transporting larger concentration as the velocity increases. This is shown in **Figure 7.33 (right)** where the highest effluent concentration magnitude

belongs to the concentration flow with the highest injection velocity. The decrease of the profile correlates to the concentration of the injected particles that is still left in the system after the breakthrough. Moreover this decrease also indicates the desorption process which happens in the system shown by the tail profile that presents after  $PV=1$ . Low gradient decrease shows low desorption process and vice versa.

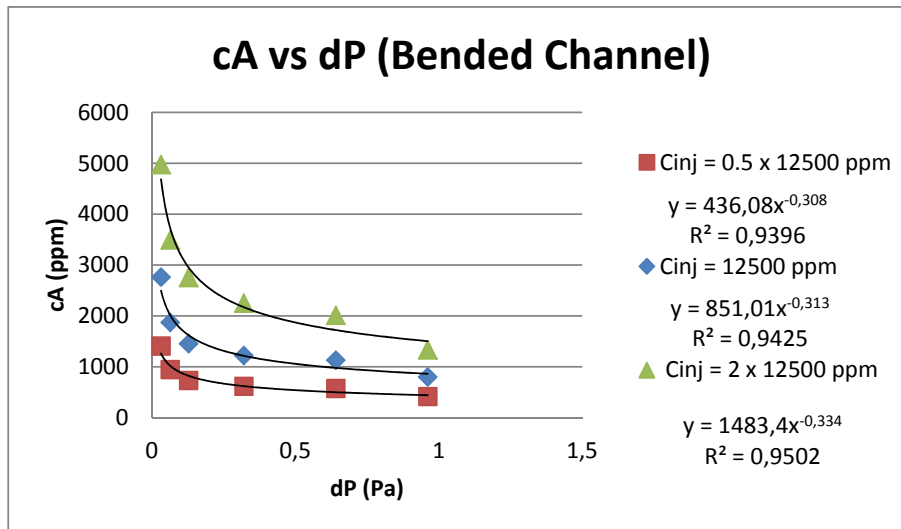


**Figure 7.34:** The plot of the effluent concentration against the inlet-outlet pressure difference for various case of injection concentration

The effluent concentration for all case is then plotted against the corresponding inlet-outlet pressure difference which is shown in **Figure 7.34**. The data obtained are grouped according to the magnitude of the injection concentration. It is discovered that the effluent concentration is inversely correlated to the inlet-outlet pressure difference. The data obtained are then regressed using power approximation. The regression equation for effluent concentration obtained for  $c_{inj} = 12500$  ppm is  $y = 851x^{-0.313}$  with  $R^2 = 0.9425$ . The regression equation for the case of  $c_{inj} = 6250$  ppm is  $436x^{-0.308}$  with  $R^2 = 0.9396$  and for the case of  $c_{inj} = 25000$  ppm is  $1483x^{-0.334}$  both with  $R^2 = 0.9502$ . Comparing to the base case of  $c_{inj} = 12500$  ppm, the equation multiplier for the  $c_{inj} = 6250$  ppm is 0.5 and for the  $c_{inj} = 25000$  ppm is 1.7 times higher than the base case. These values are surprisingly similar as the case of the single straight microchannel segment.

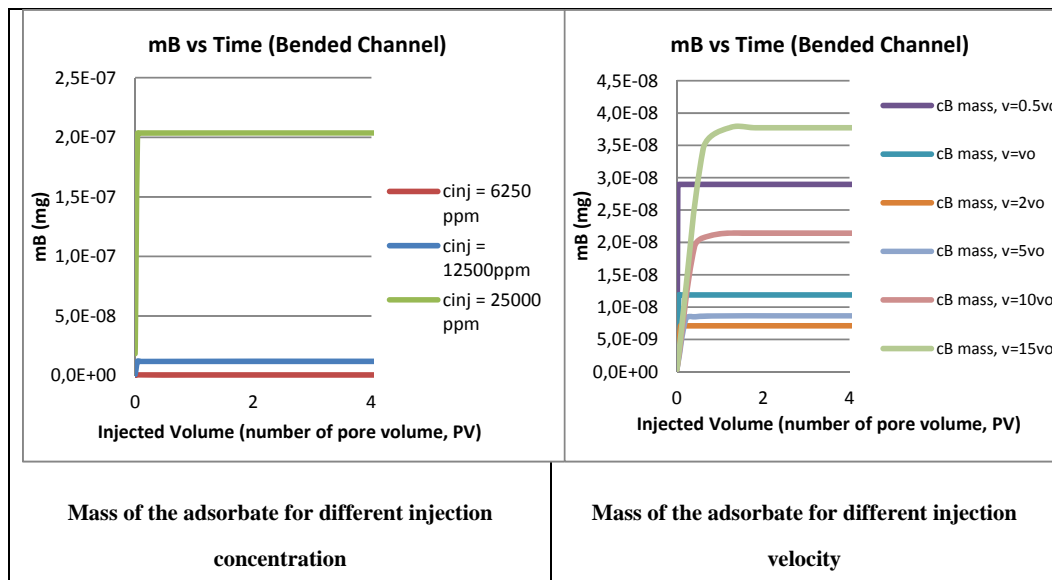


**Figure 7.35:** Adsorbate mass against the injection volume for various injection concentration (left) and injection velocity (right)

Mass of the adsorbate that presents on the microchannel wall for different injection concentration and velocity are shown in **Figure 7.35 (left)** and **Figure 7.35 (right)** respectively. The profiles of the adsorbate mass observed have a good agreement with the trend in the case of the straight microchannel segment. The magnitude of the adsorbate mass is proportional to the magnitude of the injected concentration that is shown in **Figure 7.35 (left)**. **Figure 7.35 (right)** shows the injection velocity is inversely correlated with the adsorption process. The injection velocity influences the magnitude of the adsorbate mass. The difference in the profile increase indicates that higher velocity may be able to enhance the adsorption; however, the amount of injected fluid is also has to be increased. This shows the adsorption in high velocity environment is not as efficient as the adsorption in low velocity environment. The injected concentration has more abundant time to undergo the adsorption process on the microchannel wall in the environment with low velocity.

The adsorbate mass for all cases are plotted against the inlet-outlet pressure difference in **Figure 7.36**. The adsorbate mass correlates with the inlet-outlet pressure difference, where the magnitude decreases as the pressure difference increase. After some point, the magnitude of the adsorbate mass as the pressure difference increase. There is a minimum

mass adsorbate for the inlet-outlet pressure difference introduced, however it appears no obvious relation is seen.

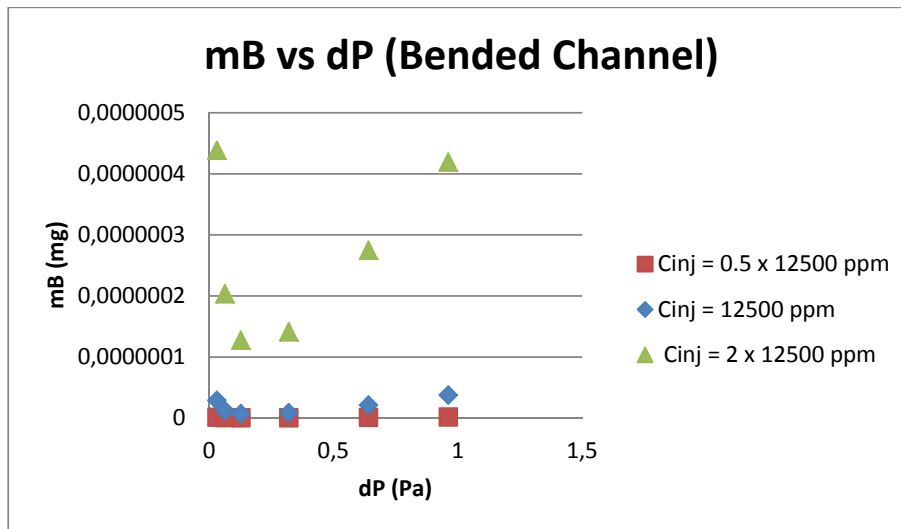


**Figure 7.36:** Adsorbate mass against the inlet-outlet pressure difference for various injection concentrations

The adsorbate concentration against simulation time for various injection concentrations and simulation time is shown in **Figure 7.37 (left)** and **Figure 7.37 (right)** respectively. Since the surface area of the microchannel is constant, the trend of the adsorbate concentration is comparable to the adsorbate mass which is discussed previously. The concentration of the adsorbate is proportional to the injected concentration. In correlation with the injection velocity, there is velocity that results minimum adsorption concentration. It is observable from **Figure 7.38** where the regression is difficult to obtain.

Finally, the Freundlich plot for  $x/m$  against the pressure difference for this study is established.  $x/m$  which represents the amount of adsorbate by the adsorbents per unit mass is denoted by the difference between the injected concentration and the effluent concentration. The pressure difference is denoted by the inlet-outlet pressure difference of the corresponding microchannel. Three equations based on three various injection concentrations are obtained using power regression approximation. The regression equation for the data obtained for  $c_{inj} = 12500$  ppm is  $y = 11795x^{0,0458}$  with  $R^2 = 0.8687$ . The regression equation for the case of  $c_{inj} = 6250$  ppm is  $12132x^{0,0213}$  with  $R^2 = 0.8675$  and for the case of  $c_{inj} = 25000$  ppm is  $11331x^{0,0995}$  both with  $R^2 = 0.892$ . The detail is shown in

**Figure 7.39.** The regression equation is found to be similar to the equation obtained from the single straight microchannel.

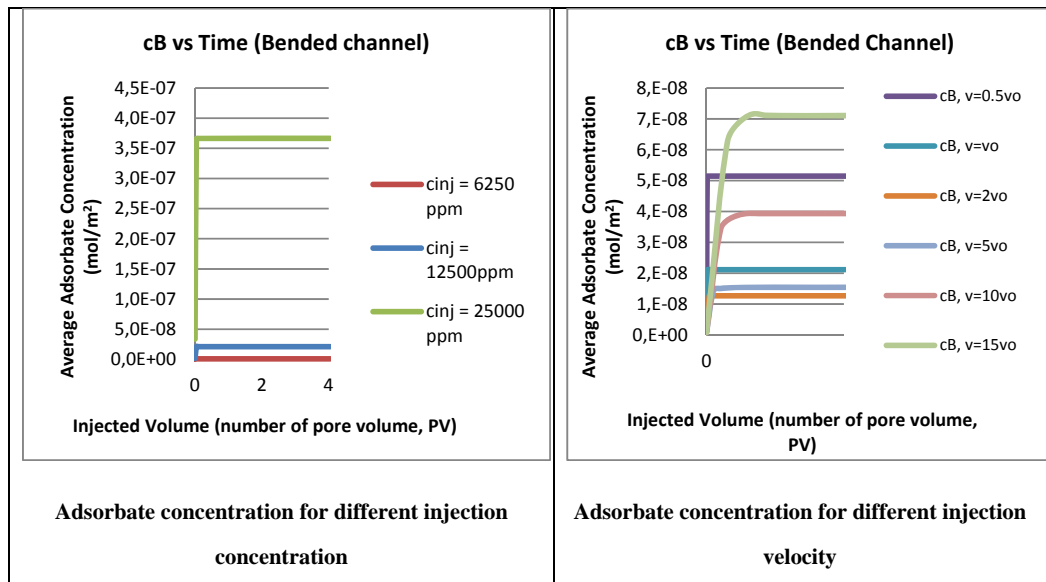


**Figure 7.37:** The plot of the adsorbate concentration against the inlet-outlet pressure difference for various case of injection concentration

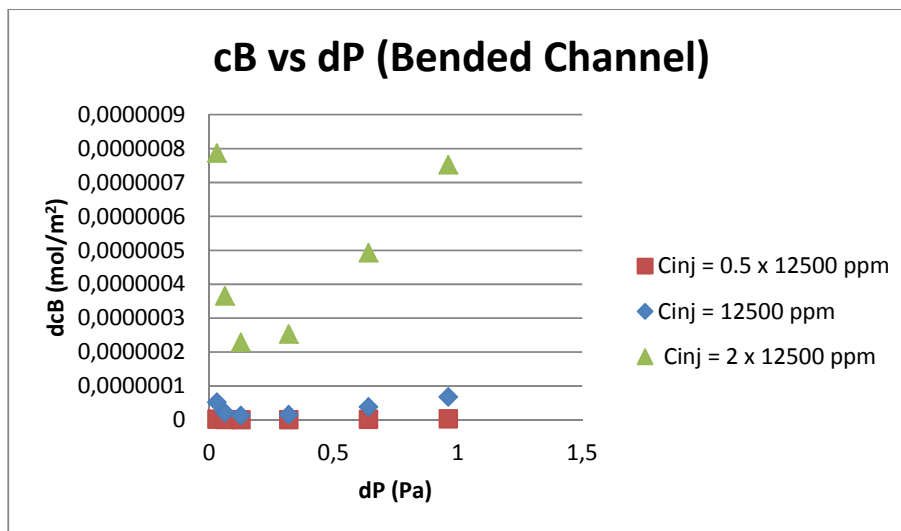


**Figure 7.38:** The plot of the adsorbate concentration against the inlet-outlet pressure difference for various case of injection concentration

It is again discovered that the equation multiplier for the effluent concentration is positively correlated proportionally to the multiplier of the

injected concentration. It is not the case with the adsorbate mass and the adsorbate concentration. This seems to occur because the concentration inside the microchannel, which is dispersed in the fluid bulk and not adsorbed on the microchannel wall, is not considered in the equation.

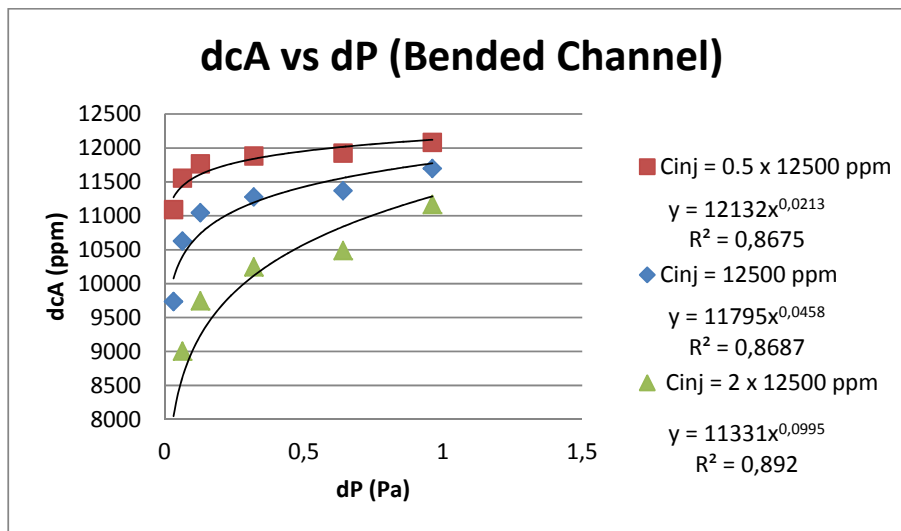


**Figure 7.39:** Freundlich plot of the bended microchannel segment

Correlation of the inlet-outlet pressure (dP) and the outlet effluent concentration (cA, ppm) and the inlet-outlet concentration difference (dcA, ppm) are obtained. The correlation is obtained by regressing the corresponding concentration magnitude with the microchannel's inlet-outlet pressure difference. The trend follows the power correlation which is in agreement with the Freundlich adsorption isotherm. However, the correlation for the adsorbate concentration (cB, mol/m<sup>2</sup>) and the adsorbate mass (mB, mg) is difficult to establish. The reason is because the mechanism of the adsorption and desorption is sensitive to the condition in the system, i.e. the concentration difference and the velocity that affect the adsorption process.

Diffusion and advection contribute significant influence to the adsorption process. In low velocity, the diffusion is more dominant than the advection. In a straight microchannel segment, diffusion is able to transport the concentration quite rapidly to the outlet boundary. This happens because the distance between the outlet and the inlet is not far. However, this does not happen for the microchannel system with larger longitudinal dimension and higher complexity. Adequate magnitude of advection is needed to transport similar concentration from the inlet to the outlet for long

microchannel. The adsorption in an environment with diffusion dominance happens more efficiently than in the environment with advection dominance. The adsorption in an environment with high advection can be enhanced by injecting plenty amount of fluid into the system more than it is required in the case with diffusion dominance.

## 7.7 Network model

A two-dimensional microchannel network model can be established using the four microchannel segment configurations, which were previously introduced in Chapter 7.2. The four microchannel configurations include single straight microchannel, single bended microchannel, T-junction microchannel and a cross-junction microchannel. The microchannel segments can be coupled with one another flexibly to create a complex pore channel network.

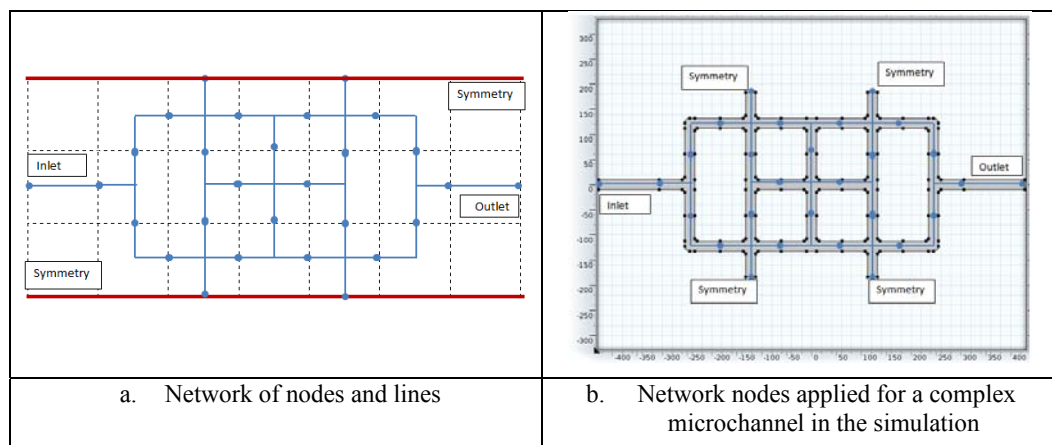


**Figure 7.40:** Network model from nodes and lines (a) to an established complex microchannel (b).

As an example, a network which consists of nodes and lines which is illustrated in **Figure 7.40a** is established. In this study, channel segments with similar lattice dimension are utilized. Initially there is no concentration in the microchannel system. A certain concentration is injected at the beginning of the simulation from the inlet boundary of the network, which is subjected to flow inside the network towards the outlet boundary. Mechanisms of adsorption and desorption between the concentration in the fluid bulk and the microchannel wall are expected due to a concentration difference between the fluid bulk and the wall. Symmetry axis is also applied on the top and bottom of the network. Applying the nodes and lines

configuration in the simulation results in fully developed microchannel network geometry as it is shown in **Figure 7.40b**.

In this study, 12500 ppm of nanoparticles concentration is injected for a fixed period at the beginning of the simulation with a constant creeping velocity of  $v_o = 8.08 \times 10^{-5} \text{ m/s}$  into the inlet boundary of the 20  $\mu\text{m}$  diameter microchannel network. The outlet pressure of the microchannel network is set to be 0 Pa. Some of the particles in the concentration are expected to be adsorbed to and desorbed from the wall of the microchannel. By conducting the simulation, the effluent concentration and the adsorbate mass and concentration are measured. The simulation is conducted in three different velocities for the sensitivity study.  $v_o = 8.08 \times 10^{-5} \text{ m/s}$  is the velocity base case and the two others are 0.5 and 2 times of the base case.

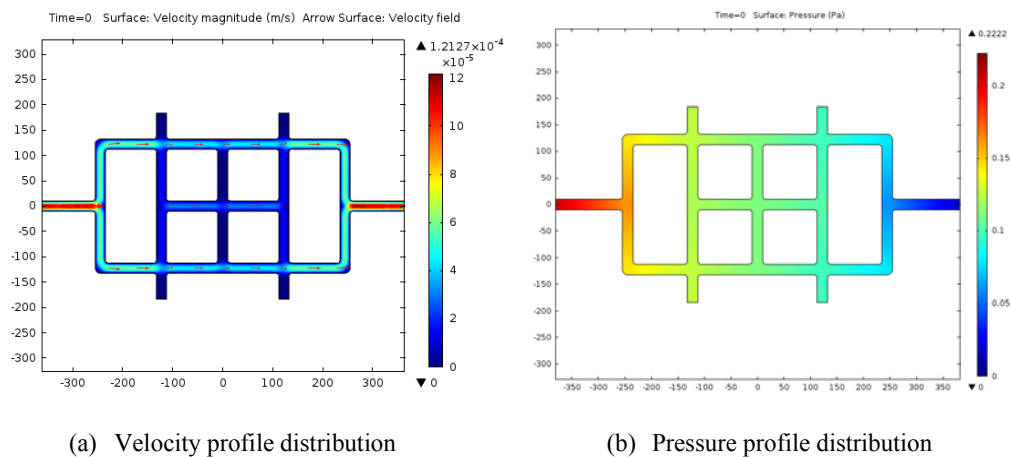
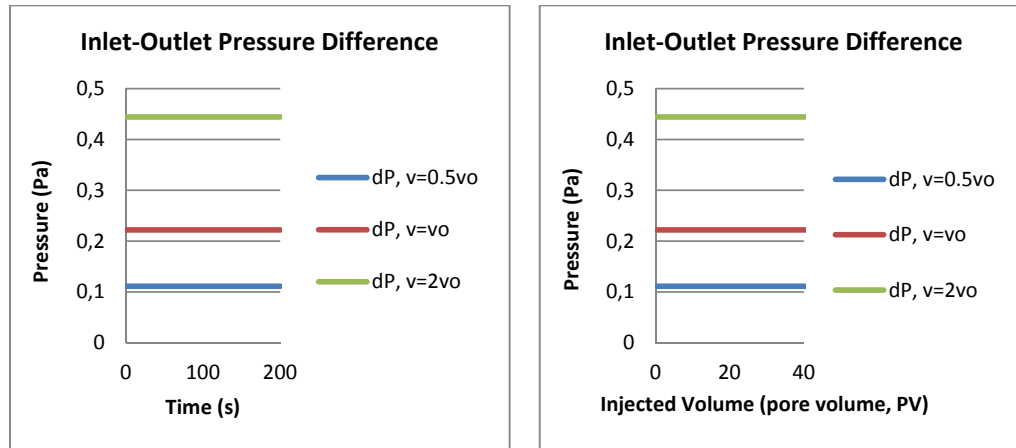


**Figure 7.41:** Velocity and pressure profile distribution in the network applied in the simulation

The typical 2D steady velocity and pressure profile distribution of the system is shown in **Figure 7.41a** and **Figure 7.41b** respectively. The 2D profile shown is only for the base case. The velocity magnitude is the highest at the inlet and the outlet boundary, and it is reduced in the microchannel with junctions. As the result of the introduced injection velocity, the highest pressure is observed in the inlet boundary, i.e. 0.22 Pa, and then is decreased smoothly until 0 Pa at the outlet. The pressure distribution in the branches between the inlet and the outlet follows the pressure gradient of the system consistently.

The inlet-outlet pressure difference of the system for various injection velocity against the time and the injected volume are shown in **Figure 7.42a**

and **Figure 7.42b** respectively. It is observed that the inlet-outlet pressure profile is steady for all time and all injection volume where the magnitude of the pressure difference is proportional with the injection velocity.

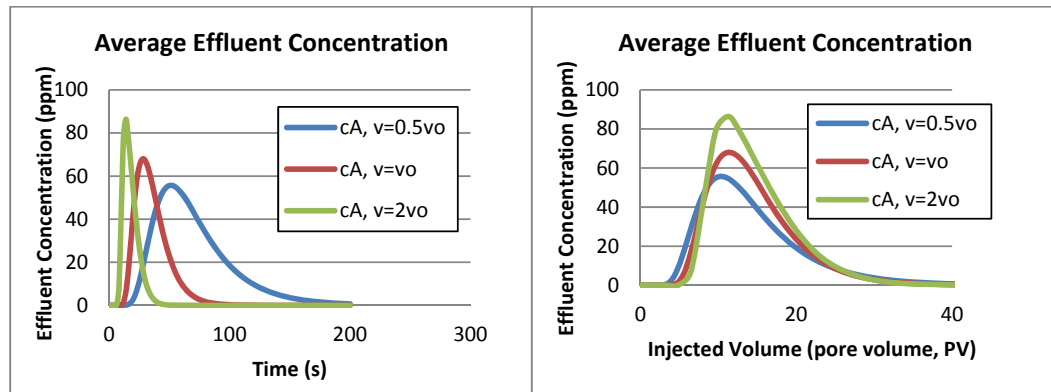


(a) Inlet-Outlet Pressure Difference vs Simulation Time (b) Inlet-Outlet Pressure Difference vs Injected Volume

**Figure 7.42:** Typical inlet-outlet difference profile of the microchannel network system

The average effluent concentration of the system for different injection velocity against the time and the injected volume are shown in **Figure 7.43a** and **Figure 7.43b** respectively. The breakthrough time indicates by starting point of the profile increase in **Figure 7.43a**. The magnitude of the breakthrough time varies inversely to the injection velocity. On the other hand, the peak magnitude of the effluent concentration is proportional to the injection velocity. This proportionality is also discovered in **Figure 7.43b**.

The amount of required injection volume is also observed from **Figure 7.43b**. Microchannel with low injection velocity needs slightly less nanoparticle injection volume to reach the outlet for a particular time compare to the case with higher injection velocity. As it was discussed previously in Chapter 4, the diffusion is more dominant to transport that disperses the injected concentration especially in a fairly short distance. The diffusion also enhances the adsorption by allowing the injected concentration to be in contact with the wall surface, where some bend surfaces might be bypassed in the case of larger advection.

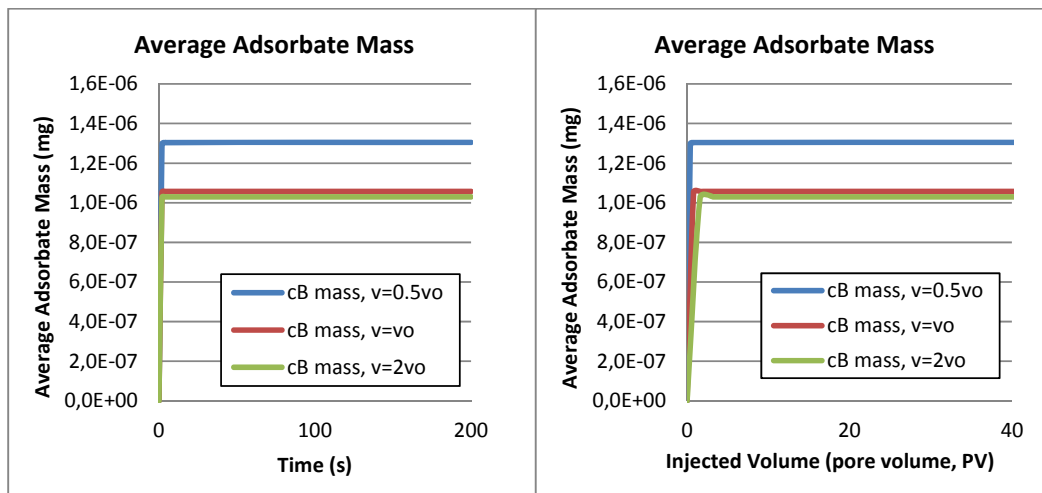


(a) Average Effluent Concentration vs Simulation Time

(b) Average Effluent Concentration vs Simulation Time

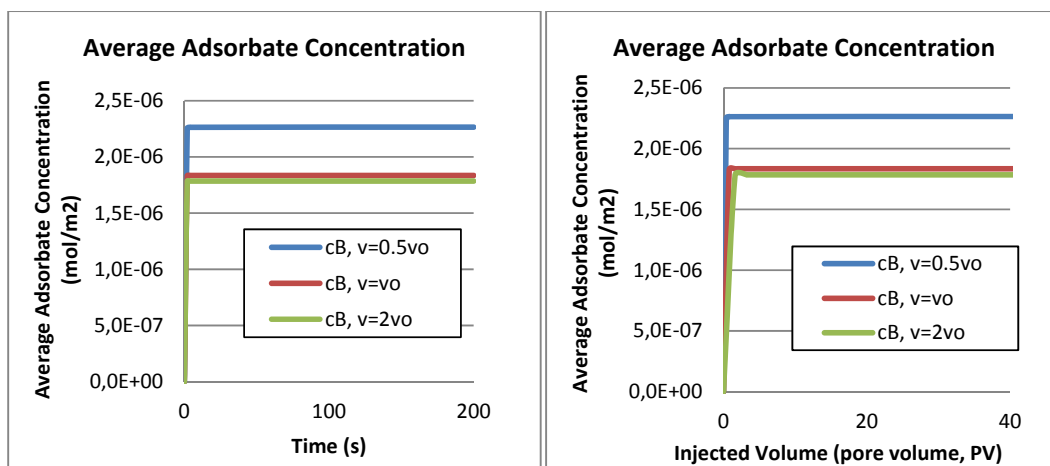
**Figure 7.43:** Typical inlet-outlet difference profile of the microchannel network system

Less magnitude in the effluent concentration profile indicates larger adsorption on the microchannel wall. The profile of the adsorbate mass of the system for different injection velocity against the time and the injected volume are shown in **Figure 7.44a** and **Figure 7.44b** respectively. It is observed from **Figure 7.44a** that the adsorption approximately happens instantly from the beginning of the simulation. The magnitude of the adsorbate mass is also varies inversely to the injection velocity. In **Figure 7.44b**, it is observed that the equilibrium adsorbate mass is achieved approximately around 1 pore volume, where the front of the main concentration bulk has transported through the outlet boundary. The surface area of the microchannel network is similar for all cases since the simulation is conducted in a similar geometry. This makes the trend of the adsorbate concentration is similar than the trend of the adsorbate. The profile of the adsorbate concentration of the system for different injection velocity against the time and the injected volume are shown in **Figure 7.44c** and **Figure 7.44d** respectively



(a) Average Adsorbate Mass vs Simulation Time

(b) Average Adsorbate Mass vs Injected Volume



(c) Average Adsorbate Concentration vs Simulation Time

(d) Average Adsorbate Concentration Mass vs Injected Volume

**Figure 7.44:** Typical adsorbate mass and concentration profile of the microchannel network system

## 7.8 Summary and Conclusion

A development of a microchannel network model has been established by combining a few preconfigured microchannel segments. The study conducted contributes in creating a flexible simulation tool to create a complex microchannel network model that established from arranging a set of basic microchannel segments that transport where the distribution of injected nanoparticles within can be investigated. This study establishes an alternative conduit to understand the distribution and adsorption-desorption

---

in porous media, where the previous studies were mostly conducted for macro-scale pore models.

There are four types of microchannel segments, which are straight microchannel, bended microchannel, T-junction microchannel and cross-junction microchannel. These microchannel segments can flexibly be coupled with one another to form complex two dimensional microchannel network models.

The concentration distribution and the adsorption/desorption in the microchannel segment is investigated. The first investigation is conducted for microchannel segments with similar surface area. The investigation is intended to investigate the effect of the channel configuration to the concentration propagation and adsorption/desorption process. The second investigation is carried out for microchannel segments with similar channel lattice dimension. Similar channel lattice dimension means that the microchannel segment is configured as a piece of puzzle that can be arranged flexibly to establish a complex microchannel network model. The investigation is subjected for a discontinuous concentration injection to study the behaviour of the injected concentration in the system.

In the case of similar microchannel surface area, it is discovered that the number of the outlet boundary, the position of the outlet boundary, and the segment configuration influence the microchannel's inlet-outlet pressure difference. It is discovered that the amount of the adsorption is affected more sensitively by the complexity of the microchannel geometry and does not correlate straightforwardly to the amount of the outlets.

In the case of similar lattice dimension, it is again discovered that pressure difference is proportional to the microchannel complexity, the surface area, and the number of the outlet boundary. It is also discovered that the adsorption has a positive correlation with the magnitude of the microchannel surface area. The number of outlet boundary also affects the pressure profile in the segment. Investigating the profile of the pressure distribution in the microchannel, the magnitude of the pressure profile decreases more rapidly towards the outlets as the number of the segment's outlet boundary increases.

Correlations between segment's inlet-outlet pressure and the adsorbate concentration are investigated using regression method. The trend follows the power correlation which in agreement with the Freundlich adsorption isotherm. However, the correlation for the adsorbate

concentration and the adsorbate mass is difficult to establish. The reason is because the mechanism of the adsorption and desorption is sensitive to the condition in the system, i.e. the concentration difference and the velocity.

Diffusion and advection influence the adsorption process significantly. The effect of diffusion is more dominant to the system than the advection in an environment with low velocity. The adsorption happens more efficiently in an environment with diffusion dominancy than in the environment with advection dominancy. The adsorption in an environment with high advection can be enhanced by injecting plenty amount of fluid into the system more than it is required in the case with diffusion dominancy.

Finally, an example of successful establishment of a typical microchannel network model by arranging the microchannel segments is presented. Pressure distribution, profiles of effluent concentration, adsorbate mass and concentration are investigated whose results are in accordance with the previous investigation steps in this thesis.

## **Chapter 8**

### **Summary and Conclusions**

#### **8.1 Assessment and Research Objectives**

The primary research motivation, aims and objectives were highlighted in Sections 1.2 and 1.3 (Chapter 1). The overall aims of this research are to establish an understanding of nanoparticles penetration into rock pores that considers the adsorption/desorption mechanism, dispersion behaviour, spatial distributions and residence times.

Because of this research, a novel development of a simulator is proposed that can model the flow, distribution, and adsorption/desorption of diluted nanoparticle inside a microchannel and microchannel network.

In this section, the research objectives are revisited and their influences on the results obtained in this work are evaluated as follows:

1. To develop a simulator that can model the flow, distribution, and adsorption/desorption of diluted nanoparticle inside a simple microchannel, key assumptions and governing equation used in developing the simulator for the concentration distribution in a microchannel which is discussed in Chapter 3. The fluid flow in the microchannel follows a creeping flow that is considered as a steady flow. The fluid flow is coupled with a concentration flow that is representing the nanoparticles transport in microchannel system. Nanoparticles in the fluid are represented by concentration because of the nature of the nanoparticle's small dimension. Adsorption and desorption mechanism occurs at the wall boundary of the microchannel that follows Freundlich adsorption isotherm. The Langmuir was also considered, however it cannot reproduce results obtained by the laboratory results that were used for validation. Finite Element Analysis (FEA) is used as the tool for the simulation.
2. To validate the simulation using experimental results, the methodology discussed in Chapter 3 is applied to reproduce results from an experiment that is discussed in the early section of Chapter 4. The simulator is used to model a core flood experimental for an injection of a PPCA concentration in a scale squeeze treatment that was conducted by Zhang et. al [221]. The effluent and adsorbate concentration from the

---

experiment from preflush and post-flush stage of PPCA concentration injection from the experiment are used for the validation. The behaviour of the PPCA concentration in the microchannel is assumed parallel with the behaviour of an injected nanoparticle concentration because both substances are treated as diluted concentration in the carrier fluid. Refer to Chapter 3, the flow channel in the core sample is converted into geometry of a single microchannel. The core is assumed to consist of small and identical parallel microchannels. One of the parallel microchannels is selected as the domain for the investigation. The length of the microchannel is similar to the length of the core in the experiment. The diameter of the microchannel follows the average pore diameter of typical Clashach sandstone. Both Langmuir and Freundlich adsorption isotherm method are investigated to establish a set of equations that fits the results from the experiment.

3. To investigate the distribution of nanoparticles in a single straight microchannel, section 4.6 in Chapter 4 is established. This section discusses the distribution of the nanoparticles in a straight microchannel for various injection velocities. In the simulation, all the method and parameters used in the validation remains similar, except the length of the microchannel, which is taken 10 times of its diameter. Taking shorter microchannel geometry for the modelling benefits the simulation time length greatly. The simulator is prepared for two geometry configurations, i.e. 2D geometry and 3D axis symmetric geometry. 2D geometry benefits to model microchannel with longitudinal variations, e.g. tortuous microchannel and 2D microchannel network model. On the other hand, 3D axis symmetric geometry is more representative than the latter to the actual sense of a cylindrical pore channel. The latter geometry is used to model concentration distribution in microchannel with various wall roughnesses. The detail for the validation is discussed in section 4.5. Sensitivity study for various injection velocities in the simulation is discussed in section 4.6. The simulation is conducted for a continuous and discontinuous concentration injection under five different injection velocities. The effect of diffusion to the concentration transport and adsorption/desorption process are also discussed in this section.
4. To investigate the distribution of nanoparticles in a single tortuous microchannel, Chapter 5 discusses the simulation of injected concentration distribution and adsorption/desorption in a single tortuous microchannel. The nanoparticles are again treated as diluted

---

concentration and the approach used in Chapter 4 is utilised. The simulations are conducted for seven microchannel geometry models with different tortuosity discussed in this chapter. The investigation covers tortuous microchannels with identical length and for microchannel with similar inlet-outlet distance, i.e. in section 5.4 and 5.5 respectively. For both investigations, the simulations are conducted for continuous and discontinuous concentration injection.

5. To investigate the distribution of nanoparticles in a single rough surface microchannel, Chapter 6 is established. This chapter discusses the simulation of a concentration injection in a single rough-walled microchannel. 3D axis symmetric geometry is used and sensitivity study for five different magnitudes of wall roughness is conducted. In this chapter, the roughness of the wall is an analogue of the alteration of the wall surface due to a significant attachment or desorption of a substance onto it. Therefore, the increase of the wall roughness reduces the internal volume of the microchannel, but increases the surface area. The effect of the microchannel wall roughness to the concentration distribution and adsorption is discussed in section 6.4. The adsorptions on the roughness asperities and in the dead end region of the microchannel are investigated in 6.4.2 and 6.4.3 respectively. In the end of this chapter, the effect of the wall roughness increase to the adsorption/desorption governing equation is discussed.

To investigate the distribution of nanoparticles in a complex microchannel network, the development of a model that represents pore channel network is discussed in Chapter 7. Four basic microchannel segments that situated in 3x3 units lattice element were developed that can be arranged flexibly to institute a more complex microchannel network. Two assessments were conducted, i.e. for segment geometries with similar surface area (Section 7.4) and for the segment geometry with similar lattice dimension (Section 7.5). The former is used for comparing the concentration distribution for each segment. The latter is used as the basic for establishing flexible arrangement of complex microchannel networks. The governing equations and assumptions for the particle transport and the adsorption/desorption mechanism that are discussed in Chapter 3 and Chapter 4 are used in the development. The concentration behaviour in each microchannel segment is investigated. An effort to find a direct correlation between the concentration behaviour and the inlet-outlet pressure difference of the segment with different

---

geometry configuration is discussed in 7.6. Finally, the simulation in a typical complex network model that is built based on the pre-established microchannel segments is discussed in section 7.6. This chapter shows that the simulator developed in this thesis is an alternative tool to model and understand the distribution and adsorption-desorption in microchannel in porous media, where the previous studies were mostly conducted for a macro-scale porous media model.

## 8.2 Conclusions

As the first step to gain fundamental understanding of nanoparticle transport and distribution in porous media, this research has successfully demonstrated a development of a simulator to model distribution and adsorption/desorption of an injection concentration in microchannel. The conclusions of this research are summarized in this section.

Adsorption and desorption is endorsed by concentration difference between the bulk fluid and the microchannel wall. In the case with less advection effect, diffusion effect disperses the particles more evenly throughout the microchannel domain and promotes adsorption process. However, the penetration coverage for the particle will not be noteworthy in this case, especially for a long and complicated microchannel configuration. The adsorption in an environment with large magnitude of advection is enhanced by injecting more plenty amount of injected particles into the system than it is required for the case where the effect of diffusion is more superior. On the other hand the desorption happens more efficiently in the case with higher effect of advection. Therefore, the system should undergo under a low advection effect to reduce the desorption occurrence.

The geometry of the microchannel also affects the adsorption process. The injected nanoparticles transport more easily in microchannels with simple configuration. The injection time and volume to reach adsorption-desorption equilibrium condition is proportional with the magnitude of microchannel curvature (tortuosity). However, the density of the adsorption distribution in this type of microchannel is less uniform. This is shown by the profile of the average adsorbate concentration at the bended microchannel wall that tends to be less than its surrounding. Bends in the microchannel reduces sweep efficiency between the bended walls and the nanoparticles in the concentration bulk. This happens because of the effect of eddies at the bends of the microchannel hinders the particles at the

---

surrounding area to be in touch with the bended walls. However, the average mass of the adsorbate is positively correlated with the microchannel tortuosity. The equilibrium adsorbate mass is typically greater as the tortuosity increases. The trend of the escalation is relatively linear for higher injection velocity, but altered exponentially as the injection velocity reduces. There are two reasons for this. The first one, the microchannel with higher tortuosity has wider surface area, allowing more mass adsorbed on to it. The second one, the bends happens in the system provides surfaces that facing towards the direction of the concentration flow. This condition enhances the contact between the nanoparticles concentration and the microchannel wall, which as well, enhances the adsorption in the system.

The effect of tortuosity to the adsorption process is more significant for lower injection velocity. In this case, the effect of tortuosity is more dominant than the advection. However, the effect of advection kinetic contributes more dominant effects to the adsorption than the tortuosity in the case with high injection velocity. This is shown by a comparable adsorption magnitude in various tortuous microchannels for a similar high injection velocity. Therefore, injection velocity should be high to enhance the distribution and the adsorption of the injected nanoparticle in a tortuous porous media. However, the tortuosity magnitude has a negative correlation with the desorption rate. Desorption happens less efficiently in a microchannel with more complex longitudinal configuration.

It is discovered that the roughness of the microchannel wall does not contribute any significant effect to the overall transport of the particle concentration in the microchannel. However, the adsorption process on the rough wall is proportional to its roughness magnitude.

Focusing at the asperities of the channel's wall roughness, the adsorption happen the least at the surface, which is the furthest from the channel centre, and the highest surface that closest to the inner channel centre. It is found that diffusion is the main driving mechanism to transport the particles into the dead end region at the channel between two asperities. Advection vortex also presents in the dead end region that hinders the particles to return to the channel after trapped inside the dead end.

An effort to establish a direct correlation between the wall roughness alteration and the adsorption has been conducted. However, the adsorption alteration due to the wall roughness increase is not comparable for both continuous and discontinuous injection. Therefore a relation between the

adsorption desorption mechanism, as a function of the microchannel wall roughness cannot be established.

Finally, a study to establish a model to simulate the distribution, adsorption and desorption process of injected particles into a complex microchannel is conducted. A set of microchannel segments with for different shape is prepared, including a straight microchannel, a bended microchannel, a T-junctional microchannel, and a cross-junctional microchannel. Each segment is situated on a 3x3-units square lattice. The study is conducted for two cases, i.e. segment with similar surface area and segments with similar lattice dimension. The former is used to investigate the distribution and adsorption/desorption contrast of the injected nanoparticle for different segment. The latter is used to arranging complex microchannel model because each of the segments can flexibly be coupled with one another to creating a complex two dimensional microchannel network model.

Initially, the pressure difference for each segment is investigated. Instead of only by the average distance between the inlet and the outlet, it is found that the number of the outlet boundary and the complexity of the segment configuration influence the microchannel's inlet-outlet pressure difference. However, the relation is not easily established because the mechanism also considers the direction of the flow inside each microchannel. Second, the adsorption magnitude is considered. It is found that the adsorption is influenced by the complexity of the microchannel geometry. However, his adsorption does not correlate straightforwardly to the amount of the outlets.

By regression method, correlations to relate the inlet-outlet pressure difference and the effluent concentration are established. The trend follows power regression trend which in agreement with the Freundlich adsorption isotherm. However, a specific correlation for the cases is difficult to establish. The reason is because the mechanism of the adsorption and desorption is complex, sensitive to the concentration contrast and requires to include effect of advection and diffusion in the mechanism.

Finally, a two dimensional simulation for a typical microchannel network model is established from a combination of the preconfigured microchannel segments formerly discussed. Pressure distribution, profiles of effluent concentration, adsorbate mass and concentration are investigated that results satisfy the ones acquired from the previous investigation steps conducted in this thesis. Ultimately, the simulator developed in this thesis

---

can be an alternative tool to model and simulate the distribution, adsorption, and desorption of injected nanoparticles in microchannel; where the previous studies were mostly conducted for a macro-scale porous media model.

Hence, this thesis proposes a framework of simulation methodology of modelling and studying nanoparticle transport and surface phenomenon in various microchannel geometry. The framework utilises simple but detail approach to simulate transport and surface phenomenon mechanism which process and results can be easily investigated. Moreover, the surface phenomenon mechanism used in this study can be altered to study other mechanisms, e.g. corrosion, hydrate deposition, etc., by only changing its governing equations and fluid properties. The microchannel domain is able to scale up into a more complex configuration.

Nevertheless, the selection of data and governing equations shown in this thesis is mostly specific for the case being discussed, i.e. transport of chemically inactive nanoparticles with that utilising Freundlich isothermal adsorption and desorption mechanism. The system is no slip, incompressible, no reaction between the nanoparticles in the concentration, no process of agglomeration and/or repulsion between the nanoparticles, and pH effect is neglected. If these assumptions are not used, the simulator is adaptable for the inclusion of more equations that satisfy the condition required. However, the current simulation has already required a high specification computer. Hence, the inclusion of more equations or scale up of the system domain demands higher computer specification. With the flexibility offered within the framework, the simulation is able to use for broader application for modelling any transport and surface phenomenon in microchannel instead of only for oil and gas industry, e.g. corrosion modelling in pipe, fluid flow in blood vein, medicine distribution in human body, etc.

### **8.3 Future Work**

Further research is recommended to extend this work and to focus on the improvements of simulator. These improvements are based on evaluation and exploration of the current limitations of the simulator. These will lead towards the development of a better simulator. The future work could address the issues as follows:

- 
1. The adsorption/desorption equation that is used in the microchannel model is derived from an experimental result from a core. PPA injected concentration is also used as an analogue of injected nanoparticle concentration injection. Experimental work including nanoparticle injection in single and network microchannel model is required to obtain validation that is more precise.
  2. Single phase and incompressible water is the fluid used in the current model. Applying different ratios of oil, gas, water and other type of fluid in current model is possible.
  3. A major limitation of the design methodology presented in this research is that it does not utilise an optimisation technique for studying the injection velocity and injection concentration to maximize the penetration distance and adsorption of the injected concentration. Therefore, there is a real need to use an optimisation technique for the simulation design. The simulation is versatile to use for developing a complex microchannel network. However, required computer resource corresponds to the complexity of the network developed.
  4. The effect of dispersion and agglomeration of nanoparticles are not considered in the simulator. The effect of dispersion and agglomeration of the injected concentration that can affect the inner diameter of the microchannel. The effect of these two parameters should be considered in the future simulation.
  5. The effect of crystallisation and deposition for the adsorption and desorption mechanism of the injected particles in the microchannel is not considered in the simulator. These two can enhance or reduce the adsorption and desorption process in the system, therefore these parameters should be considered in the future study.
  6. It also needs to develop a mechanism to arrange the predefined microchannel segment to establish a network model based on real porous media model.

---

## References

1. Gao, S., W. House, and W.G. Chapman, *Detecting Gas Hydrate Behavior in Crude Oil Using NMR*. J. Phys. Chem. B, 2006. **110**: p. 6549-6552.
2. Jr., E.D.S., *Coping with flow assurance*. Offshore Magazine, PennWell, 2005.
3. Tomson, M.B., et al., *Scale formation and prevention in the presence of hydrate inhibitors*. SPE 80255, 2003.
4. Merdhah, A.B.B. and A.A.M. Yassin, *Laboratory Study and Prediction of Calcium Sulphate at High-Salinity Formation Water* The Open Petroleum Engineering Journal, 2008. **1**: p. 62-73.
5. Crabtree, M., et al., *Fighting Scale - Removal and Prevention*. Oilfield Review - Autumn 1999, 1999.
6. Rodriguez, E., et al., *Enhanced Migration of Surface-Treated Nanoparticles in Sedimentary Rocks*. Society of Petroleum Engineers, SPE 124418 2009.
7. Norway, T.R.C.o., *Nanoparticles helping to recover more oil*. ScienceDaily, 14 June 2013.
8. Habibi, A., et al., *Reduction of Fine Migration by Nanofluids Injection, An Experimental Study*. 2011, Society of Petroleum Engineers.
9. Zies, C., et al., *Nanoparticle Transport through Porous Media: Screening Tools for Mobility Prediction*. 2012, Society of Petroleum Engineers.
10. Analytica, O. and E. Young, *Strategic Business Risk: Insurance 2008*. 2008.
11. Jessen, R., *Top 10 Risks for the Oil and Gas Industry*. JPT July 2008.
12. NPD, *Fact 2012 - The Norwegian Petroleum Sector*. 2012.
13. NPD, *Petroleum Resources on The Norwegian Continental Shelf*. 2011.
14. Harbaugh, J.W. and A. Prelat, *Research in Oil Exploration Estimation of Wildcat Well Decision-Making: Outcome Probabilities* 1973.
15. Kaufman, G.M. and P.J. Lee, *Are Wildcat Well Outcomes Dependent or Independent?* MIT Sloan School Working Paper 3373 January, 1992.
16. Menand, S., *Drilling Technology*. JPT February, 2008.
17. Neville, A., *Surface Scaling in the Oil and Gas Sector: Understanding the Process and Means of Management*. dx.doi.org/10.1021/ef300351w | Energy Fuels 2012, 26, 4158–4166, 2012.
18. Frenier, W.W. and M. Ziauddin, *Formation, removal, and inhibition of inorganic scale in the oilfield environment*. SPA books, 2008.
19. Rochaix, *Electrochimie : Thermodynamique-Cinetique*. Nathan, 1996. **1996**: p. 239.
20. Chilingar, G.V., R. Mourhatch, and G.D. Al-Qahtani, *Fundamental of Corrosion and Scaling - For Petroleum and Environmental Engineers*. Gulf Publishing Company, Houston, Texas, 2008.
21. Garverick, L., *Corrosion in the Petrochemical Industry*. Materials Park, OH, U.S.A. A S M International, 1994: p. 501.
22. Sun, W. and S. Nestic, *Kinetics of Corrosion Layer Formation: Part 1 - Iron Carbonate Layers in Carbon Dioxide Corrosion*. Corrosion, 2008. **64(4)**: p. 334-346.
23. Nestic, S., et al., *MEchanistic Modeling for CO2 Corrosion with Protective Iron Carbonate Films*. Corrosion, NACE International: Houston Tx, 2001.

24. Wake, H., *Oil refineries: A review of their ecological impacts on the aquatic environment. Estuarine Coastal and Shelf Science*. 2005. **62**: p. 131-140.
25. Martinod, A., et al., *Electrodeposition of calcareous layer: Effect of green inhibitors*. Chemical Engineering Science, 2009. **64(10)**: p. 2413-2421.
26. Sun, Y., W. Xiang, and Y. Wang, *Study on polyepoxysuccinic acid reverse osmosis scale inhibitor*. Journal of Environmental Science, 2009. **21**: p. S73-S75.
27. Kumar, T., S. Vishwanatham, and S.S. Kundu, *A laboratory study on pteroyl-l-glutamic acid as a scale prevention inhibitor of calcium carbonate in aqueous solution of synthetic produced water*. Journal of Petroleum Science and Engineering, 2010: p. 1-7.
28. Collins, I.R., et al., *The development of a novel environmentally friendly dual function corrosion and scale inhibitor*. SPE International Symposium on Oilfield Chemistry, 2001.
29. Neville, A., et al., *Assessing MMCs For Corrosion And Erosion-Corrosion Applications In The Oil Sands Industry* NACE International, 2004.
30. Graham, A., et al., *How minimum inhibitor concentration (MIC) and sub-MIC concentrations affect bulk precipitation and surface scaling rates*. SPE Production and Operations, vol. 21, pp.19-25. , 2006.
31. Martinod, A., A. Neville, and M. Euvrard, *Experimental investigation of scaling control by a non-phosphorous polymer: polyaspartic acid*. Desalination and Water Treatment, 2009. **7**: p. 86-92.
32. Kazemi, N., et al., *Preventing adhesion of scale on rock by nanoscale modification of the surface*. Society of Petroleum Engineers - SPE International Oilfield Nanotechnology Conference 2012, pp.195-199. , 2012.
33. Ayatollahi, S. and M.M. Zerafat, *Nanotechnology-Assisted EOR Techniques: New Solutions to Old Challenges*. 2012, Society of Petroleum Engineers.
34. Sanders, L., et al., *Combined Inhibitors - A New Experimental Method foa a Simultaneous Assessment of Scale and Corrosion Phenomena*. SPE 155462, 2012.
35. Ghorbani, N., et al., *Using Nanoscale Dispersed Particles to Assist in the Retention of Polyphosphinocarboxylic Acid (PPCA) Scale Inhibitor on Rock*, p.-. Society of Petroleum Engineers - SPE International Oilfield Nanotechnology Conference 2012, Editor. 2012, Society of Petroleum Engineers.
36. Total, E., *EOR Maximizing Recovery Factors*. 2008.
37. Booker, R. and E. Boysen, *Nanotechnology For Dummies* 2006.
38. Krishnamoorti, R., *Extracting the Benefits of Nanotechnology for the Oil Industry*. JPT, 2006.
39. Ju, B. and T. Fan, *Experimental study and mathematical model of nanoparticle transport in porous media*. Powder Technology, 2009. **192(2)**: p. 195-202.
40. Okuyama, K. and W. Lenggoro, *Nanoparticle Preparation and Its Application - A Nanotechnology Particle Project in Japan*. 2004.
41. Buzea, C., I.I.P. Blandino, and K. Robbie, *Nanomaterials and nanoparticles: Sources and toxicity*. Biointerphases, 2007. **2(4)**: p. MR17 - MR172.
42. Jong, W.H.D. and P.J. Borm, *Drug delivery and nanoparticles: Applications and hazards*. Int J Nanomedicine. June, 2008: p. 133-149.

43. Kwon, Y.-S., et al., *Structure And Properties of Nanoparticles Formed under Conditions of Wire Electrical Explosion*. Dans European Nano Systems Workshop - ENS 2005, Paris : France (2005), 2007.
44. Morris, J.E., *Nanopackaging - Nanotechnologies and Electronics Packaging*. 2008.
45. Das, S.K., et al., *Nanofluids Science and Technology*. 2007.
46. Faucheu, J., et al., *Properties of polymer/clay interphase in nanoparticles synthesized through in-situ polymerization processes*. 2010.
47. Bethune, D.S., et al., *Cobalt-Catalysed Growth Of Carbon Nanotubes With Single-Atomic-Layerwalls*. Nature, 1993. **363**(605-607).
48. Iijima, S. and T. Ichihashi, *Single-Shell Carbon Nanotubes Of 1-Nm Diameter*. Nature, 1993. **363**: p. 603-605.
49. McEuen, P.L., M. Fuhrer, and H. Park, *Single-Walled Carbon Nanotube Electronics*. IEEE Transactions on Nanotechnology, 2002.
50. Wang, X., et al., *Fabrication of Ultralong and Electrically Uniform Single-Walled Carbon Nanotubes on Clean Substrates*. Nano Letters 9 (9): 3137–3141. doi:10.1021/nl901260b. PMID 19650638., 2009.
51. Cui, J.B., et al., *Carbon nanotube memory devices of high charge storage stability*. American Institute of Physics, 2002.
52. Matteu, C., et al., *Current and Future Nanotech Applications in the Oil Industry*. American Journal of Applied Sciences 9, 2012.
53. Nelson, P.H., *Pore-throat sizes in sandstones, tight sandstones, and shales*. AAPG Bulletin ; March 2009; v. 93; no. 3; p. 329-340; DOI: 10.1306/10240808059. 2009 American Association of Petroleum Geologists (AAPG), 2009.
54. Suttiponparnit, K., et al., *Role of Surface Area, Primary Particle Size, and Crystal Phase on Titanium Dioxide Nanoparticle Dispersion Properties*. Nano Express Open Access, 2010.
55. Gell, M., et al., *Development and implementation of plasma sprayed nanostructured ceramic coatings*. 2001.
56. Magin, C.M., S.P. Cooper, and A.B. Brennan, *Non-toxic antifouling strategies*. Materials Today, Volume 13, Issue 4, April 2010, Pages 36-44. [http://dx.doi.org/10.1016/S1369-7021\(10\)70058-4](http://dx.doi.org/10.1016/S1369-7021(10)70058-4), 2010.
57. Ferro, G., J.-M. Tulliani, and S. Musso, *Carbon nanotubes cement composites*. ISBN 978-88-95940-36-6 2011.
58. Konsta-Gdoutos, M.S., Z.S. Metaxa, and S.P. Shah, *Highly dispersed carbon nanotube reinforced cement based materials*. Cement and Concrete Research, 2010. **40**(7): p. 1052-1059.
59. Yu, M.-F., et al., *Strength and Breaking Mechanism of Multiwalled Carbon Nanotubes Under Tensile Load*. Science 287 (5453): 637–640. doi:10.1126/science.287.5453.637. PMID 10649994., 2000.
60. Popov, M., et al., *Superhard phase composed of single-wall carbon nanotubes*. Phys. Rev. B 65, 033408, 2002.
61. Prasher, R.S., et al., *Turning Carbon Nanotubes from Exceptional Heat Conductors into Insulators*. Physical Review Letters, 2009. **102**(10): p. 105901.
62. Shi, X., et al., *Effect of nanoparticles on the anticorrosion and mechanical properties of epoxy coating*. Surface & Coatings Technology, 2009(204): p. 237–245.

63. Popov, M., et al., *Superhard phase composed of single-wall carbon nanotubes*. Phys. Rev. B 65 (3): 033408. doi:10.1103/PhysRevB.65.033408, 2002.
64. Sloan, E.D., *Clathrate Hydrates of Natural Gases*. Marcel Dekker Inc., New York and Basel, 1990.
65. Gao, S., *Investigation of Interactions between Gas Hydrates and Several Other Flow Assurance Elements*. Energy & Fuels 22 (5), 2008. **22(5)**: p. 3150–3153.
66. Peysson, Y., et al., *Flow of Hydrates Dispersed in Production Lines*. 2003, Society of Petroleum Engineers.
67. Dorstewitz, F. and D. Mewes, *Hydrate formation in pipelines*. 5th International Offshore and Polar Engineering Conference, The Hague, June 11-16, 1995.
68. Bhatia, K.H. and L.P. Chacko, *Ni-Fe Nanoparticle: An Innovative Approach for Recovery of Hydrates*. 2011, Society of Petroleum Engineers.
69. Tomitaka and H.Kobayashi, *Magnetization and self-heating temperature of NiFe<sub>2</sub>O<sub>4</sub> nanoparticles measured by applying ac magnetic field*. Journal of Physics: Conference Series 200, 2010.
70. Bae, S., S.W. Lee, and Y. Takemura, *Applications of NiFe<sub>2</sub>O<sub>4</sub> nanoparticles for a hyperthermia agent in biomedicine*. Applied Physics Letters, 2006. **89(25)**: p. -.
71. Straub, T.J., S.W. Autry, and G.E. King, *An Investigation Into Practical Removal of Downhole Paraffin by Thermal Methods and Chemical Solvents*. 1989, Society of Petroleum Engineers.
72. Haindade, Z.M.W., et al., *Enhancing Flow Assurance Using Co-Ni Nanoparticles For Dewaxing Of Production Tubing*. 2012, Society of Petroleum Engineers.
73. Prodanovic, M., et al., *Effects of Magnetic Field on the Motion of Multiphase Fluids Containing Paramagnetic Nanoparticles in Porous Media*. 2010, Society of Petroleum Engineers.
74. Ryoo, S., et al., *Theoretical and experimental investigation of the motion of multiphase fluids containing paramagnetic nanoparticles in porous media*. Journal of Petroleum Science and Engineering, 2012. **81(0)**: p. 129-144.
75. Yu, H., et al., *Transport and Retention of Aqueous Dispersions of Paramagnetic Nanoparticles in Reservoir Rocks*. 2010, Society of Petroleum Engineers.
76. Yu, H., et al., *Transport and retention of aqueous dispersions of superparamagnetic nanoparticles in sandstone*. Journal of Petroleum Science and Engineering, 2014. **116(0)**: p. 115-123.
77. Gulson, B. and H. Wong, *Stable Isotopic Tracing—A Way Forward for Nanotechnology*. Environmental Health Perspectives, 2006.
78. Technology, I.-D.f.R.a.E., *New functional tracers based on nanotechnology and radiotracer generators*. 2009.
79. Evdokimov, I.N., et al., *Emerging Petroleum-Oriented Nanotechnologies for Reservoir Engineering*. 2006, Society of Petroleum Engineers.
80. Matteo, C., et al., *Current and future nanotech applications in the oil industry*. American Journal of Applied Sciences, 2012. **9**: p. 784-793.
81. Skauge, T., K. Spildo, and A. Skauge, *Nano-sized Particles For EOR*. 2010, Society of Petroleum Engineers.

- 
82. Ogolo, N.A., O.A. Olafuyi, and M.O. Onyekonwu, *Enhanced Oil Recovery Using Nanoparticles*. 2012, Society of Petroleum Engineers.
  83. Morrow, N.R., H.T. Lim, and S. J.S. Ward, *PE Formation Evaluation*. 1986. **89**.
  84. Wasan, D.T. and A.D. Nikolov, *Spreading of nanofluids on solids*. *Nature*, 2003. **423**(6936): p. 156-9.
  85. Chaudhury, M.K., *Complex fluids: Spread the word about nanofluids*. *Nature* 2003. **423**: p. 131-132.
  86. Karoussi, O. and A.A. Hamouda, *Macroscopic and nanoscale study of wettability alteration of oil-wet calcite surface in presence of magnesium and sulfate ions*. *Journal of Colloid and Interface Science*, 2008. **317**(1): p. 26-34.
  87. Rezaei-Gomari, S., et al., *Study of the effect of acidic species on wettability alteration of calcite surface by partitioning coefficients, IFT, and contact angles*, in *Contact Angle, Wettability and Adhesion*. 2004, VSP.
  88. Neville, A., T. Hodgkiess, and A.P. Morizot, *Surface scales in sea water systems: effects of their formation on corrosion behaviour of engineering steels*. *British Corrosion Journal*, 1997. **32**(4): p. 277-282.
  89. Arjmand, O. and M. Mousavi, *Effect of a natural adsorber as nano particle hydro gel to water shut-off during enhanced oil recovery process*. 2nd International Conference and Exhibition on Materials Science & Engineering, 2013.
  90. Zhang, P., et al., *Surfactant-Assisted Synthesis of Metal-Phosphonate Inhibitor Nanoparticles and Transport in Porous Media*. 2010.
  91. Dini, E., O. Kammona, and Kiparissides, *Synthesis of Highly Crosslinked Porous Microgels For The Removal of Organic Contaminants From Aqueous Solutions*. *Transport Phenomena & Separation Processes*, 2003.
  92. Nanosolar, I., *Ultra-Low-Cost Solar Electricity Cells: An Overview of Nanosolar's Cell Technology Platform*. White Paper - September 2, 2009.
  93. Steenburgh, T.J. and A.B. Wagonfeld, *Nanosolar* Harvard Business School, 2009.
  94. Sanni, M.L., R.A. Kamal, and D.M.Y. Kanj, *Reservoir Nanorobots*. *Saudi Aramco Journal of Technology*, 2008.
  95. Economist, T., *The future of higher education: How technology will shape learning*. A report from the Economist Intelligence Unit Sponsored by the New Media Consortium, 2008.
  96. Ramakrishna, A., *Challenges of Nanotechnology*. Presentation in the Science Supercourse (<http://ssc.bibalex.org>), 2010.
  97. Mackay, E.J., *Oilfield Scale - A New Integrated Approach to Tackle an Old Foe*. 2008, Society of Petroleum Engineers.
  98. Statoil, *Overview to scale control: Introduction to Scale*. 2006.
  99. Zielinski, R.A. and J.K. Otton, *Naturally Occurring Radioactive Materials (NORM) in Produced Water and Oil-Field Equipment—An Issue for the Energy Industry*. USGS Fact Sheet FS, 1999. **142**(99).
  100. Jasinski, R., *Well Production Problems*. *Petroleum Engineering Handbook Vol. IV: Production Operation Engineering*, SPE, Texas, United States of America, 2004.
  101. Hinrichsen, C.J., *Preventing Scale Deposition in Oil Production Facilities: An Industrial Review*. NACE Int. Paper No. 61 Corrosion 98, 1998.

102. Nasr-El-Din, H.A., *New Mechanisms of Formation Damage: Lab Studies and Case Histories*. SPE 82253, 2003.
103. Fleming, N., et al., *Impact of Successive Squeezes on Treatment Lifetime and Well Productivity: Laboratory and Field Evidence*. SPE Prod & Oper 24 (3): 450–458. SPE-113657-PA. doi: 10.2118/113657-PA. , 2009b.
104. Vazquez, O., et al., *Impact of Mutual Solvent Preflush on Scale Squeeze Treatments: Extended Squeeze Lifetime and Improved Well Clean-up Time*. SPE 121857, 2009.
105. Darwish, S.F.M., A.A., *Inhibitor Squeeze Design and Returns Monitoring To Manage Downhole Scale Problem*. SPE Paper No. 88597. 2004.
106. Ferguson, R.J., *Dequest organophosphorous compounds*. J. Ind. Water Treatment, 1993. **25**(2): p. 23.
107. Oddo, J.E., *Method For Scale Inhibitor Squeeze Application To Gas And Oil Well*. United States Patent No. 5655601 – Aug. 12, 1997. 1997.
108. Bache, Ø. and S. Nilsson, *Ester Cross-Linking of Polycarboxylic Acid Scale Inhibitors as a Possible Means to Increase Inhibitor Squeeze Lifetime*. 2000, Society of Petroleum Engineers.
109. Rabaioli, M.R. and T.P. Lockhart, *Solubility and Phase Behaviour of Polyacrylate Scale Inhibitors and Their Implications for Precipitation Squeeze Treatment*. 1995, Society of Petroleum Engineers.
110. Collins, I.R., *A process and a formulation to inhibit scale in oil field production*. 1998, Google Patents.
111. Jordan, M.M., et al., *The Design of Polymer and Phosphonate Scale Inhibitor Precipitation Treatments and the Importance of Precipitate Solubility in Extending Squeeze Lifetime*. 1997, Society of Petroleum Engineers.
112. Fleming, N., et al., *Innovative Use of Kaolinite in Downhole Scale Management: Squeeze Life Enhancement and Water Shutoff*. SPE 223656, 2008.
113. Fleming, N., et al., *Innovative Use of Kaolinite in Downhole Scale Management: Squeeze Life Enhancement and Water Shutoff*. SPE Prod & Oper 24 (3): 439–449. SPE-113656-PA. doi: 10.2118/113656-PA., 2009a.
114. Fleming, N., et al., *Mechanical Alteration of Near-Wellbore Mineralogy for Improved Squeeze Performance*. 2010.
115. Baraka-Lokmane, S. and K.S. Sorbie, *Scale Inhibitor Core Floods in Carbonate Cores: Chemical Interactions and Modelling*. SPE 100515, 2006.
116. Gdanski, R., *Formation Mineralogy Impacts Scale Inhibitor Squeeze Designs*. SPE 113261, 2008.
117. Hong, S.A. and P.J. Shuler, *A Mathematical Model for the Scale-Inhibitor Squeeze Process*. SPE Production Engineering November 1988, 1988.
118. Zhang, H.R., K.S. Sorbie, and E.L. MacKay, *Modelling Scale Inhibitor Squeeze Treatments in Horizontal Wells: Model Development and Application*. SPE 37140, 1996.
119. Sorbie, K.S., *A General Coupled Kinetic Adsorption/Precipitation Transport Model for Scale Inhibitor Retention in Porous Media: I. Model Formulation*. SPE 130702, 2010.
120. Vazquez, O., K.S. Sorbie, and E.J. Mackay, *A General Coupled Kinetic Adsorption/Precipitation Transport Model for Scale Inhibitor Retention in Porous Media: II. Sensitivity Calculations and Field Predictions*. SPE 130703, 2010.

121. Kahrwad, M., K.S. Sorbie, and L.S. Boak, *Coupled Adsorption/Precipitation of Scale Inhibitors: Experimental Results and Modeling*. 2008.
122. Shen, D., et al., *Control Placement Of Scale Inhibitors In The Formation With Stable Ca-DTPMP Nanoparticle Suspension And Its Transport In Porous Medium*. 2008, Society of Petroleum Engineers.
123. Grchev, T., M. Cvetkovska, and J.W. Schultze, *The electrochemical testing of polyacrylic acid and its derivatives as inhibitors of corrosion*. *Corrosion Science*, 1991. **32**(1): p. 103-112.
124. Kan, A.T., et al., *Factors Affecting Scale Inhibitor Retention in Carbonate-Rich Formation During Squeeze Treatment*. 2004.
125. Zhang, P., et al., *Silica-Templated Synthesis of Novel Zinc-DTPMP Nanomaterials: Their Transport in Carbonate and Sandstone Media During Scale Inhibition*. 2011.
126. Kan, A.T., et al., *Enhanced Scale-Inhibitor Treatments With the Addition of Zinc*. 2009.
127. Graham, G.M., et al., *Scale Inhibitor Selection for Continuous and Downhole Squeeze Application in HP/HT Conditions*. 1998, Society of Petroleum Engineers.
128. Wang, W., A. Kan, and M. Tomson, *A Novel and Comprehensive Study of Polymeric and Traditional Phosphonate Inhibitors for High-Temperature Scale Control*. 2013.
129. Wang, S. and J. Wylde, *Scale Inhibitor Selection for Deepwater High Temperature Applications*. *Corrosion*, March 22-26 Atlanta, GA. NACE International 09278, 2009.
130. Fan, C., et al., *Ultra-HTHP Scale Control for Deepwater Oil and Gas Production*. 2011, Society of Petroleum Engineers.
131. Yan, C., et al., *Boehmite Based Sulphonated Polymer Nanoparticles with Improved Squeeze Performance for Deepwater Scale Control*. 2013, Offshore Technology Conference.
132. Yan, C., et al., *Synthesis and Sorption Study of AlOOH Nanoparticle Cross-linked Polymeric Scale Inhibitors and Their Squeeze Performance in Porous Media*. 2013, Society of Petroleum Engineers.
133. Yan, C., et al., *Sorption Study of  $\gamma$ -AlO(OH) Nanoparticle-Crosslinked Polymeric Scale Inhibitors and Their Improved Squeeze Performance in Porous Media*. 2014.
134. Vazquez, O., E.J. Mackay, and K.S. Sorbie, *Modelling The Placement of Scale Squeeze Treatments in Heterogeneous Formation with Pressurised Layers*. SPE 121856, 2009.
135. You, Z., et al., *Effect of Nanoparticle Transport and Retention in Oilfield Rocks on the Efficiency of Different Nanotechnologies in Oil Industry*. 2012, Society of Petroleum Engineers.
136. El-Amin, M.F., S. Sun, and A. Salama, *Modeling and Simulation of Nanoparticle Transport in Multiphase Flows in Porous Media: CO<sub>2</sub> Sequestration*. 2012, Society of Petroleum Engineers.
137. El-Amin, M.F., et al., *Numerical Modeling of Nanoparticles Transport with Two-Phase Flow in Porous Media Using Iterative Implicit Method*. *Applied Mathematical Modelling*, 2013.
138. Ju, B., et al., *Modeling CO<sub>2</sub> miscible flooding for enhanced oil recovery*. *Petroleum Science*, 2012. **9**(2): p. 192-198.

139. Bedrikovetsky, P., *Upscaling of Stochastic Micro Model for Suspension Transport in Porous Media*. *Transport in Porous Media*, 2008. **75**(3): p. 335-369.
140. Bedrikovetsky, P., et al., *Modified Particle Detachment Model for Colloidal Transport in Porous Media*. *Transport in Porous Media*, 2011. **86**(2): p. 353-383.
141. Yu, J., et al., *Transport Study of Nanoparticles for Oilfield Application*. 2010, Society of Petroleum Engineers.
142. van Genuchten, M.T. and A.W. J., *Analytical solution of the one dimensional convective-dispersive solute transport*. p Technical Bulletin Nr. 1661, 1982.
143. Vega, C., R.D. Kaminsky, and P.A. Monson, *Adsorption of fluids in disordered porous media from integral equation theory*. *J. Chem. Phys.*, 1993. **99**.
144. Madden, W.G. and E.D. Glandt, *J. Stat. Phys.*, 1988. **51**(537).
145. Sharma, S., et al., *Modeling and Simulation of Magnetic Nanoparticles Transport in a Channel for Magnetic Drug Targeting*. *Recent Advances in Fluid Mechanics and Thermal Engineering* 2009.
146. Liu, Y., S. Shah, and J. Tan, *Computational Modeling of Nanoparticle Targeted Drug Delivery*. American Scientific Publishers, 2012.
147. Acharya, R.C., S.E.A.T.M. van der Zee, and A. Leijnse, *Porosity-permeability properties generated with a new 2-parameter 3D hydraulic pore-network model for consolidated and unconsolidated porous media*. *Advances in Water Resources*, 2004. **27**(7): p. 707-723.
148. Acharya, R.C. and S.E.A.T.M.V.d. Zee, *Transport modeling of nonlinearly adsorbing solutes in physically heterogeneous pore networks*. *Water Resources Research* Vol 41, 2005.
149. Wu, P. and W.A. Little, *Measurement of friction factors for the flow of gases in very fine channels used for microminiature joule-thomson refrigerators*. *Cryogenics*, 1983. **23**: p. 273-277.
150. Wu, P. and W.A. Little, *Measurement of the heat transfer characteristics of gas flow in fine channel heat exchangers used for microminiature refrigerators*. *Cryogenics*, 1984. **24**: p. 415-420
151. Weilin, Q., G.M. Mala, and L. Dongqing, *Pressure-driven water flows in trapezoidal silicon microchannels*. *International Journal of Heat and Mass Transfer*, 2000. **43**: p. 353-364.
152. Wu, H.Y. and P. Cheng, *Friction factors in smooth trapezoidal silicon microchannels with different aspect ratios*. *International Journal of Heat and Mass Transfer*, 2003. **46**: p. 2519-2525.
153. Peng, X.F., et al., *Experimental investigation of heat transfer in flat plates with rectangular microchannels*. *International Journal of Heat MASS Transfer* 1995. **Vol. 38, No. I**(1): p. 127-137.
154. Niklas, M., M. Favre-Marinet, and D. Asendrych, *Numerical simulation of microchannel network with complex geometry*. *Bulleting of the Polish Academy of Sciences Technical Sciences*, 2005. **53**(4).
155. Rawool, A.S., S.K. Mitra, and S.G. Kandlikar, *Numerical simulation of flow through microchannels with designed roughness*. *Microfluid Nanofluid*, 2006. **2**: p. 215-221.
156. Lionello, A., et al., *Protein adsorption in static microsystems: effect of the surface to volume ratio*. *Lab on a Chip*, 2004.

157. Serrano, S.E., *Propagation of nonlinear reactive contaminants in porous media*. Water Resources Research, 2003. **39**: p. 1228.
158. Bashir, M.J.K., et al., *Application of response surface methodology (RSM) for optimization of ammoniacal nitrogen removal from semi-aerobic landfill leachate using ion exchange resin*. Desalination, 2010. **254**(1–3): p. 154-161.
159. Sorbie, K.S. and R.D. Gdanski, *A Complete Theory of Scale-Inhibitor Transport and Adsorption/Desorption in Squeeze Treatment*. SPE 95088, 2005.
160. Gdanski, R.D. and G.P. Funkhouser, *Successful Model of the Kinetic Release of a Phosphonate Scale Inhibitor*. Presented at the NIF International Oilfield Chemistry Symposium, Geilo, Norway, 1-4 April 2001, 2001.
161. Zeinijahromi, A., T.K.P. Nguyen, and P. Bedrikovetsky, *Mathematical Model for Fines-Migration-Assisted Waterflooding With Induced Formation Damage*. 2013.
162. Schlumberger, *ECLIPSE Reservoir Engineering Software*. Schlumberger Information Solution (SIS), 2010.
163. Rudzinski, W. and D.H. Everett, *Adsorption of Gases on Heterogeneous Surfaces*. Academic Press: London, 1992.
164. Stallons, J. and M.; Iglesia, *Simulations of the structure and properties of amorphous silica surfaces* E. Chem. Eng. Sci. 56, pp. 4205-4216, 2001.
165. Sonwane, C.G.J., C. W.; Ludovice, , *A model for the structure of MCM-41 incorporating surface roughness*. P. J. J. Phys. Chem. B , 109, 23395, 2005.
166. Coasne, B., K.E. Gubbins, and R.J.-M. Pellenq, *Temperature Effect on Adsorption/Desorption Isotherms for a Simple Fluid Confined within Various Nanopores*. Springer, Adsorption 11: 289–294, 2005.
167. Kuchta, B., et al., *Microscopic Mechanism of Adsorption in Cylindrical Nanopores with Heterogenous Wall Structure*. Langmuir 2008, 24, 4013-4019, 2008.
168. Sbai, M.A. and M. Azaroual, *A Mathematical Model for Nanoparticles Transport within Two-phase Flow in Heterogeneous Porous media*. Flows and mechanics in natural porous media from pore to field scale. Pore2Field, Paris : France, 2011a.
169. Sbai, M.A. and M. Azaroual, *Numerical modeling of formation damage by two-phase particulate transport processes during CO<sub>2</sub> injection in deep heterogeneous porous media*. Advances in Water Resources, 2011b. **34**(1): p. 62-82.
170. Skopp, J., *Derivation of the Freundlich Adsorption Isotherm from Kinetics*. Journal of Chemical Education - J CHEM EDUC 10/2009; 86(11). , 2009.
171. Binshan, J., et al., *A Study of Wettability and Permeability Change Caused by Adsorption of Nanometer Structured Polysilicon on the Surface of Porous Media*. SPE 77938, 2002.
172. Ber, O.G. and P.H.v. Hippel, *Diffusion-Controlled Macromolecular Interactions*. Annual Review Biophys. Biophys. Chem., 1985. **14**: p. 131-160.
173. Jain, S., et al., *Monte Carlo simulation of flow of fluids through porous media*. Computers & Chemical Engineering, 2003. **27**(3): p. 385-400.
174. Scheidegger, *The Physics Of The Flow Through Porous Media*. University of Toronto Press, Toronto, Buffalo N.Y. , 1974.

175. Gratton, L.C. and H.J. Fraser, *Systematic Packing of Spheres: With Particular Relation to Porosity and Permeability*. The Journal of Geology, 1935. **43**(No. 8, Part I): p. 785-909.
176. Amyx, J.W., *Petroleum Reservoir Engineering - Physical Properties*. McGraw-Hill Book Company, Inc., New York 1960.
177. Krumbein, W.C. and F.J. Pettijohn, *Manual of Sedimentary Petrography*. Appleton-Century-Crofts: New York, 1938.
178. Craft, E.C. and M. Hawkins, *Applied Petroleum Reservoir Engineering, Second Edition*. Prentice-Hall Inc., New Jersey, 1991.
179. Bear, J. and A. Verrujit, *Theory And Applications of Transport In Porous Media: Modeling Groundwater Flow and Pollution*. D.Reidel Publishing Company, Dordrecht, Holland, 1987.
180. Brown, G.O., *Henry Darcy and the making of a law*. Water Resources Research, 2002. **38**(7).
181. Freeze, R.A., *Henry Darcy and the Fountains of Dijon*. Ground Water, 1994. **32**(1).
182. Simmons, C.T., *Henry Darcy (1803–1858): Immortalised by his scientific legacy*. Springer-Verlag, 2008.
183. Darcy, H., *Les Fontaines Publiques de la Ville de Dijon (The Public Fountains of the City of Dijon*. Dalmont, Paris, 1856.
184. Cheremisinoff, N.P., *Encyclopedia of Fluid Mechanics Vol. 1: Flow Phenomena and Measurement*. Gulf Publishing Company, Houston, Texas USA, 1986.
185. Peker, S. and S. Helvaci, *Solid-Liquid Two Phase Flow 1st.Ed*. Elsevier, Amsterdam, 2008.
186. Sleigh, A. and C. Noakes, *Support material for the Civil Engineering module Introduction to Engineering Fluid Mechanics 1.1*. University of Leeds. 2009.
187. Rott, N., *Note On The History Of The Reynolds Number*. 1990.
188. McGraw-Hill, *McGraw-Hill Concise Encyclopedia of Science & Technology, Fifth Edition*. McGraw-Hill Book Company, Inc, New York, USA, 2005.
189. Payne, L.E. and W.H. Pell, *The Stokes flow problem for a class of axially symmetric bodies*. Fluid Meoh. 7, 1959.
190. Tretheway, D.C. and C.D. Meinhart, *Apparent fluid slip at hydrophobic microchannel walls*. Physics of Fluid, 2002. **14**(3).
191. Ruthven, D.M., *Principles of Adsorption and Adsorption Process*. 1984.
192. Reible, D.D., *Fundamentals of Environmental Engineering*. Springer, 1999: p. 468-470.
193. Wilke, C.R. and P. Chang, *Correlation of Diffusion Coefficients in Dilute Solutions*. A.I.Ch.E. Journal 1955: p. 264-270.
194. Sitaraman, R., S.H. Ibrahim, and N.R. Kuloor, *A Generalized Equation for Diffusion in Liquids*. Journal of Chemical and Engineering Data 1963
195. Perry, R.H., *Perry's Chemical Engineers' Handbook Sevent Edition*. 1997: p. 5-51.
196. Gray, D.D., *A First Course in Fluid Mechanics for Civil Engineers*. 2000: p. 199-200.
197. Rathakrishnan, E., *Instrumentation, Measurements, and Experiments in Fluids*. 2007: p. 50.
198. Wilcox, D.C., *Basic Fluid Mechanics*. DCW Industries Inc., California, USA, 1994: p. 214.

199. Poh, C.K., et al., *Nonintrusive Characterization Of Fluid Transport Phenomena In Hollow-Fiber Membrane Using MRI: An Innovative Experimental Approach*. Membrane Science and Technology Volume 8, 2003, Pages 89–122, 2003.
200. Zhang, H., B. Wu, and D.C.e. al, *Grup III Nitride Vapor Growth Systems: Modeling and Experiments*. Nova Science Publishers, Inc., 2006.
201. Rouquerol, F.R., J. and K. Sing, *Adsorption by Powders and Porous Solids: Principles, Methodology and Applications*. 1999.
202. Wang, L.W., et al., *Study of the performance of activated carbon–methanol adsorption systems concerning heat and mass transfer*. Applied Thermal Engineering, 2003. **23**(13): p. 1605-1617.
203. Suryawan, B., *Karakteristik Zeolit Indonesia Sebagai Adsorben Uap Air*. Fakultas Teknik Universitas Indonesia - Jakarta Indonesia, 2004.
204. Pamungkas, N.S., *Proses Perbaikan Sistem Pendingin Dengan Sistem Adsorpsi Menggunakan Karbon Aktif dan Metanol Sebagai Refrigeran*. Universitas Indonesia, Jakarta, Indonesia, 2007.
205. Jaroniec, M., *Adsorption On Heterogeneous Surfaces: The Exponential Equation For The Overall Adsorption Isotherm*. Surface Science 50 (1975) 553-564 North-Holland Publishing Company, 1975.
206. Levant, M.D. and T. Vermeulen, *Binary Langmuir and Freundlich Isotherms for Ideal Adsorbed Solutions*. J. Phys. Chem. 1901, 85, 3247-3250, 1981.
207. Antczak, G. and G. Ehrlich, *Jump processes in surface diffusion*. Elsevier Gulf, 2007. **Volume 62**(Issue 2): p. 39–61.
208. Aoki, K., P. Charrier, and P. Degond, *A Hierarchy of Models Related to Nanoflows and Surface Diffusion*. AIMS Journal 2000.
209. Masel, R.I., *Principles of Adsorption and Reaction on Solid Surfaces*. 1996.
210. Tan, K.H., *Principles of Soil Chemistry, 3rd Ed*. Marcel Dekker. Inc. New York, 1998.
211. Essington, M.E., *Soil and Water Chemistry: An Integrated Approach*. CRC Press: Boca Raton, FL, 2004.
212. Sparks, D.L., *Environmental Soil Chemistry, 2nd Ed*. Academic Press: San Diego, 2003.
213. Koperman, R., *Fractal Reaction Kinetics* Science, 1988.
214. Sips, R., *On the Structure of a Catalyst Surface* Chemical Physics, 1948. **16**.
215. Thomas, J.M. and W.J. Thomas, *Introduction to the Principles of Heterogeneous Catalysis*. Academic Press: London, 1967.
216. Sposito, G., *Derivation of the Freundlich Equation for Ion Exchange Reactions in Soils*. Soil Science Society of America, 1980.
217. Yang, C., *Statistical Mechanical Study on the Freundlich Isotherm Equation*. J Colloid Interface Sci., 1998.
218. Liu, Y., H. Xu, and J. Tay, *Derivation of a General Adsorption Isotherm Model*. J. Environ. Eng. 131(10), 1466–1468, 2005.
219. Sparks, D.L., *Kinetics of Soil Chemical Process*. Academic Press: San Diego, 1989.
220. MD, L. and V. T., *Binary Langmuir-like and Freundlich isotherms for ideal adsorbed solutions*. J Phys Chem. 1981, 1981(85): p. 3247–3250.
221. Zhang, H., et al., *Non-Equilibrium Adsorption and Precipitation of Scale Inhibitors: Corefloods and Mathematical Modelling*. 2000.

- 
222. Brigham, W.E., *Mixing Equations in Short Laboratory Cores*. SPE Journal, 1974. **14**: p. 91-99.
223. Mattiussi, C., *The Finite Volume, Finite Element, and Finite Difference Methods as Numerical Methods for Physical Field Problems*. NUMERICAL METHODS FOR PHYSICAL FIELD PROBLEMS 2000.
224. Versteeg, H.K. and W. Malalasekera, *An Introduction to Computational Fluid Dynamic - The Finite Volume Method*. Longman Scientific & Technical, 1995.
225. Zuo, W., *Introduction of Computational Fluid Dynamics*. JASS 05, St. Petersburg, FAU Erlangen-Nürnberg, 2005.
226. Burnett, D.S., *Finite Element Analysis: From Concepts to Applications*. 1988.
227. Sayas, F.J., *A gentle introduction to the Finite Element Method*. 2008.
228. Brenner, S.C. and L.R. Scott, *The mathematical theory of finite element methods, 2nd ed.* . Springer, 2002.
229. Ivan, C.D., F.B. Growcock, and J.E. Friedheim, *Chemical and Physical Characterization of Aphron-Based Drilling Fluids* SPE 77445 2002.
230. He, S., A. Kan, and M. Tomson, *Inhibition of Mineral Scale Precipitation by Polymers*, in *Water Soluble Polymers*, Z. Amjad, Editor. 2002, Springer US. p. 163-171.
231. Neville, A., et al., *Using electrochemical pre-treatments for the protection of metal surfaces from the formation and growth of calcium carbonate scale* Chemistry in the Oil Industry VII: Performance in a Challenging Environment, 2002. **p. 131-143**.
232. PTS-Laboratories-Inc, *Greenzyme Flood Summary - Greenzyme - Brazilian Crude Oil*. PTS Labs Core Analysis Services, 2005.
233. [http://www.engineeringtoolbox.com/water-thermal-properties-d\\_162.html](http://www.engineeringtoolbox.com/water-thermal-properties-d_162.html).
234. Mid-South-Chemical, *ACUMER™ 4161 - Phosphinopolycarboxylic Acid scale inhibitor and dispersant for water treatment*.
235. Clennell, B., *M. In Developments in Petrophysics;* . Geological Society Special Publication, 1997. **122**: p. 299.
236. Bouchet, R., et al., *Separation of Bulk, Surface, and Topological Contributions to the Conductivity of Suspensions of Porous Particles*. Journal of Physical Chemistry, 2012.
237. O'Connell, B.M., T.M. McGloughlin, and M.T. Walsh, *Factors that affect mass transport from drug eluting stents into the artery wall*. 2010.
238. Dullien, F.A., *Porous Media: Fluid Transport and Pore Structure*. Academic Press: San Diego, 1992.
239. Saripall, K.P., et al., *Prediction of diffusion coefficients in porous media using tortuosity factors based on interfacial areas*. Ground Water, 2002. **40(4)**: p. 346-52.
240. Yun, J., et al., *Rapid freezing cryo-polymerization and microchannel liquid-flow focusing for cryogel beads: Adsorbent preparation and characterization of supermacroporous bead-packed bed*. Journal of Chromatography A, 2013. **1284**: p. 148-154.
241. Pisani, L., *Simple Expression for the Tortuosity of Porous Media*. Transport in Porous Media, 2011. **88(2)**: p. 193-203.
242. Glossary, S.O., *Tortuosity*. <http://www.glossary.oilfield.slb.com/en/Terms/t/tortuosity.aspx>, 2015.

- 
243. Tye, F.L., *Tortuosity*. Journal of Power Sources 9. pg. 89-100 Esvier Sequoia, 1983.
  244. Carman, P.C., *Flow of Gases Through Porous Media*. Butterworths Scientific Publications, London, 1956.
  245. Barrande, M., R. Bouchet, and R. Denoyel, *Tortuosity of Porous Particles*. Anal. Chem. 2007, 79, 9115-9121, 2007.
  246. Matyka, M. and Z. Koza, *How to Calculate Tortuosity Easily?* Physcs. fluidyn PACS:47.56.+r, 47.15.G-,90,60,Np, 2012.
  247. Ghanbarian, B., et al., *Tortuosity in Porous Media: A Critical Review*. Soil Sci. Soc. Am. J., 2013. **77**(5): p. 1461-1477.
  248. Sahimi, M. and S. Arbabi, *Mechanics of disordered solids. III. Fracture properties*. Phys. Rev. B 47, 1993. **47**: p. 713.
  249. Barabasi, A.-L. and H. Stanley, *Fractal Concepts in Surface Growth*. Cambridge University, Cambridge, England, 1995.
  250. Banhart, J., *Manufacture, characterisation and application of cellular metals and metal foams*. Progress in Materials Science, 2001. **46**: p. 559-632.
  251. Anglaret, E., A. Hasmy, and R. Jullien, *Effect of Container Size on Gelation Time: Experiments and Simulations*. Physical Review Letters, 1995. **75**(22): p. 4059-4062.
  252. Coleman, S.W. and J.C. Vassilicos, *Tortuosity of unsaturated porous fractal materials*. Physical Review E 78, 2008. **016308**.
  253. Moffatt, H.K., *Viscous and resistive eddies near a sharp corner*. Journal of Fluid Mechanics, 1964. **18**: p. 1-18.
  254. Parry, A.O., P.S. Swain, and J.A. Fox, *Fluid adsorption at a non-planar wall: roughness-induced first-order wetting*. J. Phys.: Condens. Matter 8, 1996.
  255. Nabesawa, H., et al., *Polymer surface morphology control by reactive ion etching for microfluidic devices*. Sensors and Actuators B: Chemical, 2008. **132**(2): p. 637-643.
  256. Tsougeni, K., et al., *Controlled protein adsorption on microfluidic channels with engineered roughness and wettability*. Sensors and Actuators B: Chemical, 2012. **161**(1): p. 216-222.
  257. Filippova, N., *Non-Langmuir Adsorption on Planar Surfaces: Nonlinear Theory and Experiment*. J Colloid Interface Sci., 1997. **195**(1)(203-215).
  258. Scopelliti, P.E., et al., *The Effect of Surface Nanometre-Scale Morphology on Protein Adsorption*. PLoS ONE, 2010. **5**(7): p. e11862.
  259. Stroock, A.D., et al., *Patterning Flows Using Grooved Surfaces*. Anal. Chem., 2002. **74**: p. 5306-5312.
  260. Aubin, J., D.F. Fletcher, and C. Xuereb, *Design of Micromixer Using CFD Modelling*. Chemical Engineering Science, 2005. **60**(8-9): p. 2503-2516.
  261. Ansari, M.A. and K.-Y. Kim, *Shape Optimization of A Micromixer with Staggered Herringbone Groove*. Chemical Engineering Science, 2007. **62**(23): p. 6687-6695.
  262. Yun, S., et al., *Geometric Effect on Lateral Transport Induced by Slanted Grooves in Microchannel at A Low Reynolds Number*. Elsevier, 2013.
  263. Hossain, S., A. Husain, and K.-Y. Kim, *Optimization of Micromixer with Staggered Herringbone Grooves on Top and Bottom Walls*. Engineering Application of Computational Fluid Mechanic, 2011. **5**(4): p. 506-516.

- 
264. Plentovich, E.B., R.L. Stallings Jr., and M.B. Tracy, *Experimental Cavity Pressure Measurements at Subsonic and Transonic Speeds*. NASA TP-3358, 1993.
  265. Rockwell, D. and E. Naudascher, *Review – Self-Sustaining Oscillations of Flow Past Cavities*. *Journal of Fluid Engineering*, 1978. **Vol. 100**(No. 2): p. pp. 152-155.
  266. Zhang, S., R.E. Klimentidis, and P. Barthelemy, *Porosity and permeability analysis on nanoscale FIB-SEM 3D imaging of shale rock*. International Symposium of the Society of Core Analysts held in Austin, Texas, USA 18-21 September, 2011 2011.
  267. Dang, T.Q.C., et al., *Investigation of Isotherm Polymer Adsorption in Porous Media*. *Petroleum Science and Technology*, 2014. **32**(1626-1640).
  268. Lecoanet, H.F., J.-Y. Bottero, and M.R. Wiesner, *Laboratory Assessment of the Mobility of Nanomaterials in Porous Media*. *Environmental Science & Technology*, 2004. **38**(19): p. 5164-5169.

---

## APPENDIX A

Following sequence of a typical scale inhibitor squeeze procedure is listed below [100, 107]:

1. Pouring acid to clean scale and debris out of the wellbore.
2. Injecting a demulsifier or surfactant to increase the water wetness of the formation, and also improve injectivity. This is also known as the “spearhead” package.
3. Injecting a pre-flush that already contains inhibitor. The purpose is to push the spearhead and to cool down the surrounding area of the wellbore.
4. Injecting the main scale-inhibitor treatment (pill)
5. Injection of an over flush in order to push the main scale-inhibitor treatment solution to the designated depth and deep into the formation.
6. Well shut-in period to soak the formation for about 6-24 hours. In this period the inhibitor is to be adsorb/precipitate on to the rock surface.
7. Re-opening the well to let it back into production.

A scale squeeze treatment should contain fluid packages as below [105]:

1. Mutual solvent preflush, to avoid risk of sludge formation
2. Demulsifier, to prevent possible emulsion generated
3. Spacer of fresh water, to isolate different fluid solution
4. Surfactant, as a cleaning agent for the tubing and the well bore. They also said that surfactant might hinder any oily deposits from pushing into formation and affect the squeeze performance on rock matrix
5. Scale inhibitor, as the main treatment (pill)
6. Over flush with fresh water to push to inhibitor to the designated scaling location
7. Displacements, normally diesel is used to assist unloading the well after shut in period
8. Shut in time for better adsorption/desorption profile.

It is important to carefully observe in timely basis the return 'waste' concentration of the inhibitor as an indication if the scale problem has been managed effectively. Sample collection follows the procedure below:

1. One sample every  $\frac{1}{2}$  hour for the first 12 hours
2. One sample every 1 hour for the next 24 hours
3. 3 samples daily for the next three days
4. as the end point, a daily sample

## APPENDIX B

This section shows the results of the sensitivity study the parameters in the adsorption isotherm equation parameter used in Chapter 4 in order to obtain suitable adsorption equation that satisfy the experimental result. The first subsection displays the results for the Langmuir adsorption isotherm equation for a 2D microchannel geometry, the second one is for the modified Freundlich adsorption isotherm for a 2D microchannel geometry, and the third one is the modified Freundlich adsorption isotherm for a 3D axis-symmetric microchannel geometry.

### 1. Langmuir Adsorption Isotherm for 2D microchannel geometry

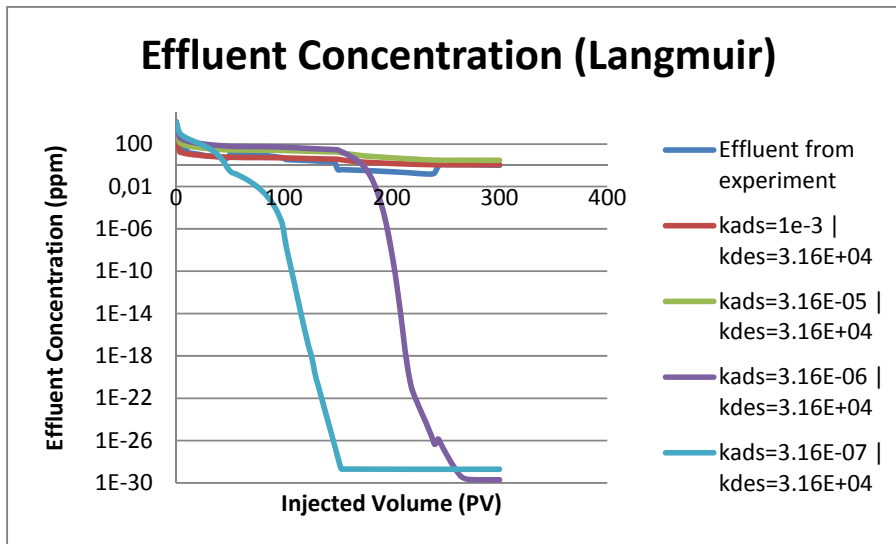


**Figure B.0.1** : Post flush effluent concentration vs injection volume for different  $k_{ids}$  between  $1 \times 10^{-3}$  and  $3.16 \times 10^{-7}$  for constant value of  $k_{ids}$   $3.16 \times 10^4$  (Langmuir Adsorption Isotherm)

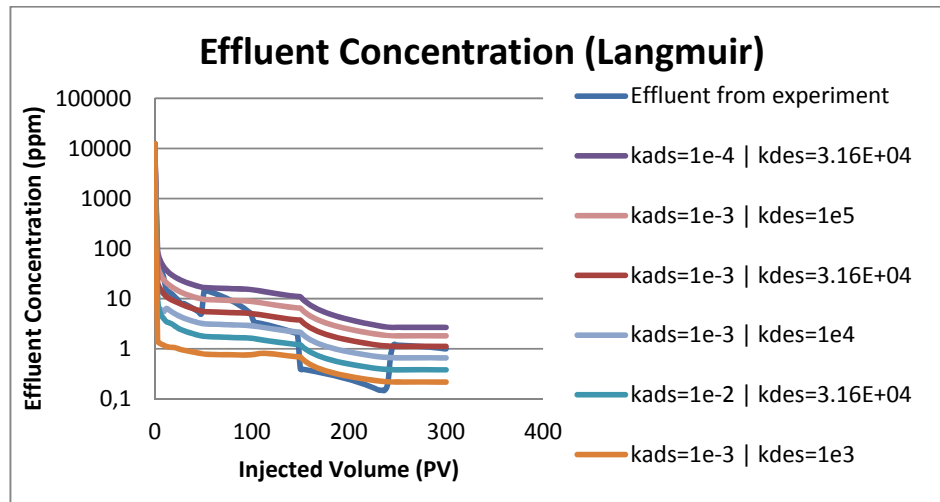


**Figure B.0.2:** Post flush effluent concentration vs injection volume for various  $k_{ads}$  and  $k_{des}$  (Langmuir Adsorption Isotherm)

## 2. Freundlich Adsorption Isotherm for 2D microchannel geometry

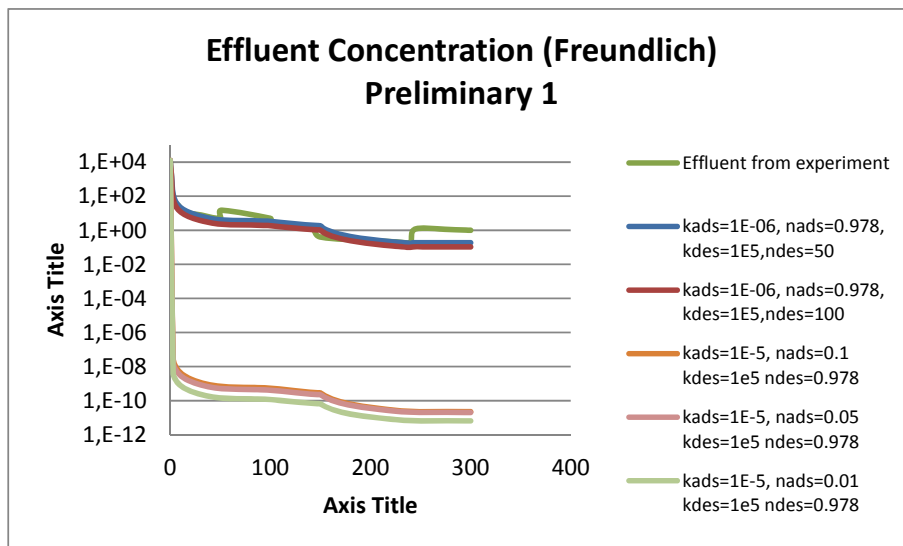


**Figure B.0.3:** Post flush effluent concentration vs injection volume for various  $k_{ads}$ ,  $n_{ads}$ ,  $k_{des}$ , and  $n_{des}$ . Preliminary study 1 (Freundlich Adsorption Isotherm)

It is challenging to find a Freundlich adsorption isotherm equation that satisfies the effluent concentration result from the laboratory experiment because the equation has four governing variables, i.e.  $k_{ads}$ ,  $n_{ads}$ ,  $k_{des}$ , and  $n_{des}$ . Therefore a preliminary study was conducted to investigate

range of those variables that near to the best fit to the experimental results. The effluent concentrations for the preliminary study are shown in Figure B3, B4, and B5.

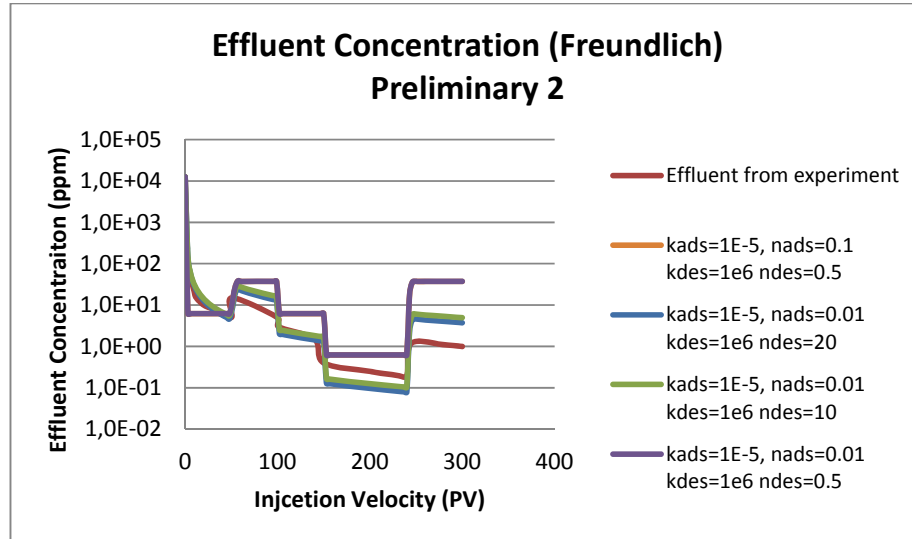


**Figure B.0.4:** Post flush effluent concentration vs injection volume for various  $k_{ads}$  and constant  $n_{ads}$ ,  $k_{des}$ , and  $n_{des}$ . Preliminary study 2 (Freundlich Adsorption Isotherm)

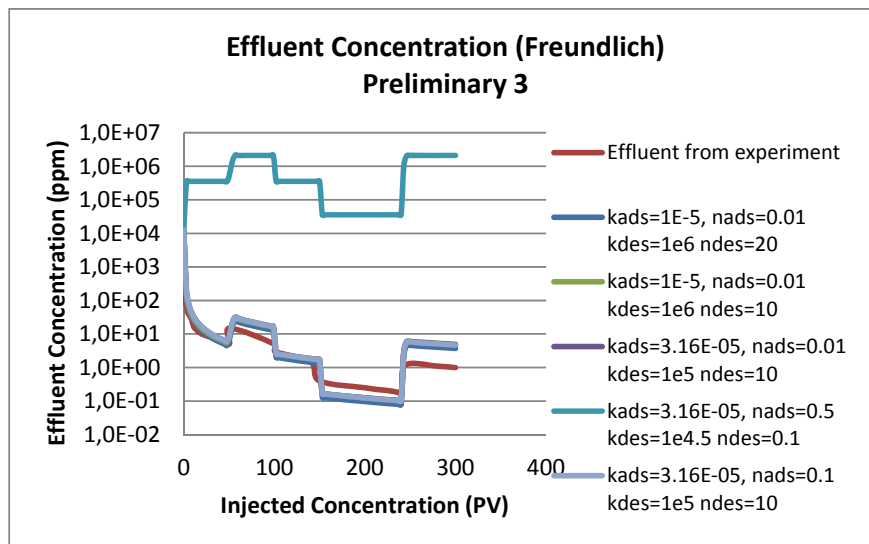


**Figure B.0.5:** Post flush effluent concentration vs injection volume for various  $k_{ads}$ ,  $n_{ads}$ ,  $k_{des}$ , and  $n_{des}$ . Preliminary study 3 (Freundlich Adsorption Isotherm)

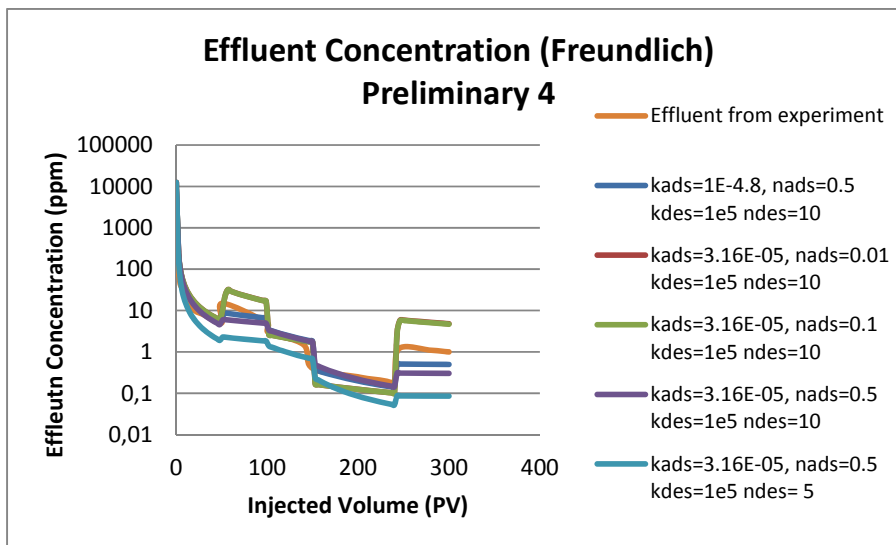


**Figure B.0.6:** Post flush effluent concentration vs injection volume for various  $k_{ads}$ ,  $n_{ads}$ ,  $k_{des}$ , and  $n_{des}$ . Preliminary study 4 (Freundlich Adsorption Isotherm)

Afterwards, it was found the range for the  $k_{ads}$  and the  $k_{des}$  for the best fit against the experiment results are  $3.16 \times 10^{-4}$  and  $3.16 \times 10^4$  respectively. Thorough investigation around these numbers with combination of various  $n_{ads}$  and  $n_{des}$  was conducted. The results for  $k_{ads}$  sensitivity are shown in Figure B.7 and Figure B.8. The results for  $k_{des}$  sensitivity are shown in Figure B.9. The results for  $n_{ads}$  sensitivity are shown in Figure B.10. The results for  $n_{des}$  sensitivity are shown in Figure, B.11, B.12, B.13 and B.14 below.

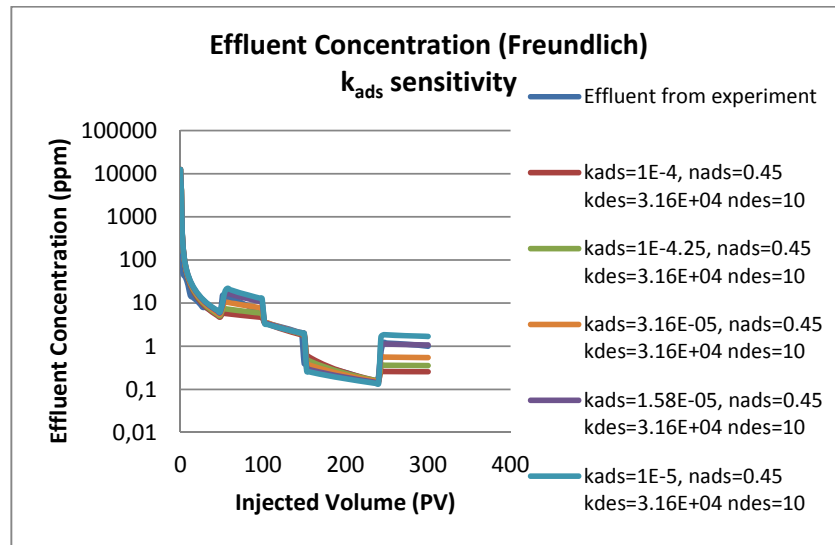


**Figure B.0.7:** Post flush effluent concentration vs injection volume for various  $k_{ads}$  sensitivity (Freundlich Adsorption Isotherm)

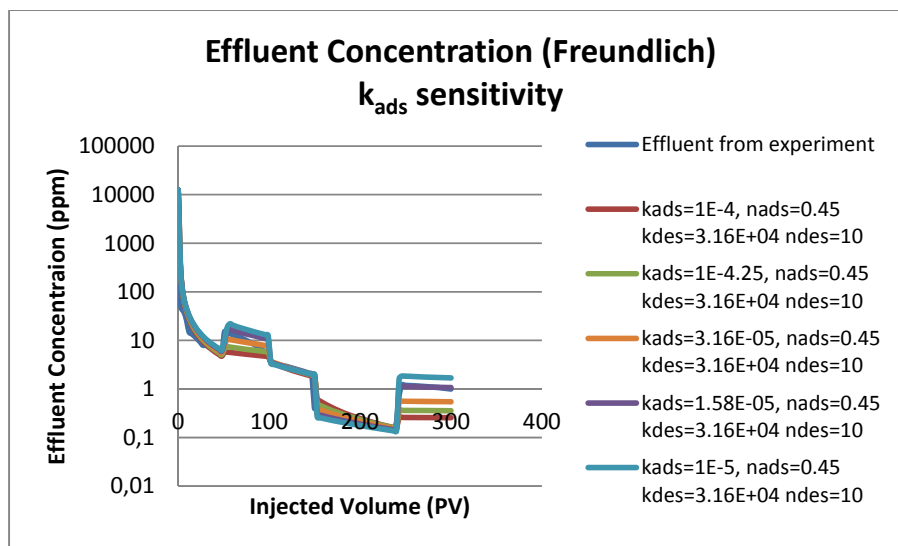


**Figure B.0.8:** Post flush effluent concentration vs injection volume for various  $k_{ads}$  sensitivity (Freundlich Adsorption Isotherm)

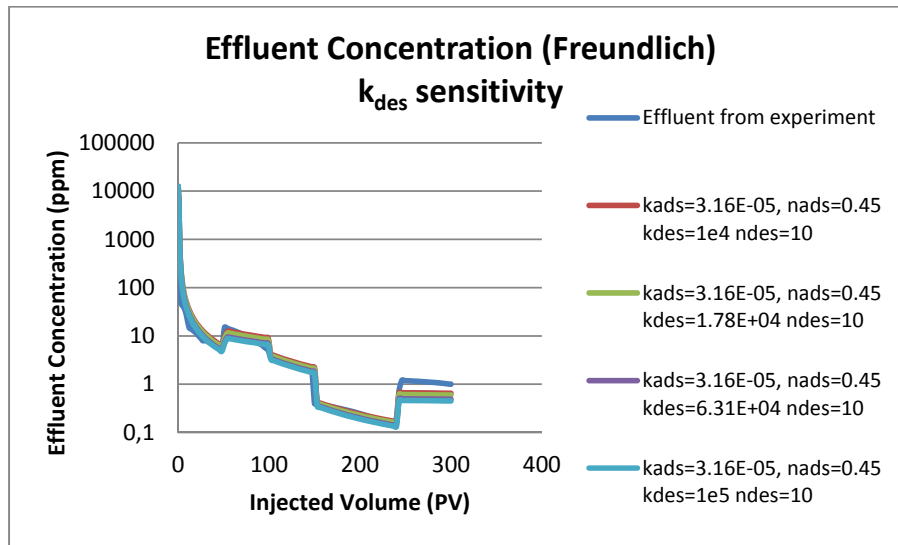


**Figure B.0.9:** Post flush effluent concentration vs injection volume for various  $k_{des}$  sensitivity (Freundlich Adsorption Isotherm)

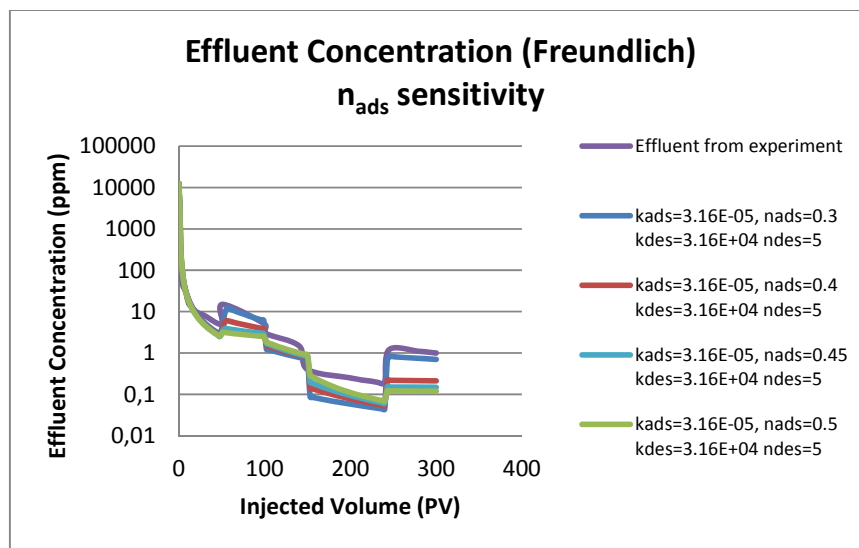


**Figure B.0.10:** Post flush effluent concentration vs injection volume for various  $n_{des}$  sensitivity (Freundlich Adsorption Isotherm)

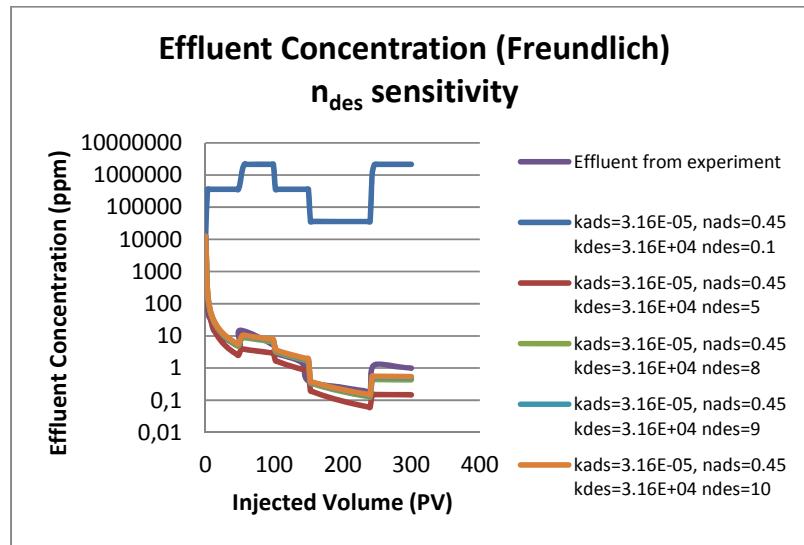


**Figure B.0.11:** Post flush effluent concentration vs injection volume for various  $n_{des}$  sensitivity (Freundlich Adsorption Isotherm)

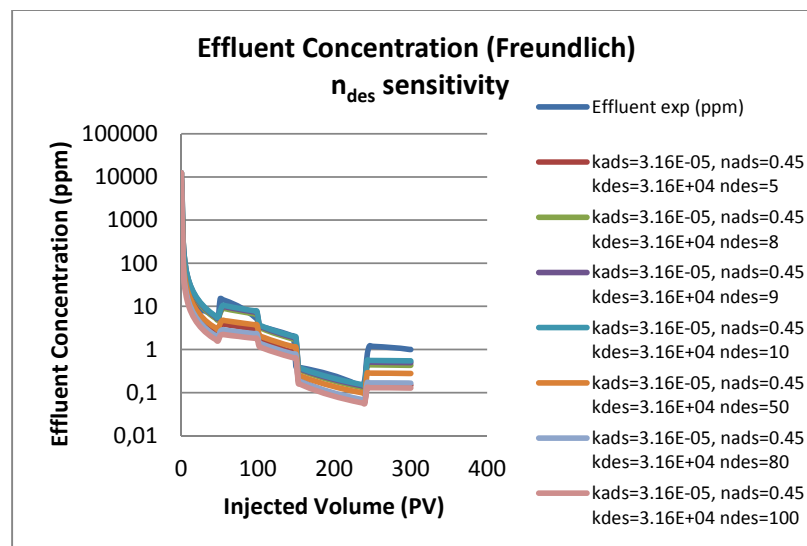


**Figure B.0.12:** Post flush effluent concentration vs injection volume for various  $n_{des}$  sensitivity (Freundlich Adsorption Isotherm)

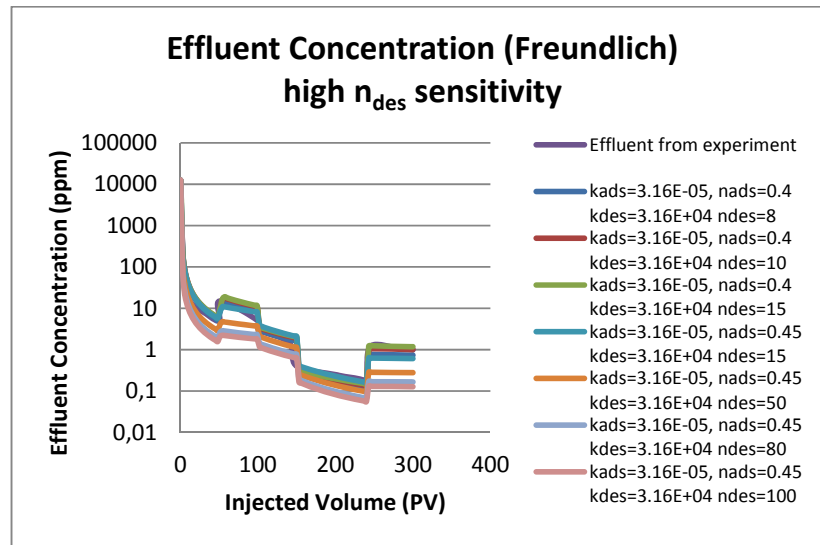


**Figure B.0.13:** Post flush effluent concentration vs injection volume for various high  $n_{des}$  sensitivity (Freundlich Adsorption Isotherm)

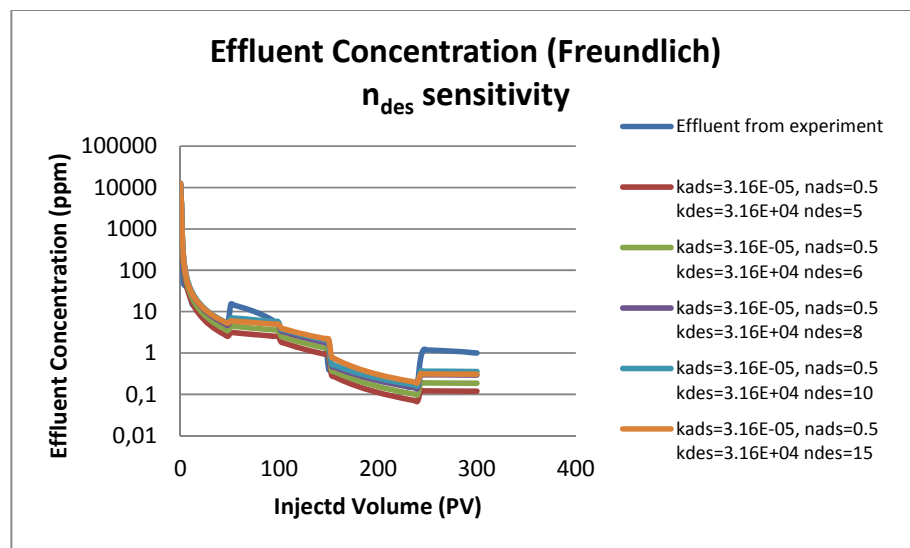


**Figure B.0.14:** Post flush effluent concentration vs injection volume for various high  $n_{des}$  sensitivity (Freundlich Adsorption Isotherm)

## **APPENDIX C-1**

The distribution profile of the injected nanoparticle concentration for various tortuous microchannels for continuous concentration injection.

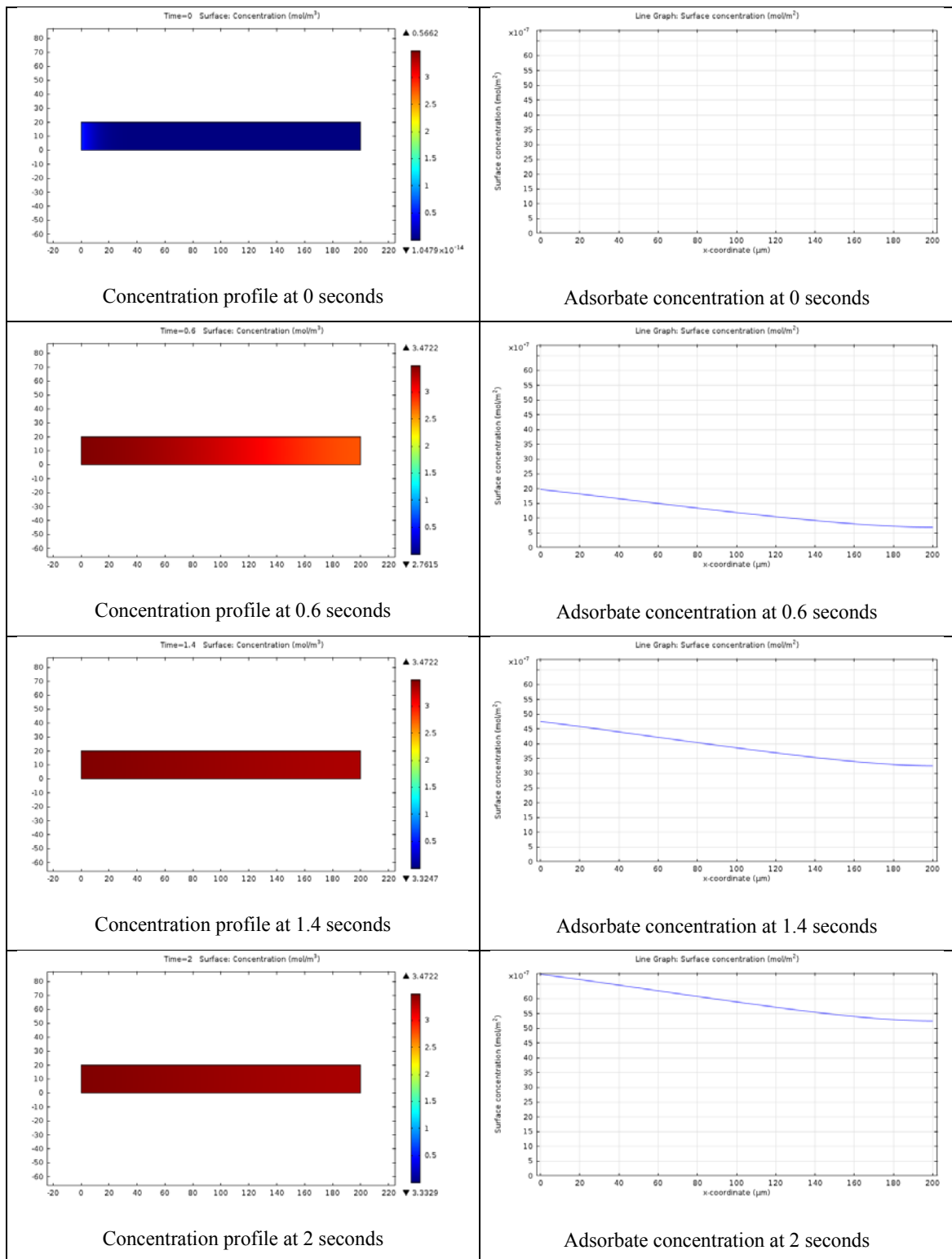


**Figure C-1.0.15** Concentration profile (left) and adsorbate concentration of the case of the continuous injection for time steps 0, 0.6, 1.4, and 2 seconds.

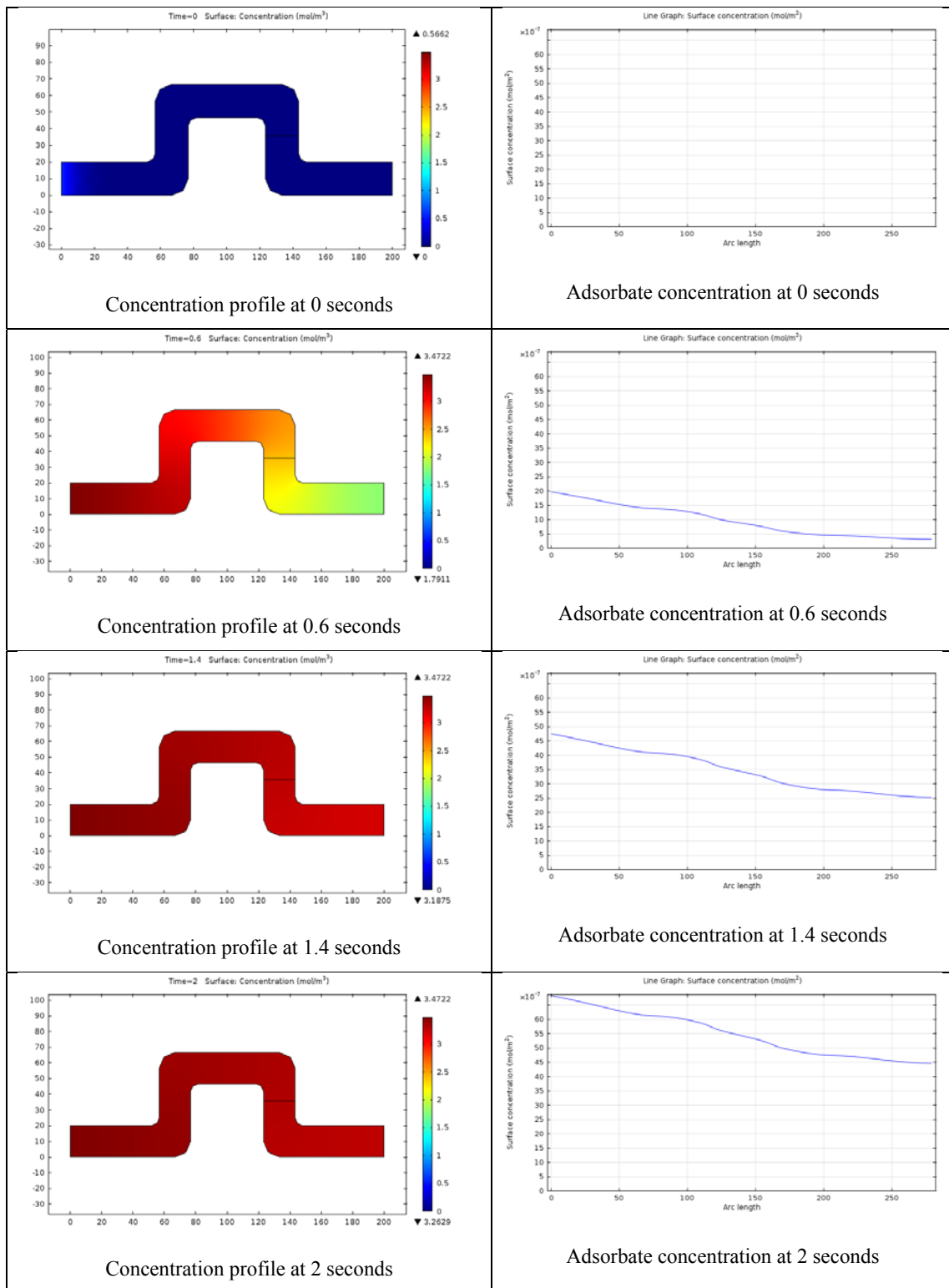


**Figure C-1.0.16** Concentration profile (left) and adsorbate concentration of the case of the continuous injection for time steps 0, 0.6, 1.4, and 2 seconds

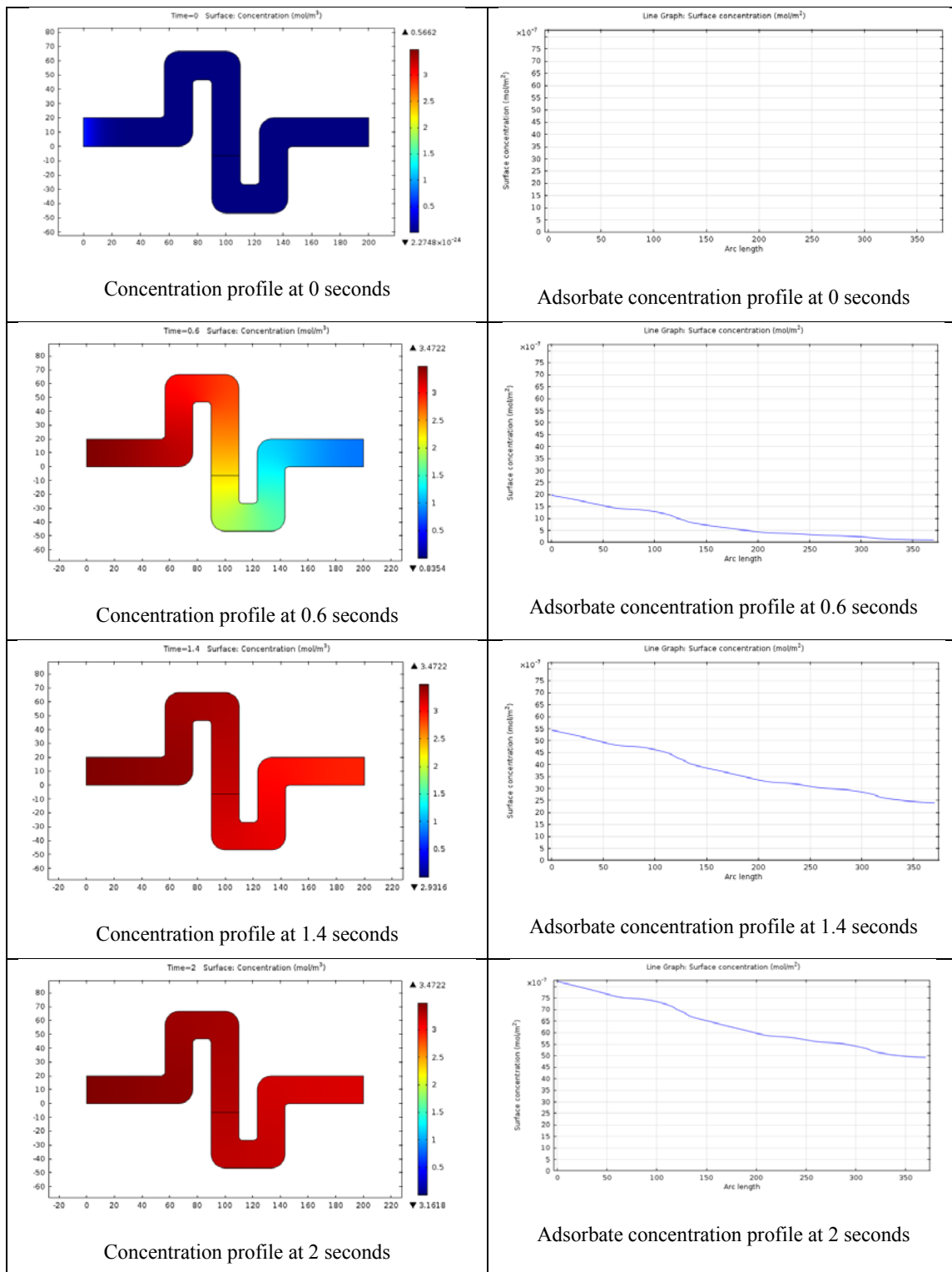


**Figure C-1.0.17** Concentration profile (left) and adsorbate concentration of the case of the continuous injection for time steps 0, 0.6, 1.4, and 2 seconds

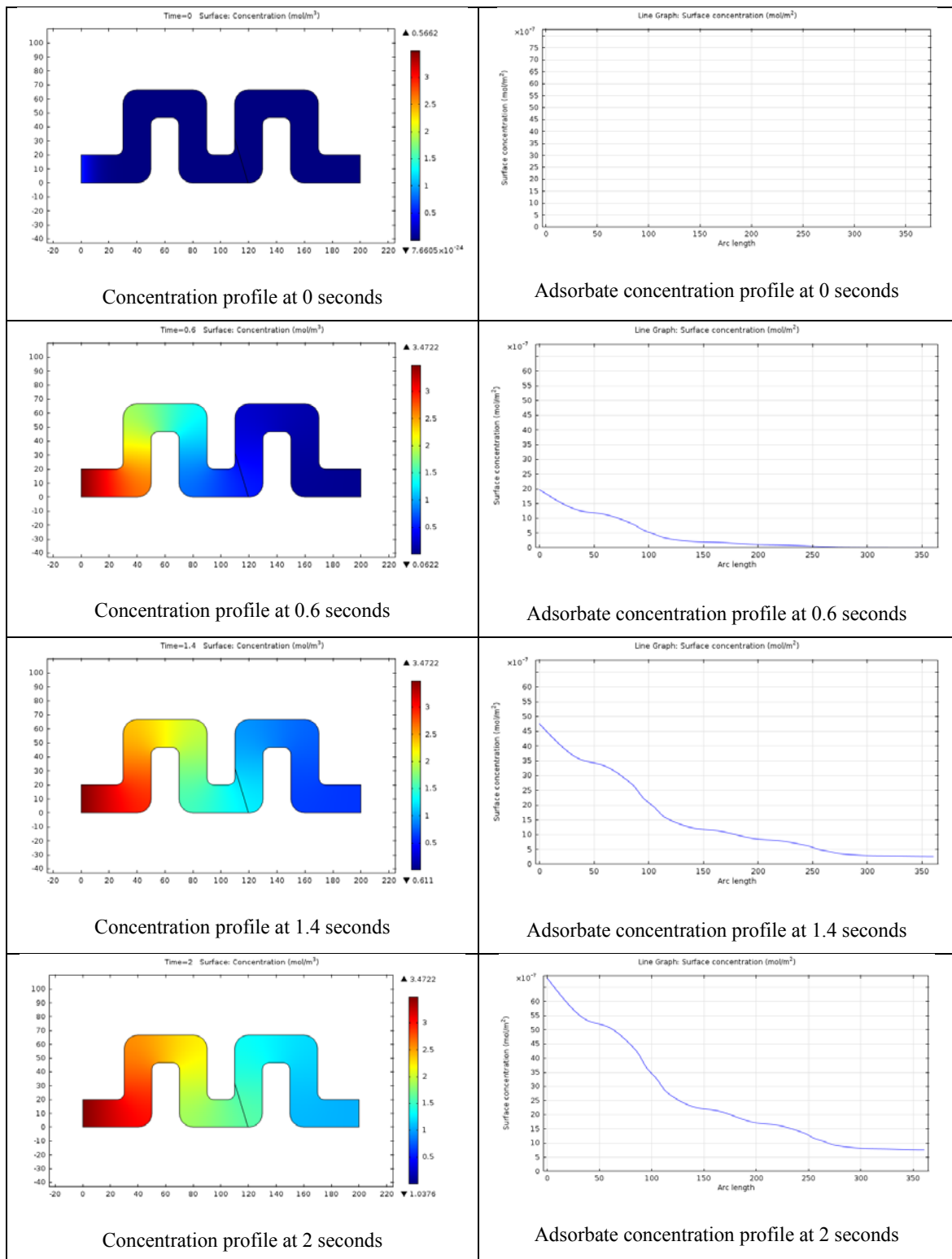


**Figure C-1.0.18** Concentration profile (left) and adsorbate concentration of the case of the continuous injection for time steps 0, 0.6, 1.4, and 2 seconds

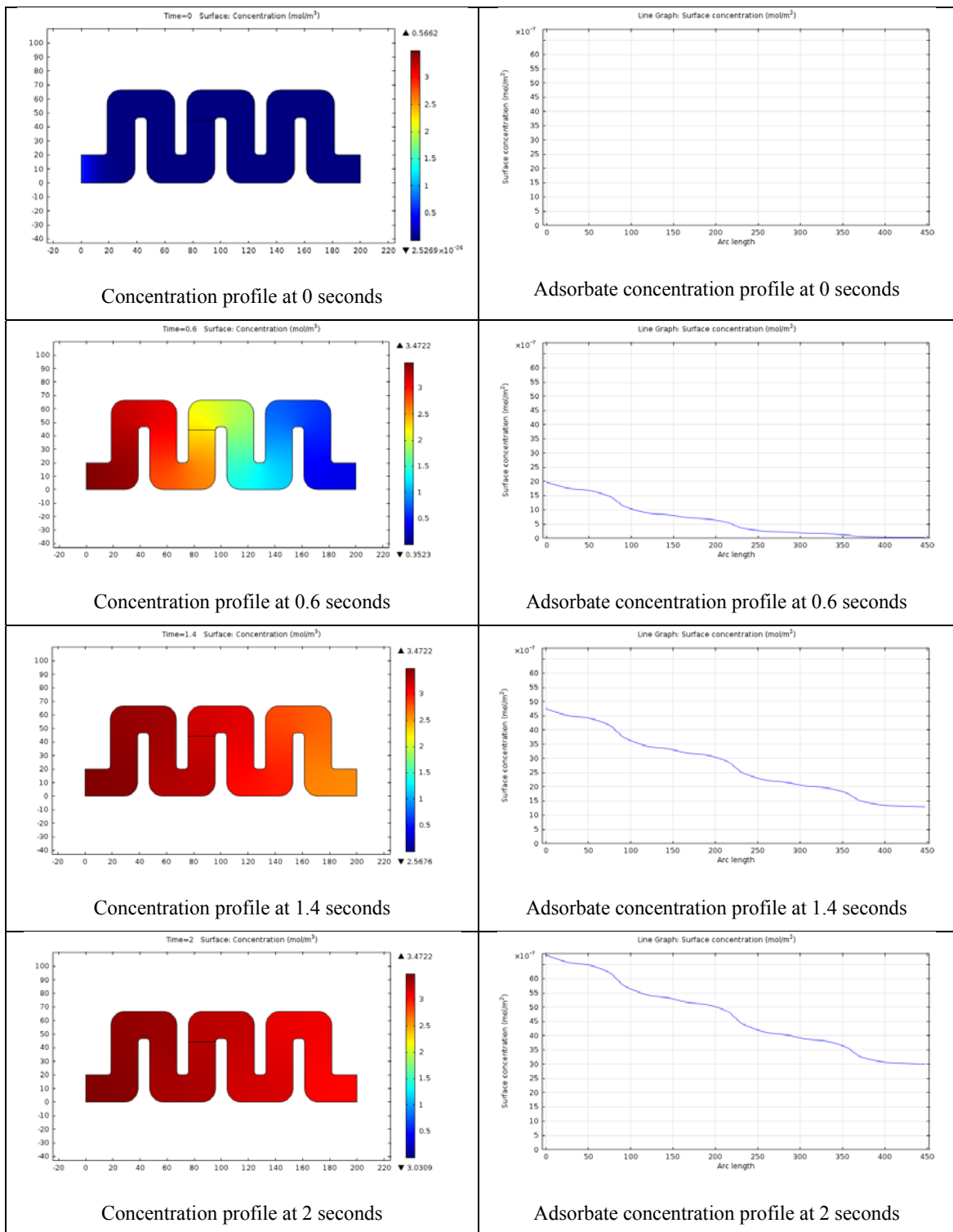


**Figure C-1.0.19** Concentration profile (left) and adsorbate concentration of the case of the continuous injection for time steps 0, 0.6, 1.4, and 2 seconds

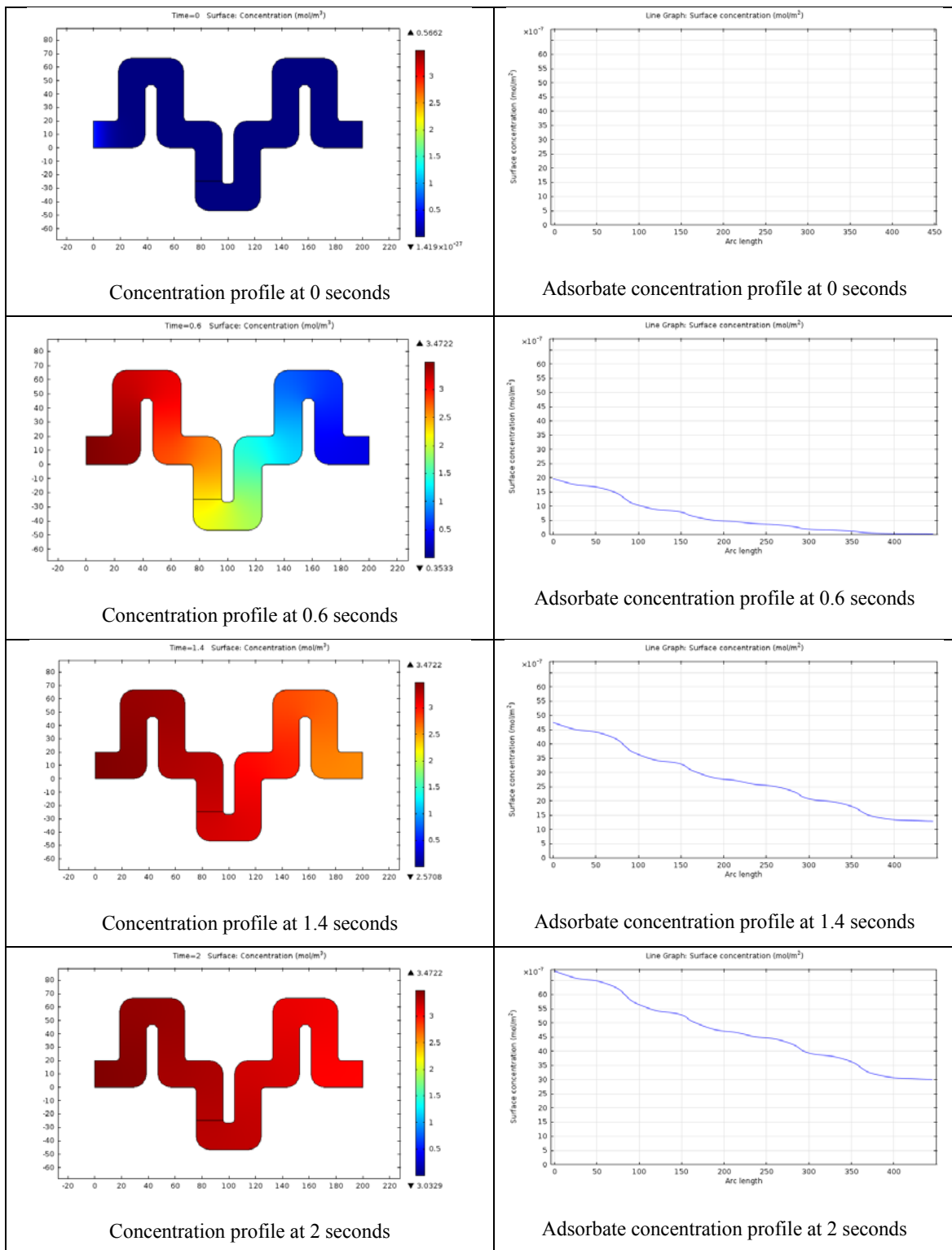


**Figure C-1.0.20** Concentration profile (left) and adsorbate concentration of the case of the continuous injection for time steps 0, 0.6, 1.4, and 2 seconds

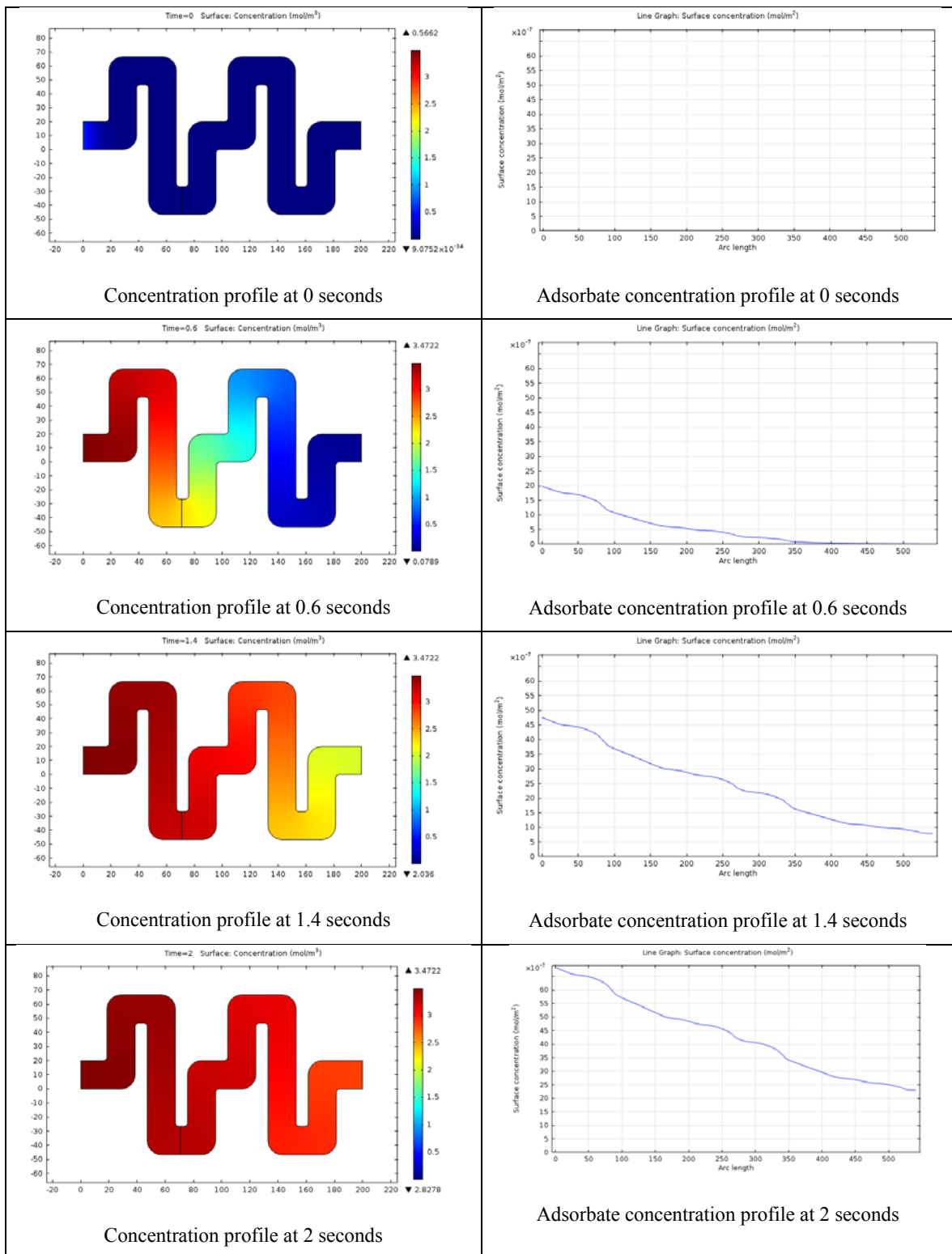


**Figure C-1.0.21** Concentration profile (left) and adsorbate concentration of the case of the continuous injection for time steps 0, 0.6, 1.4, and 2 seconds

## **APPENDIX C-2**

The distribution profile of the injected nanoparticle concentration for various tortuous microchannels for discontinuous concentration injection

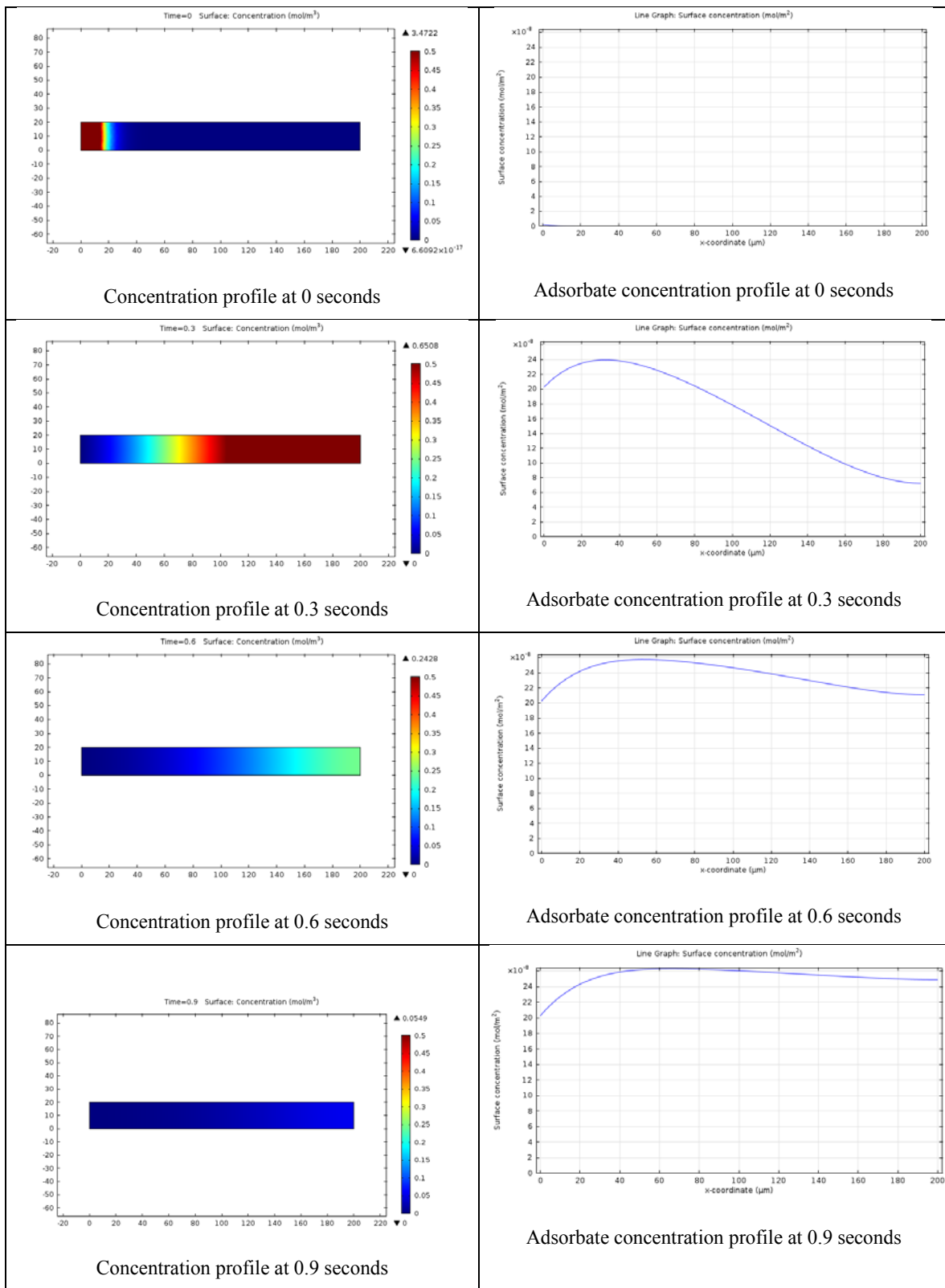


**Figure C-2.0.22** Concentration profile (left) and adsorbate concentration of the case of the discontinuous injection for time steps 0, 0.3, 0.6, and 0.9 seconds

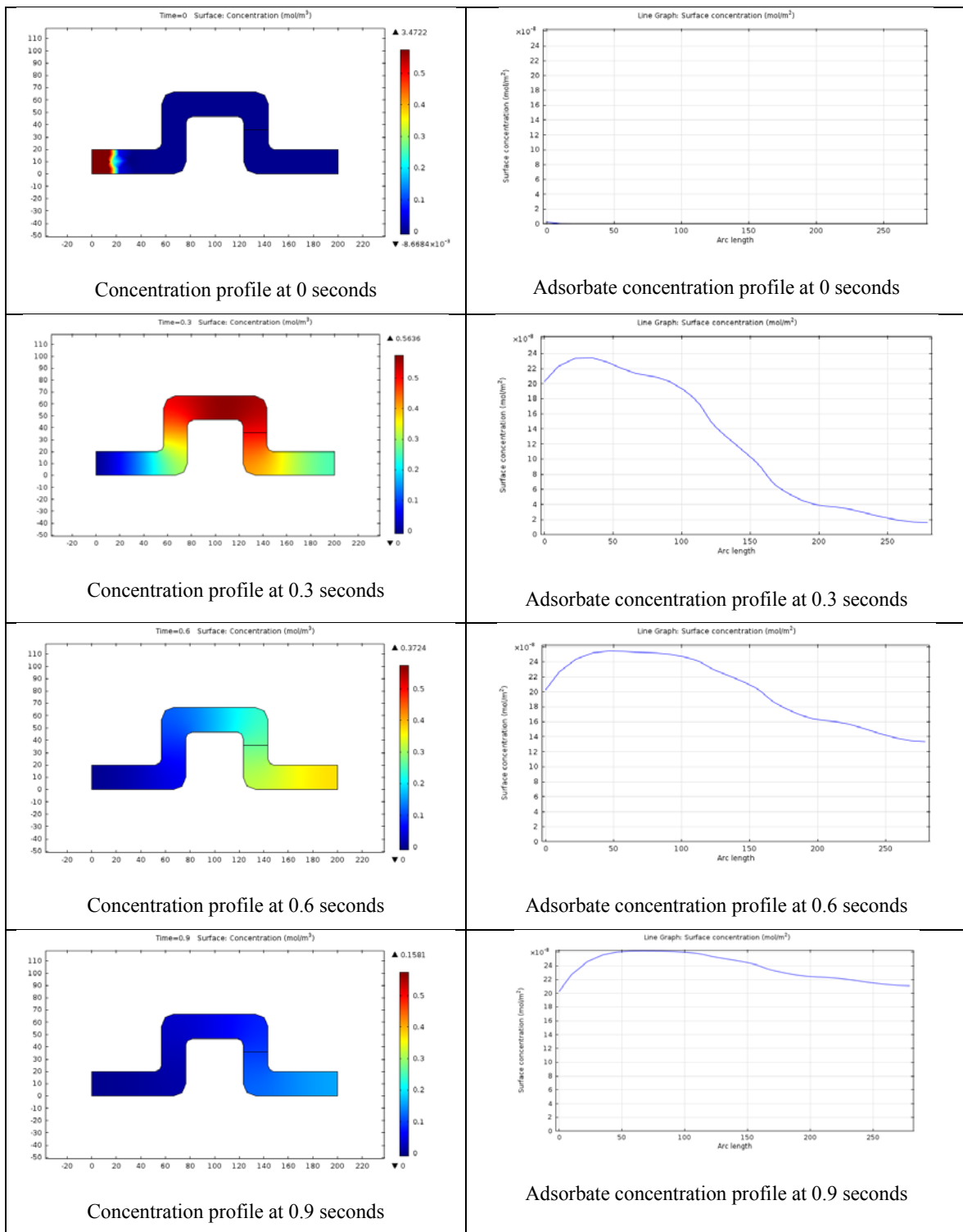


**Figure C-2.0.23** Concentration profile (left) and adsorbate concentration of the case of the discontinuous injection for time steps 0, 0.3, 0.6, and 0.9 seconds

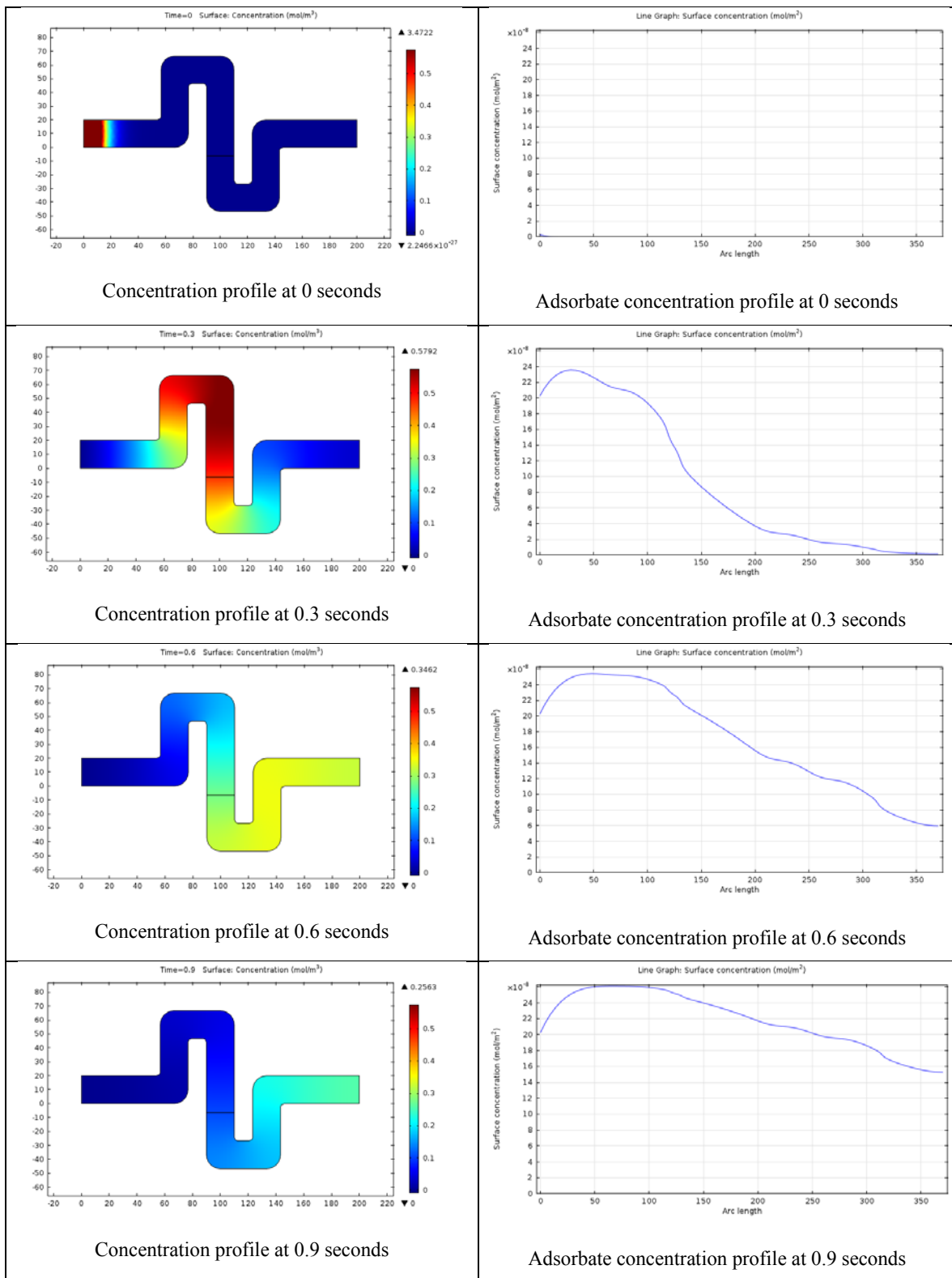


**Figure C-2.0.24** Concentration profile (left) and adsorbate concentration of the case of the discontinuous injection for time steps 0, 0.3, 0.6, and 0.9 seconds

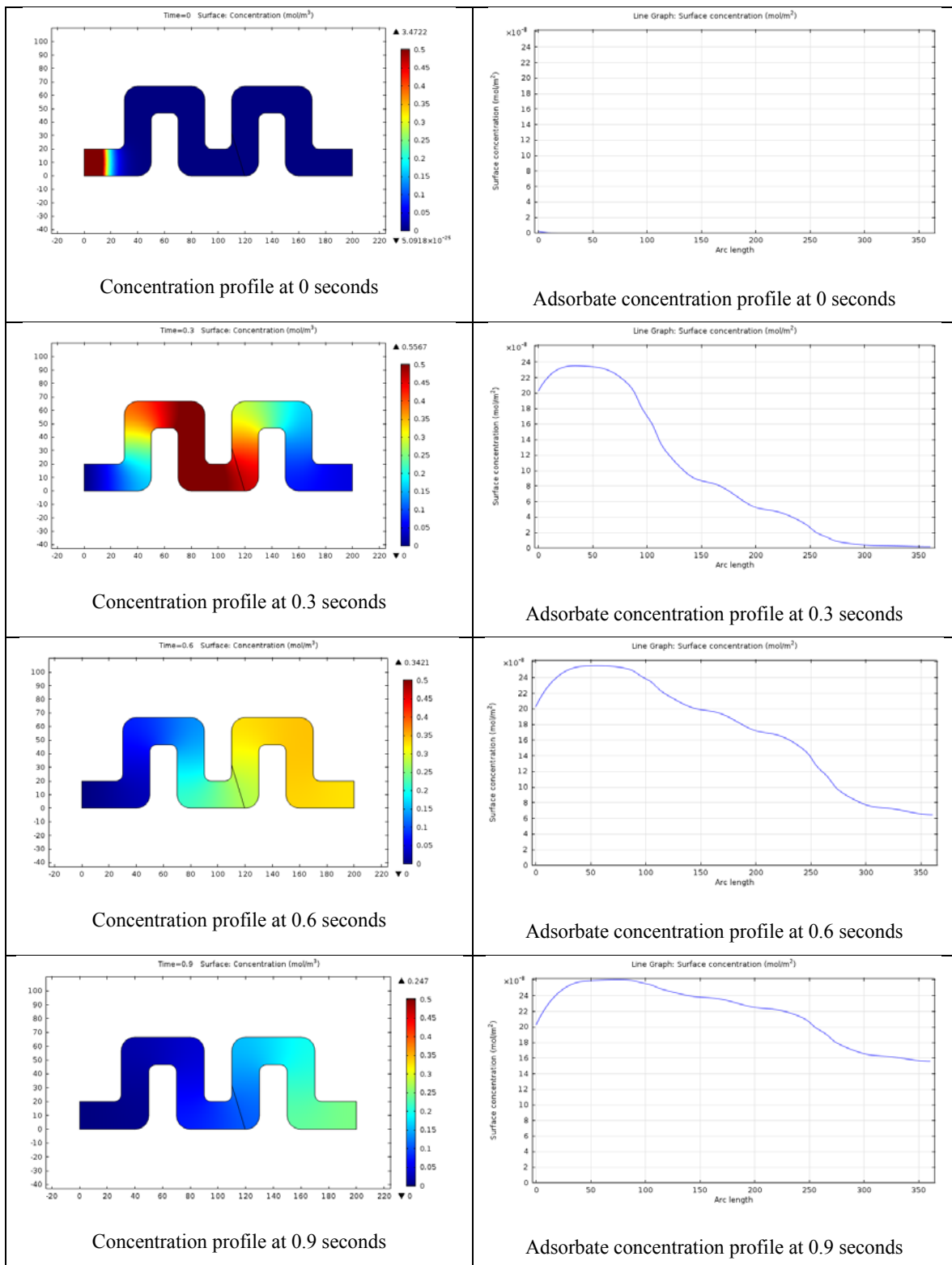


**Figure C-2.0.25** Concentration profile (left) and adsorbate concentration of the case of the discontinuous injection for time steps 0, 0.3, 0.6, and 0.9 seconds

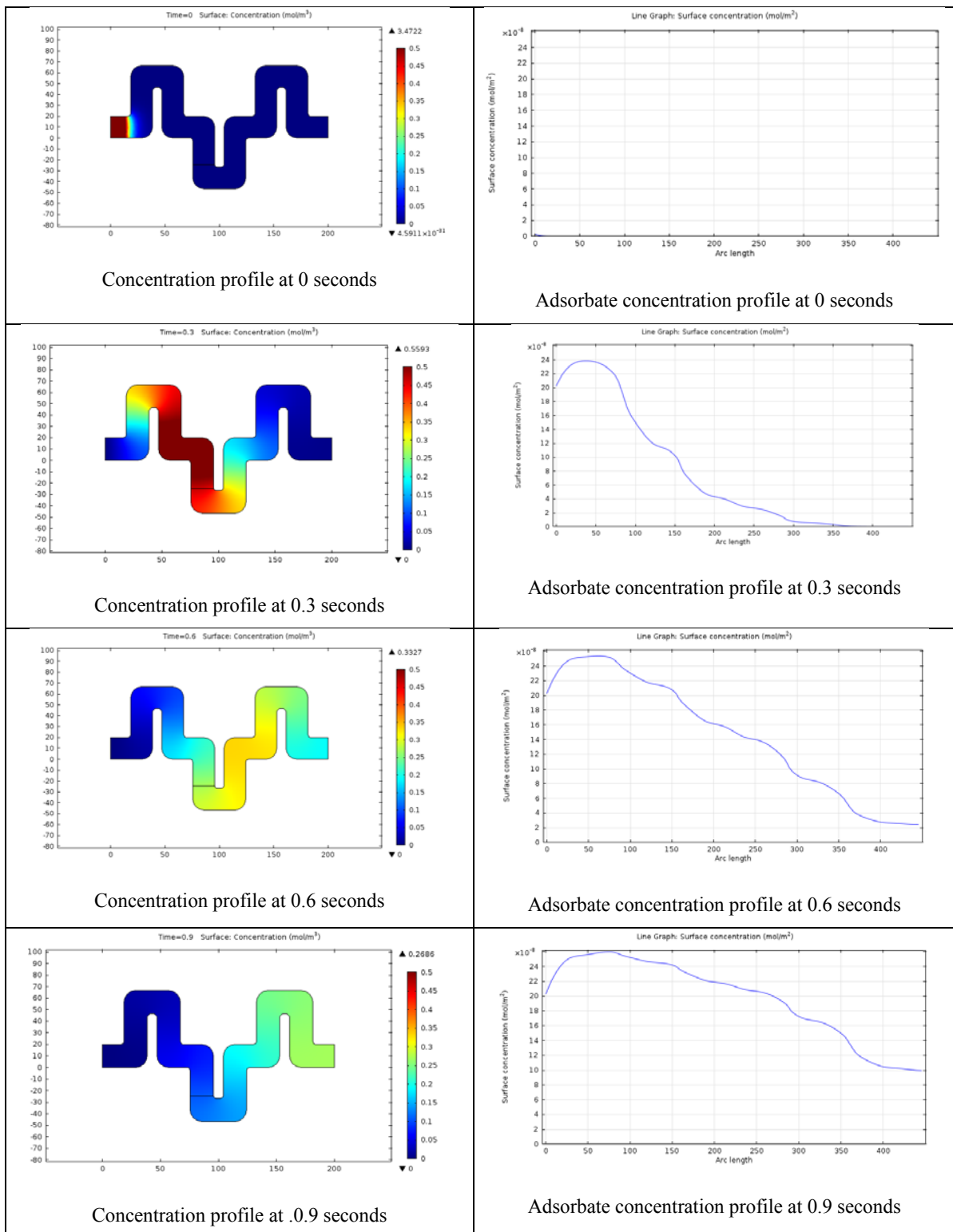


**Figure C-2.0.26** Concentration profile (left) and adsorbate concentration of the case of the discontinuous injection for time steps 0, 0.3, 0.6, and 0.9 seconds

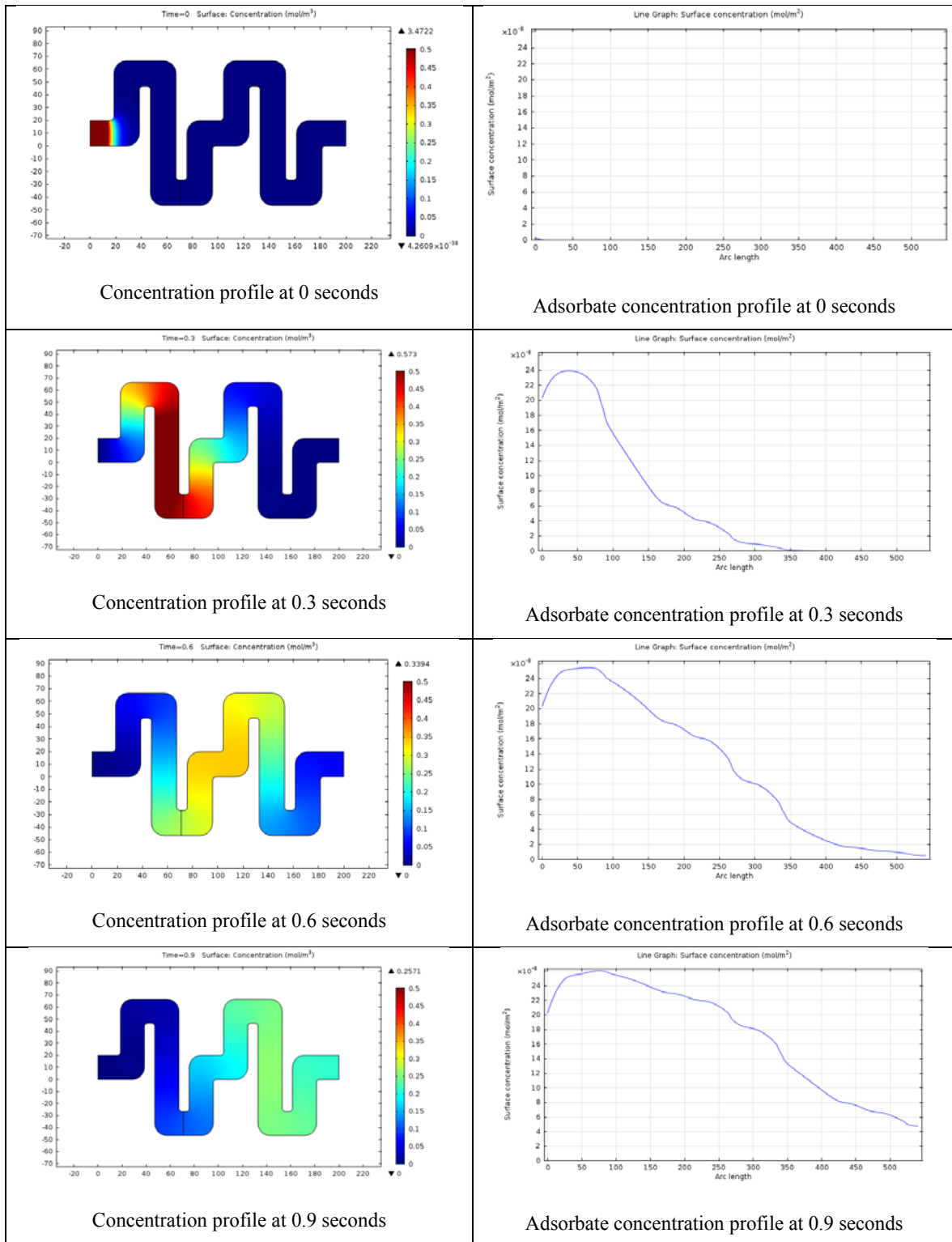


**Figure C-2.0.27** Concentration profile (left) and adsorbate concentration of the case of the discontinuous injection for time steps 0, 0.3, 0.6, and 0.9 seconds